Experimental investigation of wave induced vibrations and their effect on the fatigue loading of ships

A thesis submitted in partial fulfillment of the
requirements for the degree of
doktor ingeniør
by

Gaute Storhaug

Oslo, 11^{th} of September, 2007

Department of Marine Technology
Faculty of Engineering Science and Technology
Norwegian University of Science and Technology

Abstract

This thesis represents an attempt to reveal and explain the mysterious excitation sources which cause global wave induced vibrations of ships. The wave induced vibrations of the hull girder are referred to as springing when they are associated with a resonance phenomenon, and whipping when they are caused by a transient impact loading. Both phenomena excite the governing vertical 2-node mode and possibly higher order modes, and consequently increase the fatigue and extreme loading of the hull girder. These effects are currently disregarded in conventional ship design. The thesis focuses on the additional fatigue damage on large blunt ships.

The study was initiated by conducting an extensive literature study and by organizing an international workshop. The literature indicated that wave induced vibrations should be expected on any ship type, but full scale documentation (and model tests) was mainly related to blunt ships. While the theoretical investigation of whipping mostly focused on slender vessels with pronounced bow flare, full scale measurements indicated that whipping could be just as important for blunt as for slender ships. Moreover, all estimates dealing with the fatigue damage due to wave induced vibration based on full scale measurements before the year of 2000 were nonconservative due to crude simplifications. The literature on the actual importance of the additional fatigue contribution is therefore scarce.

The workshop was devoted to the wave induced vibrations measured onboard a $300m$ iron ore carrier. Full scale measurements in ballast condition were compared with numerical predictions from four state-of-the-art hydroelastic programs. The predicted response was unreliable, and the programs in general underestimated the vibration level. The excitation source was either inaccurately described or lacking. The prediction of sea state parameters and high frequency tail behavior of the wave spectra based on wave radars without proper setting and calibration was also questioned. The measurements showed that vibrations in ballast condition were larger than in the cargo condition, the vibration was more correlated with wind speed than wave height, head seas caused higher vibration levels than following seas, the vibration level towards beam seas decayed only slightly, and the damping ratio was apparently linear and about 0.5%. The additional vibration damage constituted 44%

of the total measured fatigue loading in deck amidships in the North Atlantic iron ore trade, with prevailing head seas encountered in ballast condition.

Four hypotheses, which may contribute to explain the high vibration levels, were formulated. They include the effect of the steady wave field and the interaction with the unsteady wave field, amplification of short incident waves due to bow reflection, bow impacts including the exit phase and sum frequency excitation due to the bow reflection. The first three features were included in a simplified program to get an idea of the relative importance. The estimates indicated that the stem flare whipping was insignificant in ballast condition, but contributed in cargo condition. The whipping was found to be sensitive to speed. Simplified theory was employed to predict the speed reduction, which was about $5kn$ in $5m$ significant wave height. The estimated speed reduction was in fair agreement with full scale measurements of the iron ore carrier.

Extensive model tests of a large 4-segmented model of an iron ore carrier were carried out. Two loading conditions with three bow shapes were considered in regular and irregular waves at different speeds. By increasing the forward trim, the increased stem flare whipping was again confirmed to be of less importance than the reduced bottom forces in ballast condition. The bow reflection, causing sum frequency excitation, was confirmed to be important both in ballast and cargo condition. It was less sensitive to speed than linear springing. The second order transfer function amplitude displayed a bichromatic sum frequency springing (at resonance), which was almost constant independent of the frequency difference. The nondimensional monochromatic sum frequency springing response was even higher. The sum frequency pressure was mainly confined to the bow area. Surprisingly, for the sharp triangular bow with vertical stem designed to remove the sum frequency effect, the effect was still pronounced, although smaller. The reflection of incident waves did still occur.

In irregular *head* sea states in ballast condition whipping occurred often due to bottom bilge (flare) impacts, starting with the first vibration cycle in *hogging*. This was also observed in cargo condition, and evident in full scale. This confirmed that the exit phase, which was often inaccurately represented or lacking in numerical codes, was rather important. Flat bottom slamming was observed at realistic speeds, but the vibratory response was not significantly increased. Stern slamming did not give any significant vibration at realistic forward speeds.

The fatigue assessment showed that the relative importance of the vibration damage was reduced for increasing peak period, and secondly that it increased for increasing wave heights due to nonlinearities. All three bows displayed a similar behavior. For the sharp bow, the additional fatigue damage was reduced significantly in steep and moderate to small sea states, but the long term vibration damage was less affected. The effect of the bulb appeared to be small. The contribution of the vibration damage was reduced significantly with speed. For a representative North Atlantic iron ore trade with head sea in

ballast and following sea in cargo condition the vibration damage reduced from 51% at full speed to 19% at realistic speeds. This was less than measured in full scale, but the damping ratio of 1-3.5% in model tests was too high, and the wave damage in following seas in cargo condition was represented by head sea states (to high wave damage due to too high encounter frequency). Furthermore, the contribution from vibration damage was observed to increase in less harsh environment from 19% in the North Atlantic to 26% in similar World Wide trade. This may also be representative for the effect of routing. The dominating wave and vibration damage came from sea states with a significant wave height of $5m$. This was in agreement with full scale results. In ballast condition, the nonlinear sum frequency springing appeared to be more important than the linear springing, and the total springing seemed to be of equivalent importance as the whipping process, which was mainly caused by bottom bilge (flare) impacts. All three effects should be incorporated in numerical tools.

In full scale, the vibration response reached an apparently constant level as a function of wave height in both ballast and cargo condition in head seas. This behaviour could be explained by the speed reduction in higher sea states. The vibration level in cargo condition was 60-70% of the level in ballast condition. Although common knowledge implies that larger ships may experience higher springing levels due to a lower eigenfrequency, a slightly smaller ore carrier displayed a higher contribution from the vibration damage (57%) in the same trade, explained by about $1m$ smaller draft. Moreover, the strengthening of the larger ship resulted in a 10% increase of the 2-node eigenfrequency. The subsequent measurements confirmed that an increased hull girder stiffness was not an effective means to reduce the relative importance of the vibration damage.

The relative importance of the excitation sources causing wave induced vibration may differ considerably for a slender compared to a blunt vessel. Therefore, full scale measurements on a $300m$ container vessel were briefly evaluated. The damping ratio was almost twice as high as for several blunt ships, possibly due to significant contribution from the container stacks. The reduced relative importance of the vibration damage with increasing wave height for the iron ore carrier in full scale was opposite to the trend obtained for the container vessel. Less speed reduction in higher sea states was confirmed, and the whipping process was apparently relatively more important for the container vessel. Both for the blunt and slender ship of roughly $300m$ length, the total fatigue damage due to vibration was of similar importance as the conventional wave frequency damage. The contribution to fatigue damage from wave induced vibrations should be accounted for, for ships operating in harsh environment with limited effect of routing, especially when they are optimized with respect to minium steel weight.

The four hypotheses were all relevant in relation to wave induced vibrations on blunt ships. Further numerical investigation should focus on the sum frequency springing caused by bow reflection and the whipping impacts at the bow quarter. The wave amplification, steady wave elevation and the exit phase must be properly incorporated. When it comes to *design by testing*, an optimized model size must be selected (wall interaction versus short wave

quality). The speed must be selected in combination with sea state. The wave quality must be monitored, and a realistic damping ratio should be confirmed prior to testing. For the purpose of investigating sum frequency excitation, a large restrained bow model tested in higher waves may be utilized to reduce uncertainties in the small measured pressures.

Acknowledgements

Prof. Torgeir Moan and Prof. Odd M. Faltinsen have been my supervisors. They took different roles, and I am deeply grateful for their contribution. They were professional, positive, supportive and understanding, and they serve as an inspiration for me and others. I am also pleased to see that Prof. Moan and Prof. Faltinsen have continued the research within this field at CeSOS.

The Department of Marine Technology granted me a four year scholarship including one year as a research assistant, and DNV awarded me a scholarship to cover other expenses. I am thankful for their funding, the opportunity I have been given and the flexibility they have shown in order for me to finish this thesis. CeSOS, Marintek and Anders Jahre's fund sponsored the experiments. The experiments were expensive, resource demanding, but rewarding. I would like to thank the staff of Marintek, in particular Ole David Økland, for their comradeship and flexibility.

DNV gratefully initiated the workshop, which gave me the opportunity to meet many good collegues: Prof. Jørgen Juncher-Jensen, Dr. Finn Rüdinger and Dr. Jelena Vidic-Perunovic from DTU, Michiel van Tongeren from DUT, Jens Bloch Helmers, Gabriel Holtsmark and Øyvind Lund-Johansen from DNV, Prof. XueKang Gu from CSSRC and Dr. Ole A. Hermundstad and Dr. Mingkang Wu from CeSOS. Thanks for many fruitful discussions and positive attitude.

DNV provided free access to extensive full scale measurements, which were helpful to my understanding of wave induced vibrations. This resulted in four papers together with my good collegues Gabriel Holtsmark and Erlend Moe from DNV and PhD student Ingo Drummen.

I enjoyed my stay in Trondheim, where I met many good colleagues, who made the time memorable and the working atmosphere excellent. Special thanks to Torgrim Driveklepp, Dr. Lars Rønning and Dr. Svein Ersdal for many evenings where world problems were

solved.

I am honored to have Prof. Jørgen Juncher Jensen (DTU), Dr. Svein Skjørdal (Grenland Group) and Prof. Sverre Steen (administrator, NTNU) as the doctoral committee. They have a strong background within the same research topic, and their publications have also served as an inspiration. I am grateful for their thorough comments and criticism of this thesis, and I am looking forward to the discussions on the day of the defense.

Finally, I would like to thank my family for all support, patience and for listening to my occasional frustration. I am also sorry for the days I was away from my kids, who were born in Oslo in September 2004. Unfortunately, only one third of the model experiments was finished by then, and there was still 9 months of the PhD period left.

This thesis is dedicated to my twins, Simen and Elias.

Contents

Nomenclature

General Rules

The variables will be defined the first time they are used.

Subscripts

D	Dipole
c	Cradle
m	Model scale
f	Full scale, or flexible
T	Total
st	Static
s	Springing
S	Source
dyn	Dynamic
max	Maximum
sum	Sum frequency
r	Rigid or response
R	Response

Superscripts

L	Loading condition
S	Sea state
env	Envelope
T	Torsethaugen
t	Total

Roman symbols

A_{33}	3D added mass
A_S	Effective shear area
A_v	Vertical projected area of cross sectional structure
A_T	Transverse projected wind area
a, a_r, a_f, a_{33}^{2D}	Sectional added mass per unit length of rigid and flexible modes
a_i	Force amplitude
a	Arm from centre of gravity to additional mass
$\overline{a}$	Coefficient in SN-curve
B, B_f	Breadth, foil width
Bn	Beaufort number
$\mathbf{B}$	Damping matrix
b, b_{33}^{2D}	Damping and 2D damping in heave due to heave
b_f, b_{hl}	Foil damping, hull lift damping
b_1, b_2, b_{tot}	Linear, nonlinear and total linearized damping
C	Constant in Bernoulli's equation
$C_{T,w,V,AA,BD}$	Total, wave, viscous, air and base drag resistance coefficient
C_F	Flat plate friction coefficient
ΔC_F	Roughness allowance
C_{aw}	Coefficient of added resistance in waves
$\mathbf{C}$	Stiffness matrix
c	Water particle speed in z-direction or foil coord length
c	Water plane stiffness per unit length or effective wet width
$\mathbf{m}$	Element stiffness mass matrix
c^{VBM}	Whipping criterion
c^{Δ}	Addition to whipping criterion due to natural decay
D	Depth or cummulative fatigue damage
D	Diameter for propeller or dynamic amplification
$\mathbf{D}$	Influence matrix for unit dipoles
$d_{n,i}$	3 hour damage in sea state i and in loading condition n
d	Distance between centre of tank and side
d	Force panel diameter
ds	Surface element length
E	Young's modulus, $2.1 \cdot 10^{11} Pa$
$E(h\|t)$	Mean nondimensional wave height given nondimensional period
F_s	Impact force
F_d	Damping force
F_h	Harmonic oscillating linear force
F_n	Froude number $= U/\sqrt{Lg}$
FXi	Axial force in sensor number i
FYi	Shear force in cut number i

FP	Force on force panel
f	Frequency in Hz [1/s], force, mode dependent factor or fraction
$f(y)$	Gaussian probability density function; Gaussian Bell
G	Shear modulus
g	Acceleration of gravity $\approx 9.81[\mathrm{m}/s^2]$
$H(\omega)$,$\lvert H(\omega)\rvert$	Transfer function and transfer function amplitude
$H(\omega_i,\omega_j)$, $\lvert H(\omega_i,\omega_j)\rvert$	Second order transfer function and absolute value
H_S	Significant wave height $[m] \approx H_0$
H	Regular wave height
H_r, H_μ	Hull roughness height
h	Submerged water height or nondimensional wave height
h	Height from point of rotation to centre of gravity.
h_{keel}	Height from point of rotation to keel
I, I_v, I_h	Area moment of inertia abt. vertical and horis. neutral axis $[m^4]$
I^t	Total mass moment of inertia $[kgm^2]$
I_m	Model mass moment of inertia about COG
$\mathbf{I}$	Diagional matrix
$\mathbf{i},\mathbf{j},\mathbf{k}$	Unit vector in x-, y- and z-direction
i	Complex number $= \sqrt{-1}$
k_i	Wave number $= 2\pi/\lambda$
k_0	Form factor or wave number
k_θ	Rotational stiffness
k_z	Shear stiffness
k	Constants in 3D added mass expressions
L	Length, normally length between perpendiculars
L_{pp}	Length between perpendiculars
L_{WL}	Length at water line
L_{OA}	Length overall
M	Total mass or moment
$\mathbf{M}$	Mass matrix
M_i	Mass for segment i
m	Mass per unit length or SN-curve inverse slope
m	Additional mass
$\mathbf{m}$	Consistent element mass matrix
m_0	Standard deviation and zero moment of spectrum
m_2	Second moment of spectrum
N	Number of samples/elements/cycles to failure or normal force
n_i	Unit normal vector in direction i
n_i	Number of cycles in stress range i
$\mathbf{n}$	Normal vector on boundary (hull) pointing into the fluid
n	Number of cycles or high frequency tail factor
n	Propeller revolutions per second
P, P_E	Power in kilowatt and engine power
P	Force per unit length

P_x	Axial force
Pi	Pressure sensor number i
$\mathbf{P}$	Force vector
p	Point on boundary (hull)
p	Probability density function
$p(h,t)$	Joint probability density function of wave height and period
$p(h\|t)$	Conditional probability density function of wave height given period
p_n^L	Probability of loading condition number n
p_i^S	Probability of sea state number i
p	Pressure
p_{av}	Average pressure from force panel
Q	Shear force
q	Field point
q_i	Principle coordinate number i
$\mathbf{q}$	Principal coordinate vector
R_T	Total wave resistance
R_{aw}	Added resistance in waves [N]
$R_{xx}(\tau)$	Autocorrelation function
$RELi$	Relative motion sensor i
R, r_i	Response amplitude (for component i)
r	Radius of gyration
$\mathbf{S}$	Influence matrix for unit sources
S	Wet surface area, or wave steepness
$S(\omega)$, $S_x(\omega)$	Wave spectrum and response spectrum
$S_{xx}(\omega)$	Spectrum of response x
$S_e(\omega)$	Encounter spectrum
S_B	Base drag area
s	Wavelet layer variable or springing build up length
s, n	s- & n- local coordinates in S-N plane
T	Draft or time
T_{AP}, T_{FP}	Draft at aft and forward perpendicular
T_P, T_Z	Peak and zero-upcrossing period
T_0	Wave period or time at end of impulse
t	t-factor from t-distribution, time or period
t	nondimensional period
t_r	t-factor for rejection based on normal distribution
U	Vessel speed, current speed or wind speed
U_e	Tangential velocity along the hull at still water level
u	Deflection in u-direction (vertical)
$\mathbf{V}$	Velocity vector for fluid particles
V_R	Relative velocity
V	Vessel speed or wind speed
$\mathbf{V}$	Velocity vector of fluid particles
W_d	Dissipated work

WPi	Wave probe number i
w	Deflection
x, y, z	x-, y- & z- global coordinates
$\overline{x}, \overline{y}, \overline{z}$	x-, y- & z- local coordinates
X_i	Unspecified sample number i
$\overline{X}$	Mean value of unspecified parameter
$X(\omega)$	Complex spectrum of response x
y	Vertical deflection
$\mathbf{y}$	Displacement vector for various degrees of freedom
z_{na}	Vertical distance from base line to neutral axis
z_c	Vertical distance from base line to apex of cone
Z	Complex number; distance between field point and hull point

Greek symbols

α	Philips constant in JONSWAP, dead rise angle of cone or stiffness ratio
β_i	Frequency/mode dependent term in the beam equation
β_i	Nondimensional frequency = ω/ω_s
β_1, β_2	ω/ω_s corresponding to specific response level on each side of the resonance peak
β	Heading angle relative to ship (0^0 is head sea)
Φ, Φ_s	Velocity potential and total steady potential
ϕ_s	Steady disturbance potential
$\phi_{1,2,T}$	Linear, second order & total potential
γ	JONSWAP peakness parameter
γ, β	Newmark-β parameters
ϵ_i	Random phase number
$\eta_{1,2,3,4,5,6}$	Motion in surge, sway, heave, roll, pitch & yaw
η_t	Total effciency coefficient
η	Maximum usage factor
ρ	Density of water; 1.025/1.0 $tonnes/m^3$ for sea water/fresh water
σ	Stress, standard deviation or a constant
σ^2	Variance
$\sigma_{\overline{X}}$	standard deviation of mean value
$\Delta\sigma$	Stress range
δ, δ_r, $\delta_{f,i}$	Damping ratio in % of rigid and flexible mode number i
δ_i	Phase angle number i
λ	Wave length
Λ	Scale; ratio of full scale dimension to model scale dimension
ζ, ζ_r	Wave amplitude, radiated wave amplitude
ζ_s, ζ_a	Steady & incident wave amplitude

ζ_I, ζ_T	Incident & Total wave amplitude
ζ_1, ζ_2	Wave amplitude corresponding to linear and sum frequency springing
ω	Vertical deflection or wetting factor (pile up)
ω_0	Wave frequency $[rad/s]$
ω_i	Wave frequency number i or natural frequency for mode i
ω_e	Encounter frequency
ω_c	Critical wave frequency
ω_d	Damped natural frequency
ω_p	Peak frequency
ω_2, ω_s	2-node natural springing frequency
ω_{EI}	Natural frequency due to pure bending stiffness
$\overline{\omega}$	Vorticity vector or eigenvalue vector
Ω	Submerged volume
Ψ_i	Mode shape number i
$\psi(t)$	Basic wavelet
$\mathbf{\Psi}$	Mode shape eigenvector
θ	Angle, vertex angle or rotation in degrees
θ_i	Phase angle (lag) for response component i
ν	Poisson ratio = 0.3 for steel, or viscosity coefficient of water = 10^{-6}
μ	Friction coefficient
μ_D	Mean value of damage
τ	Time

Abbreviations

ACCZi	Acceleration in z-direction at position i
ABS	American Bureau of Shipping
AD	Analog to digital
AP	Aft Perpendicular
B	Bichromatic
BEM	Boundary element method
BL	Base line
CL	Centre line
COG	Centre of gravity
CN	Classification Note related to DNV rules
CoV	Coefficient of Variation = standard deviation divided by mean value
CPU	Central Processing Unit (time)
CSSRC	China Ship Scientific Research Centre
DNV	Det Norske Veritas
DOF	Degree of freedom

DTU	Technical University of Denmark
DUT	Delft University of Technology
FE	Finite element
FFT	Fast Fourier Transform
FP	Forward perpendicular
FS	Full speed
GB	Gerritsma & Beukelman strip teory
GPS	Global Positioning System
HBM	Horizontal bending moment
HBM	Hoottinger Baldwin Messtechnik
HF	High Frequency
HTS	High Strength Steel (36 refers to yield stress of $355MPa$)
IACS	The International Association of Classification Societies
JONSWAP	Joint North Sea Wave Project (wave spectrum)
jpdf	Joint probability density function
kn	Knots = $0.5144m/s$
LAMP	3D sink source forward speed program developed at MIT
LCB	Longitudinal centre of buoyancy from aft part
LCG	Longitudinal centre of gravity from aft part
Lin	Linear
LNG	Liquified Natural Gas
LR	Lloyds Register
LSQR	Least square root
MIT	Massachusetts Institute of Technology
M	Monochromatic
MLER	Most likely extreme response
NL	Nonlinear
NTNU	Norwegian University of Science and Technology
O()	Order of Magnitude
Pa	Pascal = N/m^2
POSi	Position sensor number i between rigid segments
PM	Pierson-Moskowitz wave spectrum
RAO	Response Amplitude Operator
RMS	Root Mean Square
RO-RO	Roll on roll off
RS	Reduced speed
SCF	Stress Concentration Factor
SDOF	Single degree of freedom
SES	Surface Effect Ship
SN	SN-curve; Stress and Number of cycles to failure
STF	Salvesen, Tuck & Faltinsen strip theory
TIMSER	Time simulation program developed at DNV
TA	Towing force sensor aft
TF	Towing force sensor forward

TLP	Tension Leg Platform
Torsethaugen	Two peak wave spectrum
TRF	Transfer function
UK	United Kingdom
USSR	Union of Soviet Socialistic Republics
VBM	Vertical bending moment
VCG	Vertical centre of gravity above keel
VSF	Vertical shear force
VERES	2D strip theory program from Marintek
WAMIT	3D sink source zero speed program developed at MIT
WASIM	3D sink source forward speed program developed at MIT/DNV
WF	Wave Frequency
WL	Water line
2D	2-dimensional
3D	3-dimensional

Mathematical operators and other symbols

d	Derivative
∇	Mathematical differential operator $= \frac{\partial}{\partial x}\mathbf{i} + \frac{\partial}{\partial y}\mathbf{j} + \frac{\partial}{\partial z}\mathbf{k}$
∇	Displacement $[m^3]$
$\times$	Cross product of vectors
∂	partial derivative for a function with more dependents
$\frac{D}{Dt}$	material (substantial) derivative following a particle in space, $= \frac{\partial}{\partial t} + \mathbf{V} \cdot \nabla$
^{0}	Degrees
$_t$	Time derivative
$_{II,III,IV}$	Second, third and fourth derivative in space
$_{x,y,z}$	Derivative in x-,y- & z-direction
ℓ	Length, integration along the water line; finite element length
$\dot{}$	Time derivative
$\ddot{}$	Second time derivative
$\overline{X}$	Overline refers to mean value, vector symbol or nondimensional quantity
*	Complex conjugate

Chapter 1

Introduction

Ships are as a minimum designed to withstand load effects due to still water loading and wave loading. Other loads are considered depending on the ship type and intended operation. The ship is normally considered as a rigid body in the dynamic analysis carried out to determine the deflection and stress in the structure. However, in reality a ship is flexible.

When the natural frequencies are sufficiently low structural dynamics may be excited by different mechanisms. In some cases, the flexible vibration may play an important role in the fatigue and ultimate strength as well as for comfort. The present thesis focuses on the wave induced vibrations of the whole hull girder, in particular, for large conventional monohull ships. The consequence in terms of accelerated fatigue damage is the main concern.

1.1 Background and motivation for the present work

The motivation was threefold. Full scale measurements of the ship considered herein confirmed the presence of wave induced vibrations. The current ship rules disregard flexible vibrations, and comparison between numerical predictions and measurements revealed poor agreement.

The background and relevance of this work have been presented in more detail by Storhaug et al. (2003), Moe et al. (2005) and Storhaug et al. (2006). DNV personnel and others were strongly involved, thus, the references are not included in this thesis. Both the references and this thesis consider the large blunt ore carrier in Figure 1.1, which is referred to as *the ship* or *the vessel*. In the following the background is briefly summarized.

Figure 1.1: *The large blunt iron ore carrier in cargo condition.*

1.1.1 Recent experiences from a ship in operation

Inspection onboard *the ship* revealed cracks after one year of operation in the North Atlantic. The ship, built to HTS36 standard, satisfied the IACS's requirements. Obviously, these requirements were insufficient to avoid the fatigue cracks. Figure 1.2 presents a typical crack observed after one year.

Extensive finite element (FE) and wave load analyses proved that the stress concentration factor (SCF) was well above the commonly assumed SCF, and that the fatigue life was well below 20 years. Still, there was a mismatch between the predicted and observed fatigue life. As a result a DNV monitoring system was installed in 1999. The measurements confirmed basically continuous wave induced vibrations, and more measurements were carried out to determine its consequence.

The fatigue contribution from wave induced vibration became a concern (again), and DNV developed a preliminary Guidance Note to account for the vibrations. A similar ship was

Figure 1.2: *Picture of a longitudinal stiffener in deck in way of the transverse bulkhead, and located in the ballast tank. The crack originated from the bracket toe termination.*

built to increased strength standard, and the particular ship was repaired and strengthened in 2000. Further history has been given by Moe et al. (2005).

1.1.2 Comparison between measured and predicted vibration response

In January 2002 a *DNV workshop on fatigue strength analysis of ships* was arranged in Finland. DNV presented preliminary results from full scale measurements, while Jensen and Vidic-Perunovic (2002) presented suggested guidelines to avoid excessive springing vibrations. The ship was found satisfactory according to the guidelines, even so the ship *was* vibrating heavily.

A *DNV workshop on springing 2002* was initiated with participants from DNV, DTU, DUT, NTNU/Marintek and CSSRC. Ten different sea states were selected from the full scale measurements in ballast condition. The measured vibration and wave responses were

compared to predictions from four state-of-the-art nonlinear hydrodynamic codes, which all include the effect of flexibility. Wave radar measurements were used as input. All programs failed to predict reliable estimates of the hull vibrations, and in general, the predicted vibration level was too low. It was concluded that the important excitation mechanism was either missing or inaccurately described. The work was summarized by Storhaug et al. (2003). Moe et al. (2005) indicated that the measured sea states, used as input to the predictions, were overestimated. Since the calculations gave results on the lower side, the differences are expected to increase.

1.1.3 Today's rule requirements

The current IACS rules disregard wave induced vibrations as a contribution to extreme and fatigue loading. Only some nonlinear effects are included in the extreme bending moment, since bow impacts and whipping to a certain degree can be avoided by course changes and speed reduction, (Mürer 1995). Classification societies such as DNV, ABS and LR have, however, operated with their own additions related to bow impacts.

The IACS wave bending moments were also stated in the Joint Tanker Project Rules issued by ABS, DNV and LR, (DNV et al. 2004), and in the Joint Bulk Project Rules issued by IACS, (IACS 2004). In these new rules, the whipping addition from the individual classification societies has actually been removed for tankers and bulk carriers. Without adjusting the acceptance criteria accordingly, this may signify a reduction in the safety level.

Based on extensive full scale measurements carried out by DNV, the preliminary Guidance Note, proposed as a consequence of the preliminary measurements on the ship, was rejected. A revised Guidance Note was proposed, (DNV 2005b).

1.2 A dive into literature

Originally, the intention was to investigate the effect of springing. During the research it became evident that whipping must be included. In terms of the consequence for fatigue, the high frequency response due to springing and whipping may be considered as one topic. Before diving into the published documentation, and in the present context of this research, a few main terms need to be defined.

Wave induced vibration: All local and global vibrations caused by waves, such as springing, whipping, swinging (horizontal 2-node), double bottom vibration etc. In this thesis, *wave induced vibration refers to whipping and springing*, and may simply be denoted as *vibration*.

Springing: Conventionally, springing is defined as stationary resonance vibration of the vertical 2-node mode due to waves with encounter frequency coinciding with the natural 2-node frequency. In the present research this definition is refined. *Springing is stationary or apparently stationary resonant vibration due to oscillating wave loads and wave impacts that excite the vertical 2-node mode.* This includes nonlinear forces that may oscillate more locally, and small wave impacts, which due to low damping will be difficult to distinguish from stationary springing in irregular sea.

Whipping: Conventionally, whipping is defined as transient hull girder vibration caused by an impact. It is not necessarily related to waves. In consistency with the definition of springing, *whipping is detectable transient vibration due to wave impacts.* Whipping vibration may be identified by the presence of higher vibration modes, but the vertical 2-node mode is normally dominant amidships. The whipping response depends on the pressure time history of the impact, and the natural periods of the structure.

Hydroelasticity: *The interaction between the hydrodynamic loading and the elastic deformation associated with the vibration is considered.* The interaction may affect both the loading and vibration level. The importance of the hydroelasticity depends on the nature of the impact, the flexibility and the level of the flexible response.

There are also a few other terms often used that need clarification.

- **Springing frequency (period)** refers to the natural frequency (period) of the vertical 2-node vibration.
- **Wave frequency (WF)** response refers to the range of wave frequencies related to conventional *rigid body response* that is normally considered important. *Wave damage* refers to the fatigue damage from the WF response, which is wave/low pass filtered.
- **Total damage** refers to the fatigue damage from the total measured stress signal (only filtered for noise).
- **High frequency (HF)** response refers to the dynamic flexible response in particular at the springing frequency. High frequency in this context is related to the lowest natural frequency of the structure, and may appear as confusing for "noise and vibration people". The high frequency damage may also be referred to as *vibration damage*, and constitutes more than the fatigue damage from the high pass filtered stress. It is the difference between the total damage and the wave damage.

1.2.1 The beginning

The first digression of wave induced hull vibrations, irregular in time and quickly damped out, came during 1880'ies, (Schlick 1884). *Hydroelasticity* as a term was introduced in

1959, (Heller and Abramson 1959), while the methodology had already been used within the aeronautical field for several years, (McGoldrick 1960). Todd (1961) stated that transient vibrations due to slamming in case of large pitching and heaving motions were of intermittent or minor importance, but his concern was engine/propeller induced vibrations. Within this field elastic models were tested already in 1935, (McGoldrick 1935).

The terms *springing* and *whipping* were apparently introduced during the sixties, but the phenomena were known earlier. Sauvalle (1960) measured 2-node vibrations in relatively moderate sea conditions on the ore carrier *Jean Schneider*. This may be the first documentation of measured springing. Up to the mid seventies springing was sometimes used to cover both terms.

The theoretical research of wave induced vibration, in particular springing, was a result of observations made from full scale measurements carried out to investigate wave loading on large ships. This was necessary due to the trend towards increased length beyond the validity of the empirical ship rules. A 'shudder' was observed from measurements on the $216m$ Great Lakes ore carrier *Shenago II*, (Yagle 1963), lengthened by $29m$ and renamed *Charles M. Beeghly* in 1971. Cleary et al. (1971) revealed springing to be the most frequent dynamic stress mechanism on the $217m$ Great Lakes carrier *Edward L. Ryerson*. The amplitude was in a few occasions so high that it should be considered in design. These vessels were narrow (length to width ratio of up to 10), blunt and sailing on small draft in addition to being more flexible than ocean going vessels. The shallow waters on the Great Lakes reduced the natural frequency further, and the steep shores caused reflection and confusing seas, which contributed to springing.

The springing research began more or less independently and simultaneously in USSR, considering similar ships sailing on inland waters. Full scale measurements were available to Belgova (1962), who investigated springing by a theoretical approach after conducting model tests. This may be the first attempt to predict springing.

In addition to increased ship size, which reduce the natural springing frequency, there may be other factors that increased the awareness of springing during this period. The damping reduced as a consequence of increased ship size, moreover, the damping reduced for welded ships compared to riveted ships.

1.2.2 Ship measurements considering wave induced vibrations

During the mid thirties measurements were carried out onboard the vessel *San Francisco*, (Hoffman 1972). Ten years later the vessel *Ocean Vulcan* was instrumented, but first during the sixties the science of full scale measurements took off. Wave induced vibrations were frequently observed, and occasionally it was considered as noise. Gunsteren (1978) provided an overview of references with observed vibration including 4 publications on Great Lakes bulk carriers, 10 on ocean going bulk carriers, 14 on tankers and 8 on con-

tainer ships. Additional references were provided by Storhaug et al. (2003) and Moe et al. (2005). The amount of observations strongly suggest that wave induced vibration can be anticipated on all ships, not proving that it is important, but that it may contribute to the fatigue and extreme loading.

Only a few men explored wave induced vibrations in more detail. The Great Lake bulk carrier *S.S. Ontario Power*, similar to *Edward L. Ryerson*, was investigated, (Mathews and Kawerninski 1967). This vessel was strengthened for ocean going operations. Later full scale measurements of three Great Lakes vessels, *S.J. Cort* (305m), *W.C. Ford* (192m) and *C.M. Beeghly* (246m), were compared to linear theory, (Stiansen et al. 1978). Several ocean going vessels were also subjects for attention illustrated by the following list.

⋆ Bell and Taylor (1968) carried out measurements on a 47 000 dwt. tanker, partly riveted, in ballast condition with and without bulbous bow.

⋆ Nordenstrøm et al. (1970) reported extensive springing measurements from a 203 000 dwt. tanker, *Berge Commander*, in ballast and cargo condition.

⋆ Goodman (1971) referred to full scale measurements of a 192 000 dwt. tanker, *SS Myrina*.

⋆ Little et al. (1971) carried out measurements on four tankers and one bulk carrier ranging from 66 500 to 326 585 dwt. The purpose was to investigate ordinary wave loading, but all revealed wave induced vibration (whipping on the bulk carrier).

⋆ Whipping was measured on an 80000 dwt. tanker *M.T. B-Maru*, which had its bow replaced with a bulbous bow, (Tasai et al. 1971).

⋆ Skjørdal (1974) performed measurements on a 60 000 dwt. bulk ship in order to determine the cause of the vibration.

⋆ Hure (1973) reported measurements on two 250 000 dwt. tankers, *Emeraude* and *Jade*, in ballast condition.

⋆ Gran (1974) carried out preliminary measurements on a 255 000 dwt. tanker, *Esso Bonn*, on a ballast trip. Gran (1976) reported the consequence of vibration on the fatigue and extreme loading from extensive measurements in ballast and cargo condition.

⋆ Kagawa et al. (1977) carried out springing measurements on a 237 000 dwt. tanker.

⋆ Lopes and Troymann (1989) instrumented an 18 000 dwt. tanker for the purpose of evaluating the fatigue damage from springing based on a single ballast trip.

⋆ Lacey and Chen (1995) reported the consequence of springing and whipping on the fatigue and extreme loading from extensive measurements in ballast and cargo condition based on a 190 000 dwt. ARCO tanker, *California*.

⋆ Storhaug et al. (2003) reported the consequence of vibration on the fatigue damage from one year of measurements in ballast and cargo condition of *the ship*.

⋆ Moe et al. (2005) reported the consequence of vibration on the fatigue damage from extensive measurements in ballast and cargo condition of the ship.

⋆ Storhaug et al. (2006) compared the ship with a 175 000 dwt. Capesize bulk carrier with respect to vibration damage.

What knowledge can be deduced from these publications? Relevant findings about the wave induced vibrations may be summarized as follows.

- The springing vibration was higher in ballast than in cargo condition, e.g. (Bell and Taylor 1968).
- The springing vibration was reduced 10-15% by increasing the ballast level in the fore peak tank, (Lopes and Troymann 1989).
- The springing vibration was higher in head seas than in beam and following seas, e.g. (Hure 1973). In general, the decrease towards beam seas was slight, and the maximum may occur at off head seas, (Gran 1976).
- Nordenstrøm et al. (1970) indicated that the occurrence of vibration was almost independent of the heading in ballast, but following the 'normal' trend in cargo condition.
- The RMS springing stress increased with increased significant wave height to a certain value. The peak was roughly at 3 to $5m$ depending on ship size, and the decay was less on the larger vessels, (Stiansen et al. 1978).
- The springing may come in 'bursts' or 'beats', (Little et al. 1971).
- The springing vibration was relatively low at high Beaufort strength on the tankers, e.g. (Little et al. 1971).
- The vibration was sensitive to speed, e.g. (Skjørdal 1974). The vibration appeared to increase with the square of the speed, (Bell and Taylor 1968), or more and may be pronounced also at zero speed, (Gran 1974).
- The vibration increased with Beaufort strength, e.g. (Kagawa et al. 1977). The occurrence of vibration was independent of Beaufort strength in ballast, opposite to cargo condition, (Nordenstrøm et al. 1970).
- The vibration may occur without evidence of slamming, and may be unaffected by slamming, e.g. (Bell and Taylor 1968).

- The vibration may exceed the wave bending, e.g. (Bell and Taylor 1968). The springing stress amplitude was 51% in average of the wave bending stress, (Gran 1974). The wave bending moment exceeded the vibration stress on the smaller vessel first for significant wave heights above $6m$, (Stiansen et al. 1978).

- The vibration, sometimes unpleasant, was felt onboard, e.g. (Skjørdal 1974). It was visible, e.g. (Castberg and Gran 1976).

- The bulbous bow did not seem to affect the vibration level, e.g. (Bell and Taylor 1968).

- The whipping vibration and slamming often occurred when the bow enters the water, but the vibration may also originate on the up-pitching cycle resulting with a first half cycle in hogging, e.g. (Bell and Taylor 1968). Saunders (1965) explained this by rapid loss of buoyancy (one of his four excitation sources).

- Blunt ships may experience more vibration than slender ships, e.g. (Gran 1976). This was supported by the number of references on blunt ships, but their large sizes and lower damping may be contributing factors.

- Gran (1974) reported also about the apparently unstable front wave and the steady wave field which increased the bending moment significantly and linearly with speed.

- Bi-directional sea was reported, e.g. (Vidic-Perunovic 2005), which may effect the vibration level.

- The maximum of wave bending and vibration stress may not occur simultaneously, (Bell and Taylor 1968). The maximum wave bending and vibration stress can and do occur at the same time, (Stiansen et al. 1978). The combined amplitude process deviates from the Rayleigh distribution, (Gran 1980), but the wave and springing response were essentially narrow banded Gaussian processes when separated, (Gran 1977). The springing and wave stress can be considered as statistically independent variables, (Gran 1976). The combined stress was 5% larger than the square root relation, Kagawa et al. (1977).

- The heading distribution varies with trade. Even distribution was observed by Nordenstrøm et al. (1970), while dominating head seas in ballast and following seas in cargo condition were observed by Lacey and Edwards (1993).

- 26 bottom slams with severe whipping response were reported by Lacey and Chen (1995). It may also be rare events, (Storhaug et al. 2003).

- Wave conditions were in most cases based on visual observations, but in a few occasions wave buoys were used, (Cleary et al. 1971). Wave radar measurements in combination with fatigue assessment were first considered by Moe et al. (2005).

- The visual observations of the sea states overpredicted the height and underestimated the length compared to meteorological calculations, e.g. (Hure 1973).
- The vibration was observed in most sea states, e.g. (Little et al. 1971).
- Whipping was detected without significant rigid body motions, e.g. (Tasai et al. 1971).
- The whipping contribution to the total stress may be important, e.g. 55% increase to 114MPa on the bulk carrier *Fotini L*, (Little et al. 1971). Due to the whipping, the total response (127MPa static and $119NPa$ dynamic) may exceed the IACS design bending moment already at a significant wave height of above $9m$ in cargo condition, (Lacey and Chen 1995). *Mineral Seraging* and *Jordaens* showed an amplification due to whipping of 50% from full scale measurements in significant wave height of up to $8m$, (Kawakami et al. 1977). Large whipping responses were also illustrated on different warships, (Clarke 1986).
- Gran (1974) reported a 14% increase to 68MPa due to springing on a single ballast trip. Stiansen et al. (1978) stated that the maximum combined nominal stress level increased by 78% to 105MPa due to steady build up.
- A 7% increase of the 20 year extreme was estimated to come from springing, reaching a total of 118MPa, (Castberg and Gran 1976). This was probably underestimated with reference to the preliminary measurements on the single ballast trip, (Gran 1976).
- The voluntary and involuntary speed reduction may be significant in head seas, e.g. (Tasai et al. 1971). The speed reduction differed for a bulk carrier and a container vessel of similar size, (Moe et al. 2005).
- The wave spectrum energy in the high frequency tail represented an uncertainty, e.g. (Hure 1973). A possible overshoot of energy compared to standard wave spectra may correspond to a factor of two, (Goodman 1971).
- The uncertainty in damping was high, e.g. (Hure 1973). (Gran 1974) estimated the damping ratio to 1.14% from whipping, while values from spectra were 25% higher. The damping ratio in ballast condition was estimated to 0.5%, (Storhaug et al. 2006).
- The increased stiffness of the hull girder was said to be ineffective in order to reduce the relative vibration level, e.g. (Skjørdal 1974).
- The maximum nominal springing stress amplitude was measured to 61MPa, (Stiansen et al. 1978), and 40MPa, (Lacey and Chen 1995).
- Springing and whipping were difficult to separate, e.g. (Gran 1974), who also stated that whipping contributed in moderate sea states. Both springing and whipping contribute, (Little et al. 1971).

- The wave slope and natural period were defined as important parameters, (Gran 1977). The springing frequency for a given ship size had a standard deviation of $0.08Hz$, (DNV 1985).

- The fatigue damage from wave induced vibration constituted roughly by 21%, (Gran 1976), 30% (Lacey and Chen 1995), 77% (Lopes and Troymann 1989) and 44% before strengthening and 38% after, (Moe et al. 2005). The former three underestimated the contribution.

- Whipping was said to provide the major contribution to fatigue damage on landing crafts, (Clarke 1986).

- The fatigue damage rate increased when the springing share exceeded a certain limit, (Gran 1980). This may be SN-curve dependent.

- The impact slams (breaking waves against stem flare) occurred often in cargo condition, but not with a significant whipping response, (Lacey and Chen 1995).

- The momentum slamming due to sudden and fast immersion of the bow was identified 427 times during 3 months causing a nominal whipping stress amplitude above 34MPa, (Lacey and Chen 1995).

1.2.3 Model experiments considering wave induced vibrations

Model tests were performed to investigate physics under more controlled environment, to validate computer programs or as an alternative to less reliable computer programs. The results have often be regarded as the 'truth', without considering the uncertainties.

A method to measure the wave bending moment by a jointed model was developed by Lewis (1954), but the first elastic model test was carried out by McGoldrick and Russo (1956), who investigated 'whipping' on *SS Gopher Mariner*. Belgova (1962) performed later model experiments of an inland vessel with respect to linear springing in regular waves. The findings from selected references are listed and commented upon in the following.

- The flexibility has been represented in three ways: Backbone segmented model, (Achtarides 1979), continuous models, (Tasai 1974) and segmented model with local springs, (Jullumstrø and Aarsnes 1993). The latter may provide a more reliable estimate of the bending moment.

- Flexible models were not always Froude scaled, e.g. (Slocum and Troesch 1982). Artificial low frequency will give higher hydrodynamic damping and possibly coupling with rigid modes.

- Continuous stiffness models gave too high springing frequency, e.g.(Tasai 1974), or too high damping, e.g. (Hashimoto et al. 1978).

- The wave quality in the model tank was poor, especially for short waves, e.g. (Hoffman 1972). It is necessary to investigate this prior to springing tests.
- Restrained models were investigated, e.g. (Slocum and Troesch 1982). These may be used to indicate the excitation sources and the coupling effect.
- Strip theory was not applicable for short waves less than roughly half the ship length and for high speeds, e.g. (Moeyes 1976). Strip theory may not be applicable for predicting springing.
- Higher harmonics were investigated in regular waves, e.g. (Kumai 1974). The contribution may come from whipping as well as springing, and the effect in irregular sea is uncertain.
- The higher order effects reduced in magnitude compared to the second order effect, e.g. (Hashimoto et al. 1978). The second order effect may be more important.
- Second order springing was investigated, e.g. (Kawakami and Kiso 1976). The importance was 30% in one sea state, (Slocum and Troesch 1982). More sea states must be considered.
- 2-segment models were used often, e.g. (Slocum and Troesch 1982). A small change in the mode shape might be important for the springing level, e.g. (Hoffman and van Hoof 1976), hence 2-segmented models may affect the springing response.
- The damping did not appear to be speed dependent for conventional designs, e.g.(Tasai 1974).
- The damping was speed and frequency dependent, e.g. (Hoffman and van Hoof 1976).
- The damping was often not properly addressed, e.g.(Goodman 1971).
- The elastic effect due to large whipping events was described as deflections traveling from bow to stern in sagging and from stern to bow in hogging, (Kawakami et al. 1977). This represents the presence of several modes.
- The blockage was not often considered, e.g. (Moeyes 1976). This may make it more difficult to capture the springing peak.
- Nonlinearities appeared to increase for shorter waves and higher speeds, e.g. (Moeyes 1976).
- Water tight sealing between segments was sometimes omitted, e.g. (Malenica et al. 2003). This may create additional damping and hydrodynamic forces.
- No aft part slamming was observed in low waves, but it was observed in high head sea waves due to a flat aft part, (Takarada et al. 1993).

- The static loading due to forward speed might be significant, e.g. (Moeyes 1976).
- Model tests were performed in head sea with only a few exceptions, e.g. (Watanabe and Sawada 1985).
- Bottom slamming might occur in ballast condition, but not in cargo condition. The former gave more vibration, e.g. (Watanabe and Sawada 1985).
- The springing response increased with increased flexibility, (Kapsenberg and Brizzolara 1999).
- The amplitudes including whipping deviated from the Rayleigh distribution, e.g. (Watanabe and Sawada 1985).
- Springing increased with speed, but the linear springing was less sensitive to speed than the second order springing, (Slocum and Troesch 1982).
- Hump-hollow behaviour of matched resonance or excitation forces was observed, e.g. (Slocum and Troesch 1982). Hump-hollow behaviour was not observed by (Achtarides 1979).
- Coupling between rigid body modes and springing was insignificant, e.g. (Achtarides 1979).
- Coupling between rigid body modes and springing was significant, e.g. (Slocum and Troesch 1982). This was derived based on unrealistic high natural period excited by second order springing, while the coupling appeared insignificant for linear springing.
- The waves in the aft part in head seas were significantly modified, e.g. (Takarada et al. 1993), possibly reducing the importance of the aft part.
- The excitation force in the aft part contributed significantly to the springing level, e.g. (Achtarides 1979). This may be based on the lack of excitation rather than high excitation.
- A transom stern gave twice the springing level compared to a cruiser stern, e.g. (Hoffman and van Hoof 1976). This could be due to lower damping and better matching of hump-hollow behaviour for the transom stern.
- The whipping doubled the total bending moment, e.g. (Takarada et al. 1993).
- Local hydroelastic effects in the bow part of a high speed vessel were insignificant, e.g. (Kapsenberg and Brizzolara 1999), due to too long rise time.
- Fatigue damage contribution from vibration was estimated to 30-45% in a few head and bow quartering sea states, but it was low in beam and following seas, e.g. (Dudson et al. 2001). This was the first model experiment where the vibration damage was evaluated. The natural frequency was too low, and the ship was a prototype.

1.2.4 Springing and whipping theories

The hydrodynamic theories considering ship responses in waves evolved from the fifties, and the superposition principle for irregular waves was first applied by St.Denis and Pierson (1953). A decade later flexible structure was introduced in the linear springing theory by Belgova (1962), while Kaplan et al. (1969) was probably the first who considered whipping. He solved the structural response both directly and with modal modes. A brief overview of some of the theories is provided in the following.

Simplified theories were developed to understand the behaviour of the structural response, and to indicate the importance of certain effects. Usually, analytical response of prismatic beams was considered without proper description of the excitation loads. Bishop et al. (1973) explained the terms *ship/wave matching* and *resonance encounter* herein referred to as hump-hollow behaviour and linear springing. Faltinsen (1980) considered linear springing from Froude-Kriloff excitation as well as simplified whipping. He illustrated the small effect of the restoring forces on the springing period. Hamid (1980) considered higher harmonics from second to fourth order and confirmed the importance of coupling with rigid modes. Sele (2001) evaluated the springing response from second order Froude-Kriloff excitation of bi-directional wave trains coming from arbitrarily directions. The effect may be significant for opposite wave directions and similar wave frequencies. Senjanovic et al. (2001) investigated whipping and pointed out that the maximum bending moment may not occur at the midship section, and the bending moment converges faster than the shear force with respect to number of modes included.

Linear springing strip theories constitute the dominating part of the springing references starting with Belgova (1962). Salvesen et al. (1970) developed a strip theory, which was often used as a basis for hydroelastic theory. They used the Haskind relation to estimate the diffraction forces. This theory is referred to as *STF*. Ertekin et al. (1995) confirmed that the Haskind(-Hanaoka) relation also applied to hydroelasticity. Another strip theory that has been widely used was developed by Gerritsma and Beukelman (1967), later modified by Gerritsma et al. (1974). This theory is referred to as *GB*. The STF theory appears to be more mathematical consistent accounting for the diffraction, while the GB theory was based on a relative motion hypothesis (between the ship and incident waves). Diffraction was approximated, often in combination with the obsolete Smith correction factor. Both theories were extended to nonlinear theories by others to consider nonlinear springing or whipping. The theories were not applicable for modified short waves relevant for springing, and for this purpose more complex theories are necessary. The strip theories may be more useful for whipping predictions, and to illustrate the importance of certain effects. They are also far more efficient than CPU demanding 3D simulations.

Linear hydroelastic slender body theory considering the Helmholtz equation to account for some modification of short waves along the ship was first considered by Skjørdal (1978) and Skjørdal and Faltinsen (1980). The structural response was solved directly, and both the

hydrodynamic and structural damping were regarded as important. The predicted vibration deviated significantly from model experiments of a tanker, but still it was a significant improvement compared to the GB theory. Slender body theory has also been applied by others, (Price and Wu 1986; Wu et al. 1991).

The linear high speed strip theory, (Faltinsen and Zhao 1991b; Faltinsen and Zhao 1991a), was refined to account for hydroelasticity by Wu et al. (1993). The high speed strip theory accounts for interaction of the steady field stepped from the bow and backwards. The steady field was known when the unsteady field was solved. The hydroelastic theory was applied to academic ship shaped structures. This theory was also applied by Hermundstad et al. (1994), and later refined by Hermundstad et al. (1999) to account for interaction between hulls of a catamaran.

Several linear 3D theories have been considered, e.g. (Price and Wu 1985; Bishop et al. 1986; Keane et al. 1991; Du et al. 1998; Bingham et al. 2001). The theories consider both mono and multihulls with different accuracy with respect to how the forward speed effects were handled. The forward speed will in general enter all parts of the theory, e.g. free surface condition, body boundary condition and source and force formulations. These parts were handled in different ways. Irregular frequencies may cause difficulties in some formulations as they may appear in the frequency range of the physical resonance frequencies.

Watanabe (1968) was probably the first who investigated *nonlinear* springing due to change of buoyancy and momentum from relative motion on non vertical ship sides, in particular at the bow. The ship was assumed to be restrained from moving in accordance to observations made on a 50 000 dwt. bulk carrier. The resulting force gave higher harmonics, which was believed to be the important mechanism. Subsequently, several Japanese researchers investigated higher harmonics effects, e.g. (Kumai 1972).

Jensen and Pedersen (1979) developed a quadratic strip theory in the frequency domain including flexible effects. The second order effects were related to perturbation of added mass, damping and non vertical sides at the still water line. The linear theory was optionally represented by the STF or GB theory. The flexibility was represented by a Timoshenko beam and modal superposition. The theory was further described by Jensen and Dogliani (1996), who predicted a 10% increase of the fatigue damage of a container vessel due to the elastic effects. The second order effect dominated the elastic contribution. The computer software has been widely applied in many references, e.g. (Jensen and Pedersen 1981; Jensen and Petersen 1992; Jensen 1993; Hansen et al. 1995; Naess 1996; Jensen 1996; Jensen and Wang 1998). The theory was recently modified to account for bi-directional seas as an additional second order contribution, (Vidic-Perunovic 2005). Comparison with full scale measurements confirmed that the second order effect from bi-directional sea improved the predictions in wave systems of opposite directions. Nonlinear springing was also considered by Søding (1975).

A second order perturbation theory was derived by Slocum (1983). Simplifications were introduced by assuming slender body theory, wall sided ships and zero speed. Limited calculation results were compared to model test results, (Slocum and Troesch 1982). He et al. (2004) refined this theory. Different approaches were used to solve the Helmholtz equation in head and oblique seas with empirical matching in between. The nonlinear terms consisted of the velocity square term from Bernoulli's equation, and solution of the second order near field problem for diffraction. Correction factors based on model tests were used for the latter.

The 3D program WAMIT developed at MIT include second order effects, but it was only valid for zero speed. It was applied to *the ship* by Birkenes (2000), and significant sum frequency springing was predicted. Problems with irregular frequencies and convergence were encountered.

Nonlinear whipping theories predict the response in time domain. Most of these were strip theories. Kaplan et al. (1969) developed a linear strip theory for oblique seas with bow flare slamming. The linear motions were input to the nonlinear force predictions, which accounted for the buoyancy and the material derivative of the added mass times the vertical velocity. The damping was defined as speed dependent. The calculations indicated that the 3-node mode was unimportant. Kaplan and Sargent (1972) extended the theory to include bottom slamming and linear springing in head seas. Convolution integrals were used to produce time domain results from frequency domain, but the three effects were considered separately. Many of the strip theories employ the bottom slamming approach by Ochi and Motter (1973), e.g. (Antonides 1975; Chen 1980; Gu et al. 1989; Domnisoru and Domnisoru 1997; Gu and Moan 2002), while others apply the expressions by Stavovy and Chuang (1976), e.g. (Aksu et al. 1991; Gu et al. 2003). Many other nonlinear strip theories have also been presented, e.g. (Yamamoto et al. 1978; Schlacter 1989; Xia et al. 1995; Xia et al. 1998; Wu and Hermundstad 2002; Gu and Moan 2002; Gu et al. 2003), but the presence of overlapping forces have in general not been properly dealt with.

Xia and Wang (1997) applied nonlinear hydroelastic slender body theory to a warship and the S175 container vessel. Experimental data from the latter was often used. The nonlinearities consisted of nonlinear restoring, Froude-Kriloff and momentum forces, and it was concluded that the linear 3D theory overestimated the rigid body motions and gave poor predictions of the bending moments. The elastic effects were small in the investigated sea states.

Wu et al. (1996) applied the high speed strip theory, and extended it to nonlinear hydroelastic theory. The time series were derived by convolution integrals, and the predictions were compared to experimental results of a catamaran. The nonlinear effects were significant, but differences from model tests were observed. This theory was later compared to linear hydroelastic theory in (Wu and Moan 1996).

There were only a few nonlinear 3D programs. Aksu et al. (1991) applied the slamming theory by Stavovy and Chuang (1976) on predefined hull elements on 3 barges. Lin et al. (1997) presented whipping predictions using the 3D nonlinear program LAMP(-2). This program includes nonlinear Froude-Kriloff and restoring. The impact loads were applied to a beam model, hence hydroelastic effects were disregarded. Comparison was made with model experiments of a naval ship, showing that the calculations underpredicted the whipping response, though the rigid body response was almost captured. A similar theory was described by Tongeren (2002), who used the DNV program WASIM to calculate the hydroelastic response of *the ship*. The pressure was calculated up to the undisturbed wave, and the nonlinear effects were basically the same as in LAMP(-2). The difference between linear and nonlinear response was small.

Is there anything to learn from these theories and their application? Obviously, a great deal of effort has been put into the development of these theories, validation against experimental data, application on different designs and comparison with other computer programs. Some of these programs are commercialized, and may be used to predict design loads. The main conclusion is, however, that *no program can reliable predict the whipping and springing response for a general design*. They may still reveal that certain effects are important, but the magnitude can not be trusted. Different projects have confirmed that the difference between the programs are considerable, e.g. (Xia et al. 1995; Watanabe and Soares 1999; Storhaug et al. 2003). Still some statements can be made from theories considering springing and whipping.

Springing

A few statements based on the linear and nonlinear springing theories are provided.

- The response predictions was sensitive to the location of the springing frequency versus the hump-hollow in the transfer function, e.g. (Bishop et al. 1973).
- Springing was only slightly affected by changing trim and mass distribution, e.g. (Chen 1980).
- The springing was higher in low than high draft, (Chen 1980).
- The coupling between flexible and rigid body modes were disregarded, e.g. (Kawakami and Kiso 1976).
- Hamid (1980) confirmed that coupling was important.
- The slender body theory appeared to be insufficient for predicting linear springing of blunt ships, e.g. (Skjørdal and Faltinsen 1980).
- The hydroelastic effect increased with flexibility and speed, e.g. (Hermundstad et al. 1994). The former was not evident in (Hansen et al. 1995).

- The structural damping may be neglected for high speed ships due to large hull lift damping, e.g. (Hermundstad et al. 1994).
- The bilge keel and transom stern damping in addition to wave making appeared to be important, e.g. (Søding 1975).
- The interaction between the hulls of multihull ships may be important, e.g. (Bingham et al. 2001).
- The second order effect from restoring due to non vertical walls appeared to be small, e.g. (Søding 1975).
- The second order effects from strip theory appeared to give a small elastic contribution on tankers and a significant effect on container vessels, e.g. (Jensen and Pedersen 1981).
- The second order contribution to the elastic effects may be dominating on container vessels, e.g. Jensen and Dogliani (1996).
- The second order nonlinear effects (without hydroelasticity) may increase the fatigue damage by 50-100% on container vessels, e.g. (Jensen 1993).
- The springing was found unimportant for another large high speed container vessel, (Jensen and Wang 1998). Significant whipping was estimated on this ship with another theory.
- The high frequency tail of the wave spectra was not well defined, but it was important, (Chen 1980).
- Springing may be important in developing seas, (Chen 1980).
- The importance of considering non uniform steady flow and translating-pulsating Green's functions were confirmed by Du et al. (1998).

Whipping

A few statements based on the time domain whipping theories are given in the following.

- The 3-node mode may be unimportant for whipping, e.g. (Kaplan et al. 1969). 3 modes may be sufficient for the dynamic response, (Antonides 1975). 5 modes were enough to ensure convergence, (Senjanovic et al. 2001).
- A SES may experience significant whipping, e.g. (Brown et al. 1981).
- A small change on the pitch motion may significantly change the slamming force on a SES, e.g. (Brown et al. 1981).

- The rigid body motions was insignificantly changed by slamming, e.g. (Antonides 1975; Yamamoto et al. 1978).
- The whipping effect was insignificant for a tanker, but significant for a container vessel, e.g. (Yamamoto et al. 1978).
- The slamming process in time may be described by a Poisson process, e.g. (Ochi and Motter 1973). This was not recognized by Hansen and Thayamballi (1995) due to clustering effects.
- Whipping may be more sensitive to speed in high sea states, e.g. (Chen 1980).
- Whipping was larger in developing seas, (Chen 1980).
- Reducing speed was the most efficient way of reducing the whipping response, (Chen 1980).
- Whipping was more important in head seas, (Schlacter 1989).
- The bottom emergence force may improve the predictions, (Schlacter 1989).
- 50% difference was observed from four programs used to predict wave bending moment in regular head sea. The difference increased for increasing flare, (Xia et al. 1995). The difference between several programs increased with increased wave height, and the agreement was poor, (Watanabe and Soares 1999).
- Inertia loads and memory effects must be included, (Xia et al. 1998).
- Nonlinear von Karman and nonlinear modification of radiation forces were important as well as nonlinear restoring and Froude-Kriloff forces, (Wu and Hermundstad 2002).
- The nonlinearities increased the fatigue damage by 10-100%, while the elastic effects increased the fatigue damage by 100-900%, but it was sensitive to damping and natural frequency, (Gu and Moan 2002).
- Shorter vessels may experience more nonlinear effects, e.g. (Wu and Moan 1996).
- Slamming effects may contribute significantly to whipping from the aft part in strip theories, e.g. (Storhaug et al. 2003). This effect may not be realistic.
- Kutta condition was important in the exit phase of wet deck slamming, (Ge 2002).

Comparing findings from full scale measurements, model tests and theories reveal several contradictory results, and some were also obvious. Some findings were used as input to the preparation of the model tests, and for comparison with subsequent results. Moreover, they may increase the general knowledge of the phenomena, and may serve as references for interested readers.

1.3 Purpose of the work

The original objective was to investigate fatigue damage related to springing, but no clear approach was predefined. Several relevant topics were considered, e.g.

- ⋆ Fatigue strength methodology including effects of mean stress, residual stress, SN-curves, SCFs, crack propagation and counting procedures in relation to the small vibration.
- ⋆ The structural representation and solution methods including a method to predict structural damping, and practical means to increase it.
- ⋆ Statistical methods to estimate short and long term contribution to fatigue and extreme loading, i.e. how the wave frequency and high frequency response should be combined.
- ⋆ Excitation sources from wave loading by a numerical or an experimental approach.
- ⋆ Description of the wave environment, i.e. wave energy spreading, energy distribution and the energy in the high frequency tail, obtained from wave measurements by buoys, radars, satellites and wind models.

The DNV workshop on springing and the literature investigation pointed out the springing/whipping excitation sources as the main uncertainty, though certainly several of these points above deserve more attention. First after two and a half years (after one year with subjects and one year as a teaching assistant), it was decided to *carry out model experiments with the primary objective to reveal the dominating excitation source of the wave induced vibrations, which contribute to the fatigue damage*. Secondary objectives were to suggest how the excitation sources can be included in numerical predictions, how model experiments ought to be carried out for the purpose of design verification, suggest improved geometry design to reduce the vibration level and propose ship rule formulas to limit the effect of the wave induced vibrations.

1.4 Outline of the thesis

The background, motivation and literature investigation were covered in this chapter, and the remaining part of the thesis is divided into the following sections

- ⋆ The hypotheses, which may explain the observed vibration, are presented in Chapter 2, which also cover other theoretical issues employed in the present research.
- ⋆ Simplified analyses of whipping from stem flare impacts are presented in Chapter 3 for an idealized vessel in ballast and cargo condition in head sea. The speed reduction as a function of sea states is also covered.
- ⋆ The model design, setup and strategy are shown in Chapter 4. Moreover, practical procedures used to evaluate the time series with respect to damping and transfer functions, and a couple of methods to distinguish nonlinear and linear springing, and springing from whipping are described. It deals also with the calibration of sensors and waves.

⋆ Chapter 5 presents the results and discussion. The results consist of damping estimates, wave amplification at the bow, added resistance in waves, transfer functions and fatigue damage. Observations illustrated by time series of different responses are displayed.

⋆ Results from full scale measurements, in particular damping, speed reduction and fatigue damage as a function of wave height, are shown in Chapter 6. Comparisons with model test data are also presented.

⋆ Finally, Chapter 7 presents a brief summary followed by conclusions from the different tasks, contribution and recommended future work.

A more detailed amount of theoretical aspects is presented in the appendices.

Chapter 2

Theory

This chapter describes briefly selected theoretical issues which are relevant and related to springing and whipping, while Appendix A summarizes some of the basic hydrodynamic theory. Section 2.1 deals with the hydrodynamic hypotheses, which may contribute to explain the significant ship vibrations observed. The hypotheses constitute the contribution in this chapter. Section 2.2 elaborates on the various formulations of structural behaviour employed, while Section 2.3 describes the different damping mechanisms, which influence the resonance response. The remaining sections outline theoretical aspects relating to time series analysis, spectral analysis, sea state models, transfer functions and fatigue damage analysis.

2.1 Hydrodynamic theory

The governing equations of potential theory are quoted in Appendix A.1. They were used to calculate the high frequency added mass of general 2D sections. The added mass was combined with structural formulations to calculate the mode shapes and natural frequencies, both as input to hydroelastic analysis and to determine appropriate locations, stiffness and design of the flexible joints in the model test.

In the subsequent subsections the main excitation hypotheses are outlined. A simple approach to estimate the speed reduction, which reduces the vibration response, is also included.

2.1.1 Hypothesis 1: Steady wave elevation

When a ship moves forward in calm water it creates steady waves, which are independent of time from a reference system fixed to the ship. The steady wave field has four obvious

effects.

1. The unsteady waves are superimposed on the steady wave elevation. To incorporate the steady water elevation in numerical predictions may affect the results.

2. The interaction between the steady and unsteady waves may be significant. The interaction may vary along the hull, e.g. it may be more pronounced in the bow region in head seas. This may increase the generalised springing excitation force.

3. The steady wave field contributes to trim and sinkage (squat), which also affects the force distribution along the hull.

4. The steady wave may cause breaking bow waves and instabilities.

The relevance of these effects may differ for blunt ships compared to slender ships. The dominating literature on springing considers blunt ships, and the steep bow waves may cause the incident waves to break, which may result in stem slamming.

The total steady velocity potential can be written as the summation of the free stream and the steady disturbance potential

$$\Phi_s = -U \cdot x + \phi_s \tag{2.1}$$

This expression assumes a coordinate system fixed to the ship with incoming current moving with the speed of U in the negative x-direction with the ship at rest. The Froude number can be assumed low, and the flow may be solved based on linear theory represented by a double body approximation (horisontal flow at the still water line). Once the disturbance potential is determined, the Bernoulli's equation, Eq.(A.5), can be used to find an estimate of the wave elevation around the ship relative to the still water line. In centre line and water line at the bow, i.e. at the stagnation point, a simple expression for the surface elevation is derived from Bernoulli's equation.

$$\zeta_s = \frac{U^2}{2g} \tag{2.2}$$

The speed is important, and at $15kn$ the wave elevation is roughly $3m$. Similarly, the steady elevation along the hull can be expressed as

$$\zeta_s = \frac{1}{2g}(U^2 - U_e^2) \tag{2.3}$$

where U_e is the tangential velocity at the intersection between the still water line and the hull.

For a cylinder or a sphere the tangential velocity can be written

$$\begin{aligned} U_e^{cyl} &= 2U \cdot sin(\theta) \\ U_e^{sphere} &= \frac{3}{2}U \cdot sin(\theta) \end{aligned} \tag{2.4}$$

The 3D case has a maximum difference from the 2D case at 90^0, giving a smaller wave trough at the side, while the difference at stem and stern is zero. The trough may in this case be larger in absolute value than at the crest. Turbulence and vortex shedding may influence the results for blunt bodies.

The wave elevation around an elliptic bow, which is defined by a source and a free stream, is more realistic. Both a 2D and 3D source are considered. The key point is to find the stream function value at the stagnation point in order to find the shape of the geometry, and finally the tangential velocity along the shape at water line. Linear theory and double body approximation are implicitly assumed. The 3D stream function is only applicable in the axisymmetric case. Figure 2.1 illustrates schematically the steady wave elevation around the approximate bow geometry for a speed of $15.2kn$. The singularity point for the 2D case is moved slightly away from the origin in order to get the same stagnation point. The breadth at infinite x-position corresponds to the ship breadth of $53m$. The rise up of water is wider in the 3D case, but the bluntness is also larger. The trough at the bow quarter is -1.0m in the 3D case and -1.8m in the 2D case. The elevation at the stem is $3.1m$. The illustration is certainly in qualitatively agreement with observations on blunt ships (but not necessarily on slender ships).

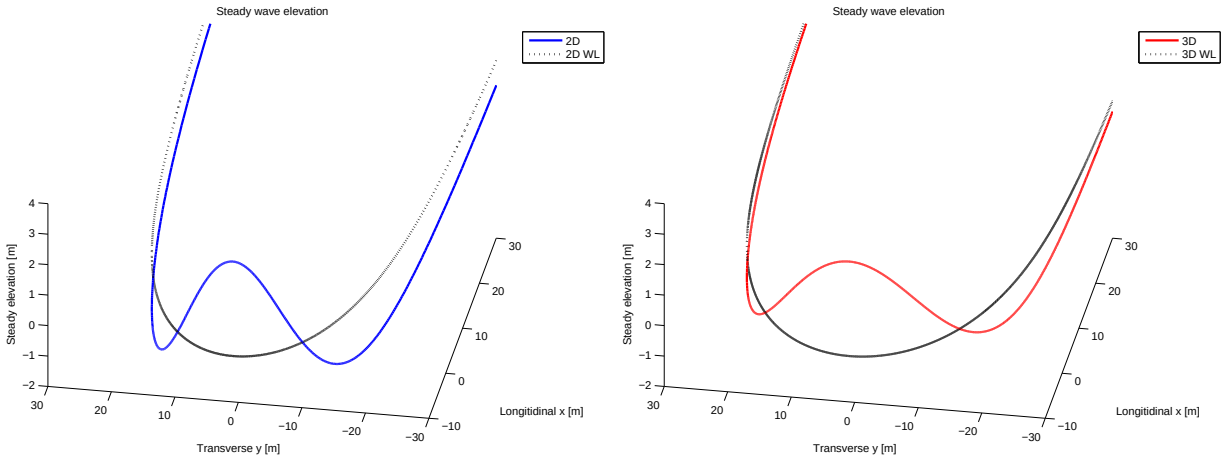

Figure 2.1: *Schematic illustration of steady wave elevation around the bow in the 2D (left) and 3D (right) case.*

For a real ship, the whole wetted geometry influences the steady velocity field and the wave elevation around the hull. Nonlinear theory is necessary to describe it accurately, and the viscous boundary layer may affect the behaviour in the aft ship.

The behaviour of the stem wave depends on the loading condition. Baba (1976) showed that wave breaking resistance contributes with about 5% to the wave resistance. In deep draft condition, short waves with unstable crests in front of the bow were observed, while in shallow drafts condition the short waves broke. The 'necklace vortex' around the hull,

caused by the breaking waves in the bow, was said to have its origin from a phenomenon similar to the hydraulic jump. A bulb may reduce the wave breaking resistance in ballast condition, and *if the wave breaking resistance is related to springing, it may reduce the springing excitation*. The bulb was originally believed to cause nonlinear springing excitation due to its shape, (Ohkusu 1980).

The interaction between the nonlinear steady wave field and linear unsteady wave field has been investigated by a few, (Bertram 1998; Nechita 2001). The interaction had a significant effect on the motions and response, and the elevation was sensitive to the ship shape. The interaction increases with speed.

2.1.2 Hypothesis 2: Amplification of incident wave at the bow

In head seas the bow reflects the incident waves causing an amplification of the wave amplitudes. A basic result can be derived for a 2D regular wave, which is reflected by a fixed vertical wall of infinite extent. From linear theory, the solution corresponds to a standing wave with *double* amplitude compared to the incident wave amplitude, ζ_a.

The amplification is affected by the finite ship size and forward speed. In short small waves, the ship motions will in practise be zero, and the ship will appear to be of infinite size. This problem has been solved earlier in relation to added resistance in waves, assuming the hull to be vertical at the water line. The wave amplitude is derived in Appendix A.2 from the velocity potential expressed by Faltinsen et al. (1980).

A simple expression of the amplification at the stem in head sea, expressed as the ratio of the total amplitude to the incident wave amplitude, is

$$\frac{\zeta}{\zeta_a} = \frac{\omega_e}{\omega_0}(1 + \frac{2}{\frac{\omega_e^2}{\omega_0^2} + 1}) \tag{2.5}$$

where ω_e refers to the encounter wave frequency, Eq.(A.28), and ω_0 is the wave frequency. This expression will later be compared to experimental data.

The amplification versus wave period at three different speeds is illustrated in Figure 2.2. The amplification increases for lower periods and higher speeds. The wave periods causing springing by first order (linear) and sum frequency (second order) excitation are defined at the intersections with the two rising curves. A springing period of $2s$ is assumed, hence, linear springing in head sea is excited by wave periods of $4s$ at a speed of $15kn$, giving an amplification of 3. For the same speed, waves of $7s$ cause sum frequency excitation with an amplification of 2.7. This is higher than the amplification of 2 for a fixed wall. The increased splash zone due to forward speed may also be predicted by linear 3D panel theory, but the linear springing theory considers only the wet area below the mean still water line. An inaccurate (smaller) splash zone is predicted by 2D strip theory. The splash

zone refers to the area which is partly dry and partly wet due to relative motion between the ship and the surface motion. The effect of the splash zone, causing nonlinear forces, are regarded as important.

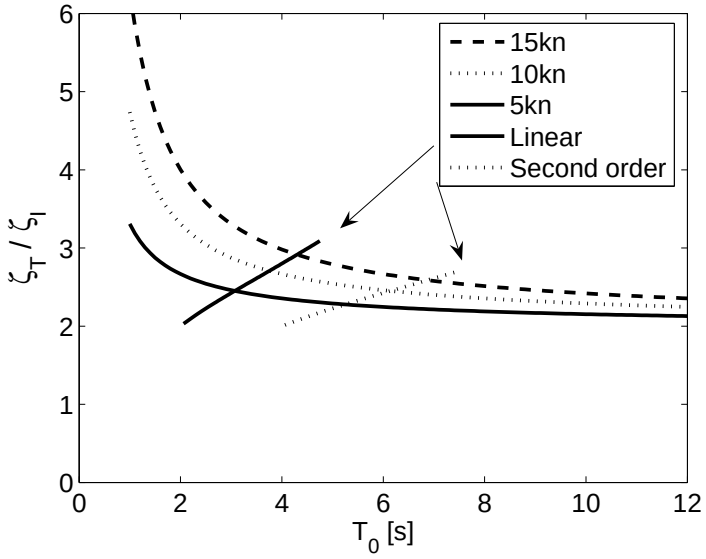

Figure 2.2: *Amplification of head sea incident waves at the stem versus the wave period at three speeds (decaying curves). Wave periods exciting linear and sum frequency springing are defined at the intersections with the two rising curves. A springing period of 2s is used.*

The amplification is reduced compared to Eq.(2.5) in longer waves, since the vessel starts to move, and the ship can no longer be considered as large compared to the incident waves.

2.1.3 Hypothesis 3: 3D impact forces

The combined effect of the steady wave and amplification of the incident wave result in a wetted hull surface area that differs from the area commonly considered in numerical predictions. The velocity of the water surface increases due to the reflection, and impacts may occur, since the bow geometry deviates from wall sided shape away from the still water line. In particular flare effects may be significant, but also the bilge area at the bow quarter (bottom flare) may induce impacts due to the steady wave trough and the negative amplification.

The impact force in head seas may be written, (Faltinsen 1990)

$$F_s = \max(V_R^2 \frac{dA_{33}}{dh}, 0) - A_{33}\frac{dV_R}{dt} + \rho g \Omega(t) + \rho \Omega(t) \frac{d^2\zeta}{dt^2} \tag{2.6}$$

$$V_R = \frac{d\eta_3}{dt} - x\frac{d\eta_5}{dt} + \sum_{i=3}^{n} \dot{q}_i(t)\Psi(x = L_{pp}/2) + U\eta_5 - \frac{d\zeta}{dt}$$

where V_R is the relative velocity, which is positive upwards, and ρ is the density of water. Eq.(2.7) includes rigid body motion in heave, η_3, and pitch, η_5, flexible modes such as the 2-node springing mode ($i = 3$), angle of attack term due to pitch and forward speed and movement of the water surface. The interaction between the steady and unsteady flow is neglected. q is the time dependent amplitude of the flexible mode shape, and Ψ is the time independent orthogonal mode shape at the position of the impact. The angle of attack term for unrealistic flexible structures should also include the derivative of the flexible modes at the bow.

The first term in the impact force is often referred to as *the slamming force*, assumed to act only when the bow enters the water. The other terms are often neglected, but could be important especially in the exit phase, e.g. (Ge et al. 2002). The second term is an inertia term, while the third and fourth term are due to the hydrostatic and Froude-Kriloff force. Ω is the volume of the body getting wet relative to the steady water level and A_{33} is the high frequency 3D added mass.

How is the added mass found? 2D expressions may be useful, e.g. Wagner's analysis of a wedge is well known, (Faltinsen 1990), and an improved analytical formulation for skewed impact of a wedge with exact boundary condition was derived by Driveklepp (2000). 3D expressions, which may be more relevant for blunt ships, are however rare. Faltinsen and Zhao (1997) derived the added mass for a cone following Wagner's approach, which is valid for small angles, while Shiffman and Spencer (1951) derived the added mass for a cone of any deadrise angle based on approximate formulations. The latter formulation is described in Appendix A.3, and it may represent the stem flare geometry. Alternatively, Chezhian (2003) used a generalised Wagner's theory, and Zhao and Faltinsen (1998) used a fully nonlinear theory to investigate slamming on academic and axisymmetric bodies.

2.1.4 Hypothesis 4: Second order velocity potential and wave elevation

In perturbation theory the total velocity potential without forward speed can be expressed as

$$\phi_T = \phi_1 + \phi_2 + ... \tag{2.7}$$

where the linear velocity potential, ϕ_1, is proportional to the wave amplitude, ζ, and the second order velocity potential, ϕ_2, is proportional to ζ^2. Inserting Eq.(2.7) into the free surface boundary conditions A.8, and keeping terms up to second order, the free surface condition for the second order potential can be written

$$\begin{aligned} \phi_{2tt} + g\phi_{2z} = &-\frac{\partial}{\partial t}(\phi_{1x}^2 + \phi_{1y}^2 + \phi_{1z}^2) + \\ &\frac{1}{g}\phi_{1t}\frac{\partial}{\partial z}(\phi_{1tt} + g\phi_{1z}) \text{ on } z = 0 \end{aligned} \tag{2.8}$$

Faltinsen (1990) considered two waves moving in opposite directions in deep water

$$\phi_1 = \frac{g\zeta_1}{\omega_1} e^{k_1 z} \cos(\omega_1 t - k_1 x + \delta_1) + \frac{g\zeta_2}{\omega_2} e^{k_2 z} \cos(\omega_2 t + k_2 x + \delta_2) \tag{2.9}$$

and derived the solution for the sum frequency effect

$$\phi_2 = \frac{2\zeta_1\zeta_2\omega_1\omega_2(\omega_1+\omega_2)}{-(\omega_1^2+\omega_2^2)^2 + g|k_1-k_2|} e^{|k_1-k_2|z} \sin[(\omega_1+\omega_2)t - (k_1-k_2)x + \delta_1 + \delta_2] \tag{2.10}$$

If the wave number, k, is the same, there is no decrease of the second order pressure with depth, z, and no traveling wave.

A secondary effect of the second order perturbation theory is the additional wave elevation increasing the crest and reducing the trough. Considering a single regular wave in deep water, the second order potential is zero, but the wave elevation to second order can be expressed as

$$\zeta = \zeta_a \cos(kx - \omega t) + \frac{1}{2} k \zeta_a^2 \cos(2(kx - \omega t)) \tag{2.11}$$

Figure 2.3 illustrates the effect of the second term for a typical wave height and wave period exciting sum frequency springing. This secondary second order term is apparently small, and Storhaug et al. (2003) indicated that the excitation from the second order incident waves did not explain the high measured vibration response on the blunt iron ore carrier with vertical sides.

The expressions for the second order velocity potential were derived for arbitrary headings. Helmers (2001) derived it for regular waves and applied it to a barge. Sele (2001) extended it to irregular sea, still without diffraction and applied it to a barge, and Vidic-Perunovic and Jensen (2004) implemented the undisturbed wave into a second order strip theory, and compared numerical predictions with full scale measurements from the ship.

The bow will reflect incident waves as explained in Section 2.1.2. This effect is relevant for all ships, not only in bi-directional sea. The effect is similar, but not the same as the second order effect in Eq.(2.10). The real ship has finite extent, forward speed and 3D geometry. The forward speed appears in the free surface condition, the body boundary condition and possibly in the force formulations. At zero speed this has been investigated on a TLP, (Winterstein et al. 1994), by the program WAMIT, (MIT 1998). The uncertainty is related to how the pressure decays with draft and the extent of the bottom area with effective pressure in the case of forward speed.

2.1.5 Speed reduction due to added resistance in waves

Full speed in high sea states is unrealistic, and the vibration level is known to be sensitive to the speed. Accordingly, it is necessary to predict realistic speeds as input to the model

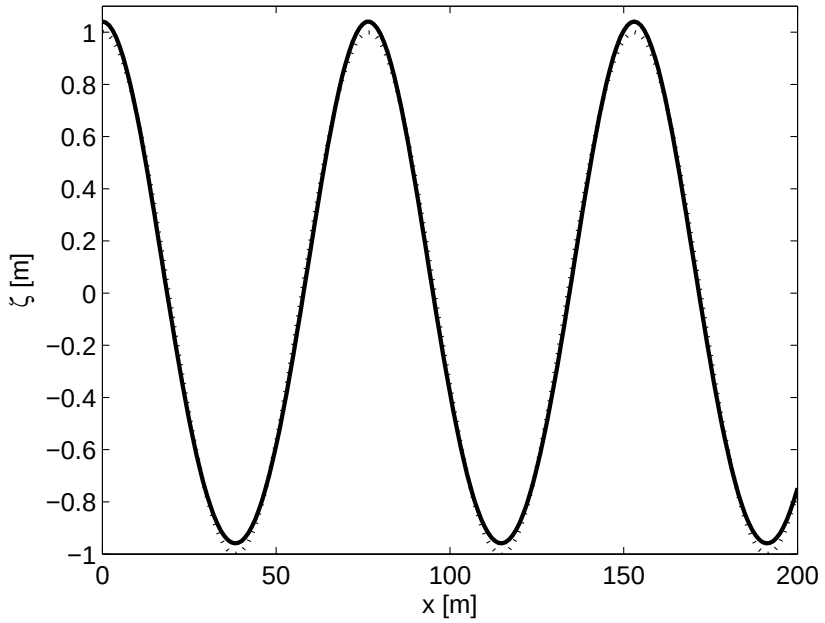

Figure 2.3: *The second order (cont. line) versus linear (dashed) regular wave train.* $\zeta = 1m$, $T = 7s$.

experiments, also since one of the objectives is to compare model test results with full scale measurements.

The total wave resistance, R_T, represented by the total resistance coefficient, C_T, is written as

$$C_T = \frac{R_T}{0.5\rho S U^2} \tag{2.12}$$

where S is the wet surface of the actual loading condition. The total resistance can be divided into different components, and the following components are considered in calm water

$$C_T = C_w + C_V + C_{AA} + C_{BD} \tag{2.13}$$

C_w is the wave making component, C_V is the viscous friction, C_{AA} is the air resistance and C_{BD} is the base drag resistance. The form factor method is used on the viscous part. Appendix A.4 provides a more detailed description.

The next resistance component is the added resistance *due to waves*, C_{aw}. The added resistance in waves depends on the sea state, and a speed reduction of $5kn$ is typical for the sea states dominating the fatigue damage, (Moe et al. 2005). The added resistance in waves has contributions from bow reflection in the short wave length regime and from

larger ship motions in the longer wave length regime. Assuming short waves, which are totally reflected by the ship, an analytical expression was derived by Faltinsen et al. (1980)

$$\frac{R_{aw,1}}{\zeta_a^2} = \frac{1}{2}\rho g(1 + \frac{2\omega_0 U}{g}) \int_\ell \sin^2(\theta) n_1 d\ell \tag{2.14}$$

θ is the local angle displayed in the coordinate systems of Figure A.8, where n_1 is also the unit normal of the hull geometry (corresponds to N). This expression is integrated around the non-shadow part of the ship, ℓ, which is the intersection between the still water line and the hull as illustrated in Figure A.8. Assuming head sea, and the bow to be shaped as a circle with a radius of $B/2$, the added resistance in short waves is written

$$\frac{R_{aw,1}}{\zeta_a^2} = \frac{1}{3}\rho g(1 + \frac{2\omega_0 U}{g})B \tag{2.15}$$

For a wedge section with half apex angle, θ, the expression becomes

$$\frac{R_{aw,1}}{\zeta_a^2} = \frac{1}{2}\rho g(1 + \frac{2\omega_0 U}{g}) \sin^2(\theta) B \tag{2.16}$$

Faltinsen (1990) showed some reference values for realistic ship shapes, and the value for the ship is slightly smaller than Eq.(2.15). This reflection contribution may be valid up to wave lengths of half of the ship length, but up to 70% of the ship length is used. Between 70 and 100%, a linear decrease to zero is assumed.

The second contribution comes from ship motions, when the relative motion in the bow and stern region becomes pronounced. It is relevant for wave lengths from the ship length and above in head seas, but it depends on the forward speed. Faltinsen et al. (1980) provided resistance in waves for a ship with block coefficient of 0.8 versus the nondimensional encounter frequency. A similar shape is assumed for other speeds, and a Gaussian shape is used to reproduce it

$$C_{aw,2} = \frac{R_{aw,2}}{\rho g \zeta_a^2 B^2/L} = 8.75 \exp \frac{(\omega_e \sqrt{L/g} - 3.25)^2}{2\sigma^2} \tag{2.17}$$

where $\sigma = 0.4$. $C_{aw,1}$ is made nondimensional in the same way as $C_{aw,2}$, but based on $R_{aw,1}$. The total added resistance in waves is the sum of these two components. The shape of each contribution and the total wave resistance curve are shown in Figure 2.4.

The added resistance in irregular sea is the sum of the individual waves defining the sea state, hence

$$R_{aw,T} = \sum_{i=0}^{n} (C_{aw,1,i} + C_{aw,2,i}) \rho g \zeta_i^2 \frac{B^2}{L_{WL}} \tag{2.18}$$

where the individual wave amplitude, ζ_i, is found from the wave spectrum, $S(\omega)$, as in Eq.(2.90).

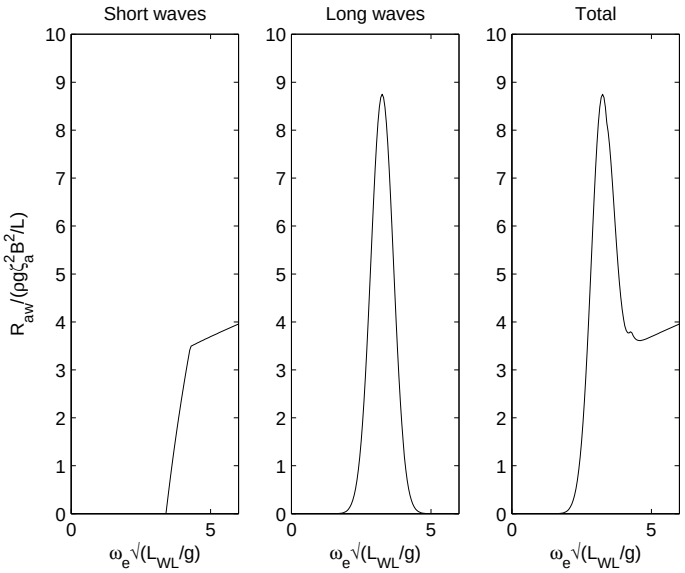

Figure 2.4: *Nondimensional added resistance in waves versus nondimensional frequency.*

The power due to the total resistance must be in balance with the total delivered (available) effect of the propulsion system.

$$R_T \cdot U + R_{aw} \cdot U = P \cdot \eta_t \tag{2.19}$$

where P is the engine power and η_t is the total efficiency coefficient of the propulsion system. At least two of the terms, and possibly also the still water part, are influenced by the waves. The calculation of the total efficiency coefficient was rejected. The trust versus speed was found unreliable. The calculations were sensitive to the propeller revolution. The data were obtained from similar ships and were inaccurate. Therefore, a fixed efficiency coefficient independent of speed and propeller revolution was applied, assuming that the maximum power was utilized. Further description of the coefficients is given in Appendix A.4.

2.2 Structural representation

The structural representation of the hull depends on the design and response of interest. In many cases a beam model, such as the Timoshenko beam, is sufficient, while e.g. cruise ships with many discontinuous decks require refined models. Responses as torsion (warping), racking, pitch connecting moments may require FE models, but thin walled beam elements may be an alternative, (Wu 2002). The approaches, which were used to calculate mode shapes, natural frequencies and responses in this study, are presented in the following. The approached includes modal decomposition of bending deformation in Section 2.2.1, analytical formulations including shear deformation in Section 2.2.2, FE representation in Section 2.2.3 and segmented beam formulation with rotational springs for

comparison with model tests in Section 2.2.4. The analytical derivations were used to illustrate the modes shapes and for comparison with numerical FE analysis. A program for the latter was developed and used to provide input modes to the hydroelastic calculations reported by Storhaug et al. (2003).

2.2.1 Modal decomposition

The modal decomposition is extensively used to analyse the elastic behaviour of ships. The method is illustrated by describing the expressions used in the simplified analysis in Section 3.1.

The equation of motion describing the vertical motion, $y(x,t)$, of a flexible beam, when bending deformation and elastic support are included, can be written

$$(m+a)\ddot{y} + b\dot{y} + EIy^{IV} + cy = P(x,t) \tag{2.20}$$

The equation is based on homogeneous sectional properties per unit length, e.g. mass m, added mass a, force P and water plane stiffness c. EI is the sectional bending stiffness and b is the damping. The dots represent the time derivative, while the superscript, ^{IV}, denotes the space derivative. The time independent boundary conditions

$$y^{II}(\pm\frac{L}{2}) = 0 \text{ and } y^{III}(\pm\frac{L}{2}) = 0 \tag{2.21}$$

refer to zero shear force and moment at the ends.

The flexible eigenmodes are deduced from the homogeneous equation by setting $P = b = c = 0$. The natural frequencies of the flexible responses are insignificantly influenced by the water plane stiffness, (Faltinsen 1980), but the water plane stiffness is essential in calculation of the rigid body response. The equation can be solved by separation of variables

$$y(x,t) = \sum_{i=1}^{n} q_i(t)\Psi_i(x) \tag{2.22}$$

where q is the principal coordinate or amplitude, and Ψ is the eigenvector or mode shape. Five analytical mode shapes are displayed in Figure 2.5. The mode shapes must be able to describe both the rigid body response (quasi-static) and the vibration.

By combining Eq.(2.22), Eq.(2.20) and performing some manipulations, the beam equation is converted into a set of independent equations representing the flexible responses, $i = 3, 4, 5...$

$$\ddot{q}_i(t) + 2\delta_i\omega_i\dot{q}_i(t) + \frac{EI}{m+a_i}\beta_i^4 q_i(t) \approx \frac{f^i}{(m+a_i)L}\int_{-L/2}^{L/2} P(x,t)\Psi_i(x)dx \tag{2.23}$$

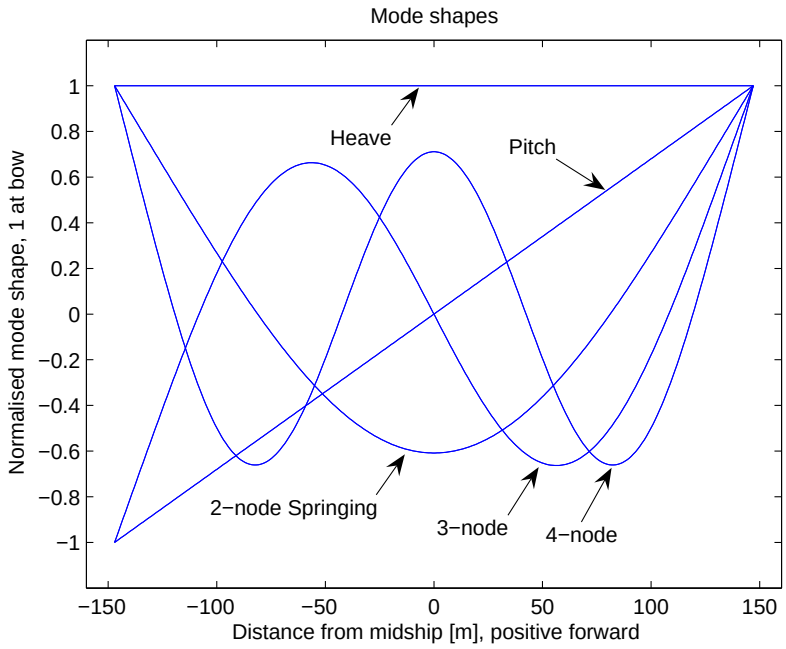

Figure 2.5: *The five first mode shapes for a homogeneous Euler beam including heave and pitch.*

The $\approx$ sign indicates that the f^i constants are approximated. The added mass, damping ratio, δ, and the β-coefficient are mode (frequency) dependent, and the total response is the sum of the individual responses. Further description is given in Appendix A.5.

The hydrodynamic theory, the representation of the structural flexibility and the model set-up should be selected depending on the purpose of the model test. The right hand side of Eq.(2.23) is defined as the *generalised force*. The integrand is a multiplication of the force per meter times the mode shape. The force from the harmonic load exciting resonance has typically 5 to 15 oscillations along the ship, while the springing mode has one oscillation, hence the response is affected by the accuracy of the force and mode distribution. The integration may be less sensitive to local loads in the bow or stern region. The effect on how to split the model in case of whipping was investigated by Økland et al. (2003).

The bending moment can be calculated as

$$VBM = EI\frac{\partial^2 y}{\partial x^2} = EI\sum_{i=3}^{n} q_i(t)\Psi^{II}(x) \tag{2.24}$$

The rigid body modes do not directly contribute to the moment, since the curvature is zero, while the flexible modes contribute to both quasi-static response and vibration. The alternative way is to obtain the moment from the difference of the inertia forces and the excitation, radiation and restoring forces integrated forward of the transverse cut. This

is the conventional way of doing it and then the rigid modes contribute. The quasi-static response actually requires many modes in order to provide an accurate distribution along the ship, while the dynamic flexible response only requires a few. The stress is calculated as

$$\sigma = \frac{VBM}{I}(z - z_{na}) = E(z - z_{na}) \sum_{i=1}^{n} q_i(t)\Psi^{II}(x) = E(z - z_{na}) \sum_{i=3}^{n} q_i(t)\Psi^{II}(x) \quad (2.25)$$

where z is the distance from base line to the actual position considered, and z_{na} is the distance from base line to the neutral axis. Sagging gives positive stress in deck.

2.2.2 Analytical solution of the beam equation with shear deformation

For long slender beams, with low height to length ratio, the bending stiffness dominates, while for short high beams the shear deformation dominates. For a ship both effects may be relevant. The ratio may be related to the distance between the nodes. The beam equation, without damping but including shear deformation, was derived based on procedures outlined by Bergan et al. (1981). The solution for a free-free beam was not found in the literature, but was derived here to check the accuracy of the FE program, and to illustration the importance of shear deformation on the natural frequency. The equation is expressed as

$$m\frac{\partial^2 y}{\partial t^2} + \frac{\partial^2}{\partial x^2}(EI\frac{\partial^2 y}{\partial x^2}) - m\frac{EI}{GA_S}\frac{\partial^4 y}{\partial x^2 \partial t^2} = P(x,t) \quad (2.26)$$

where A_S is the effective shear area and $G = E/2(1+\nu)$ is the shear modulus. The water plane stiffness is neglected.

The solution procedure is the same as for a beam with only bending stiffness, (Faltinsen 1980). The homogeneous equation is considered, and the method of separation of variables is used, which gives one differential equation for time and one for space. The equation for space is solved by inserting a solution on the form $\Psi(x) = Ce^{sx}$, which gives a characteristic equation with four roots. The solution may be written

$$\Psi(x) = C_1 \sin a_1 x + C_2 \cos a_1 x + C_3 \sinh a_2 x + C_4 \cosh a_2 x \quad (2.27)$$

where

$$\begin{aligned} a_1 &= \sqrt{\frac{ab + \sqrt{(ab)^2 + 4a}}{2}} \\ a_2 &= \sqrt{\frac{-ab + \sqrt{(ab)^2 + 4a}}{2}} \\ a &= \omega^2 \frac{m}{EI} \\ b &= \frac{EI}{GA_S} = \frac{2(1+\nu)I}{A_S} \end{aligned} \quad (2.28)$$

By using the four boundary conditions for the free-free beam, expressions for the eigenvalues can be derived by combining these four equations to remove the unknown C-coefficients.

$$\begin{aligned} a_1 \tan(a_1 L/2) &= -a_2 \tanh(a_2 L/2) \text{ for } i = 1, 3, 5... \\ a_2 \tan(a_1 L/2) &= a_1 \tanh(a_2 L/2) \text{ for } i = 2, 4, 6... \end{aligned} \tag{2.29}$$

Eq.(2.29) must be solved numerically. Once a_1 and a_2 are estimated, a is determined as

$$a = \frac{a_1^4}{1 + b a_1^2} \tag{2.30}$$

and the natural frequency becomes

$$\omega_i = \sqrt{\frac{EI}{m}} a \tag{2.31}$$

The four equations are combined again to remove the C-coefficients. The last C-coefficient is removed by normalizing the mode shapes to give unit deflection at the bow, hence

$$\Psi(x) = \begin{cases} \frac{1}{(\frac{a_2}{a_1})^2+1} \frac{\cos a_1 x}{\cos a_1 L/2} + \frac{1}{(\frac{a_1}{a_2})^2+1} \frac{\cosh a_2 x}{\cosh a_2 L/2} & i = 1, 3, 5... \\ \frac{1}{(\frac{a_2}{a_1})^2+1} \frac{\sin a_1 x}{\sin a_1 L/2} + \frac{1}{(\frac{a_1}{a_2})^2+1} \frac{\sinh a_2 x}{\sinh a_2 L/2} & i = 2, 4, 6... \end{cases} \tag{2.32}$$

These mode shapes approach the mode shapes of pure bending for small values of b or large values of A_S, when $a_1 \approx a_2$.

To illustrate the importance of the shear deformation, a rough approximation is derived assuming that $a_1 \approx a_2$. The eigenvalues are solved from

$$\begin{aligned} \tan(a_1 L/2) &\approx -1 \text{ for } i = 1, 3, 5... \\ \tan(a_1 L/2) &\approx 1 \text{ for } i = 2, 4, 6... \end{aligned} \tag{2.33}$$

with the approximate solution

$$a_1 \approx \frac{\pi}{L}(2i + 1) \tag{2.34}$$

Finally, the natural frequency is related to the frequency from pure bending, ω_{EI}

$$\omega_i = \sqrt{\frac{EI}{m}} a = \omega_{EI} \cdot \sqrt{\frac{1}{1 + b a_1^2}} \tag{2.35}$$

To provide a numerical example, the following properties are assumed

$$L = 300m, I = 700m^4, \nu = 0.3, A_S = 2m^2$$

The springing frequency is 0.90 times the frequency from pure bending stiffness. For the 3-node and 4-node mode, the reduction factors are 0.78 and 0.67. From accurate calculations, the reduction factors are 0.94 for springing and 0.83 for the 3-node mode.

The corresponding mode shapes and bending moments are shown in Figure 2.6. The mode shapes differ less than the moments, which is calculated from

$$VBM = EI(\frac{\partial^2\Psi(x)}{\partial x^2} + \frac{1}{GA_S}m\omega^2\Psi(x)) \tag{2.36}$$

The moment from the *normalized* mode shape is reduced to 92% of the moment for pure bending stiffness. The significant change in the frequency indicates that shear deformation ought to be included, in particular for higher modes.

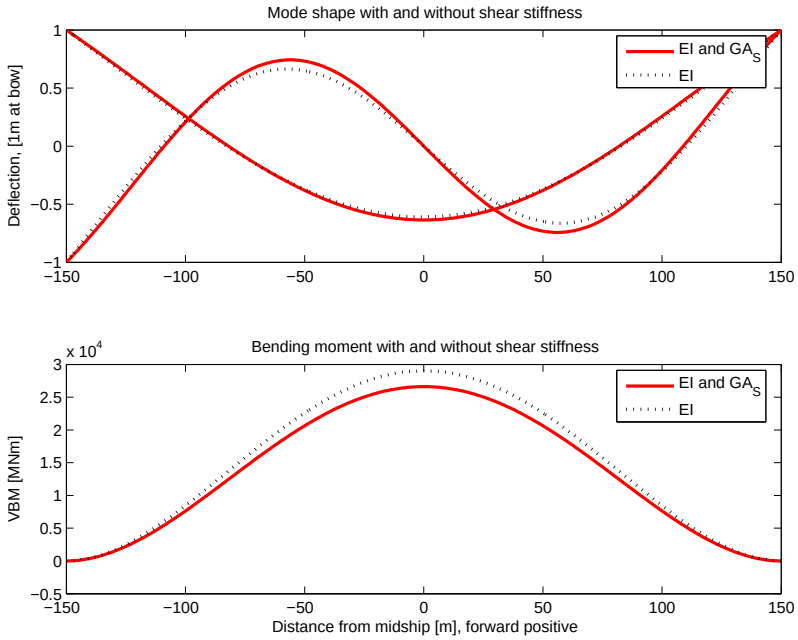

Figure 2.6: *The effect of shear deformation and moment on the springing (and the 3-node) mode based on realistic dimensions.*

From Figure 2.6, a few observations can be made. A bending moment of $3000MNm$ gives a deflection of $10cm$ at the ship ends. Assuming a sectional modulus in deck amidships of $60m^3$, which is a reasonable value for a 300m ship, gives a nominal vibration stress amplitude of $50MPa$. If the derivative of the mode shape is considered, and a man is standing in one end of the ship, the $10cm$ at the other end would look like a vibration amplitude of $42cm$ in his reference system. High vibration response will therefore be visible, and the visible deflection (including the quasi-static effect) can be used to indicate the level of the vertical bending moment amidships.

Minor effects of damping, rotational mass and end pressures are presented in Appendix A.7.

2.2.3 Finite element approach

A small program based on finite beam elements was developed to provide input of flexible modes to the program VERES, (Buarø et al. 1999), which was used by Storhaug et al. (2003). The equation of motion is written

$$\mathbf{M}\ddot{\mathbf{y}} + \mathbf{B}\dot{\mathbf{y}} + \mathbf{C}\mathbf{y} = \mathbf{P}(t) \tag{2.37}$$

where $\mathbf{M}$, $\mathbf{B}$ and $\mathbf{C}$ are the mass, damping and stiffness matrices. $\mathbf{y}$ and $\mathbf{P}$ are the displacement and force vectors. The eigenvectors and natural frequencies are derived from the homogeneous equation

$$\mathbf{M}\ddot{\mathbf{y}} + \mathbf{C}\mathbf{y} = \mathbf{0} \tag{2.38}$$

by using the method of separation of variables

$$\mathbf{y} = \mathbf{\Psi}\mathbf{q} \tag{2.39}$$

A harmonic solution of the time dependent principal coordinate vector, $\mathbf{q}$, is assumed. The natural frequencies and thereafter the eigenvectors, $\mathbf{\Psi}$, are then derived from

$$(\mathbf{C} - \omega^2\mathbf{M})\mathbf{\Psi} = \mathbf{0} \tag{2.40}$$

The matrix element formulations of stiffness and mass are quoted in Appendix A.6. The stiffness matrix includes bending and shear deformation. The mass matrix, which includes rotational mass, assumes an even mass distribution within the element. Alternatively, the masses are lumped to the element ends, which give a diagonal mass matrix with zero elements outside the diagonal. The rotational masses may be skipped, and the equation system may have to be reduced depending on the eigenvalue solver.

The FE program is verified against the analytical solution presented in Section 2.2.2 for a homogeneous beam with lumped mass distribution and small rotational mass. Realistic data corresponding to the ship are used. The convergence of the maximum bending moment for the springing mode versus the number of elements is presented in Figure 2.7. Roughly 10 elements are necessary to represent the springing mode, and the convergence study verifies the accuracy of both the FE program and the analytical solution.

2.2.4 Segmented models

The stiffness distribution in the model tests differs from the real ship. The model consists of stiff segments produced by mounting the ship's hull onto a rigid steel frame. In between the stiff segments, flexible joints are inserted. The flexibility is therefore restrained to specific locations, and the stiffness is discontinuous.

Ge (2002) used a segmented model consisting of rigid bodies connected by flexible beams. In the present study the design of the flexible joints are refined to make the stiffness adjustable to achieve the requested natural frequency. It is convenient with a different stiffness

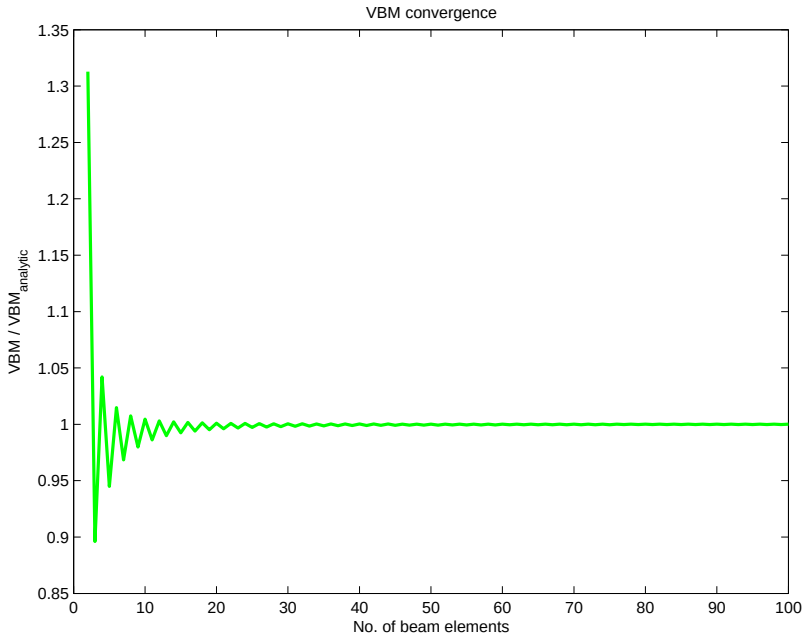

Figure 2.7: *Convergence of the FE midship 2-node moment versus the number of elements.*

formulation based on rotational and shear spring stiffness instead of beam elements. The stiffness based on the moment M and the shear force Q is written

$$k_\theta = \frac{M}{\theta} \qquad (2.41)$$
$$k_z = \frac{Q}{z}$$

These properties were obtained from calibration measurements and from modelling the joint by 3D BEAM, (DNV 2005d). The definition of the local stiffness and mass matrices are presented in Appendix A.8. They are inserted into a matrix system similar to Eq.(2.40). Appendix A.8 presents confirmation of the expressions versus SESAM (DNV 2005f), analytical solution and results by Økland (2002).

2.2.5 Single degree of freedom system

By invoking modal analysis the resulting set of dynamic equations of motion is uncoupled. Characteristic features of the behaviour of SDOF systems with linear damping and stiffness are presented in Appendix A.9.

2.3 Damping

The damping is a key parameter in resonance phenomena. It influences both the amplitude and number of significant vibration cycles in case of whipping. The damping may be caused

by internal and external mechanisms, and it may be linear or nonlinear. In all cases damping is dissipation of energy during a cycle. The lost energy (work) can be expressed as the area inside a closed hysteresis in a force-displacement diagram, e.g. (Langen and Sigbjørnsson 1979).

$$W_d = \oint F_d dy \tag{2.42}$$

where F_d is the total damping force and y is the displacement. A few relevant damping mechanisms will be described.

2.3.1 Linear damping

Linear hydrodynamic damping is typically caused by wave generation due to the motion of the vessel. It is frequency dependent, and typically approaches zero for high and small frequencies. Faltinsen (1990) presented a linear 2D hydrodynamic damping, relating outgoing waves to the motion of the vessel

$$b_{33}^{2D} = \rho(\frac{\zeta_r}{|\eta_3|})^2 \frac{g^2}{\omega^3} \tag{2.43}$$

ρ is the density, η_3 is the heave motion and ζ_r is the radiated wave amplitude. The damping coefficient is multiplied with the velocity in the equation of motion, i.e. $b_{33}^{2D} \cdot \dot{y}$.

Foils may introduce speed dependent damping, b_f, due to lift and heave velocity. The lift for a 2D flat plate is expressed by e.g. Newman (1977). Since the heave velocity will change the effective angle of attack, the quasi-steady damping can be expressed as

$$b_f = \rho U c \pi B_f \tag{2.44}$$

where c is the cord length and B_f is the width of the foil.

Forward speed may give hull lift damping. Sele (2001) wrote it as

$$b_{hl} = U\Psi(x_{transom})^2 a_{33}^{2D}(x_{transom}) - U\int_L \Psi \frac{\partial \Psi}{\partial x} a_{33}^{2D} dx \tag{2.45}$$

This is further explained by Faltinsen (2005). Similar contributions may be identified from coupling terms, as expressed by Faltinsen (1990) for rigid body motions in linear strip theory.

A third speed dependent damping term is often used in theoretical investigations, e.g. (Goodman 1971). It is similar to the prior term, and it is multiplied with the mode shape squared and integrated along the hull. The contributing parts are located at the bow and stern.

$$U\frac{\partial a_{33}^{2D}}{\partial x} \tag{2.46}$$

The three latter expressions are all linearly dependent on speed.

Elastic materials do not have a hysteresis curve indicating dissipation of energy during a cycle, because it follows the same path for both loading and unloading. However, steel structures in practise have welds including cracks. These give hysteresis curves under cyclic loading. Elliptic hysteresis curves for steady state harmonic loading indicate linear damping. The hysteresis damping of materials is defined as independent of frequency, but may be amplitude dependent. For instance, Bergan et al. (1981) expressed this as

$$b \cdot y \frac{\dot{y}}{|\dot{y}|} \tag{2.47}$$

The structural damping may also be expressed as proportional to the displacement, but in phase with the velocity. In this case it may be expressed as a complex stiffness, e.g. (Langen and Sigbjørnsson 1979)

$$c(1 + ib)y \tag{2.48}$$

2.3.2 Nonlinear damping

Viscous hydrodynamic damping is often nonlinear, and it may be written

$$b_2 \dot{y}|\dot{y}| \tag{2.49}$$

where $\dot{y}$ is here the relative vertical velocity. It has contributions typically from bilge keels, skin friction, eddy-making and transom stern effects, and the forward speed influence the results. The rudder may provide both viscous and foil damping, with vortex shedding as a related phenomenon.

Coulombs damping is another nonlinear contribution due to friction. The damping force may be expressed as

$$\mu N sign(\dot{y}) \tag{2.50}$$

where N is the normal force and μ is the friction coefficient, e.g. (Langen and Sigbjørnsson 1979).

Finally, water impacts, when occurring in the flat stern geometry as a consequence to violent vibration, may actually contribute as a nonlinear damping due to antisymmetric loading.

2.3.3 Methods to estimate linear and nonlinear damping

The effect of the damping is illustrated for the linear SDOF system described in Appendix A.9. The linear damping can be estimated based on the decay curve after an

impulse loading. Hammering tests are practical for model tests, while dropping the anchor or using a shaker are more convenient for a real ship. The damping ratio is estimated as

$$\delta = \frac{1}{2\pi n} \ln(\frac{x_i}{x_{i+n}}) \tag{2.51}$$

where x_i is the peak value of amplitude no. i. Alternatively, the half-power bandwidth method can be used, (Clough and Penzien 1993). The damping ratio is estimated as

$$\delta = \frac{\beta_2 - \beta_1}{2} \tag{2.52}$$

where β_1 and β_2 is the ratio of the frequency to the natural frequency placed on each side of the resonance peak, and corresponding to the response level of the peak value divided by the square root of two. The difference is therefore the width at this particular response level of the transfer function.

In full scale, the methods above may not be feasible, and damping must be estimated based on irregular response. The half-power bandwidth method, Eq.(2.52), can however also be used in this case. The width should then be taken at half the peak value, and not at $1/\sqrt{2}$ times the peak value. Further, the damping in irregular sea states can be estimated by a linear spectral approach outlined in (Rüdinger 2003; Storhaug et al. 2003). Basically, it fits the analytical spectrum from the SDOF system to the spectrum based on FFT of the time series. The analytical relation between the response spectrum, $S_x(\omega)$, and the excitation spectrum, $S(\omega)$, is written

$$S_x(\omega) = |H(\omega)|^2 S(\omega) = \frac{1}{(\omega_s^2 - \omega^2)^2 + 4\delta^2\omega_s^2\omega^2} S(\omega) \tag{2.53}$$

The excitation spectrum is assumed to be described by the high frequency tail of the wave spectrum.

$$S(\omega) = \frac{A}{\omega^n} \tag{2.54}$$

The slope parameter n, the coefficient A, the springing frequency ω_s and the damping ratio δ are determined by unconstrained nonlinear optimization using the MATLAB function *fminsearch*. Guessed input values are necessary to control the procedure. A Hanning window is used with 4096 FFT points defining the resolution. The frequency interval is also important, since the total response is not described by a SDOF system.

Storhaug et al. (2003) estimated the slope parameter n to be close to 4, which would be representative for Torsethaugen wave spectrum rather than the JONSWAP spectrum. By considering other loading conditions and ships, it was however confirmed that this slope factor was not necessarily representative for the high frequency tail behaviour of the wave spectra. This may be due to the hump-hollow behaviour of the excitation. To obtain a

proper estimate of the high frequency slope, the expressions should be modified.

The following procedure may be used to determine the nonlinear damping of the viscous type. It was used to check the nonlinearities of the damping in e.g. Figure 5.5. The homogeneous equation of motion including viscous damping may be formulated as

$$m\ddot{y} + b_1\dot{y} + b_2\dot{y}|\dot{y}| + cy = 0 \tag{2.55}$$

where b_2 is the damping coefficient related to the viscous part, while b_1 is related to conventional linear damping. This equation can be linearized within each period by requiring equivalent linear energy dissipation per cycle from the damping terms, e.g. (Faltinsen 1990; Huse 1993). The equation is reduced to

$$m\ddot{y} + b_{tot}\dot{y} + cy = 0 \tag{2.56}$$

where

$$b_{tot} = b_1 + \frac{8}{3\pi}\omega y_0 b_2 \tag{2.57}$$

y_0 is the response level for the cycle considered. The total damping b_{tot} from the decay curve can be plotted versus $\frac{8}{3\pi}\omega y_0$. The crossing with the y-axis defines the linear b_1 damping, while the slope represent the viscous damping coefficient b_2.

2.4 Transfer functions

2.4.1 Linear transfer functions

The response, $y(t)$, to a linear system exposed to a linear oscillating force, $f(t)$

$$f(t) = a_i \cos(\omega_i t) \tag{2.58}$$

is described by

$$y(t) = r_i \cos(\omega_i t + \theta_i) \tag{2.59}$$

where θ_i is the phase lag, ω_i is the forced frequency and a_i and r_i are amplitudes. The ratio of response amplitude to force amplitude for all frequencies are defined as the linear transfer function amplitude, referred often to as the *transfer function*

$$|H_1(\omega_i)| = \frac{r_i}{a_i} \tag{2.60}$$

while $H_1(\omega_i)$ is the complex transfer function, which contains information about the phase relations.

The transfer functions are made nondimensional as shown in Appendix B.2.2.

2.4.2 'Nonlinear' transfer functions

'Nonlinear' quasi-transfer function is defined as the ratio of the maximum response amplitude and the wave amplitude. The purpose is to illustrate the relative importance of the higher harmonics at the encounter frequency. The force is assumed to create a response consisting of the encounter response plus higher harmonic responses as

$$y(t) = \sum_{i=1}^{N} r_i \cos(i\omega_i t + \theta_i) \tag{2.61}$$

The quasi-transfer function is now defined as

$$|H_N(\omega_i)| = \frac{max(y) - min(y)}{2a_i} \tag{2.62}$$

where the maximum and minimum values are identified within each encounter period. The higher harmonics depend on the excitation level, hence, higher excitation amplitudes will increase the contribution from the higher harmonics and the transfer function is only partly nondimensional.

2.4.3 Second order transfer functions

If the excitation force consists of two frequency components

$$f(t) = a_i \cos(\omega_i t + \theta_i) + a_j \cos(\omega_j t + \theta_j) \tag{2.63}$$

the response including second order effects can be written

$$y(t) = r_1 \cos(\omega_i t + \theta_1) + r_2 \cos(\omega_j t + \theta_2) + r_3 \cos((\omega_i + \omega_j)t + \theta_3) + r_4 \cos((\omega_i - \omega_j)t + \theta_4) + r_5 \tag{2.64}$$

The second order transfer function is derived from a part of this response as

$$|H(\omega_1, \omega_2)|_{sum} = \frac{r_3}{a_i a_j} \qquad |H(\omega_1, \omega_2)|_{dif} = \frac{r_4}{a_i a_j} \tag{2.65}$$

In this study only the sum frequency effects are considered, hence it represents only the first quadrant of the 3D transfer function, which should be symmetric about the 45^0 line where $\omega_1 = \omega_2$.

Results are presented only for the vertical bending moment, which is made nondimensional in the following way

$$H_{VBM}(\omega_{1,e}, \omega_{2,e}) = \frac{VBM}{\zeta_1 \zeta_2 \sqrt{k_1 k_2} \rho g B L^2} \tag{2.66}$$

A monochromatic wave amplitude, ζ, is considered as equivalent to two waves of half amplitude. The wave numbers $k_i = 2\pi/\lambda$, are necessary to make the moment nondimensional, since the square of the wave amplitude is also employed.

A more detailed procedure on how the linear, 'nonlinear' and second order transfer functions are established is presented in Section 4.6.1 and 4.6.3. Nonlinear systems may also be assessed in alternative ways, e.g. (Schetzen 1980).

2.5 Time series analysis

The methods used to evaluate the time series with respect to mean values, amplitudes, phases and uncertainties are outlined in the following. The processes are assumed stationary, ergodic and Gaussian distributed. The Gaussian distribution of the vibration response was illustrated by Storhaug et al. (2003).

2.5.1 Estimate of amplitudes

The linear transfer function is established by different methods. The first method removes the mean value and defines the zero crossing process. Between the zero crossings, the local maximum and the local minimum are identified, and these are coupled to define the amplitude as half of the difference. By combining pairs of these, the mean amplitude, a, is estimated.

$$a = \frac{1}{N}\sum_{i=1}^{N}\frac{max(x) - min(x)}{2} \tag{2.67}$$

This method is useful in order to estimate the uncertainty represented by the standard deviations, Appendix B.3. Filtering may be necessary.

The second method assumes a sinusoidal signal, and finds the amplitude from the standard deviation of the whole times series using all time samples,

$$a = \sqrt{2}\cdot\sigma \text{ where}$$
$$\sigma^2 = \frac{1}{n-1}\sum_{i=1}^{n}(x_i - \overline{x})^2 \tag{2.68}$$

which is useful when only one single frequency is present. Alternatively, filtering may be applied.

The third method finds the amplitude from the standard deviation of the discrete wave spectrum (when the mean value is zero).

$$a = \sqrt{2}\cdot\sigma \text{ where}$$
$$\sigma^2 = \sum_{i=1}^{n} S(\omega_i)d\omega_i \tag{2.69}$$

This method is useful when several distinct peaks in the spectrum exist, and the amplitudes corresponding to the different frequencies are to be determined.

The fourth method fits a series of sinusoidal components to the signal using a least square fit.

$$\sum_{i=1}^{N} A_i \sin(\omega_i t_j) + B_i \cos(\omega_i t_j) = R(t_j) \tag{2.70}$$

The subscript $_j$ refers to each sample in the selected time series of the response, R, while subscript $_i$ depends on the chosen frequencies which are used in the fitting procedure. The coefficients A and B are solved using the MATLAB function *lsqr*. The same resolution as the FFT is used, and zero frequency is included to capture the mean level. For each frequency the sin and cos pairs can be rewritten as

$$r_i \cos(\omega_i t_j + \theta) \tag{2.71}$$

Hence, it is useful for finding the phases between components. Iteration on the frequency is necessary for long time series.

The fifth method, referred to as *unconstrained nonlinear optimization*, finds the minimum of a function containing several unknown parameters. The function is the mean of the squared difference between the time series and the expression $r_i \cos(\omega_i t_j + \theta)$. An initial estimate of the unknown parameters is necessary, and the method becomes less robust when the number of parameters increases. The MATLAB function *fminsearch* is applied.

In principle, all these methods should provide the same answer, which will confirm the correctness of the methods used. In each case at least two methods are used.

2.5.2 Spectral density

The response spectrum illustrates distinct frequency effects, indicates noise and can be used for filtering purposes. The spectrum is obtained from the time series. Two different methods are considered.

The first method (Wiener-Khintchine Theorem) derives the spectrum by first establishing the autocorrelation function. Assuming a continuous time series, this is written

$$R_{xx}(\tau) = \lim_{T\to\infty} \frac{1}{2T} \int_{-T}^{T} x(t)x(t+\tau)dt \tag{2.72}$$

$$S_{xx}(\omega) = \frac{1}{\pi} \int_{-\infty}^{\infty} R_{xx}(\tau) e^{-i\omega\tau} d\tau \tag{2.73}$$

It assumes that the stochastic process is ergodic, i.e. the ensemble average can be evaluated as a time average of a single record. The process should be at least weakly stationary.

The second method applies Parseval theorem to find the autospectral density function, herein referred to as the *spectrum*

$$S_{xx}(\omega) = \lim_{T\to\infty} \frac{1}{2T}|X(\omega)|^2 \tag{2.74}$$

The second method is more efficient, and FFT is applied to the discrete finite time series. The definition in MATLAB differs from Eq.(2.74) with reference to factors and integration boundaries, which are accounted for. The inverse FFT reproduces the filtered time series.

For a finite time series, the end effects may become pronounced for short time series in combination with a narrow band filter. A rough filter (cut off) is used to remove the part of the spectrum outside the frequency interval of interest, and the applied filter did not change the phasing between the harmonics. The resolution of the discrete FFT is

$$\Delta\omega = \frac{2\pi}{dtN} \tag{2.75}$$

which may be rather large, if the time series is short.

The cross correlation function, R_{xy}, defined by replacing $x(t)$ in Eq.(2.73) with $y(t)$, is used to define the phase between a response and a reference response, y. The period, T_0, of the reference response in regular waves is found by the autocorrelation at the first local maximum, $\tau = T_0 > 0$. The response period is found in the same way, and the ratio defines the phase lag.

Smoothing the raw FFT spectrum gives a better appearance, rather than the spiky appearence from the discrete spectrum. Moreover, using the smoothed spectrum will provide more reliable estimates of certain characteristics such as the peak period. This method has therefore been employed when necessary. A Gaussian distribution, referred to as a Gaussian Bell, is defined as

$$f(x) = \frac{1}{\sqrt{2\pi}\sigma} \exp \frac{(x-\overline{x})^2}{2\sigma^2} \tag{2.76}$$

where σ is the standard deviation. The original spiky discrete spectrum was smoothed by moving this Gaussian Bell through the frequency range and thereby weighting each specific value based on the Gaussian distribution. A wide bell will remove all details, while a narrow will not make a difference. A standard deviation of $0.125 rad/s$ was used, and 95% of the interval considered was then confined within $0.5 rad/s$. The springing peak will become lower and wider. The smoothing will provide end effects, reducing the values at the lower and upper end to half. This does not matter, because it is above or below the frequency range of interest.

2.5.3 Wavelet transformations

The wavelet transformations may be used to evaluate the quality of a time series, e.g. to detect when the short waves break down in towing tanks, to identify relations between waves and response, or between different responses, and to detect/count special events. In this thesis it was used to evaluate the wave quality of short waves.

Wavelet analysis is a method to investigate properties of time series. While Fourier analysis provides the spectrum, the wavelet analysis provides also a time or space variation of the spectrum. E.g. for a stochastic process and for an impulse process, the Fourier analysis may give the same spectrum. A single extreme peak in the time series is smeared out. The wavelet analysis will give a spectrum which reveals the single extreme peak at other frequencies than the main components indicating a special event. Fourier analysis may alternatively be used over a time interval that is shifted gradually.

Newland (1993) considered orthogonal wavelets, which is useful, because efficient algorithms similar to FFT can be utilized. Harmonic discrete wavelets were only briefly described. His method involved a specific frequency resolution limited by the number of time samples used. This is not convenient, since small changes in the frequency can be of interest. Moreover, the square maps used to visualise the spectrum give a poor resolution in time for the lower levels of low frequency.

Donoho et al. (1999) offers MATLAB routines, and *cwt.m* was modified to serve the purpose of this research. Each octave band (according to Newland (1993)) was divided into new layers to increase the resolution with corresponding new different wavelet components. The same routine is also modified to visualise the square map for a continuous wavelet moving through the whole time series rather than being distributed at specific points. The basic wavelet used is expressed as

$$\psi(t) = e^{i\frac{\omega_0}{s}(t-\tau)} e^{\frac{1}{2}(\frac{t-\tau}{s})^2} \tag{2.77}$$

where $1 < s < 2$ defines the width at each layer, and s is doubled for each octave. τ is the mid point of the wavelet, which was moved through the time series by changing τ stepwise.

The wavelet method does not appear to be well understood from a physical point of view. An alternative method, which may be more promising is the Hilbert-Huang transformations, (Trulsen and Krogstad 2001; Veltcheva 2001). Huang et al. (1998) developed the method and provided a detailed description of it.

2.6 Waves and sea states

2.6.1 Irregular waves and spectral density

A sea state consists of irregular waves. In linear theory the irregular waves is developed as superposition of regular waves. The sea state is commonly represented by a wave energy spectrum such as JONSWAP, (DNV 2000)

$$S(\omega) = \alpha g^2 \omega^{-5} \exp[-\frac{5}{4}(\frac{\omega}{\omega_p})^{-4}]\gamma^{\exp[-0.5(\frac{\omega-\omega_p}{\sigma\omega_p})^2]}$$

$$\alpha = \frac{5}{16}\frac{H_S^2\omega_p^2}{g^2}\cdot(1-0.287\ln(\gamma))$$

$$\sigma = 0.07 \text{ when } \omega \leq \omega_p \text{ and } \sigma = 0.09 \text{ when } \omega > \omega_p \tag{2.78}$$

where γ is the peakness factor, ω_p is the spectral angular peak frequency and α is the generalised Phillips' constant. The significant wave height, H_S, and peak period, $T_P = \frac{2\pi}{\omega_p}$, are input values defining the sea state. From a measured spectrum the significant response and zero up-crossing can be estimated as

$$H_S \approx 4\sqrt{m_0} \tag{2.79}$$

$$T_Z = 2\pi\sqrt{\frac{m_0}{m_2}} \tag{2.80}$$

$$m_0 = \int_0^{\omega^*} S(\omega)d\omega \tag{2.81}$$

$$m_2 = \int_0^{\omega^*} S(\omega)\omega^2 d\omega \tag{2.82}$$

This can also be estimated from the time series. A one side spectrum is assumed with an upper limit, ω^*, which is limited by the length of the time series or noise. The zero crossing period is more sensitive to the cut off at the ends than the significant wave height due to ω^2. The relation between the peak period and the zero up-crossing period, T_Z, for JONSWAP is written

$$T_P = T_Z\sqrt{\frac{11+\gamma}{5+\gamma}} \tag{2.83}$$

JONSWAP is representative for developing seas, while Pierson-Moskowitz (PM) wave spectrum is a special case with $\gamma = 1$ representing fully developed sea and unlimited fetch. The PM spectrum *based on wind input* is written

$$S(\omega) = \frac{A}{\omega^5}e^{-\frac{B}{\omega^4}} \text{ where}$$

$$A = 0.0081g^2 \text{ and } B = 0.74(\frac{g}{V})^4 \tag{2.84}$$

where V is the wind speed $19.5m$ above the water surface, (Myrhaug 1998).

Torsethaugen double peak wave spectra include both swell and wind sea, (Torsethaugen 1996). The high frequency tail behaviour differs from JONSWAP and PM. The exponent n in ω^{-n} from Torsethaugen may be closer to four rather than five in the other two spectra. This affects the springing predictions as illustrated by Tongeren (2002). The wave energy spreading, represented by $\cos^p(\theta)$ or bi-directional spectra, is relevant in full scale, (Storhaug et al. 2003; Vidic-Perunovic 2005), but the effects are not considered during the model tests.

The encounter response or encounter wave spectra are converted into response or wave spectra by considering the encounter frequency relation in Eq.(A.28). Rewriting the frequency relation, accounting for head to beam seas (not following sea; absolute signs), gives

$$\omega_0 = \frac{g}{2U\cos(\beta)}(-1+\sqrt{1+4\omega_e\frac{U}{g}\cos(\beta)}) \quad -90^0 < \beta < 90^0 \tag{2.85}$$

The relation between the wave and encounter frequency spectrum is given as

$$\begin{aligned} S(\omega)d\omega &= S_e(\omega_e)d\omega_e \\ S(\omega) &= S_e(\omega_e)(1+2\frac{U}{g}\omega\cos(\beta)) \end{aligned} \tag{2.86}$$

and the wave and encounter frequency are related values through Eq.(2.85).

Wave breaking is avoided during the model tests to reduce the change of the spectra to a minimum. The breaking (steepness) criterion for a regular wave is written

$$H < \frac{\lambda}{7} = \frac{\frac{g}{2\pi}(\frac{2\pi}{\omega_0})^2}{7} \tag{2.87}$$

while for irregular sea, the following criterion is assumed applicable in the towing tank

$$S = \frac{2\pi H_s}{gT_P^2} < 0.03 \tag{2.88}$$

to avoid a single wave breaking in the tank. The waves along the towing tank represent an approximation to real sea states, since it is no wind in the towing tank. Especially, the energy in the high frequency range is expected to be reduced along the tank due to lack of wind. The breaking criterion

$$S = \frac{2\pi H_S}{gT_Z^2} < \begin{cases} \frac{1}{10} & \text{for} \quad T_Z \leq 6s \\ \frac{1}{15} & \text{for} \quad T_Z \geq 12s \end{cases} \tag{2.89}$$

stated in (DNV 2000) agree well with Eq.(2.88). Linear interpolation is used in between the ranges.

To generate a time series of the wave elevation, the individual regular wave components were derived by dividing the wave spectrum into many blocks. Each block had a specific

frequency interval, $d\omega$. The individual wave amplitudes were estimated by a single block as

$$\zeta_i = \sqrt{2S(\omega_i)d\omega} \tag{2.90}$$

where ω_i is the mid frequency in the block. The sea state with waves moving in the negative x-direction was assembled as

$$\zeta = \sum_{i=1}^{n} \zeta_i \cdot cos(\frac{\omega_i^2}{g}x + \epsilon_i + \omega_i t) \tag{2.91}$$

where ϵ_i is a random number between 0 and 2π. The amplitude could also have been a stochastic variable, (Wang 2001), but this was not important in this context.

2.6.2 Wave heights exciting linear and second order springing

It may be of interest to know the wave amplitudes that excite the linear and second order springing response. The second order transfer function at resonance depends on the wave amplitude squared as well as the damping level. In this thesis the sum frequency springing response obtained from model experiments was corrected based on the corresponding exciting wave height and period to illustrate the relative importance of the monochromatic sum frequency springing and linear springing. This is further explained in Section 4.9.

An investigation by Myrhaug and Kvålsvold (1992) and Myrhaug and Kvålsvold (1995) were utilized. The joint distribution of wave heights and periods was established by Weibull fits to wave measurements. This means that it was possible to find an estimate of the mean regular wave height given the wave period in a specific irregular sea state. This is further described in Appendix A.10. Based on mid interval significant wave height in the Beaufort scale in Appendix A.10, the mean regular wave heights exciting the linear and monochromatic second order springing as a function of the Beaufort strength are shown in Figure 2.8. The wave height exciting second order springing is roughly half a meter higher and two seconds longer than the waves exciting linear springing in head seas. The lower plot presents also the zero up-crossing period and the specific wave periods exciting springing, and the middle plot displays the significant wave height corresponding to the Beaufort strength. The wave heights increase with Beaufort strength, even though the speed reduction from full scale measurements was accounted for.

2.7 Fatigue damage

Cracks causing leakage are unacceptable. Crack growth or fatigue may be divided into three phases: Initiation, crack growth and sudden fracture (or crack arrest). In this context, the crack growth phase due to high cycle fatigue is considered. Initial cracks will always exist as small air voids in welded materials. According to current design practise,

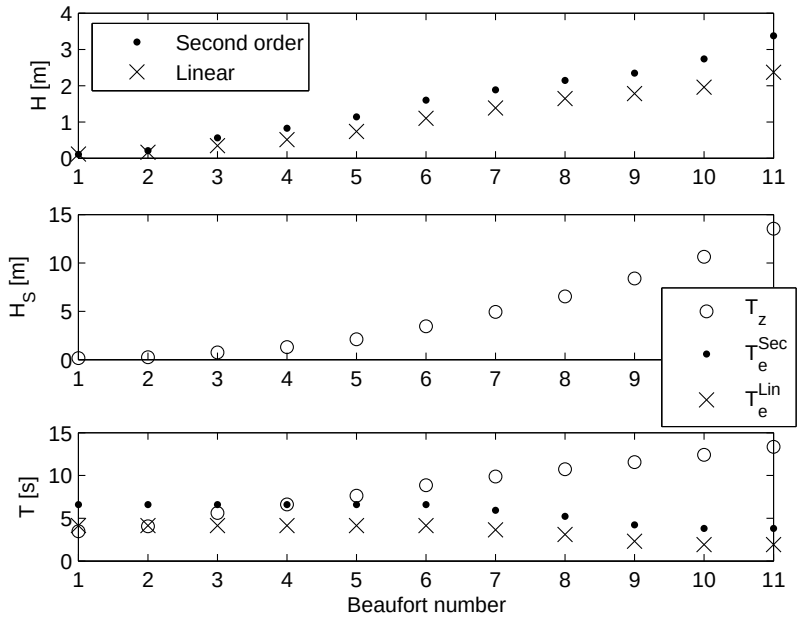

Figure 2.8: *Mean regular wave heights, H (upper plot), exciting linear and monochromatic sum frequency springing in head sea state at realistic speeds as a function of the Beaufort strength. The speeds are interpoated between pars of speed in knots and significant wave height (15/0,15/4,10/5,7.5/6,5/7,2.5/8,0.1/9,0.1/20). The significant wave height in middle plot and the zero crossing period, T_Z, in the lower plot correspond to the Beaufort number. In the lower plot the wave periods corresponding to linear, T_e^{Lin}, and monochromatic sum frequency, T_e^{Sec}, springing are also shown.*

the fatigue life is defined as the time it takes for an initial crack to grow through the thickness of the plate. Such short cracks are difficult to detect by visual inspections.

The strength formulation is in accordance to DNV Classification Note on fatigue, (DNV 2005a). The cumulative fatigue damage is calculated by Palmgren-Miner's rule

$$D = \sum_{i=1}^{k} \frac{n_i}{N_i} \leq \eta \tag{2.92}$$

where n_i is the number of cycles for a specific stress range in block i, and N_i is the number of cycles to failure at the same constant stress range. The summation should be less than $\eta = 1.0$ or some lower value depending on consequence and access for inspection. Miner-Palmgren's rule disregards the effect of the loading sequence, and from Wirshing (1981) the mean value and coefficient of variation (CoV) are estimated to $\mu_D \cong 0.8$ and $CoV \cong 0.3$.

The number of cycles to failure as a function of the stress range is defined by the SN-curve for a welded joint in air or with cathodic protection. The SN-curve is based on a welded,

but grinded joint without any SCF. The SN-curve corresponds to a 2.3% probability of failure, hence the mean fatigue life is about twice. The SCF is multiplied with the nominal stress range to define the total stress range, $\Delta\sigma$. The two slope SN-curve is written

$$\log(N) = \log(\overline{a}) - m\log(\Delta\sigma) \tag{2.93}$$
$$\log(\overline{a}) = 12.65 \quad m = 3 \quad \text{when } N \leq 10^7$$
$$\log(\overline{a}) = 16.42 \quad m = 5 \quad \text{when } N > 10^7$$

The mean stress level is disregarded, and the residual stress is assumed to be tensile at yield, but the effects are otherwise disregarded. Thickness effects are also neglected assuming a thickness below $25mm$.

The full scale measurements of the actual iron ore carrier were evaluated by (Storhaug et al. 2006), and an equivalent slope of $m = 4$ for the wave frequency damage and $m = 3.7$ for the vibration damage were determined based on several years of measurements. This is useful when scaling long term results due to different stress levels, and it is used in Section 6.5.

2.7.1 Rainflow counting

Based on the stress time series established from the measurements, the stress cycles, which result in fatigue damage, need to be determined. For a general wide band process, the Rainflow counting method has been verified by experiments, (Strating 1973), to count cycles that contribute to the crack growth. The rigid body response is a slightly wide band process, while the vibration response is a narrow band process, but the combined effect is certainly a wide band process. The counting procedure results in an exceedance diagram of stress ranges. The standard fatigue calculations can subsequently be applied. Further description of Rainflow counting may be found in for instance (Almar-Næss 1985; ASTM 1998; Glinka and Kam 1987), with an alternative in (Jiao and Moan 1990).

2.8 Long term fatigue analysis

The short term damage, during a typical sea state of tree hours, is established through Rainflow counting of the measured time series. For shorter time series simple time extrapolation to three hours is carried out.

To estimate the fatigue damage during 20 years of service, the damage is estimated for all the relevant sea states defined by a scatter diagram. The scatter diagram presents the different sea states with their probability of occurrence. The sea states are characterised by combinations of significant wave height and zero up-crossing period. The important sea states in North Atlantic and World Wide trade (scatter diagram; i.e. combinations of significant wave height and period) are illustrated in Section 4.7.1.

The current investigation only accounts for a vessel in head sea, but ballast condition, cargo condition and port time were considered. The long term fatigue damage was calculated as the weighted sum

$$D = \frac{20 \cdot 364 \cdot 24}{3} \sum_{n=1}^{N^L} \sum_{i=1}^{N^S} p_n^L p_i^S d_{n,i} \tag{2.94}$$

where p refers to the probability of loading condition, ^{L}, and sea state, ^{S}. $d_{n,i}$ is the corresponding fatigue damage for a specific three hour sea state and loading condition. For the ship, the time in port, ballast and cargo condition were 33.3% each in the North Atlantic trade, (Moe et al. 2005).

Since, there was not enough time to carry out experiments for all sea states in a scatter diagram, extrapolation and interpolation was carried out based on a response surface method, which is described in Section 2.8.1.

2.8.1 Use of response surface to extrapolate results

The model was tested in some representative sea states. These were selected to reveal the trends of the fatigue damage due to vibration and wave excitation. A rough procedure was derived to extrapolate the fatigue damages from the selected sea states to calculate the total fatigue damage for the whole scatter diagram. The method is referred to as the *response surface method*. Results from the equations below are illustrated in Section 5.4.5.

The hydrodynamic loading phenomena that cause the vibration damage in different sea states are not fully known, e.g. both springing and whipping contribute. Hence, empirical equations were tested to represent the distribution of the fatigue damage for the whole scatter diagram. The empirical equations expressing the response surfaces were fitted to the results of the fatigue damage in the different sea states. The WF damage and HF damage were considered separately. Similarly, the ballast and cargo condition were handled separately.

The total fatigue damage in the different sea states was described by the equation $D_T(h,t)$. h refers to the significant wave height, while t refers to the zero up-crossing period. The total fatigue damage was the sum of the WF damage, $D_{WF}(h,t)$, and the HF damage, $D_{HF}(h,t)$. How the fatigue damage is calculated is explained in Section 4.7. Polynomial expressions were chosen as

$$D_{WF}(h,t) = a_0 + a_1 h + a_2 t + a_3 ht + a_4 h^2 + a_5 t^2 + a_6 h^2 t + a_7 h t^2 + a_8 h^2 t^2$$

$$D_{HF}(h,t) = b_0 + b_1 h + b_2 t + b_3 ht + b_4 h^2 + b_5 t^2 + \tag{2.95}$$

$$b_6 h^2 t + b_7 h t^2 + b_8 h^2 t^2 + b_9 \sin^8\left(\frac{2\pi h}{20}\right)) \tag{2.96}$$

The equation for the vibration damage, similar to the equation for the wave frequency damage, did not represent the vibration damage satisfactorily. More terms in the polynomial series gave unreliable answers. Based on the behaviour of the vibration damage, a sinusoidal term was added. The exponent of 8 was used due to a significant increase in vibration damage observed between 3 and $4m$ significant wave height. Such a sudden increase was not observed for the periods. The value of 20 gave a sinusoidal peak at $5m$, which appeared to give a natural peak for the reduced speed case. In full speed the sinusoidal term was less important due to a rapid growth of the vibration damage as a function of sea state (and speed). The importance of this term may therefore vary for a blunt and a slender ship with different speed behaviour and different excitation sources. It may also vary with the dominating sea states, in case a less harsh envionment is considered. The same procedure is however expected to be feasible also for other ship types.

The expressions for wave frequency and vibration damage are nonlinear in h and t, however, the expressions are linear in the unknown coefficients a_i and b_i. A least square fit by the MATLAB function *lsqr(A,B)* was performed to the measured data considering the matrix relation, e.g. for the wave frequency damage

$$\begin{aligned} A \cdot X &= B \\ A_i &= [1 \; h_i \; t_i \; (h_i t_i) \; (h_i^2) \; (t_i^2) \; (h_i^2 t_i) \; (h_i t_i^2) \; (h_i^2 t_i^2)] \\ X &= [a_0 \; a_1 \; a_2 \; a_3 \; a_4 \; a_5 \; a_6 \; a_7 \; a_8]' \\ B_i &= D_{WF}(h_i, t_i) \end{aligned} \tag{2.97}$$

X and B are column vectors, $_i$ denotes row number i, and $'$ refers to the transposition symbol. Matrix A is made up of all the rows of A_i, and h and t are chosen equal to the values for the tested sea states. This matrix is therefore known, and row i refers to damage from a specific sea state where h and t are fixed. 12 to 39 sea states were considered.

To control the behaviour of the parameters slightly, zero points were introduced along the edge of the scatter diagram where the wave heights were zero. Such wave heights will cause zero fatigue damage. In addition zero points were introduced along the edge where the periods were zero. The latter is not really physical or have much meaning, since such sea states do not exist. It however controls the prediction towards steep sea states, which are unlikely to occur. When negative damage in a sea state was predicted, the damage was set to zero. Basically, it is important to cover a good spread of the sea states in both period and height for this procedure.

A few obvious uncertainties exist. The first uncertainty relates to the goodness of the least square fit. This uncertainty is indicated by the difference in the predicted and measured fatigue damage from only the selected sea states, and constitutes as much as 10% in the original ballast condition. The second uncertainty relates to the equations ability to extrapolate/interpolate the fatigue damage to the region outside/in between the selected sea states. The method is applied to both few and many sea states in one loading condition.

The deviation in the results will indicate the magnitude of uncertainty related to the small number of sea states selected. The third uncertainty relates to the stochastic behaviour of the short time series in irregular sea. Despite these uncertainties, the response surface method will illustrate the location of the important sea states, and the relative importance between the WF and HF damage.

Chapter 3

Simplified analysis of vibration response and speed reduction

The purpose of this chapter is to illustrate the contribution to vibration from impacts on the upper bow/stem flare area based on the hypotheses in Section 2.1. The amplification of the incident waves due to reflection from the blunt bow, the additional steady wave elevation at the stem and the impact force on a half cone are considered. This effect is referred to as *stem flare whipping*, which is simulated in regular and irregular head sea. Nonlinear springing is not included, but Froude-Kriloff excited linear springing is included in the simulations.

The speed is estimated in different sea states in Section 3.2. A set of speeds are selected for the subsequent model tests.

3.1 Simplified analysis of whipping from stem flare impacts and linear springing

Whipping may contribute to the high frequency response. Since the damping is low, it is possible that whipping of small magnitudes superposed on the springing vibration still appear as springing. The impacts may occur often, hence the whipping vibration may still be present when a new impact occurs. The new impact will either increase or reduce the vibration level depending on the phasing.

The simplified hydroelastic analysis employs the Euler beam formulation, modal superposition and simplified strip theory. The linear excitation consists of the Froude-Kriloff

pressure which may excite linear springing. The second loading comes from impacts on the bow/stem represented by a half cone. Impacts exciting whipping occur when the combined effect of steady water elevation, incident waves, reflected waves and ship motions make the water surface hit the half cone. The steady water elevation, incident and reflected waves are calculated based on an infinite vertical wall representing the bow and moving forward with the vessel's speed. Total reflection is assumed also for the longer waves, and it constitutes a diffraction effect localized to the bow. The numerical analysis in time is solved by a Newmark-β scheme with iterations to account for the hydroelastic effect. Iterations are necessary to get feedback from the vibration response on the hydrodynamic excitation forces. Further explanations are given in Section 2.1.1 - 2.1.3, 2.2, 2.6 and Appendix A.3 and A.5. A program was made for this purpose.

The dimensions and sectional properties are listed in Table 3.1. The added mass of the flexible modes given in Table 3.1 is lower than the actual added mass for these frequencies, but it is used to achieve a natural springing frequency close to $3.32 rad/s$ in ballast condition, as for the real ship.

Table 3.1: *Properties of a rectangular ship used in simplified assessment.*

Property	Value	Unit
Density of water, ρ	1025	$[kg/m^3]$
Acceleration of gravity, g	9.81	$[m/s^2]$
Young's modulus, E	$2.1 \cdot 10^{11}$	$[N/m^2]$
Length, $L = L_{pp}$	294	$[m]$
Breadth, B	53	$[m]$
Draft, T, Ballast/Cargo	11.33/18	$[m]$
Deck height above BL in bow, z	27	$[m]$
Neutral axis above BL, z_{na}	10.8	$[m]$
Distance from BL to apex of cone, z_c	18.8	$[m]$
Area moment of inertia, I	680	$[m^4]$
Speed, U	7.8	$[m/s]$
Deadrise angle of cone, α	50	$[^\circ]$
Wave heading, β (0=head sea)	0	$[^\circ]$
Sectional mass, m= ρBT	615502/977850	$[kg/m]$
Sectional water plane stiffness, $c = \rho g B$	532928	$[kg/(ms^2)]$
Damping ratio for rigid modes, δ_r	0.4	$[-]$
Damping ratio for flexible modes, $\delta_{f,i}$	$0.005(2i-5)$	$[-]$
Added mass for rigid modes, a_r	2m	$[kg/m]$
Added mass for flexible modes, a_f	0.5m	$[kg/m]$
Natural springing frequency, ω_s	3.22/2.56	$[rad/s]$
Natural rigid body frequency, ω_r	0.54/0.43	$[rad/s]$

The cone geometry is an idealization of the real geometry. Figure 3.1 illustrates the differ-

ence. The cone is shown with an angle corresponding to 60 and 40°. The former is close to the stem angle, while the latter is close to the flare angle. Due to the 3D geometry an angle of 50° was chosen. The effective angle differs due to the slope of the water surface and the flow along the bulb. The added mass formulation by Shiffman and Spencer (1951) was applied. The cone is assumed with infinite extent upwards, hence water on deck is disregarded. 3 flexible modes in addition to pitch and heave are considered.

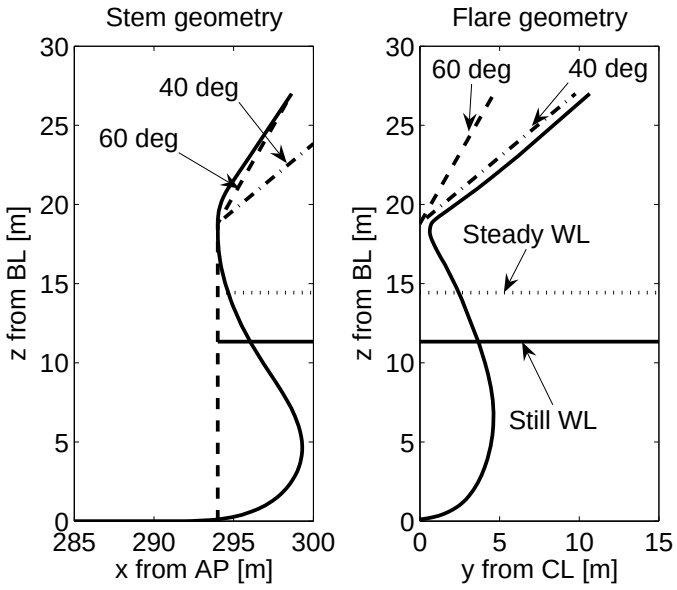

Figure 3.1: *Stem and flare geometry at FP of the real ship compared with two cone angles. The steady wave elevation at 15kn is illustrated.*

3.1.1 Simulations in regular waves in ballast condition

In regular waves the impact event is well defined in case the water hits the half cone. Linear springing occurs only if the encounter frequency is equal to the springing frequency. The impact force refers to all the load components in Section 2.1.3 that constitute an impact of short duration. For illustration, a typical impact force distribution is provided in Figure 3.2. The wave height corresponds to the response at $15kn$ in Figure 3.5. It is seen that the conventional slamming is only a part of the total force, and *the exit phase may be as important as the entry phase*. The water level on the cone is indicated by the hydrostatic force. The maximum force corresponds to 200kN, and it is observed that the hydroelastic effect on the loading is insignificant (the thick continuous line is on top of the dashed line). The small hydroelastic effect means that the global vibration of the hull girder does not significantly affect the magnitude of the impact load. The duration of the impact is about $0.8s$, hence it acts almost like an impulse, since the natural period is $2s$. The important feature is the difference between the negative and positive area below the total force curve, resulting in an effective negative force. For other impacts the relative magnitudes varies,

and the force may neither be impulse like nor effectively negative. Note, it appears from the Figure 3.2 that the inertia and 'Froude-Kriloff' term is similar. If the vessel is not moving much the relative velocity and the surface velocity would be similar according to Eq.(2.7), and if also the added mass are similar to the displaced mass, then the inertia term would be similar to the 'Froude-Kriloff' term. This is actually the case here.

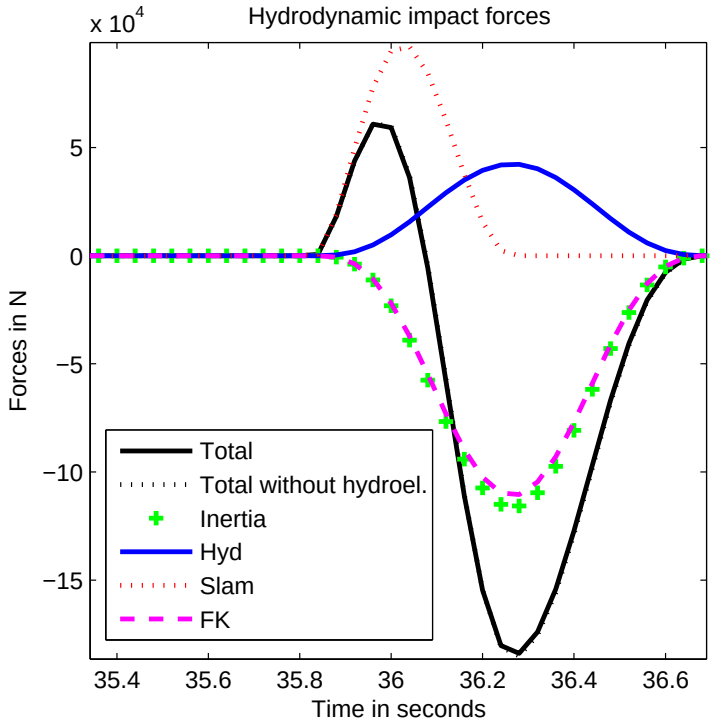

Figure 3.2: *Illustration of the total impact force distribution on the half cone ($\alpha = 50°$) in regular waves. Slamming=Slam, 'hydrostatic'=Hyd, inertia=inertia and 'Froude-Kriloff'=FK; $H = 5m$, $U = 15kn$, $T = 5.9s$.*

The steepness criterion for regular waves in Eq.(2.87), given in Section 2.6, is used to investigate the sensitivity of vibration in full speed of $15kn$ as a function of the regular wave height, H. It provides an upper limit of the vibration response in head waves. The results are presented as nominal stress amplitude of both the high frequency (HF) vibration and the wave frequency (WF) response in Figure 3.3. The HF vibration may include both linear springing and stem flare whipping, but both excitation sources may not contribute simultaneously in the simulations. The hump-hollow behaviour is observed for both the WF and HF response. Moreover, the linear resonance and the second harmonic are observed at an encounter period of 2 and $4s$.

It is not evident when the water touches the cone in Figure 3.3. Due to the short waves, the vessel does not move significantly in the simulations. If an incident wave amplification

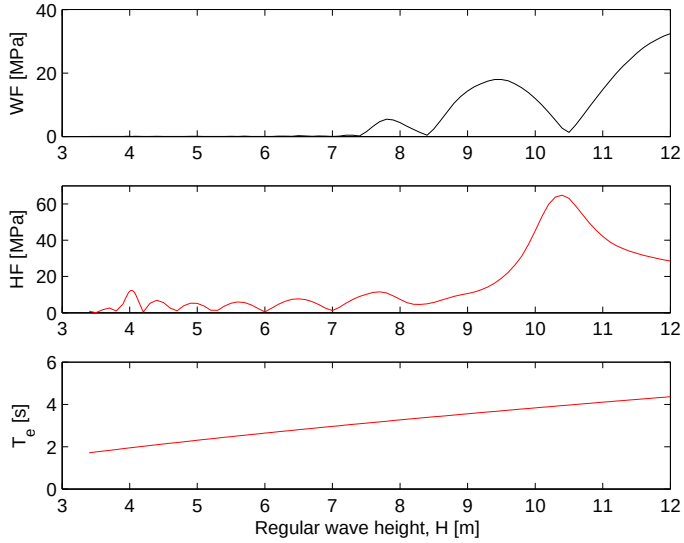

Figure 3.3: *The upper limit of HF due to linear springing and whipping and WF nominal stress amplitudes in regular head waves based on the steepness criterion (1/7);* $U = 15kn$, $\alpha = 50°$.

of 3 is assumed, a wave height of $2.9m$ is enough to touch the cone's apex. The 'linear' springing peak will then include a small effect from the impact force, hence *nonlinear forces may contribute also when the encounter frequency coincides with the springing frequency*. The submergence of the cone becomes up to $1.6m$ in the case of 'linear' springing. The second harmonic peak has an amplification of 2.7, and the motion of the vessel is still small. The water reaches the deck level at $9.3m$ wave height, and the speed will be reduced considerably. Hence, the predicted HF amplitude is most conservative. According to the steepness criterion, it is theoretically possible to induce large stem flare whipping.

To investigate the sensitivity to wave periods, a regular wave height of $5m$ is chosen in combination with full speed of $15kn$. Figure 3.4 presents the WF and HF nominal stress amplitude versus the encounter period. The lowest wave period does not satisfy the breaking criterion, while the upper wave period of $15s$ captures the rigid body response peak. The springing peak and hump-hollow behaviour are evident. A sudden drop of the vibration level is observed at roughly $3.5s$, since the amplification of the incident waves are reduced, and the waves do no longer cause impacts on the cone. The second harmonic at $4s$ encounter period (lower plot) is therefore not present. This indicates that *only short high waves may contribute to stem flare whipping in ballast condition*, and no significant contribution is expected from long waves. The simulated wave periods include those which can cause linear springing, hence linear springing is contributing in addition to stem whipping at $2s$ encounter period. The apparent vibration at higher wave periods above $6s$ is partly due to transient effects in the time series, and due to end effects in the FFT procedure used to estimate the regular filtered response. The vibration level above $6s$ is therefore

somewhat conservative.

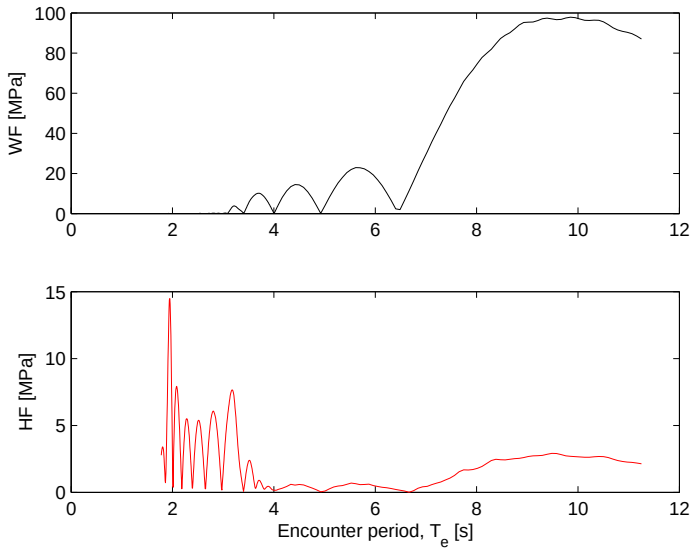

Figure 3.4: *WF and HF vibration amplitude versus the wave encounter period;* $U = 15kn$, $H = 5m$. *The HF response above 6s is affected by transients in short simulations.*

The effect of speed on the HF response is investigated for a wave height of $5m$ and wave period of $5.9s$. This is a steep wave, which reduces the speed, and for this wave the second order effect should appear at $8.5kn$. Figure 3.5 presents the HF nominal stress amplitude. The magnitude of the impact force at $8.5kn$ indicated that the water surface barely touched the cone, hence, in this case the HF response is insignificant. The vibration shows a strong speed dependence at higher speeds, and below $10kn$ the HF response is insignificant in ballast condition.

3.1.2 Simulations in irregular waves in ballast and cargo condition

Real waves are irregular, even though there may be clustering of waves with similar amplitude and frequency, e.g. (Wist 2004; Hansen and Thayamballi 1995). JONSWAP wave spectra with a γ factor of 2 is used. Results for irregular sea states with a peak period of $10s$ and varying significant wave height are shown in Figure 3.6 for ballast and cargo condition in full speed. The stress is presented as nominal standard deviation stress. For ballast condition, the HF vibration is linear up to a significant wave height of $4m$, where the slope seems to change due to whipping. Up to this level the response is due to linear springing from Froude-Kriloff pressure along the ship. The vibration levels are in general low and the whipping appears to be insignificant. In cargo condition, the HF response is nonlinear due to whipping, and the vibration level becomes significant in higher sea states,

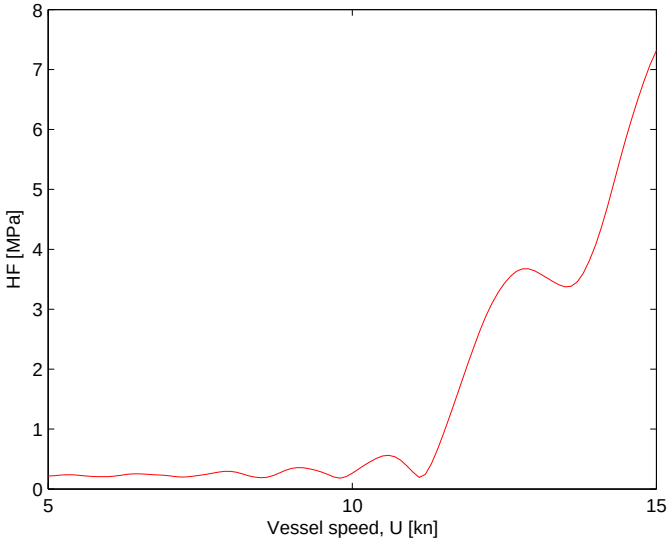

Figure 3.5: *HF vibration amplitude versus speed; $H = 5m$, $T = 5.9s$.*

e.g. above $4m$ significant wave height. The WF response shows a linear behaviour with increasing wave height, without influence from whipping (meaning that the whipping has no effect on the global motions as the coupling is nonlinear). The curves in Figure 3.6 should not be expected to be smooth due to the stochastic nature of the simulated sea states and the length of the simulations.

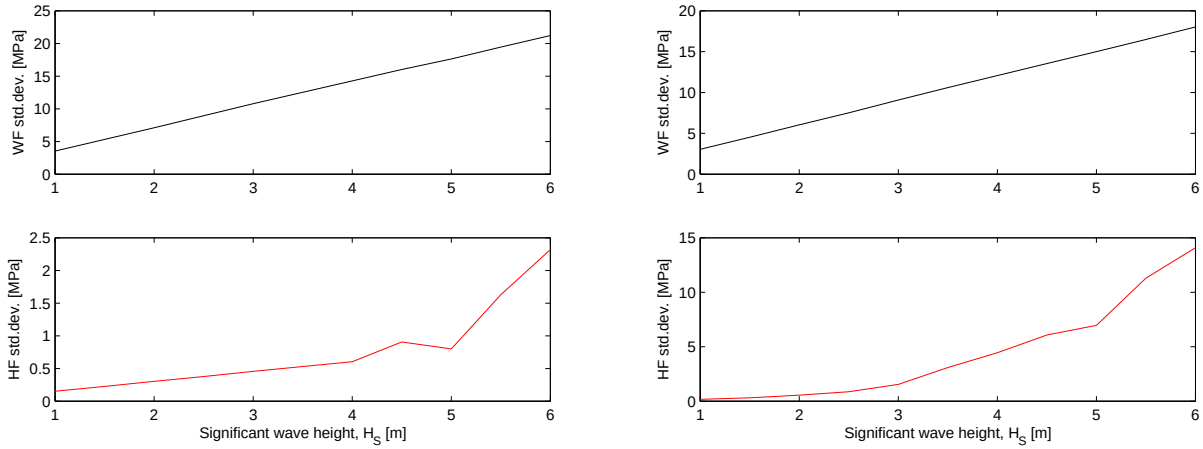

Figure 3.6: *Standard deviation of nominal stress for WF and HF (due to springing and stem flare whipping) versus significant wave height. $U = 15kn$, $T_P = 10s$, Ballast=left, Cargo=right.*

The sensitivity of the peak period is investigated at a significant wave height of $5m$ and

speed of $15kn$. The lower peak period corresponds to the breaking criterion for irregular sea. Figure 3.7 shows a nonlinear decreasing trend of the HF stress for increasing peak period in both ballast and cargo condition. The vibration level is in general low for ballast, but it is significant for cargo condition in particular at low peak periods below e.g. $12s$.

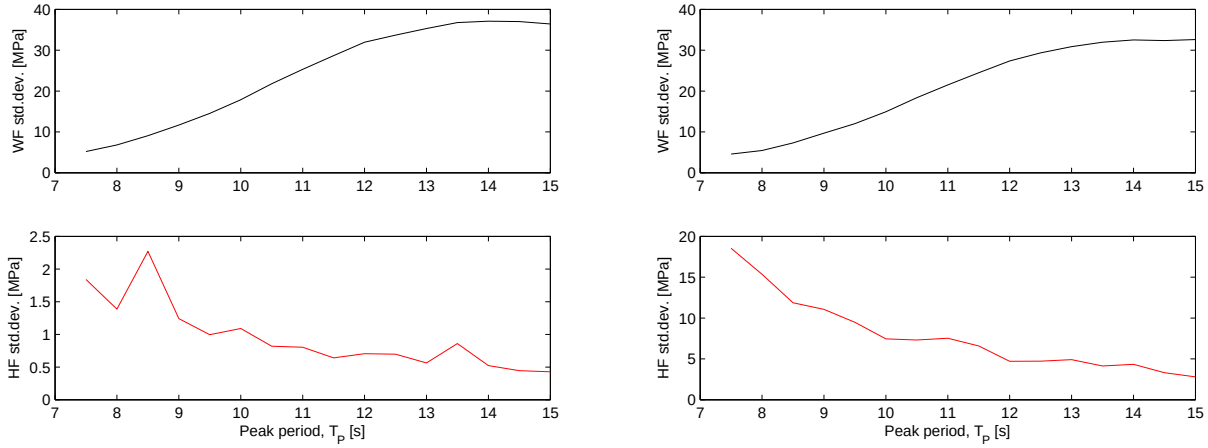

Figure 3.7: *Standard deviation of nominal stress for WF and HF (due to springing and stem flare whipping) versus the peak period. $U = 15kn$, $H_S = 5m$, Ballast=left, Cargo=right.*

The vessel speed in $5m$ significant wave height is less than $15kn$. The HF vibration versus the speed is shown for a peak period of $10s$ in Figure 3.8 for ballast and cargo condition. The HF vibration increases with speed in a slightly nonlinear manner, while the WF stress remains almost unchanged. A speed reduction of a few knots reduces the vibration to half. Again the HF response is low in ballast, but may be significant in high speeds above $10kn$ in cargo condition.

Impacts in real sea states may be complex and sensitive to various parameters. An impact event in irregular waves is shown in Figure 3.9. After the first slam, a large negative peak is observed followed by an oscillatory behaviour without any significant conventional slamming. The impact force may or may not cause significant vibration depending on the magnitude and integrated effect. This simply illustrates the complexity of the excitation, and it indicates that this oscillating behaviour may provide a whipping response that is difficult to distinguish from conventional springing.

Questions have been raised whether slamming on *anchor bolsters* could contribute to the vibration response on the iron ore carrier considered as the main case in this study. The two bolsters have a diameter of about $4m$, and they are $1m$ deep as illustrated in Figure 1.1. The lower part is located about $22m$ above base line. They are expected to constitute a minor effect in ballast condition, since they are located well above the apex of the cone.

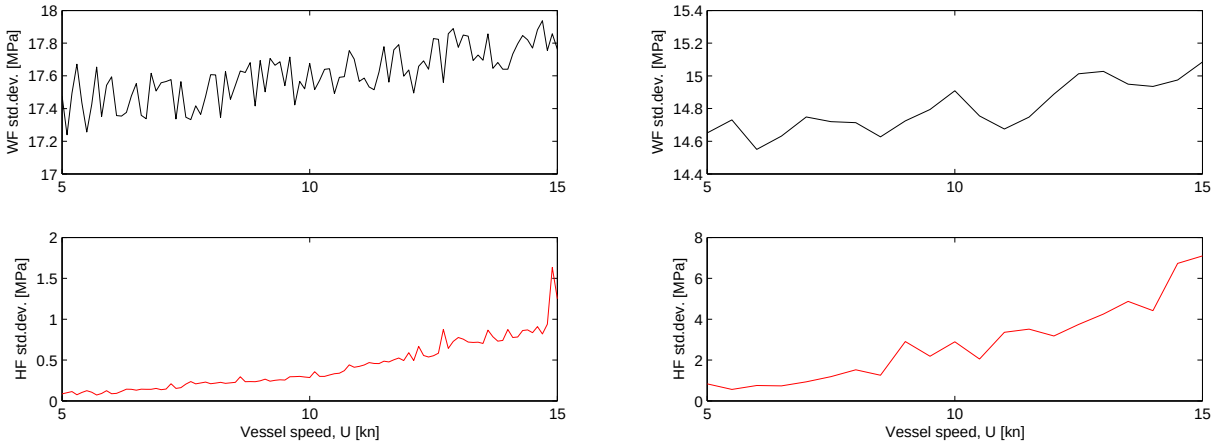

Figure 3.8: *Standard deviation of WF and HF vibration versus vessel speed,* $H_S = 5m$, $T_P = 10s$. *Ballast=left, Cargo=right.*

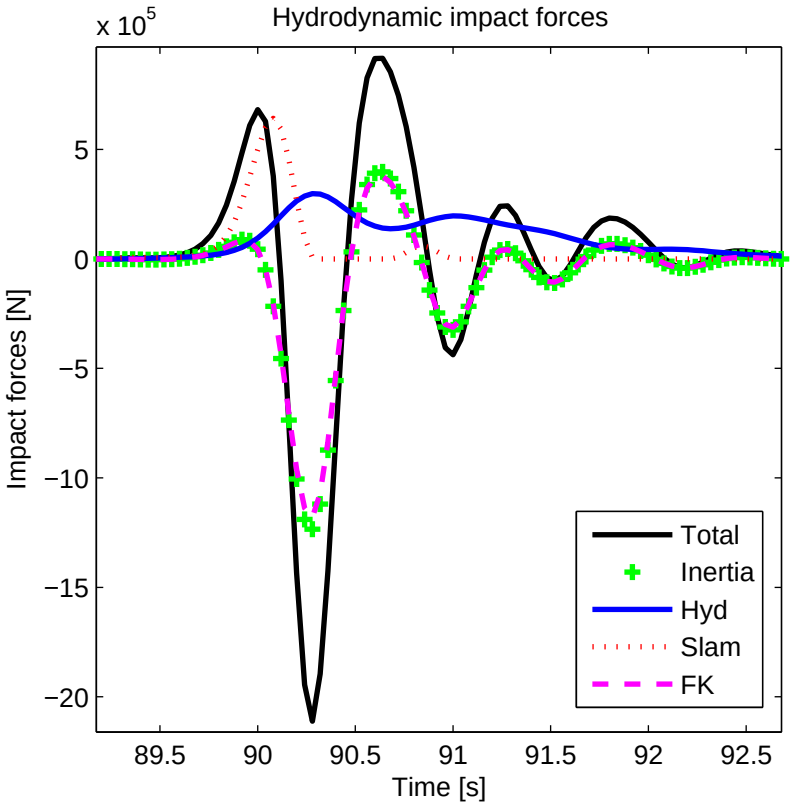

Figure 3.9: *Illustration of the different force components of an impact in irregular sea.* $H_S = 5m$, $T_P = 15s$, $U = 15kn$ *in ballast condition.*

The angle between the water surface and the anchor bolster may however cause a slamming

like impulse and contribute in cargo condition. The slamming force on the anchor bolsters may be included as a refinement of the procedure.

3.2 Calculated speed reduction in different sea states

Since the fatigue damage due to wave induced vibrations is sensitive to the speed, it is of interest to estimate the involuntary speed reduction in various sea states. The theory in Section 2.1.5 is employed to estimate the involuntary speed reduction in irregular waves, which are represented by a JONSWAP spectrum with peakness factor, γ, of two. Table 3.2 presents the input values.

Table 3.2: *Overview of input parameters.*

Parameter	Notation	Value	Unit
Density of salt water	ρ	1025	kg/m^3
Acceleration of gravity	g	9.81	m/s^2
Viscosity coefficient	ν	10^{-6}	m^2/s
Roughness height	H_r	150	μm
Diameter propeller	D	8.4	m
Beam at water line	B	53	m
Draft at AP, Cargo / Ballast	T_{AP}	19.04 / 12.06	m
Draft at FP, Cargo / Ballast	T_{FP}	18.01 / 11.33	m
Length at water line, Cargo / Ballast	L_{WL}	288.7 / 287.907	m
Centre of buoy. forw. of midship, Cargo/Ballast	LCB	10.93 / 12.498	m
Displacement, Cargo / Ballast	∇	237553 / 145963	m^3
Wet calm water surface, Cargo / Ballast	S	23160/18441	m^2
Base area, Cargo / Ballast	S_B	12.32 / 0	m^2
Maximum engine power	P_E	19966	kW

Figure 3.10 shows an example of the speed estimate for a total propulsion efficiency factor of 0.7 in cargo condition and for a sea state with $9m$ significant wave height and $11s$ zero up-crossing period. The calm water resistance increases with speed to the power of 3, while the added resistance in waves increases in a more linear fashion. The maximum speed is estimated at the intersection between the total required effect and the horizontal line denoting the maximum available power, and it is about $6kn$ in this case. The maximum speed in calm water was estimated to $15.7kn$. The speed reduction is defined relative to the maximum speed in calm water.

Table 3.3 shows the speed reduction in different sea states. The maximum power was assumed independent of speed and sea state. The maximum speed in calm water in ballast condition is estimated to $16.6kn$ based on a realistic propulsion efficiency coefficient of 0.7.

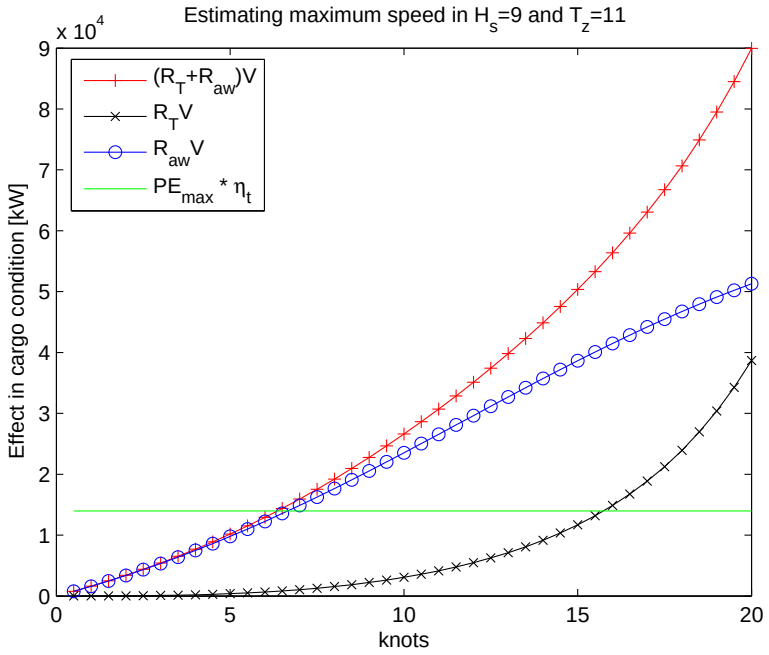

Figure 3.10: *Calm water resistance and added resistance in waves in cargo condition versus the maximum available efficient power,* $PE_{max} \cdot \eta_t$*;* $H_S = 9m$*,* $T_Z = 11s$*.*

A constant total efficiency coefficient is questionable, hence, two values were considered. The result indicates that the speed reduction is insensitive to the total efficiency coefficient. Some sensitivity to the zero up-crossing periods was observed in higher sea states. It is expected that the speed reduction is more sensitive to the zero up-crossing period than reflected in the predictions, since the nondimensional added resistance in waves was assumed independent of speed.

The speed reduction was considered in the model tests, except in the original ballast condition. Based on the uncertainties in the calculations and possible voluntary speed reduction, the following speeds for the different sea states were chosen as shown in Table 3.4.

Table 3.3: *Estimated speed loss due to added resistance in waves.*

H_S	T_Z	Cargo $\eta_t = 0.7$	Cargo $\eta_t = 0.9$	Ballast $\eta_t = 0.7$	Ballast $\eta_t = 0.9$
U_{max}		15.7	16.8	16.6	17.6
3	6	1.2	1.1	1.3	1.1
3	7	1.2	1.0	1.2	1.1
3	8	1.2	1.0	1.3	1.0
3	9	1.3	1.1	1.4	1.1
3	10	1.5	1.2	1.6	1.3
4	7	2.1	1.8	2.3	1.9
5	8	3.5	2.9	3.8	3.2
5	9	4.2	3.4	4.6	3.6
5	10	4.5	3.8	4.9	4.1
5	11	4.0	3.5	4.4	3.8
7	9	8.3	7.3	9.2	8.2
7	10	8.0	7.4	8.7	8.1
7	11	7.0	6.6	7.6	7.1
9	11	9.4	9.2	10.1	9.8

Table 3.4: *Selected speeds in different sea states and loading conditions.*

H_S	Speed in cargo condition, U $[kn]$	Speed in ballast condition, U $[kn]$
3	13.2	15
4	13.2	15
5	13.2 and 10	15 and 10
7	13.2 and 5	15 and 5
9	13.2 and 0	15 and 0

Chapter 4

Experimental methodology and analysis procedures

The strategy of the model tests is described in Section 4.1 followed by a brief description of the experimental model setup with sensors and the applied scaling laws in Section 4.2. The main uncertainties are listed in Section 4.3 before the procedures to evaluate the data are outlined, i.e.: Damping in Section 4.4, mode shapes in Section 4.5, linear, 'nonlinear' and second order transfer functions in Section 4.6 and fatigue damage in Section 4.7. A new method, developed to identify whipping, is presented in Section 4.8, while a method to illustrate the relative importance of linear and second order springing is described in Section 4.9. In general, results from these procedures are presented in Chapter 5.

4.1 Strategy of the test program

The literature study, simulations based on simplified theory, the use of existing hydroelastic computer codes and the hypotheses provided the background to establish a strategy, which is outlined below. However, it was not possible to answer all of the questions raised.

The main goal was to identify the causes of the wave induced vibrations on large blunt ships. A set of conditions, listed in the following, were defined to approach this problem.

- The hull geometry in (Storhaug et al. 2003) was selected so as to make it possible to compare model and full scale results, which is unique. The literature indicated that large size and blunt bows were important parameters, and the selected ship represents many Capesize bulk carriers and tankers.

⋆ The model should have realistic structural dynamic properties including higher order modes. This implied Froude scaling and distributed stiffness.

⋆ The hydrodynamic damping should be separated from the structural damping, since the literature was indistinct on this point. The damping may be frequency dependent also in air, and a design that made it possible to achieve the same natural frequency in air and in water was desirable.

⋆ The moment should be measured along the hull. The moment should be converted into deck stress for comparison with full scale measurements.

⋆ The neutral axis should be realistic, to avoid false contributions from horizontal impact forces, e.g. breaking waves against the vertical stem.

⋆ The model should not be restrained from rigid heave and pitch motions, since restrained models may provide less response than unrestrained models due to coupling effects.

⋆ Towing forces should be measured to be able to relate relative motion in the bow to added resistance in waves.

⋆ Short waves, exciting springing, should be considered. Short waves have poor quality making it desirable to use a large model. The wave quality should be monitored.

⋆ Head waves and high speed produce large vibrations. This is also the first step for comparison with numerical predictions (and other experiments). Hence, the tests could be performed in a towing tank. The sensitivity to speed should be investigated.

⋆ Realistic speed should be used to achieve realistic relative importance of excitation loads.

⋆ Ballast condition produces higher vibrations than cargo condition, but the stem flare may contribute significantly in cargo condition. Hence, both loading conditions should be considered. A change in trim was of interest and may increase the loading on the stem (bow) flare, while reducing the springing loads.

⋆ Different wave heights, which may "attack" different geometry with different nonlinear effects, should be considered (for each wave length).

⋆ Both regular and irregular waves should be considered. They may reveal different physical effects, and indicate the combined effect. Representative sea states for long term predictions and trends should be selected.

⋆ The bow and stern were areas of main concern. Pressure cells, slamming panels, relative motion sensors, shear force transducers and video cameras should be used to reveal the mechanisms. Special attention should be given to the bow based on the hypotheses.

⋆ The bulb geometry (and flare) is one cause of second order excitation. The blunt bow reflects incident waves, and this constitutes another second order excitation. The effect of bow geometry should be investigated, first by testing the original geometry, then by testing a bow without bulb and flare, and finally by testing a sharp bow with reduced bow reflection.

4.2 Experimental setup

4.2.1 Model description

A large model of a bulk carrier was constructed in model scale of 1:35 ($\Lambda = 35$), Figure 4.1. The hull was made of divinycell foam with glassfibre coating. Plywood was used internally to increase the local strength, and a large heavy triangular steel frame was mounted inside the hull. The purpose of the steel frame was to make each segment rigid. Flexible joints were inserted in between the rigid segments to obtain the requested natural frequencies, and the flexibility was confined to the flexible joints. To make the model rigid, the flexible joints could be locked. The $1500kg$ steel frame reduced the need for and served as supports for the ballast weights. The displacement in cargo condition was roughly $5.6tonnes$.

The hull geometry is presented in Figure 4.2. The ship has vertical sides at the ballast water line (11-12m above BL) in the fore ship, while in the aft ship the geometry is rather flared. The stem includes both a bulb and a stem flare, which starts just above the draft in cargo condition (18.5m above BL). The geometry is conventional, and the main dimensions of the model are presented in Table 4.1.

Table 4.1: *Main ship particulars of the model with different bows*

Length overall, L_{OA}, bow 1 and bow 2 in ballast cond.	$8.70m$
Length overall, L_{OA}, bow 2 in cargo condition	$8.55m$
Length overall, L_{OA}, bow 3	$8.84m$
Length between perpendiculars, L_{pp}, bow 1 and bow 2	$8.40m$
Length between perpendiculars, L_{pp}, bow 3	$8.69m$
Breadth moulded, B	$1.51m$
Depth moulded, D	$0.77m$
Design draft, T	$0.54m$
Draft ballast condition, T	$0.334m$
Trim ballast condition, $T_{AP} - T_{FP,bow1}$	$0.021m$
Draft cargo condition, T	$0.529m$
Trim cargo condition, $T_{AP} - T_{FP,bow1}$	$0.029m$
Neutral axis above BL, $z_{n.a.}$	$0.22m$

The model was divided into six segments assembled to allow measurements of forces in five cuts. Moreover, three of the middle cuts were made flexible, reducing the number

Figure 4.1: *Picture of the 8.7m model with the steel frame and transverse triangular end plates, which defined the location of the flexible joints and global load sensors.*

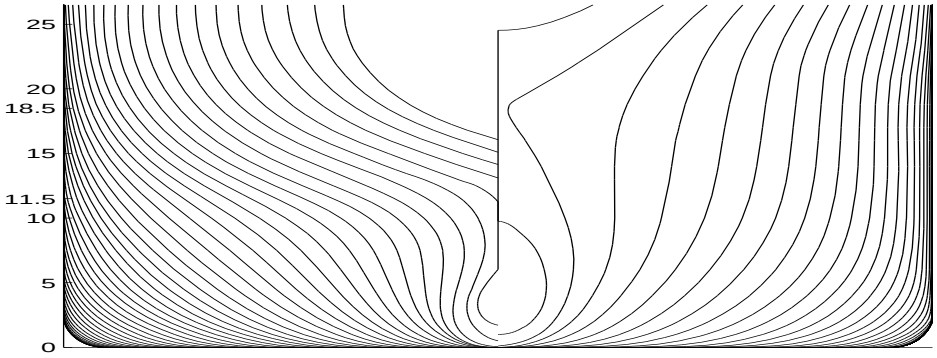

Figure 4.2: *Ship geometry with bulb, stem flare and aft ship flare. The drafts are typically 11-12m and 18.5m in ballast and cargo condition.*

of stiff segments to four. The segments and cuts were numbered from the aft. The first *rigid* segment consisted of segment 1 and 2. The second rigid segment was segment 3, the third was segment 4 and the fourth consisted of segment 5 and 6. The positions of the five cuts are presented in Figure 4.3, which shows the steel frame design inside the segmented model. Cut 1 and 5 were rigid cuts included to measure shear forces with possible nonlinear stern and bow forces. Shear forces were also measured at cut 2 and 4, while moments were measured at cut 2, 3 and 4 at the quarter lengths where the joints were flexible. The stiffness of the flexible joints could easily be adjusted by a sophisticated arrangement. Further description of the measuring positions and flexible joints are described in Appendix B.1.1.

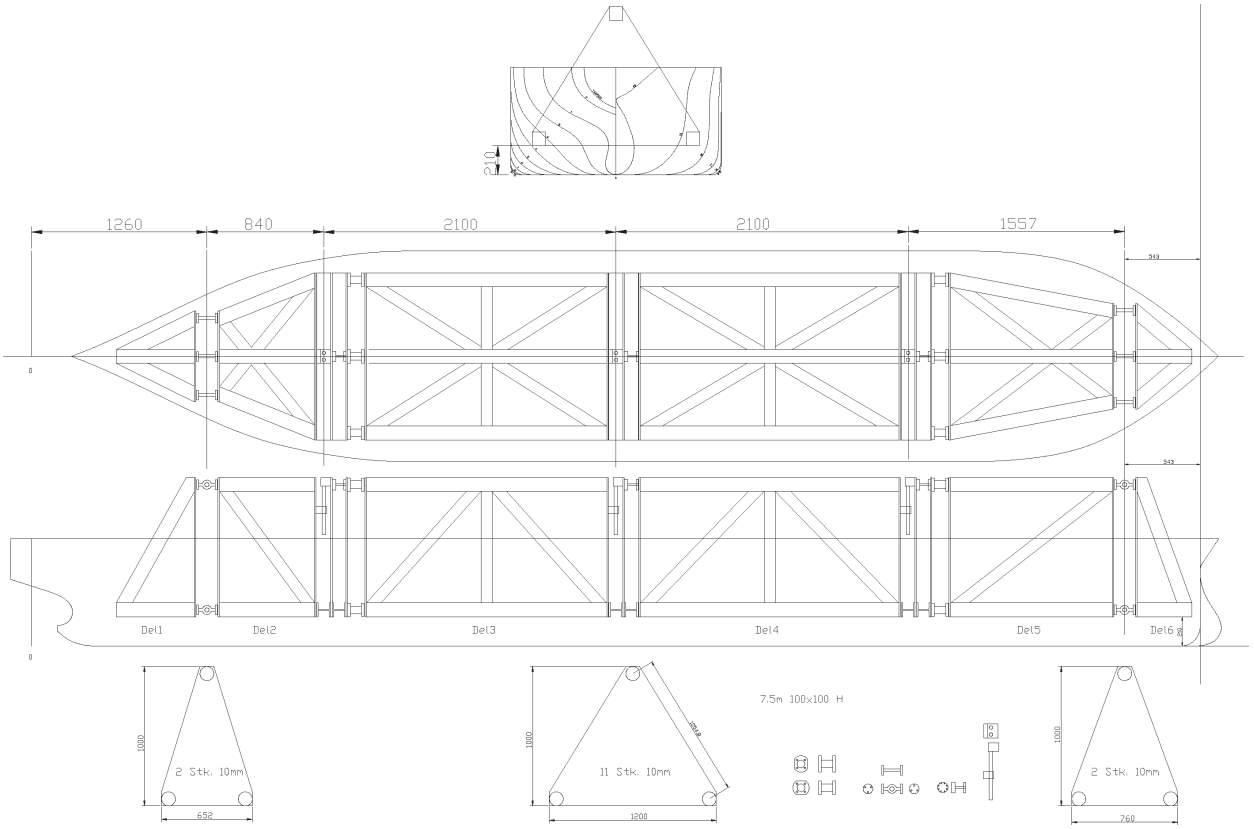

Figure 4.3: *Work drawing of steel frame, flexible joints and measuring positions. The cuts are indicated relative to AP. The neutral axis is indicated in the top figure.*

Three different bow shapes were tested as shown in Figure 4.4. The difference between bow 1 and bow 2 was related to removal of the bulb in ballast condition, and removal of bulb and stem flare in cargo condition. Bow 3 differed considerably. The bow was sharp triangular with a vertical stem. Less than 10% of the total length was modified when the bows were replaced. Bow 3 was placed on the cradle, which was used to estimate the mass moment of inertia in pitch and COG, as seen on the lower right picture in Figure 4.4.

Figure 4.4: *The three bows. Bow 1 = Upper, Bow 2 (cargo) = Lower left, Bow 3 = Lower right. Bow 3 (segment 5 and 6) is placed on the cradle. All bows have significant bilge radius (bottom flare).*

The mass properties of the segments and the pendulum test procedure are presented in Appendix B.1.2. The uncertainty in the mass moment of inertia of each rigid segment was less than 6%. The difference between the three ballast conditions or the three cargo conditions exceeded the individual uncertainty, due to slightly different mass distribution and bow design. The maximum difference of 19% was related to the rigid bow segment for ballast 1 and 3 condition. Appendix B.1.2 presents also the discrepancy between the mass properties of the model and the down scaled values from realistic loading conditions. The agreement was satisfactory for the cargo condition. The mass moment of inertia in ballast

condition was more than twice the down scaled values for segment 3 and 4. The reason was the number and weight of the end plates. The discrepancy affected the higher order modes, changing the relative ratio of the three natural frequencies and mode shapes. The springing mode was only slightly affected, since the requested frequency was still achieved.

4.2.2 Measurement devices and their locations

Different measuring devices and sensors were used to measure wave heights, axial forces, shear forces, accelerations, global motions, local deflection, towing forces, speed, relative motions, pressures and slamming forces. Moreover, two video cameras were employed. Totally about 60 channels were used.

The axial force sensors were the most important sensors, and the axial forces were converted into hull girder bending moments. From these sensors, vibration stress and fatigue damage were estimated. Heave, pitch, speed and waves were measured as well as the shear forces, pressures, slamming forces and relative motions, which may reveal something about the physics. Local deflections and accelerations (and moments) were used to estimate the mode shapes, while cameras were used to indicate wall interaction, steady waves, breaking waves and green seas on deck. The local deflections between the rigid segments were also used to estimate the rotational stiffness.

The moments were measured at 2.24, 4.34 and $6.44m$ from AP corresponding to 0.27, 0.52 and $0.77L_{pp}$. The axial force transducers were placed in the top of the steel frame adjacent to the springs as illustrated in Figure 4.3. The locations of all sensors as well as their type and manufacturer are described in Appendix B.2.3.

4.2.3 Model scaling laws and nondimensional properties

Scaling laws are an essential part of model experiments. For investigation of rigid body motions and global loads, Froude scaling is the basic scaling law (ratio of inertia to gravity). The Froude number, F_n, is defined by

$$F_n = \frac{U}{\sqrt{Lg}} \tag{4.1}$$

The Froude number is required to be the same in model, m, and full scale, f. This defines the model speed

$$U_m = U_f \sqrt{\frac{L_m}{L_f}} = \frac{U_f}{\sqrt{\Lambda}} \tag{4.2}$$

The frequencies of gravity waves on infinite water depth follow the dispersion relation

$$\omega^2 = kg = \frac{2\pi}{\lambda} g \tag{4.3}$$

where k is the wave number and λ is the wave length. The dimensions such as the wave length is scaled by Λ. Making the frequency nondimensional with respect to the dispersion relation and requiring that the ratio should be the same in model and full scale, gives the scaling of the frequency and time (used to slow down videos)

$$\begin{aligned} \omega_m \sqrt{\lambda_m/g} &= \omega_f \sqrt{\lambda_f/g} \\ \omega_m &= \omega_f \sqrt{\Lambda} \end{aligned} \tag{4.4}$$

The second basic scaling law relates to the flexibility of the hull girder. The natural frequency of a homogeneous beam Eq.(A.55) and the frequency scaling law Eq.(4.4) are combined to derive the scaling law for the bending stiffness.

$$EI_m = EI_f \frac{\rho_m}{\rho_f \Lambda^5} \tag{4.5}$$

The shear stiffness was disregarded, but may be included, (Achtarides 1983). By using the sophisticated design of the flexible joints, it was not necessary to care much about the exact stiffness. This was achieved by adjusting the stiffness to get the requested frequency according to Eq.(4.4). Further scaling and nondimensional quantities are listed in Appendix B.2.

Other physical effects such as viscous effects may be present, but scaling was disregarded. A thin wire was glued around a section in the bow area to initiate turbulence in the boundary layer, and the bilge keels were omitted to minimize the damping for the 2-node mode, (Sele 2001).

4.3 Uncertainties in the experimental data

In general uncertainties are inherent in experimental results, but they are also present in numerical predictions due to inaccurate idealization and solution procedures. The uncertainties are determined to indicate the goodness of the results. It is necessary when previous experience is lacking, and it may constitute a significant part of the total time necessary to carry out the experiments. Without assessment of the uncertainties, the quality of the results are reduced and the results may become worthless.

Some of the equipment and sensors, which were used in this experiment, have already been used in earlier projects, and convincing experience has been gained. The uncertainty analyses were therefore concentrated on those sensors which were new, and those which were of significant importance for the main results. For the remaining sensors and equipment, the author relied on the good workmanship of the staff at MARINTEK.

It is customary to divide the total uncertainty into *bias* errors and *precision* errors. The former is a systematic, fixed or constant error, while the latter is a random component

related to repetitions.

The bias error is often related to the equipment for measurements and undesirable physical effects which may not be fully realized. One may not be aware of its presence. A large part of the bias error was removed by calibration. Some bias error was still present, and it was indicated by using different sensors to measure the same quantity. All sensors were calibrated before they were mounted, while a few critical sensors were calibrated also after mounting. In any case, zero setting, by use of the measurement system CATMAN (HBM 2004), was carried out before each run to reduce effects of drifting and changed initial conditions. In general uncertainty analysis based on bias errors has not been carried out.

The precision error was related to the measurement procedure and the stochastic nature of properties. Each repetition was based on slightly different initial conditions. The precision error was handled by repeating the tests to establish the distribution and confidence intervals including rejections of wild readings. The precision error was established by a procedure outlined in Appendix B.3. It resulted in a mean value, a 95% confidence interval of sample values and a 95% confidence interval of the mean value. It was realized that the assessment used to determine the numerical results also contains uncertainties, and alternative procedures were utilized to determine the same quantity.

A number of uncertainties are listed in the following. These are put into groups related to wave and tested conditions (circle), to instrumentation (dot) and to model design (diamond). Some uncertainties are related to random errors, while others are related to gross systematic errors. The importance is referred to as insignificant (I), minor (M) or significant (S), although all uncertainties have not been quantified.

- The output wave elevation and frequency differed from the requested values (S).
- The effective distance with good wave quality was not always sufficient to achieve maximum steady state vibration response in short waves (S).
- The wave elevation and wave frequency changed along the tank in particular for short steep waves, but changes were also observed in long waves probably due to water depth difference (S).
- Scattered waves from the model were reflected by the side wall and affected the loading in the stern part for long waves and low speeds (S).
- Undesirable low frequency surge motion changed the encounter frequency initially (M).
- Wave disturbances originated from many sources: Previous runs, wave maker, dampers, rough surface along the tank, reflection from the beach and changes in water depth (S).
- Limited number of repetitions (M).

- ○ Inaccurate combination of speed and wave frequencies requested to excite the resonance peak (S).

- Wrong calibration factors inserted into the measurement system (M).
- Round off and limited number of significant digits written to file in relation to poor range setting of sensors, in particular pressure sensors (M).
- Sampling frequency (100 Hz) which was too low to capture slamming and acceleration peaks (M).
- Switching of cables between the 60 sensors (M).
- Wrong use of AD cards (M).
- Loss of sensor signals during a run (M).
- Calibration of relative motion devices on idealized straight geometry (M).
- Numerical analysis procedures used to estimate properties, e.g. damping estimates from spectral methods (S).

- ◇ The damping was mostly nonlinear and the behaviour differed (S).
- ◇ The stiffness was weakly nonlinear (S).
- ◇ Guidance springs to keep the model on a straight course affected the towing resistance occasionally (M).
- ◇ The predicted rigid body motion was affected by the flexible response and location of the "Nypos-tree" (M).
- ◇ Mounting of some sensors and loading of the model caused changes, which were disregarded in the calibration (M).
- ◇ Leakage and absorbed water changed draft and trim and introduced damping (M).
- ◇ Rigid motions affected the towing forces (I).
- ◇ Overloading of sensors or material (M).
- ◇ Some sensors may be affected by temperature changes (I).
- ◇ The design of the wave probes was not optimal for its use as moving wave probes (circular instead of foil like) (M).
- ◇ Wall effects due to blockage causing increased effective speed in a channel, and different boundary conditions than in numerical simulations (M).

◇ The elevation of the track and towing carriage close to the wave maker introduced changes in estimated motions and wave heights (I).

◇ Improper quality of initial produced bearings (S) and improved bearings (M).

The number of uncertainties is large, but most of them were insignificant, minor, reduced, removed or quantified. E.g. switching of cables was discovered based on physical insight, and the results was corrected. If this had not been detected, it would have introduced a severe bias error into parts of the experiments. A more detailed description of the uncertainties and calibration procedures are provided in Appendix B.4 focusing on the global force transducers. In addition differences in physical properties like mode shapes, mass distribution and high frequency tail of sea states may deviate from observed on a real ship, but this is an uncertainty related to the idealization error.

Several authors pointed out the difficulties with model testing in short waves due to poor wave quality, e.g. (Hoffman and van Hoof 1976; Goodman 1971). Some also failed to produce waves exciting linear springing, (Dong and Lin 1992; Domnisoru and Domnisoru 1997). Before the present tests started up, MARINTEK was requested to assess the length of the tank which exhibited homogeneous wave conditions for the purpose of springing tests, (Stansberg 2004). A separate study was conducted to calibrate the waves prior to the model tests, and results are presented in Appendix B.5 and Section 4.3.1. The sensitivity of springing response to changes in speed and wave frequencies is also discussed.

Uncertainty analysis of experiments within marine technology was carried out more thoroughly by Ersdal (2004), and a general description was provided by Coleman and Steele (1989).

4.3.1 Visualization of wave quality using Wavelet

The assessment of regular and irregular wave quality in Appendix B.5 confirmed that it was necessary to measure the waves during the experiments. The location of the drastic change in wave quality was not identified in Appendix B.5, but Figure B.10 gave an indication in one specific case. Wavelet analysis was carried out to determine the length with satisfactory quality, referred to as the *effective* length measured from the wave maker. Wave probe WP3 on the towing carriage was used. A clear criterion was not defined, but the effective length was determined based on visual inspection of the Wavelet spectra.

Figure 4.5, 4.6 and 4.7 present the Wavelet spectra as compared to the wave energy spectra for the shortest waves supposed to excite linear springing. Even though the quality based on the low amplitude waves in Figure 4.5 appears poor, the frequency is quite regular. The quality decreased with increasing wave height. The Wavelet spectra provided a visualization of the effective length, while the wave spectra only indicated that the higher waves had more disturbances. The end of the time series represented a distance $15m$ from the wave

maker. The speed was $1.3m/s$, and the effective length was estimated by visual inspection to be $27m$, $47m$ and $66m$ for the highest, middle and lowest wave. The wave quality was better than expected from Stansberg (2004), and it was decided to capture also the linear springing response in the model tests.

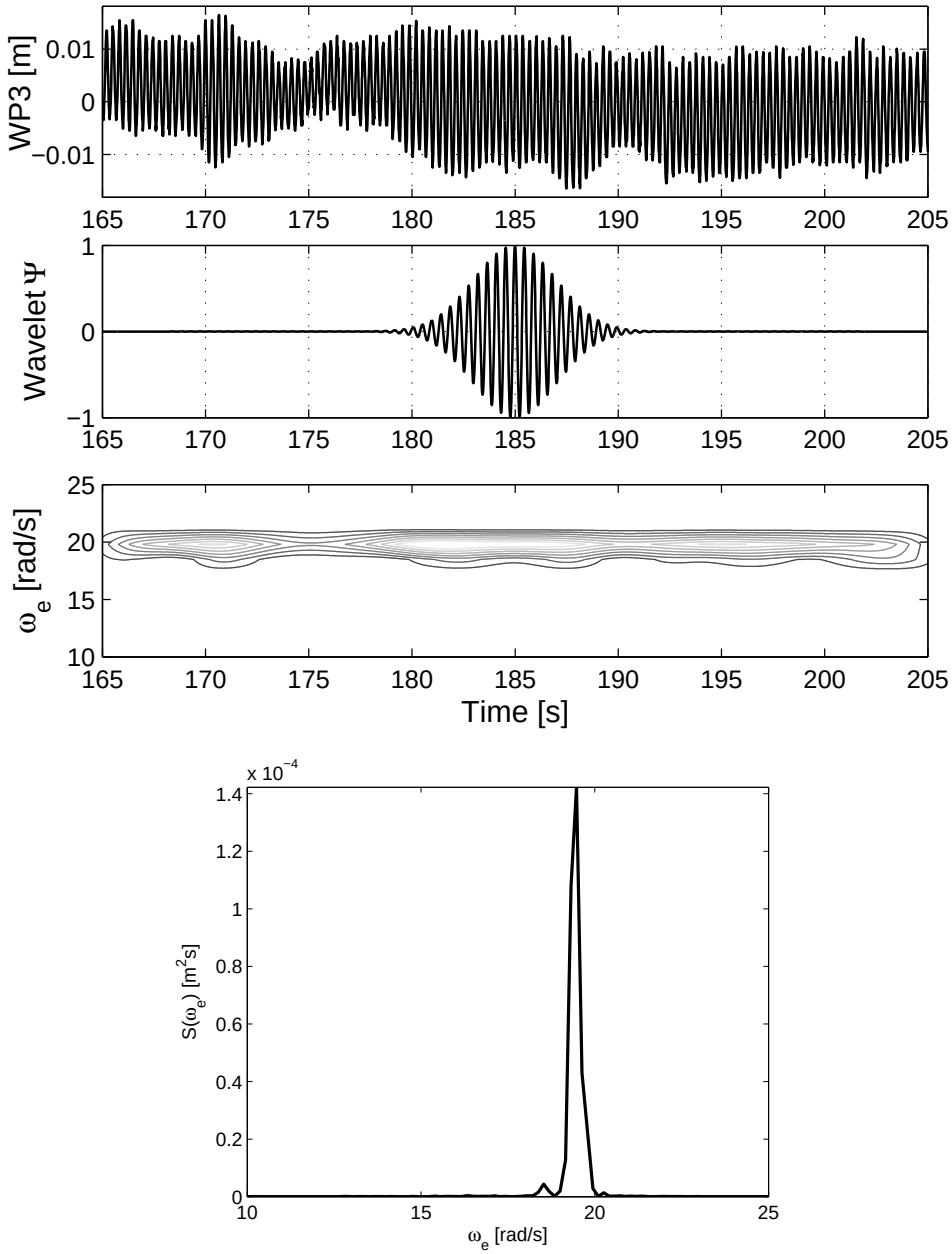

Figure 4.5: *Wavelet (upper three: Time series, extended nondimensional basic wavelet and Wavelet spectrum) and FFT wave spectrum (lower) for short waves intended to excite linear springing for $H = 0.7m$, $T = 4.14s$ in full scale.*

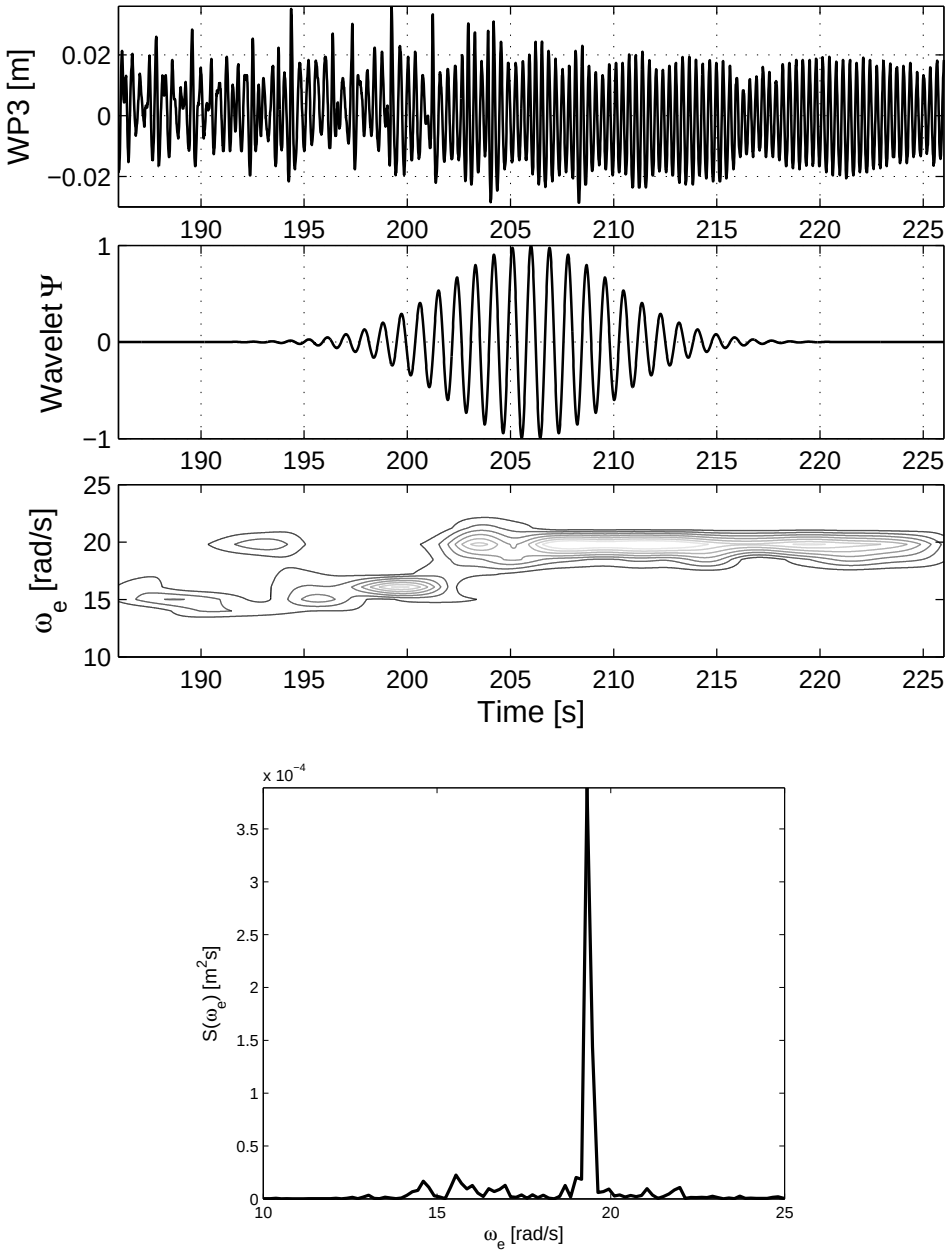

Figure 4.6: *Wavelet (upper three: Time series, extended nondimensional basic wavelet and Wavelet spectrum) and FFT wave spectrum (lower) for short waves intended to excite linear springing for $H = 1.4m$, $T = 4.14s$ in full scale.*

The time series of the lowest wave displays low amplitudes at $53m$, possibly caused by observed disturbance from side-wall dampers located at a distance 40-45m from the wave maker. The dampers were removed in the subsequent model tests. The highest waves

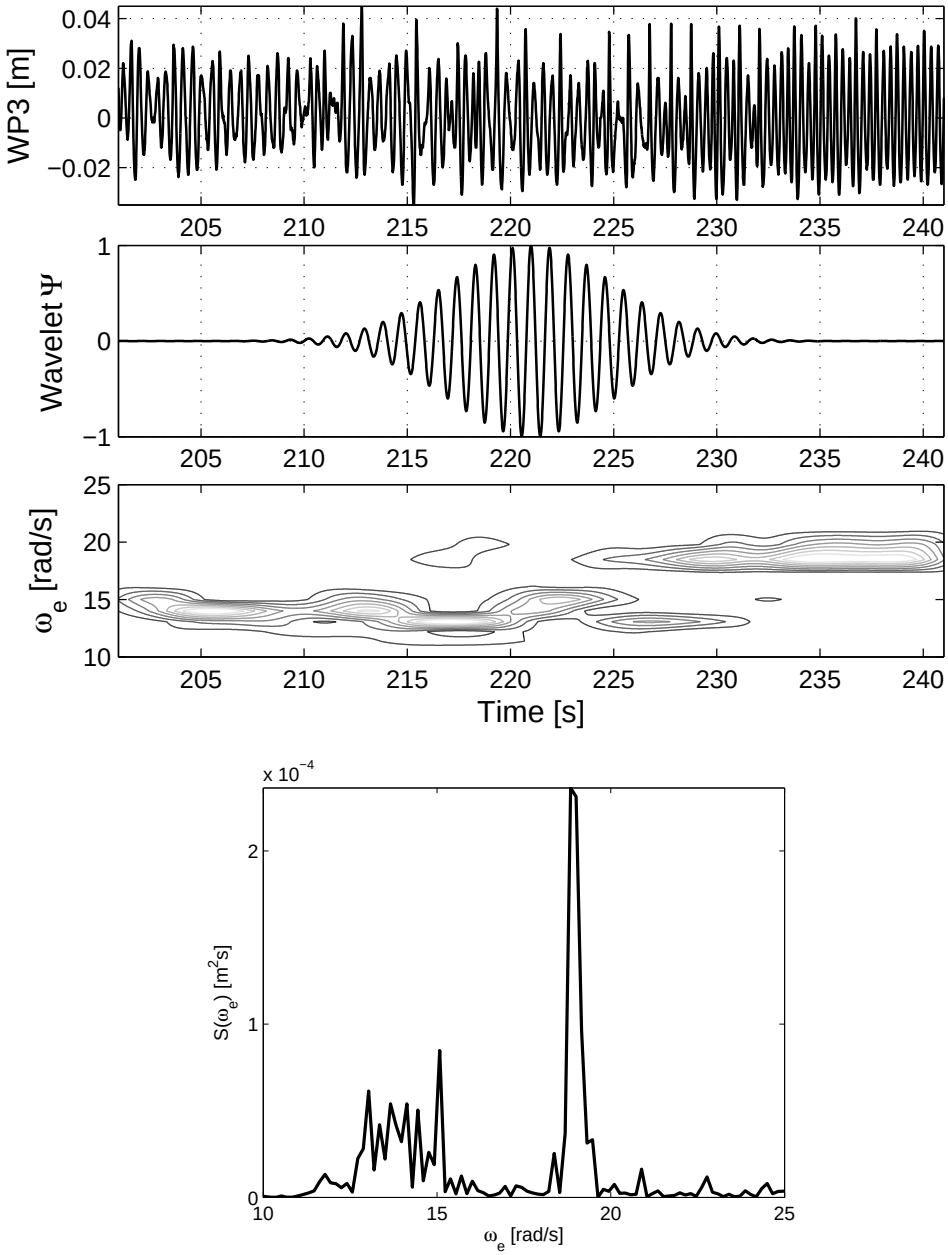

Figure 4.7: *Wavelet (upper three: Time series, extended nondimensional basic wavelet and Wavelet spectrum) and FFT wave spectrum (lower) for short waves intended to excite linear springing for* $H = 2.1m$, $T = 4.14s$ *in full scale*

display also slightly lower frequency than requested. The reason is somewhat unclear, but could be both wave maker and wave propagation related. Based on the estimated distance of $30m$ to build up maximum linear springing response, the two highest waves were expected to provide poor results. The fixed wave probe, WP1, was moved from 10 to $5m$

from the wave maker to increase the effective running distance. Fortunately, whipping from running the model into the larger front waves of the wave trains caused often a more rapid build up of the response, but still it was observed occasionally that the springing response did not reach its maximum. For linear effects it was however not critical to capture the highest waves.

The highest waves intended to excite second order springing did not confirm instabilities for the investigated distance of $85m$, except when waves were breaking continuously (requested wave height above steepness criterion was also tested).

4.4 Procedure for estimating damping and natural frequency

4.4.1 Damping by decay tests

Decay tests were carried out in water and in air to estimate the damping according to Section 2.3.3. The axial force at midship section was considered. In air the model was placed on two supports located below the two node points, or by hanging the model in ropes. The damping in calm water was evaluated in zero and forward speed. The vibration was excited by a sledge hammer or by hand.

A number of decay curves were produced in each run, and the whole time series was filtered to remove the mean level and other vibration modes. Three methods were applied to estimate the damping.

The first method utilized cycle-by-cycle decay from Eq.(2.51). A $n = 10$ cycle interval was found appropriate to reduce the uncertainty. The damping values are presented versus the amplitude in Figure 4.8 as expressed in Eq.(2.57), and the mean value and standard deviations were calculated from the scatter.

The second method considered the envelope process by fitting a decay curve as

$$FX_3(t) = R(t_0)\exp^{-\delta\omega_{max}(t-t_0)} \tag{4.6}$$

to the positive peak values. t_0 represents the start of the interval with the start amplitude $R(t_0)$. The frequency ω_{max} corresponds to the vibration peak of the spectrum. The start amplitude $R(t_0)$ and the damping ratio δ were determined by a nonlinear fit using the MATLAB function *fminsearch*. Fits were performed at both high and low response levels in each decay interval, and the damping ratios at high and low levels were compared to indicate the presence of nonlinearities. Figure 4.9 shows an example of fits made nondimensional with respect to the start value.

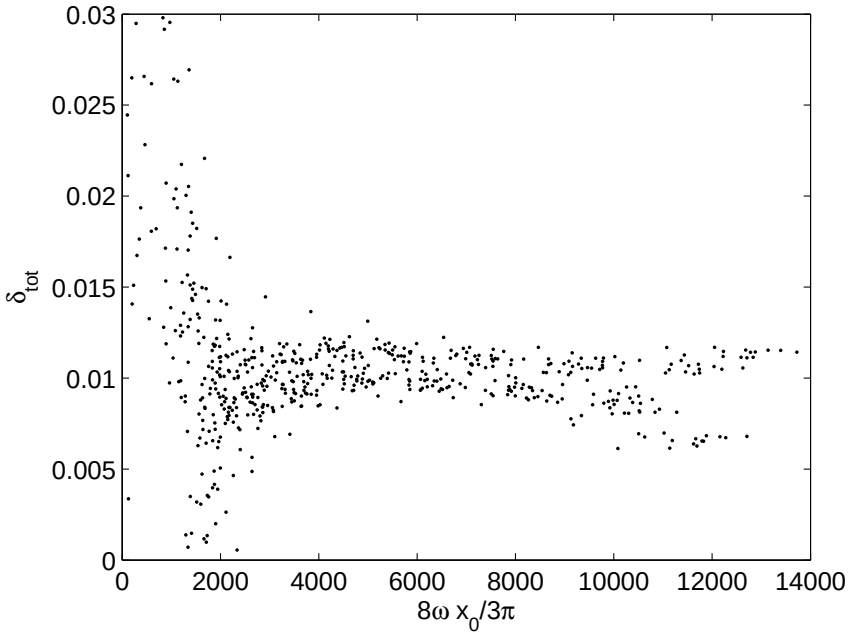

Figure 4.8: *Nonlinear damping ratio estimated from cycle-by-cycle method for ballast 2 condition in calm water at zero speed. The slope indicates the nonlinear contribution, which is close to zero in this case. x_0 is the vibration amplitude in N from the midship axial force transducer, and ω is about 20rad/s.*

The third method was based on fitting harmonic decay curves to the filtered decay curves according to

$$FX_3(t) = R(t_0)\exp^{-\delta\omega(t-t_0)}\cos(\omega(t-t_0)+\theta) \tag{4.7}$$

The natural frequency ω, the damping ratio, the start value and the phase, θ, were estimated again using *fminsearch*. An example is shown in Figure 4.10. Results are presented in Section 5.1.1.

4.4.2 Damping estimates in irregular sea

The damping in irregular sea states was estimated using the spectral method described in Section 2.3.3. The analytical expression of the response spectrum was fitted to the measured spectrum derived by the MATLAB function *psd*. A mowing Hanning window was used with a initial width of 2048 time samples, and the interval was chosen from 0.5rad/s below to 1.0rad/s above the natural frequency (in full scale values).

Different effects may introduce uncertainties

- The width of the frequency interval.

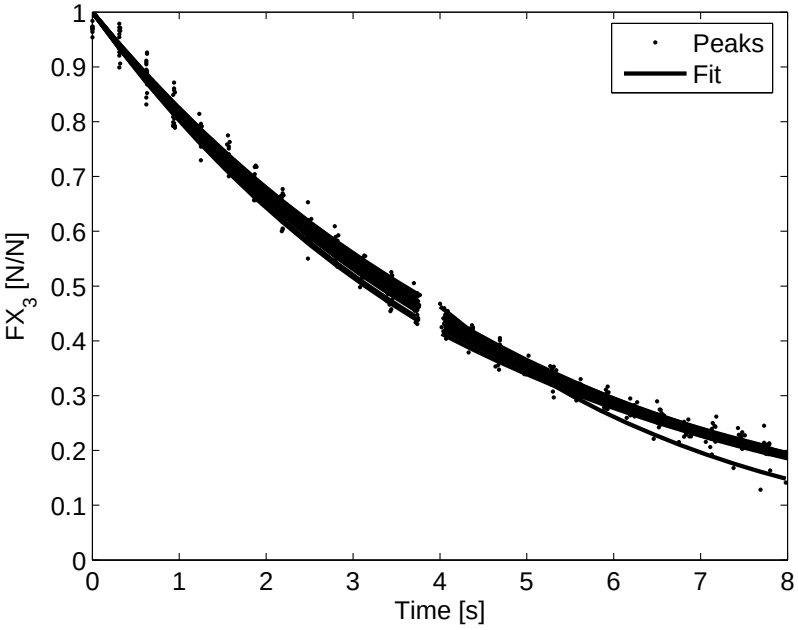

Figure 4.9: *Double envelope fit to peak values from filtered decay curves for ballast 2 condition in calm water at zero speed. 8s corresponds to 26 cycles.*

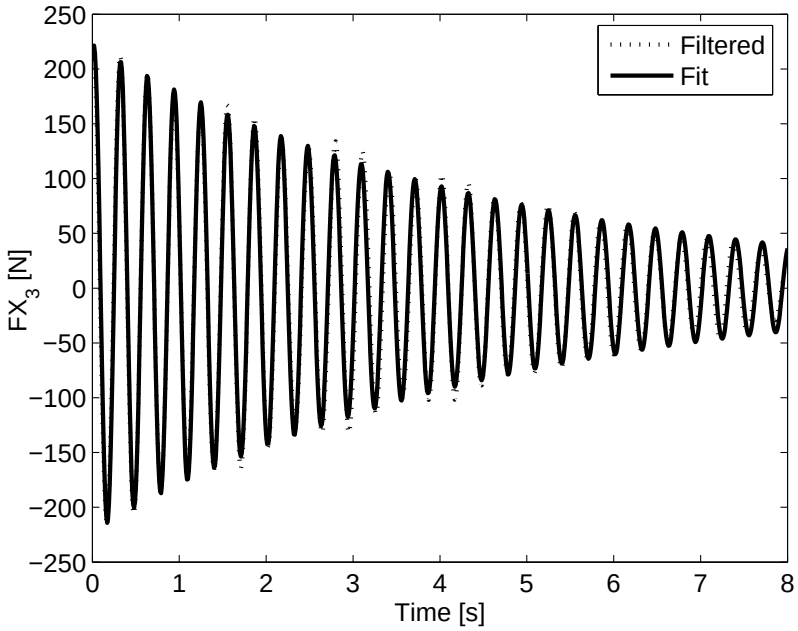

Figure 4.10: *Harmonic fit to a filtered decay curve for ballast 2 condition in calm water at zero speed.*

- The width of the Hanning window (number of sample points).
- The sampling frequency and length of the time traces.
- The hump-hollow behaviour of the excitation, which was not included by the analytical SDOF system.
- Low springing response compared to the surrounding wave frequency response.
- White noise in the measured signal.
- Rigid body motions changing the wet surface and added mass, thereby changing the natural frequency and making the damping apparently larger.

The length of time series corresponded to more than six minutes with a sampling frequency of $100Hz$, and the model was tested in head seas with significant vibration response. The main uncertainties were therefore related to the change of the natural frequency in the waves, and the effect of the number of sample points and width of the considered frequency interval, which will be illustrated in the results.

An example of a fit from the model tests is shown in Figure 4.11. The springing peak is clear and a second peak from the 3-node vibration is observed. Results are presented in Section 5.1.2.

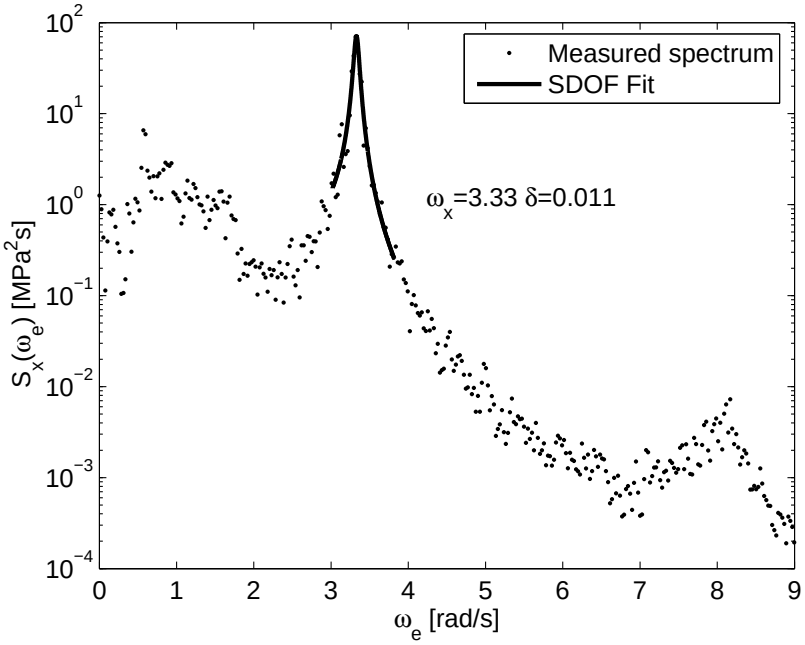

Figure 4.11: *Fit of analytical spectrum to measured spectrum in ballast 2 condition for the sensor amidships, $H_S = 2m$, $T_Z = 5s$, $U = 15kn$.*

4.5 Estimation of mode shapes.

The modes shapes in the experiments represent an idealization of the real mode shapes. A few approaches were used to study the effect of various idealizations, including the following mode shapes, which was investigated for ballast 1 condition

1. The real mode shape measured onboard and provided by DNV based on accelerometers.
2. The measured segmented mode shape from experiments.
3. The calculated segmented mode shape based on model mass properties and stiffness with and without 2D added mass distribution.
4. The calculated continuous mode shape from FE model based on full scale mass and stiffness distribution and 2D added mass distribution.

The mass distribution, mode shapes and cross sectional properties are listed in Appendix B.7.

The mode shapes in the model tests were derived from the accelerations or moments. The mode shape from acceleration, when the excitation was harmonic with frequency ω, were estimated from

$$w = -\frac{\ddot{w}}{\omega^2} \tag{4.8}$$

while the deflection from the moment was estimated based on the rotational stiffness. A narrow band filter was applied to remove disturbance from swell in the regular waves, which were supposed to excite springing. This was necessary when the mode shapes were derived from the moment.

Figure 4.12 compares the calculated and measured mode shape of the segmented model, which was run in ballast 1 condition in a regular wave exciting springing. The stiffness in the calculations was based on the mean rotational stiffness in Table B.6. The mass was based on the measured mass of ballast 1 condition in Table B.1, while the 2D added mass was predicted at infinite frequency based on the theory in Appendix A.1.1. The 95% confidence interval of the mean value from the measured mode is shown. It was estimated based on the peak values from the individual cycles during the last $10s$ of the run. The agreement of the mode shapes is satisfactory, but the calculated natural frequency exceeds the measured by 5% ($3.49rad/s$ versus $3.30rad/s$ as full scale values). The large discrepancy is explained by the large uncertainty in the measured rotational stiffness, which appears to be too high also since the added mass was too high (without 3D effects). The dry mode shape differs from the wet mode, which ought to be considered in numerical predictions.

The calculated three wet mode shapes of the segmented model in ballast 1 condition are shown in Figure 4.13. The 3-node mode may produce a contribution to the high frequency

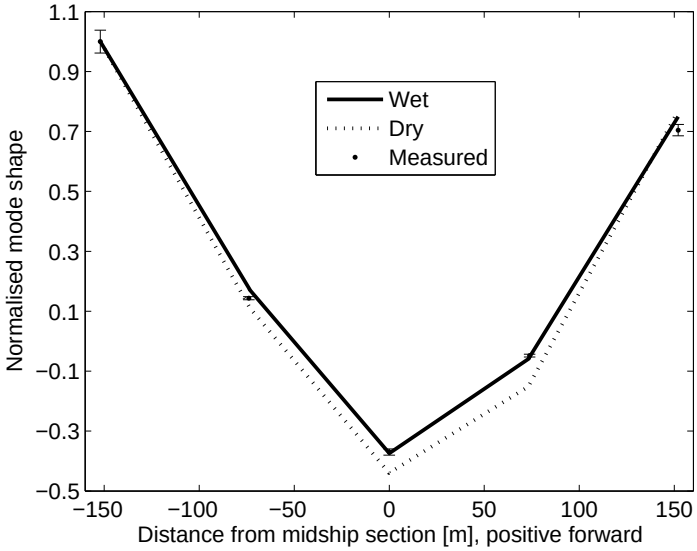

Figure 4.12: *Wet and dry calculated 2-node mode compared to measured "resonance" mode from ballast 1 condition,* $H = 1.4$, $T = 4.14$, $\omega_e = 3.30 rad/s$ *in full scale. The modes are normalized, and the 95% mean confidence interval is shown for the measured mode.*

response at the midship section in case of whipping. The shear deformation did not influence the results for the segmented model, since the shear stiffness was chosen deliberately high.

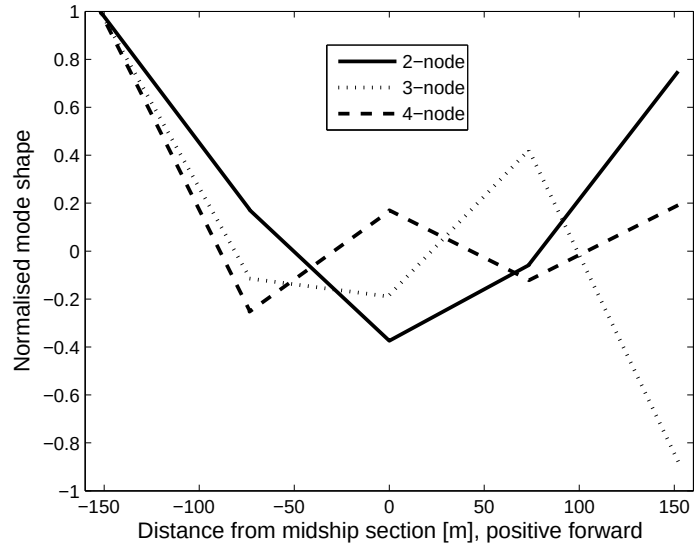

Figure 4.13: *The calculated wet segmented mode shapes in ballast 1 condition with natural frequencies of 3.5, 9.6 and 15.9rad/s.*

The segmented model was an idealization of the real flexibility. The wet continuous mode shapes were calculated based on realistic distributions of mass, 2D added mass, bending and shear stiffness using 50 finite beam elements. The first three mode shapes are shown in Figure 4.14. In contradiction to the segmented model, the 3-node mode displays only a small moment at midship section. Moreover, the ratio of the natural frequency from the segmented and continuous model increases for the higher modes. Changes in the number of flexible cuts, locations and stiffness distribution of the segmented model were considered initially, without finding a significantly improved design compared to the chosen one.

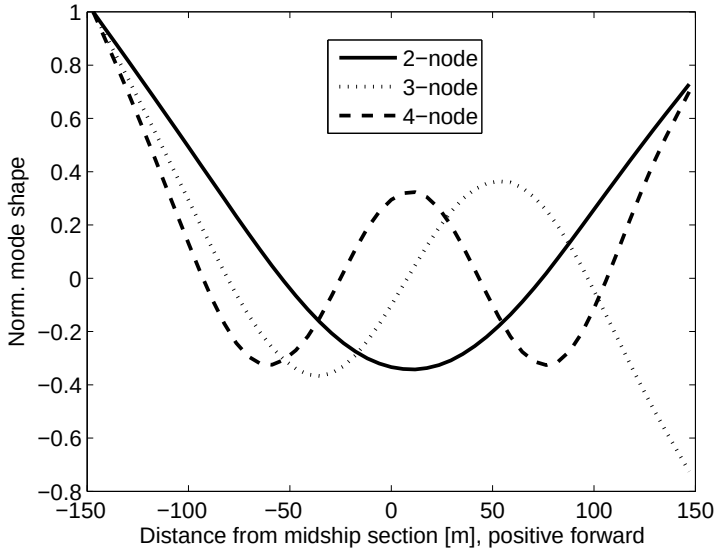

Figure 4.14: *The calculated wet continuous mode shapes in ballast 1 condition have natural frequencies of 3.0, 6.6 and 10.8rad/s.*

The first two mode shapes for the segmented and continuous FE model are compared to the real measured full scale mode shapes in Figure 4.15. The segmented modes were based on the model mass in ballast 1 condition, while the realistic mass was used in the calculations of the continuous FE model. The natural frequencies from full scale measurements were 3.15 and $6.78 rad/s$. The natural frequency of 3.15 differs from results presented elsewhere of $3.32 rad/s$. The measurements were carried out in the English Channel, which has an average water depth of about $54m$. If a 2D cross section of a rectangle with draft of $12m$ and a beam of $53m$ is assumed, figures in (Faltinsen 1990) suggest that the added mass is roughly twice of the displaced mass, and that the added mass in heave is increased by about 10% on $54m$ water depth. This yields a reduction from 3.32 to $3.21 rad/s$. It is therefore reasonable to conclude that the reduced frequency was a result of shallow waters rather than an unconventional ballast condition. The difference in the continuous mode shapes may come from inaccurate shear stiffness distribution and lack of 3D added mass

effects in the calculations, but the ratios of the frequencies for the 2 and 3-node modes shapes are good. Despite the difference in mode shapes and frequencies, the chosen configuration with three flexible cuts with identical stiffness distributed to the quarter lengths was considered acceptable.

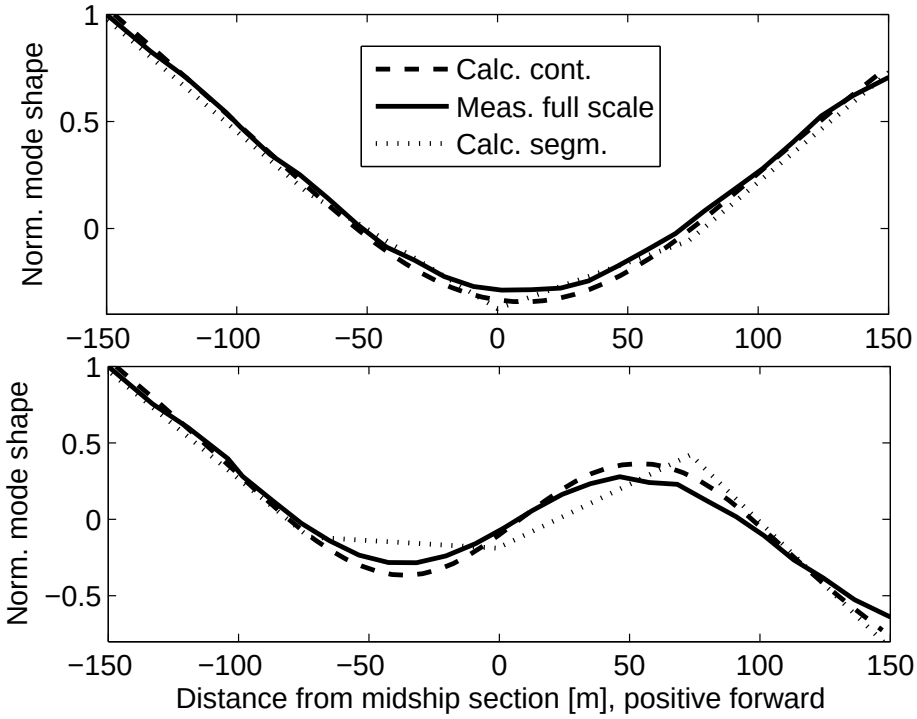

Figure 4.15: *Comparison of the 2 and 3-node mode shapes obtained from the segmented model (based on model mass), the continuous FE model (based on real mass and estimated stiffness) and full scale ballast condition. The natural frequencies are 3.5, 3.0 and 3.15rad/s for the 2-node, and 9.6, 6.6 and 6.78rad/s for the 3-node mode.*

Note that the 3-node mode from the segmented mode shape has a higher frequency relative to the continuous FE model and the real mode shape, despite that the mass moment of inertia for the rigid segments were too high. This is a general problem for segmented models, and the relative increase of the frequency for the higher modes is due to "restrained" deformations.

4.6 Procedure for estimating transfer functions

4.6.1 Linear transfer functions

According to Section 2.4.1, the linear transfer functions were estimated from regular wave responses, and they were made nondimensional according to Appendix B.2.2, e.g. the

moment was made nondimensional as

$$\overline{VBM} = \frac{VBM}{\rho g \zeta_a B L^2} \tag{4.9}$$

The transfer functions were determined at full speed of 15 and 13.2kn in ballast and cargo condition, respectively, and the frequencies covered the range from linear springing to rigid body response. In the following, the procedures to establish the transfer function will be explained using some results for illustration.

Each regular wave run defined a single point in the transfer function. How this single point was determined is explained in the following. A time interval with a duration of 10 to 80s was selected, and the FFT was applied to identify the encounter frequency from the spectrum. A filter, with a width of about 20% of the encounter frequency, was applied to remove disturbances. The inverse FFT reproduced the harmonic time series. Thereafter, different procedures were utilized to determine the amplitudes, phases, mean values and frequencies (the expressions in parentheses refer to the notation used in the figures for the different methods).

1. The zero crossing and peak process were identified. The amplitude from each couple of maximum and minimum was determined (Peak), and the mean and standard deviation (uncertainty) were calculated.

2. Amplitudes were estimated based on the standard deviation of the filtered time series (Time).

3. Amplitudes were estimated based on the standard deviation of the filtered spectra (Spec).

4. The amplitude, phase and frequency were derived using a nonlinear fit (Fit) to the filtered time series for each cycle along the selected time series. The mean and standard deviation of the three parameters were calculated.

5. The least square fit (LSQR) was used to estimate the amplitude, frequency and phase from the selected raw time series. The resolution from the FFT was not sufficient to ensure that the best fit was achieved, and iteration was used within the resolution of the FFT with a small step to ensure a good fit.

6. The mean value was obtained from this least square fit and the sample mean of the selected raw time series (Raw). The former method was more accurate.

7. The frequencies were determined from the peak in the spectrum (Max spec), the nonlinear fit and the least square fit.

8. The phase lags were found by a spot check (Spot) in the middle of the selected interval, from the nonlinear fit, the least square fit and from the auto correlation

function (AutoC) derived by the MATLAB function *xcov*. The phases were defined as a lag to the relative motion at COG. A narrow band filter resulted in larger end effects for amplitudes, but better estimates of the phase relations. The end effects were accounted for in the estimate of the amplitudes.

The transfer functions were plotted versus the encounter frequency along the x-axis, and not the nondimensional frequency $\omega_e\sqrt{\frac{L_m}{g}}$. Further description is given in Section 2.5.1.

Some results will be shown to illustrate the alternative methods described above. The heave transfer function (amplitudes) are presented in Figure 4.16 for ballast 1 condition. The transfer function approaches one for long waves and zero for short waves. Notice that the heave motion in practice is zero above $6rad/s$. The 95% confidence interval of the mean amplitude is typically less than 10% when the heave motion is significant. Satisfactory agreement is observed between the different methods.

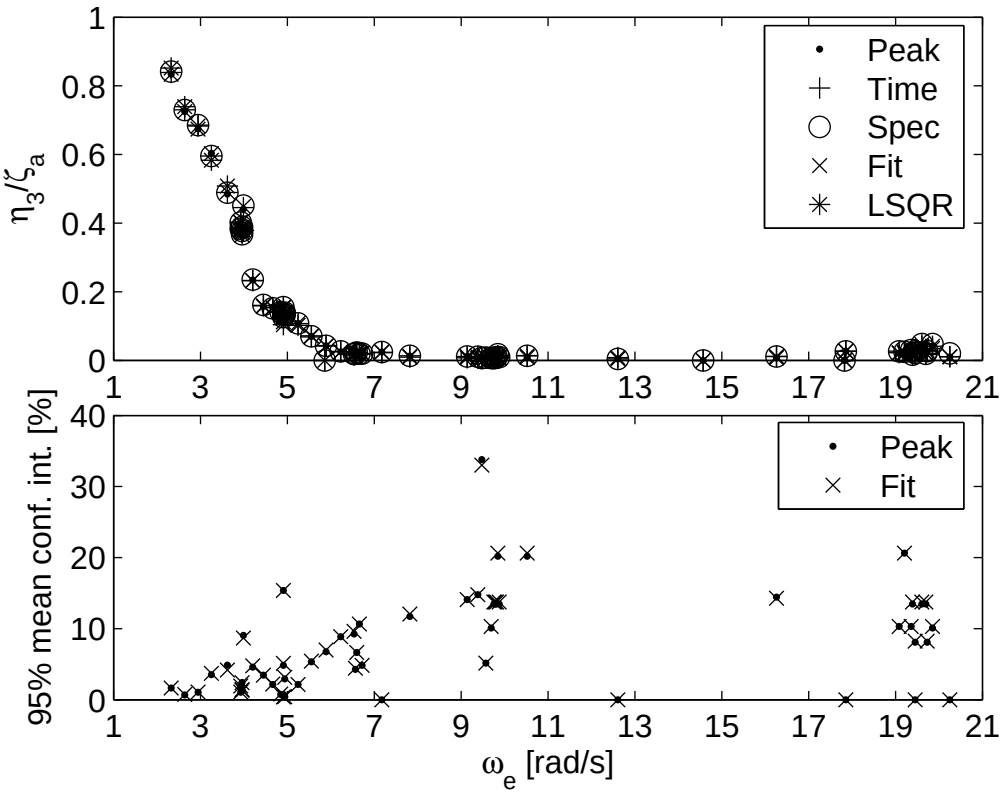

Figure 4.16: *Linear transfer function of heave motion for ballast 1 condition. 95% confidence interval of the mean amplitude is illustrated. Definition of methods is described in the text.*

The phases corresponding to the heave transfer function are presented in Figure 4.17. The 95% confidence interval of the mean phase is typically below 10^0. The uncertainties are

less at lower frequencies. The phases change significantly with frequency, but also to some extent with amplitude due to nonlinear responses in higher waves. The auto correlation method is considered as the more robust method.

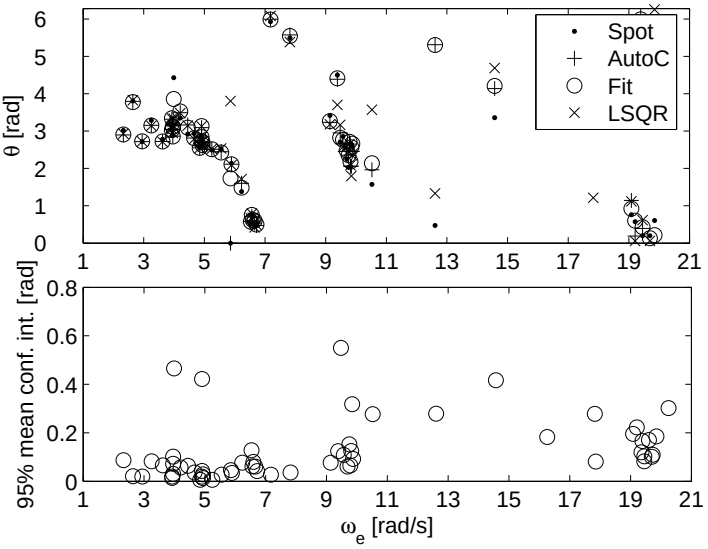

Figure 4.17: *Phases for linear heave motion of ballast 1 condition. 95% confidence interval of the mean phase is illustrated. Definition of methods is described in the text.*

The ratio of the frequency is illustrated in Figure 4.18. The ratio indicates when disturbances, e.g. swell from previous runs, affect the results. The 95% interval of the mean frequency confirms that the uncertainties in the frequencies in general are low, but that higher waves tend to increase the uncertainty.

Finally, the mean heave motion is shown in Figure 4.19. The mean motion was caused by forward speed with trim and sinkage in the order of 2-3cm. The track was also elevating towards the wave maker, increasing the apparent sinkage for shorter waves. The elevation of the track was maximum 3cm, but the average during the measured runs was about 1cm. The mean values may also indicate improper zero setting or nonlinear additions in higher waves.

Figure 4.20 presents the transfer function of pitch including phases. The pitch approaches the wave slope for long waves and zero for short waves. The pitch motion is in practice zero above 5rad/s. The model did not move in pitch and heave for encounter frequencies above 6rad/s, and the first, second and third order springing in Figure 4.22were not expected to be significantly affected by coupling between global ship motions and hydroelastic resonance response. This does however not mean that there is no coupling between rigid ship motions and whipping, when even higher order harmonics may be involved and

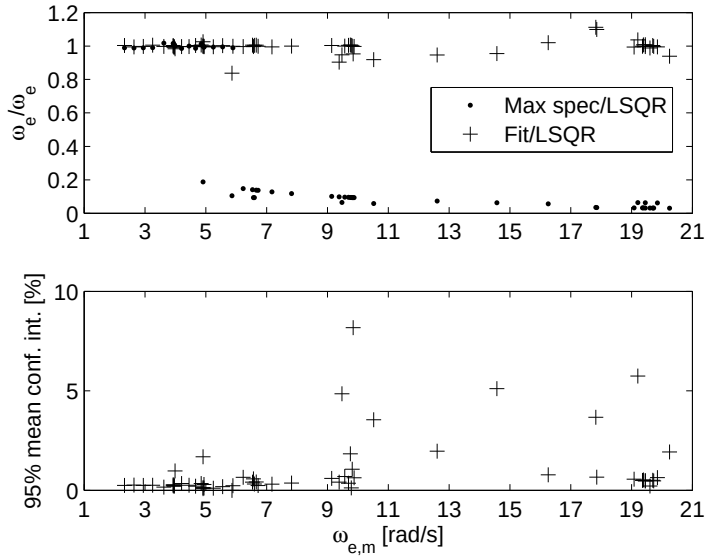

Figure 4.18: *Ratios of frequencies corresponding to heave motion of ballast 1 condition and the 95% confidence interval of the mean frequency from the nonlinear fit. Definition of methods is described in the text.*

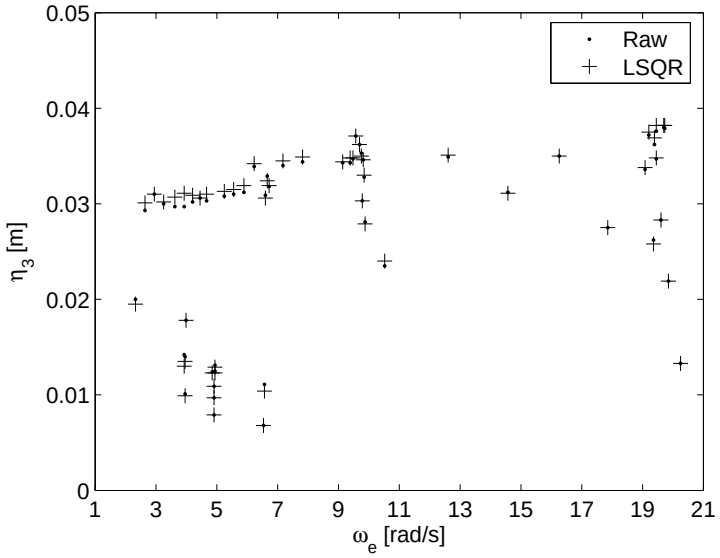

Figure 4.19: *Mean sinkage (positive) in forward speed corresponding to heave motion of ballast 1 condition (some of the lower points at 9 and 20rad/s corresponds to lower speeds).*

the encounter frequency is lower.

Figure 4.21 presents the transfer function for the bending moment at midship section including phases. The bending moment shows a rigid body response peak at 4rad/s and a

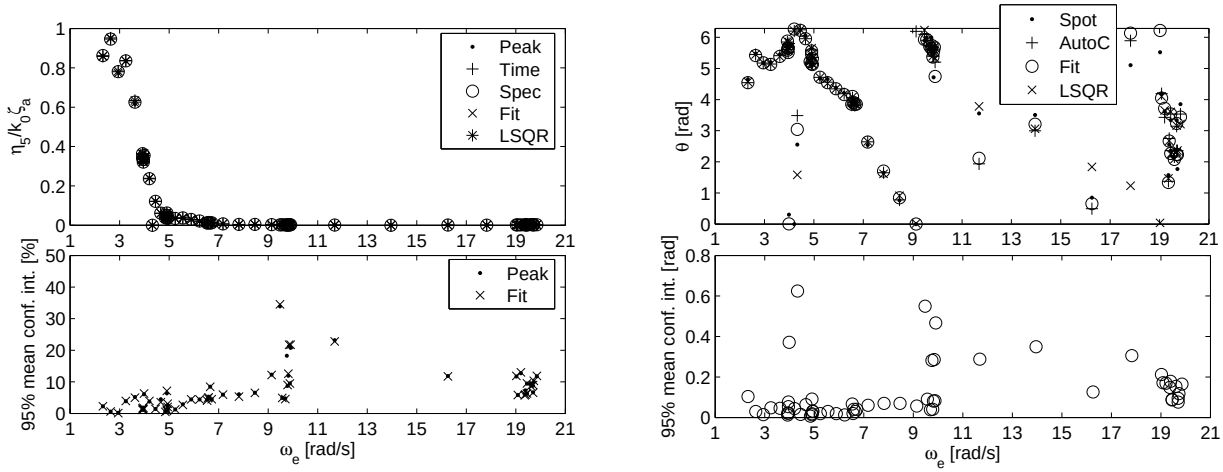

Figure 4.20: *Linear transfer function of pitch including phases of ballast 1 condition and the 95% confidence intervals of the mean amplitude and phase.*

linear springing peak at $19.5 rad/s$. The first and second cancellation period in the bending moment may be visible. The 95% confidence interval of the mean moment amplitude is typically in the order of 4%, and the nondimensional value of the rigid body moment peak is about 0.02. The wall interaction appears to affect the transfer functions at encounter frequencies below $3.5 rad/s$.

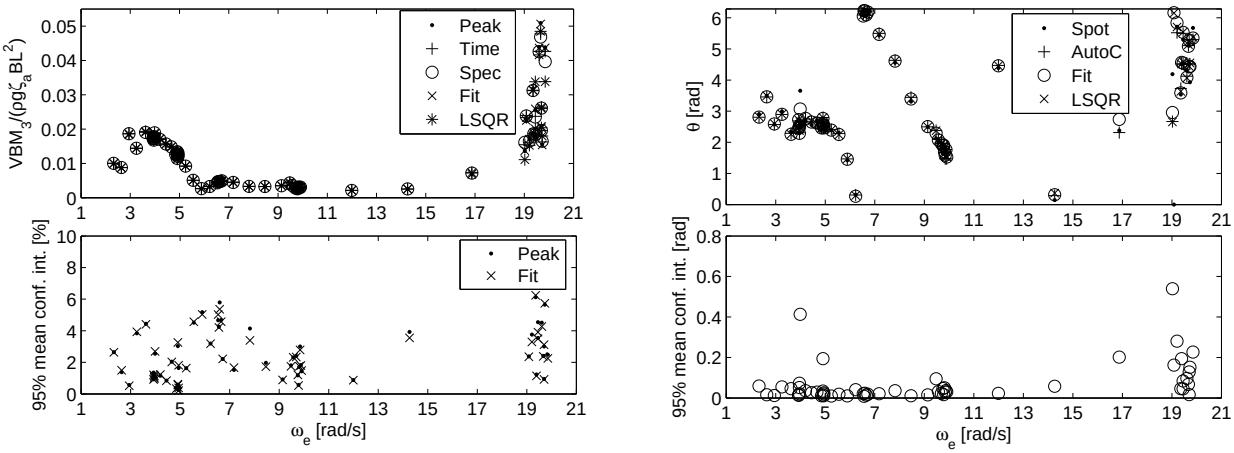

Figure 4.21: *Linear transfer function of vertical bending moment at midship section including phases for ballast 1 condition, and the 95% confidence intervals of the mean amplitude and phase.*

A first estimate of the critical frequency of wall interaction is formulated as

$$\omega_c = \frac{Lg}{U4d} \tag{4.10}$$

where d is the distance between the center of the ship and the side wall. It assumes that the radiated wave from the bow is reflected by the wall and hits the stern, and that the generated wave front moves with the group velocity in deep water. This gives a wave frequency of $3.0 rad/s$ corresponding to an encounter frequency of $4.2 rad/s$ ($4.8 rad/s$ in cargo condition). A frequency below this is necessary to provide a significant effect on the bending moment, and the observed $3.5 rad/s$ agrees well with this estimate in ballast condition. Converted to full scale, the wall interaction starts at a period above $14s$. The *wall interaction must be anticipated in longer waves and at lower speeds.* Appendix C.1 shows that the apparent false predicted transfer function values at low periods actually are well reproduced in the different loading conditions, confirming that they are a result of physical wall interaction due to this unconventional large model.

4.6.2 'Nonlinear' transfer functions

'Nonlinear' is quoted, because the transfer function is defined to illustrate the total response (NL) at the encounter frequency, as explained in Section 2.4.2. A narrow band filter is also used to determine the transfer function value of the higher harmonic (HF), which may coincide with the resonance frequency. The ratio of the HF frequency to the encounter frequency displays the relative value of the n^{th} order multiple. The second order multiple is related to the hypothesis 4 and the higher order multiples are related to hypothesis 3. This 'nonlinear' transfer function is compared to the linear transfer function. In all cases, the peak analysis described in Section 4.6.1 is applied. In this way the relative importance of the total nonlinear and wave induced vibration effect is displayed.

Figure 4.22 illustrates the 'nonlinear' transfer function and the frequency ratios. All results are made nondimensional based on the linear wave amplitude. The higher harmonics, in particular the second and third order multiple, are pronounced. The frequency plot shows that the spectral peak at twice the encounter frequency is largest for the second order effect (hypothesis 4), while the spectral peak at three times the encounter frequency is largest for the third order effect. The third order effects become important especially for the highest waves (hypothesis 3), while the second and first order effect appear to be strong also in small waves, especially since the second order effect is also present outside resonance. For fourth and fifth order effects, the nonlinear effect come from nonlinear geometry rather than the elastic effects, since the linear and HF response do not add up to the total nonlinear response. The uncertainty in the HF components is higher than for the encounter and nonlinear response, which may be partly explained by low vibration values in longer waves. The maximum peak in the response spectrum at a frequency of $17 rad/s$ occurred at a slightly different frequency than the encounter frequency, and this indicated that the surge motion was too large (and was controlled in subsequent runs).

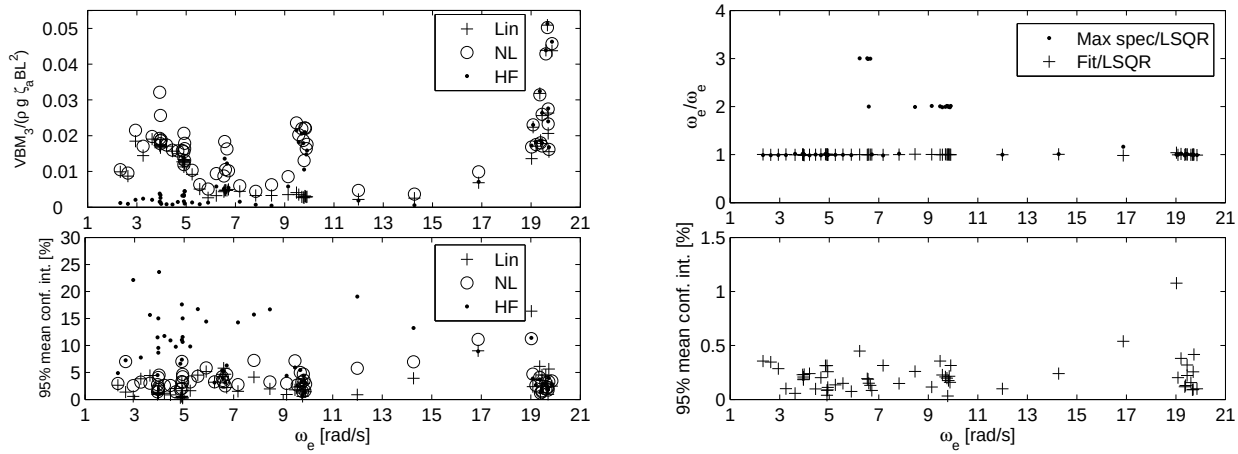

Figure 4.22: *'Nonlinear' transfer function of vertical bending moment (left plots) taken as maximum range divided by wave height for midship section in ballast 1 condition. The frequency ratios are shown to the right. The 95% mean confidence intervals for the linear, high frequency and nonlinear response and frequency are displayed.*

4.6.3 Second order transfer functions

Two component waves were run in order to investigate the sum encounter frequency effect at $\omega_{1,e} + \omega_{2,e}$. This sum frequency was supposed to coincide with the 2-node springing frequency, ω_s. Monocromatic waves with sum encounter frequency $2\omega_1$ equal to the springing frequency were also considered. The intention was to observe how the sum frequency effect related to hypothesis 4 changed with increasing ratio $\omega_{2,e}/\omega_{1,e}$. The ratio of one corresponds to monochromatic waves. Further explanation is given in Section 2.4.3.

Nonlinear damping affected the vibration level, except in ballast 2 condition. The nonlinear damping deteriorated the appearance of the second order transfer function when different wave heights were considered. Therefore, only waves of the same height were analyzed. Figure 4.23 and 4.24 show the spectra and the filtered time series components in one run. The two wave components ($WP3$) are located with encounter frequencies at 8 and $12 rad/s$. The bending moment ($FX3$) at midship section is small at the encounter frequencies, while it is large at the sum frequency of $20 rad/s$. Small sum frequency effects are observed on the pressure at the stem ($P3$), but not on the wave or relative motion ($REL1$) in the bow due to small steepness. This sum frequency pressure comes from the radiation due to the vibration of the hull and from the sum frequency excitation due to the incident waves. It was difficult to separate these two small pressure components to illustrate the importance of the second order excitation from the reflected waves, so this is not shown.

The determination of the amplitude at the encounter frequencies and sum frequency were based on three methods.

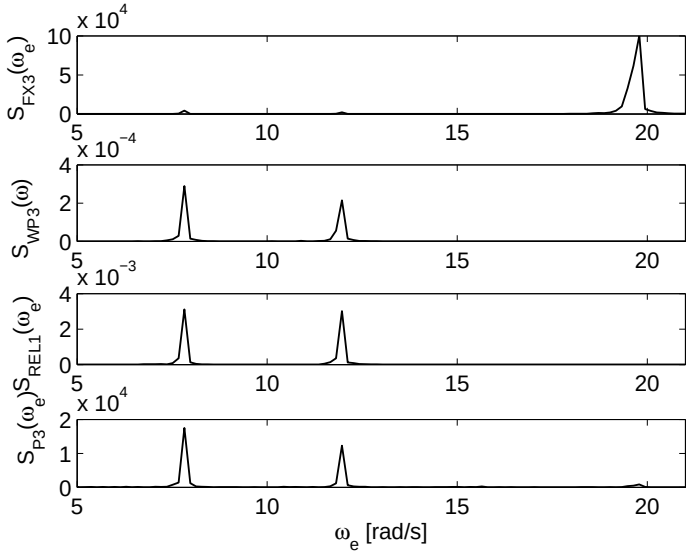

Figure 4.23: *Spectra for a bichromatic wave exciting resonance in ballast 1 condition (run 1071). FX3 = Axial force (bending moment), WP3= Wave elevation, REL1= Relative motion in the bow and P3= Pressure at stem. Unit is basic unit squared times time, e.g. N^2s for $FX3$.*

1. The first estimate was taken from the standard deviation of the filtered time series, Eq.(2.68).

2. The second estimate was taken from the peak analysis of the raw signal based on zero crossings for the longest encounter period, Eq.(2.67). This represents the total nonlinear combination.

3. The third estimate came from the least square fit to the raw signal, Eq.(2.70). Iteration for each of the three frequencies was necessary to find good peaks. The least square fitting procedure provided also phase information, which was disregarded.

The least square procedure is illustrated in Figure 4.25. The raw signal is compared to the fitted signal using all components and using only the three dominating components. Satisfactory agreement is observed.

The second order transfer function was presented with the frequencies in the xy-plane and the responses in z-direction. The encounter responses were presented, for comparison, on the 45^0 diagonal in the xy-plane where $\omega_{1,e} = \omega_{2,e}$. The unidirectional transfer function for sum frequency is symmetric about the 45^0 diagonal, since $|H(\omega_{1,e}, \omega_{2,e})| = |H(\omega_{2,e}, \omega_{1,e})|$, and two points were plotted for each sum frequency combination. The results are presented in Section 5.3.2.

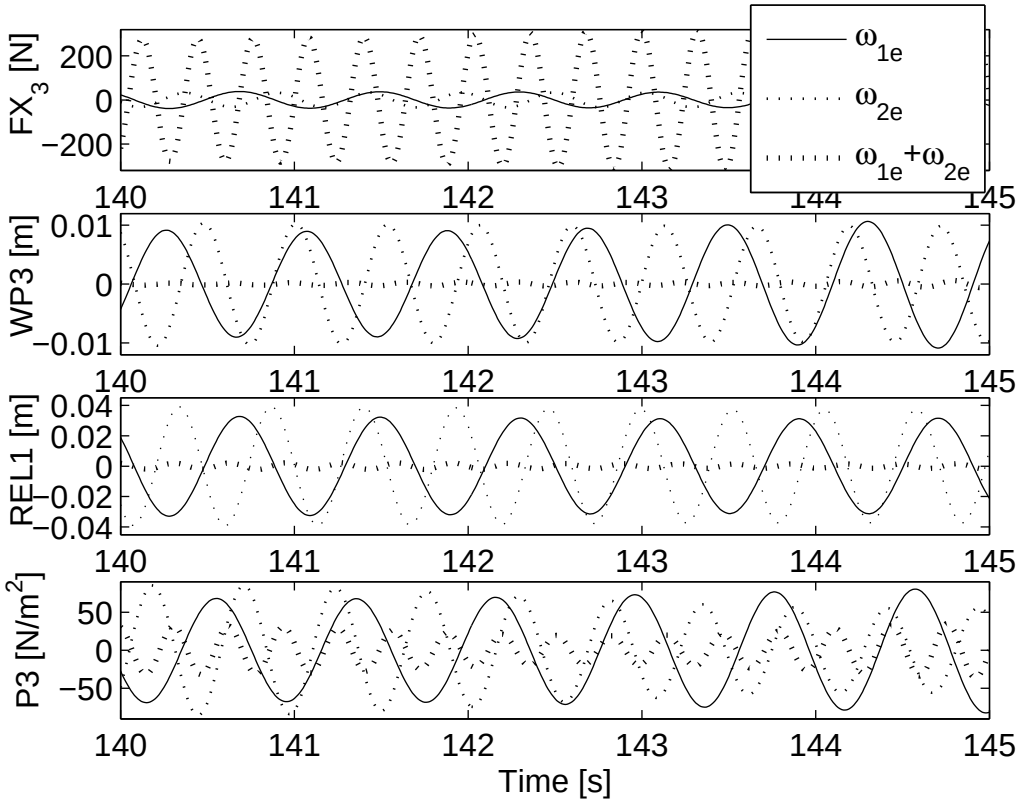

Figure 4.24: *Filtered time series for a bichromatic wave exciting resonance in ballast 1 condition (run 1071). FX3 = Axial force (bending moment), WP3= Wave elevation, REL1= Relative motion in the bow and P3= Pressure at stem.*

4.7 Procedure for calculation of fatigue damage

The procedure to determine the short term fatigue damage is outlined in the following.

1. The different runs in each sea states were merged, and the time was scaled with $\sqrt{\Lambda} = \sqrt{35}$. Each sea state amounted to about 38 minutes in full scale.

2. The time series of the axial force were converted into full scale hot spot stress in deck. A moment arm of $0.88m$ and scaling according Eq.(B.10) to full scale bending moment were applied. A section modulus derived by NAUTICUS, (DNV 2005c), of $53.92m^3$ (43.92/46.52) was used at midship section (aft quarter/fore quarter) to convert moment to stress. The nominal stress was multiplied with a SCF of 2.0, representative for e.g. the hot spot on the longitudinal stiffener flange in way of the transverse web frame.

3. The total time series was derived by filtering the measured time series to remove everything above $2.0Hz$. The wave stress time series was derived by filtering above $0.35Hz$. Smooth filters were applied.

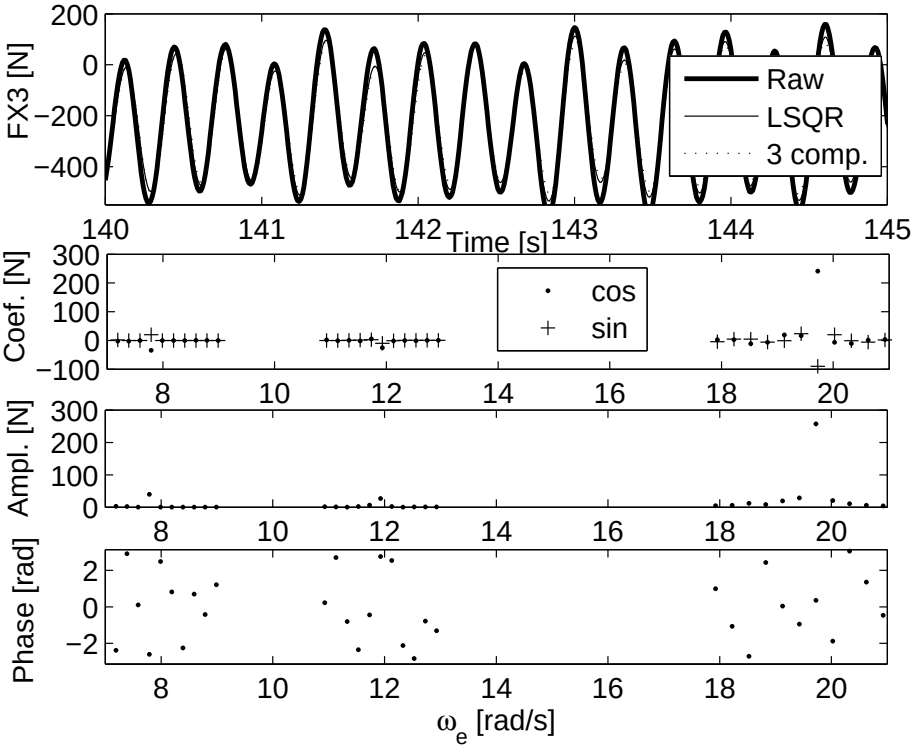

Figure 4.25: *Least square fit to time series of bending moment (FX3) due to a bichromatic wave giving resonance in ballast 1 condition (run 1071). The coefficients in front of the sinusoidal terms, amplitudes and phases are illustrated.*

4. The stress time history relevant for fatigue analysis was obtained by Rainflow counting of the total and wave frequency (WF) stress time series.

5. A two slope SN-curve for welded joints in air or with cathodic protection, (SN-I in (DNV 2005a)), and Miner Palmgren's rule were applied.

6. The total and WF damage were calculated from the total and wave stress.

7. The vibration damage was calculated as the difference between the total and WF damage.

The rainflow counting was performed utilizing the DNV program TIMSER, (Mathisen 1988; Mathisen 2001). The procedure has been validated against other procedures with good agreement, and the current procedure is referred to as the hot spot stress approach. Further description is given in Section 2.7.

4.7.1 Scatter diagrams and investigated sea states

The model was tested in different sea states listed in Appendix B.6. An overview of these sea states compared to the North Atlantic and World Wide scatter diagrams is presented

in Figure 4.26. The scatter diagrams illustrate the probability of occurrence, which were taken from DNV CN 30.5, (DNV 2000). The selected sea states were chosen from areas with high and low probabilities. A ship operating in World Wide trade will in general encounter lower sea states with shorter periods than in the North Atlantic trade. One key issue relates to how these scatter diagrams influence the vibrations and wave damage.

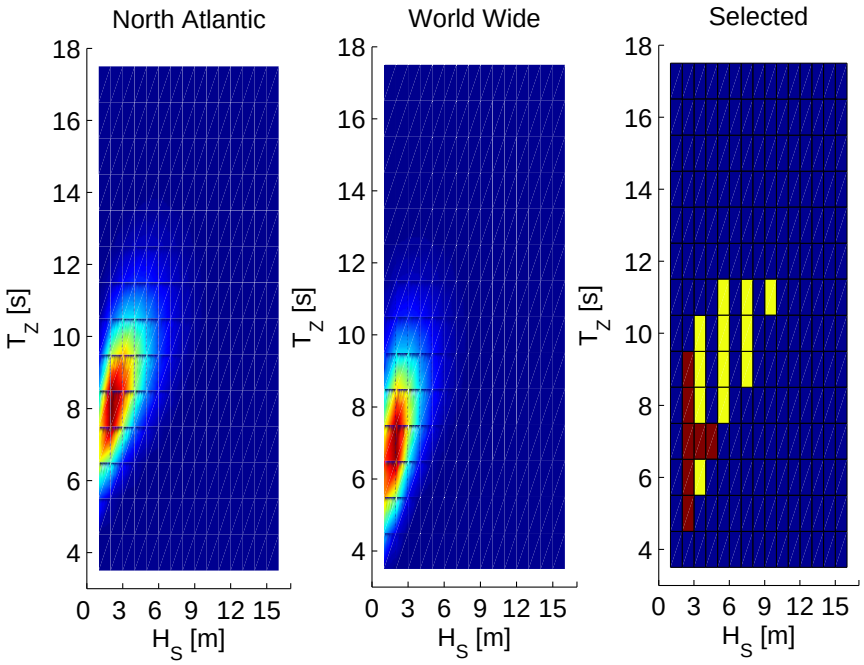

Figure 4.26: *Scatter diagrams (H_S versus T_Z) for North Atlantic and World Wide trade compared to the investigated sea states. The light cells were tested in all combinations of bow design and loading condition at full speed, while the darker cells were also tested for ballast 2 and cargo 2 condition.*

4.8 Method for identifying whipping

It is difficult to separate whipping and springing, e.g. (Gran 1974). This is not an issue when evaluating the implication of specific measurements, however it is necessary to know which effects to include in theoretical predictions when the results are to be generalized. For this reason a method was derived to distinguish the phenomena by identifying whipping events from the model test time series. The intention is to illustrate the importance of hypothesis 3 related to whipping impacts relative to the linear and second order springing (hypothesis 4).

The method is based on the envelope process of the filtered 2-node vibration response. If the slope of the envelope curve exceeds the maximum possible slope from springing, a whipping event is identified. The key point is to establish a reliable or sensible criterion

for the maximum springing slope.

Assuming a lightly damped SDOF-system, originally at rest, produces the following envelope process

$$\frac{u^{env}(t)}{u_{st}} = \frac{1}{2\delta}(1 - e^{-\delta\omega_s t}) \tag{4.11}$$

where δ is the damping ratio, u is the response in time, and ω_s is the springing frequency of the forced loading. The subscript *st* refers to the static deflection. The maximum slope of the envelope process is given by the derivative at $t = 0$. It is difficult to define the start of the impact, and the derivative after one springing period is chosen as a good approximation.

$$\frac{u^{env}(t = T_s)'}{u_{st}} = \frac{\omega_s}{2} e^{-\delta 2\pi} \tag{4.12}$$

The response and envelope process, representing the 2-node springing of the model, are shown in Figure 4.27.

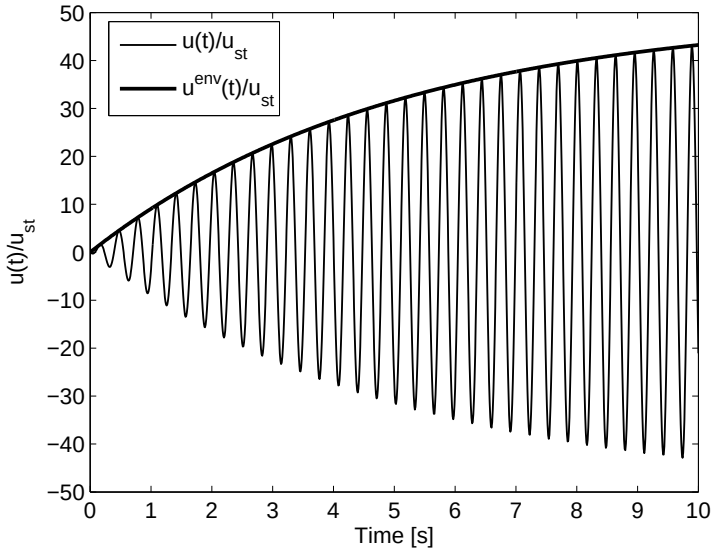

Figure 4.27: *Dynamic response and envelope curve from a constant harmonic loading of a SDOF-system, which initially is at rest,* $\delta = 0.01$ *and* $\omega = 20 rad/s$.

The static response can be related to the maximum springing response as

$$u_{st} = 2\delta u_{dyn,max} \tag{4.13}$$

and to define a criterion, the maximum springing response must be determined. The springing vibration is assumed to come from *lin*ear and *sum* frequency excitation, and the

two processes is assumed to be independent, which is reasonable. The maximum of the total response is approximated by

$$u_{dyn,max} = \sqrt{u^2_{dyn,max,lin} + u^2_{dyn,max,sum}} \tag{4.14}$$

The maximum values refer to the linear springing peak from the linear transfer function and the nonlinear springing peak from the second order transfer function. The second order transfer function is assumed to contain only springing excitation, and higher order effects are assumed to be caused only by whipping. The static bending moment is written

$$VBM_{static} = 2\delta\sqrt{(\overline{VBM_{lin,max}}\zeta_1\rho gBL^2)^2 + (\overline{VBM_{sum,max}}(\frac{\zeta_2}{2})^2 k_2\rho gBL^2)^2} \tag{4.15}$$

The subscript $_1$ refers to the wave amplitude at the encounter frequency of linear springing, while subscript $_2$ refers to the wave amplitude (wave number) at the encounter frequency of the sum frequency monochromatic springing. The criterion for the slope of the envelope process becomes

$$c^{VBM} = \omega_s\delta e^{-\delta 2\pi}\sqrt{(\overline{VBM_{lin,max}}\zeta_1\rho gBL^2)^2 + (\overline{VBM_{sum,max}}(\frac{\zeta_2}{2})^2 k_2\rho gBL^2)^2} \tag{4.16}$$

This criterion is used to identify a sudden increase of the response, i.e. whipping.

For a whipping event causing a sudden decrease in the vibration level due to opposite phasing with the existing vibration, the natural decay due to the damping is assumed to contribute to the decrease (as a small additional effect). The additional decrease is strictly dependent on the initial vibration level. In order to define a general initial level, the decay is related to the reduced response during one vibration cycle at an initial vibration level of two times the significant vibration amplitude for the sea state. The correction based on this chosen reference level is written

$$c^{\Delta} = 4 \cdot \sqrt{E(VBM^2_{HP})}(1 - e^{-\delta 2\pi}) \tag{4.17}$$

The subscript HP refers to the high pass filtered bending moment capturing the dynamic 2-node response, while $E(VBM^2)$ is the variance of the bending moment time series with zero mean. When applied to a sudden decay of the positive envelope process, the decrease exceeding $-c^{VBM} - c^{\Delta}$ indicates a whipping event, which reduces the vibration level.

The wave amplitudes are estimated as two times the expected mean wave height for the linear and sum frequency wave period in accordance with Appendix A.10. The combination of the linear and sum frequency response at full speed with high wave amplitudes makes the criterion strict. The probability of springing to exceed the criterion is low, while it is likely with whipping response below the criterion. The criterion is therefore intended to identify detectable and significant whipping events.

4.8.1 Procedure

The procedure is illustrated for ballast 2 condition in a sea state of $4m$ significant wave height and $7s$ zero up-crossing period at full speed of $15kn$. The time series is filtered, keeping the interval between 12.5 and $25rad/s$, and the envelope process is identified between local maxima above zero. The slope is calculated by the Euler method. The nondimensional peak values estimated for the bending moment amidships are $\overline{VBM}_{max,lin} = 0.065$ and $\overline{VBM}_{max,sum} = 1.6$ taken from Figure 5.15 and 5.20, respectively. Figure 4.28 presents the detected whipping events marked with circles at the second end of the slope. The moment is represented by the axial force transducer at midship section, FX_3, and the slopes are displayed in the lower plot. An axial force of $1000N$ corresponds to $25MPa$ nominal stress level in deck.

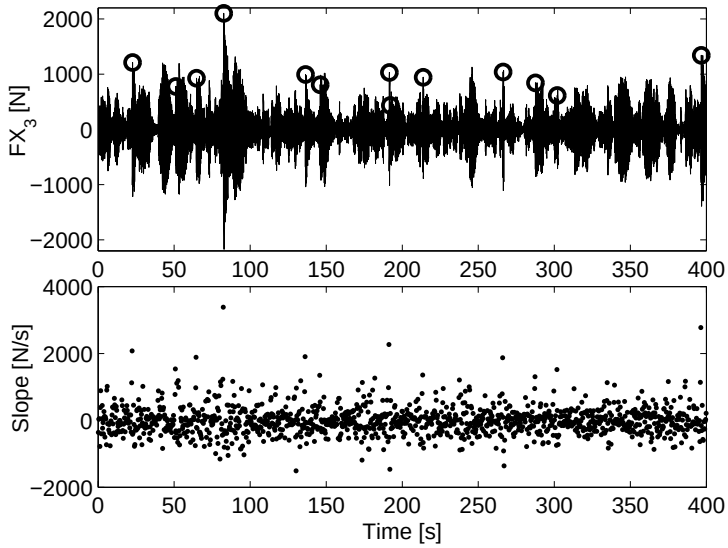

Figure 4.28: *Whipping events (both decrease and increase) identified for bending moment (FX3) at midship section, $H_S = 4m$, $T_Z = 7s$, $U = 15kn$. 1000N corresponds to 25MPa nominal stress amplitude in deck amidships. Note time in model scale.*

The cumulative probability distribution of the envelope process is derived from 1400 slopes. The criteria, which are not symmetric about zero, are shown in Figure 4.29. 12 slopes exceed the criteria with some margin, and intuitively these represent the actual whipping events. Note that the exact number of whipping events could not be determined in these model tests, so that this methods only indicates the number of significant whipping events. The total number of real whipping events including the small whipping events are unknown. The goodness of the method can therefore be debated, but Figure 4.29 indicates that the criterion appears to be reasonable. The criterion fits well into the distribution of slopes where the largest slopes are well separated from the rest.

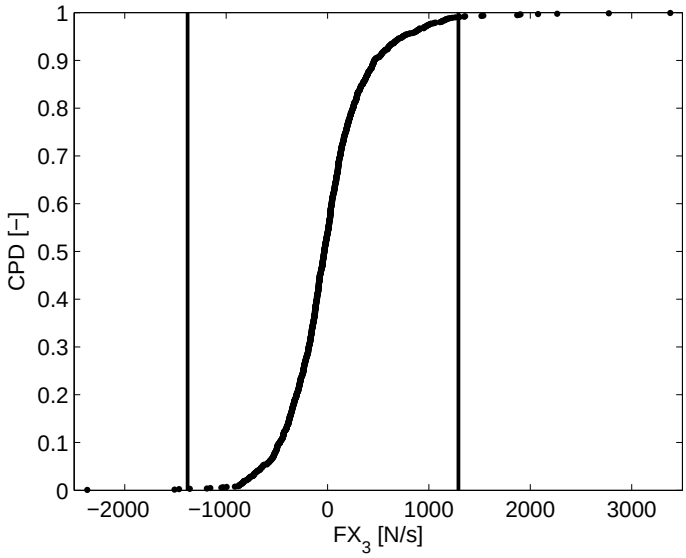

Figure 4.29: *Cumulative probability distribution of the envelope slopes of FX_3 versus the criteria, $H_S = 4m$, $T_Z = 7s$, $U = 15kn$. 3000 N/s corresponds to about 25MPa nominal stress amplitude in deck amidships.*

To estimate the relative importance of springing and whipping, the identified whipping events are used to define an artificial whipping process. This is created based on the amplitudes at the aft end of the slopes exceeding the criteria. This implies a sudden increase or decrease followed by a logaritmic decay. To separate the whipping and springing contribution, it is assumed that the processes are independent. The standard deviation of springing stress is calculated as $\sigma_{spring} = \sqrt{\sigma_{Tot}^2 - \sigma_{Whip}^2}$, where $_{Tot}$ refers to the measured vibration and $_{Whip}$ refers to the artificial whipping process. The probability of a slope indicating whipping is also calculated. This procedure will be applied to all sea states in Section 5.7.

The method may also be applied to the negative envelope process to check whether there is a difference. As illustrated in Figure A.15 the whipping maxima differ in sagging and hogging, and whipping may be caused by both an upward and a downward force.

4.9 The relative importance of linear and monochromatic second order excitation

A simple approach is applied to investigate the importance of the monochromatic second order effect ($2\omega_e = \omega_s$), as compared to the linear springing as a function of the wind speed. The second order effect in this simplified procedure is handled as a linear effect, but the second order resonance peak must then be corrected for each sea state. The analysis

is not consistent with the correct formulation of general second order analysis, but the intention is to illustrate the importance of the hypothesis 4 related to nonlinear springing relative to linear springing, and for this purpose the methodology is sufficient. The relative importance is shown in Section 5.6.

An artificial (simplified) 'nonlinear' transfer function is established based on Figure 5.15, which shows the nondimensional 'nonlinear' midship bending moment from ballast 2 condition as a function of the encounter wave frequency. The rigid body response is represented by a transfer function of the following Gaussian shape

$$\overline{VBM}_r = 0.02e^{-\frac{(\omega_e-\omega_p)^2}{2\sigma^2}} \tag{4.18}$$

where $\sigma = 1.25$ denotes the width. The magnitude of 0.02 is taken from Figure 5.15.

The **linear** resonance peak is defined by the SDOF system

$$\overline{VBM}_s = \frac{0.065 \cdot 2 \cdot 0.01}{\sqrt{(1-\beta^2)^2 + (2\delta\beta)^2}} \tag{4.19}$$

where $\beta = \frac{\omega_e}{\omega_s}$ and ω_s is the springing frequency. The value of $2 \cdot 0.01$ reflects the resonance level for the damping ratio in ballast 2 condition, and 0.065 corresponds to the nondimensional magnitude of the linear resonance peak in Figure 5.15.

The **second order** contribution is established by replacing the frequency ratio in Eq.(4.19) with $\beta_2 = \frac{2\omega_e}{\omega_s}$, and replacing the 0.065 factor with 0.048, corresponding to the peak of the second order resonance in Figure 5.15. The frequency ratio defined as this makes the 'nonlinear' peak at the encounter frequency of half thickness compared to the linear resonance peak, and this is necessary since the actual vibration due to the second order effect occurs at the frequency corresponding to the linear resonance. The second order effect is also proportional to the wave amplitude squared, and therefore the second order vibration has to be corrected for the wave amplitude at the encounter frequency. The correction used is $\zeta/1.05$, where 0.048 is the nondimensional second order peak value in Figure 5.15 corresponding to the wave height of $2.1m$. The wave amplitude, ζ_a, in an irregular sea state is estimated as the expected mean wave amplitude according with Appendix A.10. The mean wave height versus Beaufort numbers are presented in Figure 2.8. The artificial monochromatic second order contribution must accordingly be corrected for every sea state, but the response spectrum can be established assuming a linear transfer function.

The second order resonance curve in the transfer function is displayed at the encounter frequency, consistent with the 'nonlinear' transfer function. The peak is of half width compared to the linear resonance curve, and this shape is combined with the wave spectrum to produce the response spectrum. The vibration will still occur at the same frequencies as the linear resonance. An example of the 'nonlinear' transfer function, with the second order effect corrected for a Beaufort number of 6, is shown in Figure 4.30. Torsethaugen

wave spectrum is assumed, and it requires the significant wave height as input, which is taken from the Beaufort scale in Table A.1. Torsethaugen requires also the peak period. The relation between significant wave height and zero up-crossing period in Appendix A.10 is utilized, and the zero up-crossing period is converted to the peak period using Eq.(2.83) assuming a γ of two. The wave spectrum is converted to encounter spectrum to consider the correct encounter wave frequency. The measured speed reduction in full scale taken from Moe et al. (2005) is used in the estimate of the wave amplitude, which is necessary for correction of the second order response.

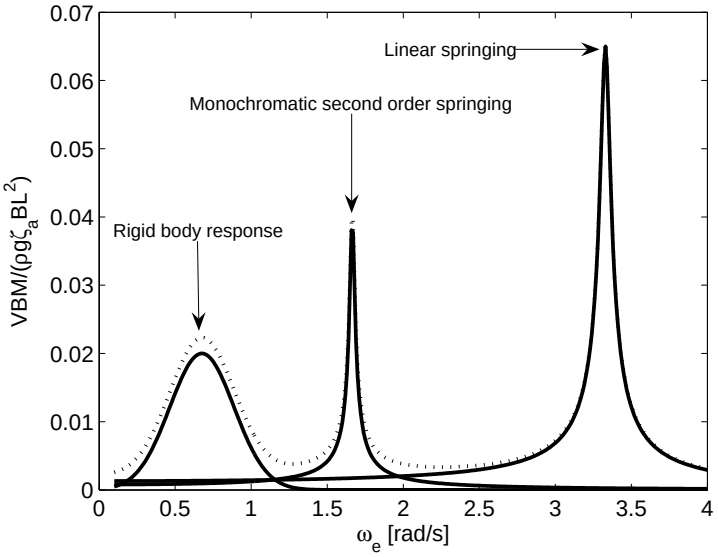

Figure 4.30: *Illustration of the artificial nondimensional 'nonlinear' transfer function of the midship bending moment (VBM) in a typical sea state for $Bn = 6$; $U = 10.9kn$, $\delta = 0.01$. The monochromatic second order springing peak is corrected based on the estimated mean wave amplitude for each sea state (Beaufort number). The dotted line is the total nondimensional response. The continuous lines refer to the rigid body, the monochromatic sum frequency and linear springing peak.*

The wind based PM wave spectrum in Eq.(2.84) assumes fully developed sea. It predicts higher significant wave heights than the Beaufort scale at high Beaufort strengths (19m reference height instead of 10m). For comparison, the Torsethaugen and PM wave and encounter spectra at Beaufort 6 are shown in Figure 4.31. The Torsethaugen wave spectrum is more peaked with a higher peak period than the PM spectrum. The encounter spectra are moved towards higher frequencies due to the forward speed, and at $1.66rad/s$ corresponding to the second order springing, the wave energy from PM is higher.

The wave spectra are combined with the artificial transfer function to calculate the response spectrum by $S_R(\omega_e) = |H(\omega_e)|^2 S(\omega_e)$, where $H(\omega_e)$ is the artificial encounter trans-

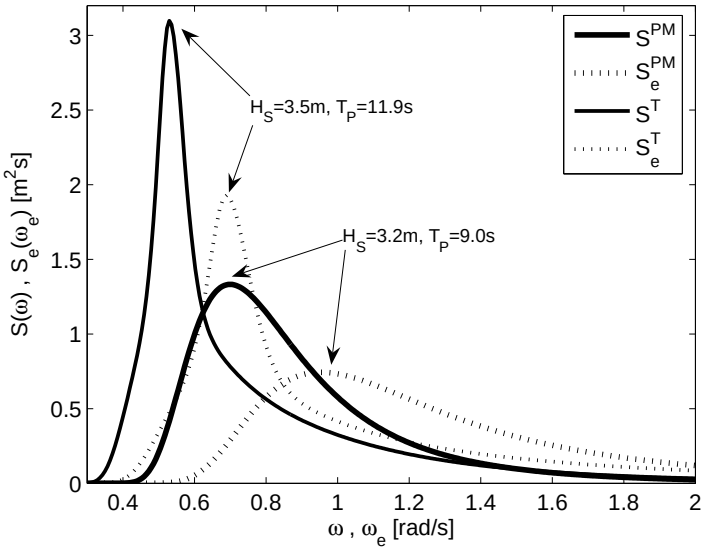

Figure 4.31: *Illustration of Torsethaugen (T) and PM wave and encounter spectra for* $Bn = 6$, $U = 10.9kn$.

fer function. This can be done since the 'nonlinear' monochromatic springing is considered as a linear effect herein. The response spectra are shown in Figure 4.32 based on the Torsethaugen wave spectrum. The second order effect is displayed at the frequencies where the vibration actually occurs instead of at the encounter frequency corresponding to the monochromatic peak in Figure 4.30. The energy from the wave spectrum is however taken from the encounter frequency corresponding to the monochromatic 'half width' peak. The monochromatic second order effect is about twice as high as the linear contribution for this sea state.

The nondimensional bending moment is converted into full scale stress in MPa (for comparison with full scale measurements). The nondimensional bending moment is multiplied by $\rho g B L^2/10^6/53.92$, where 53.92 is the section modulus in deck amidships and 10^6 is used to get the stress in MPa. The standard deviation of the filtered high pass nominal stress is calculated for the linear and second order response. The second order response refers to the sum of the second order and linear response. The phasing of the wave frequency components are generated by a random phase lag, hence the response from the linear and sum frequency effect will also be independent, and they can be combined accordingly. Note that this is not the case for the second order effect of the incident waves, i.e. the second order effect related to the incident waves satisfying the second order free surface condition, as illustrated in Figure 2.3. The results are displayed in Section 5.6.

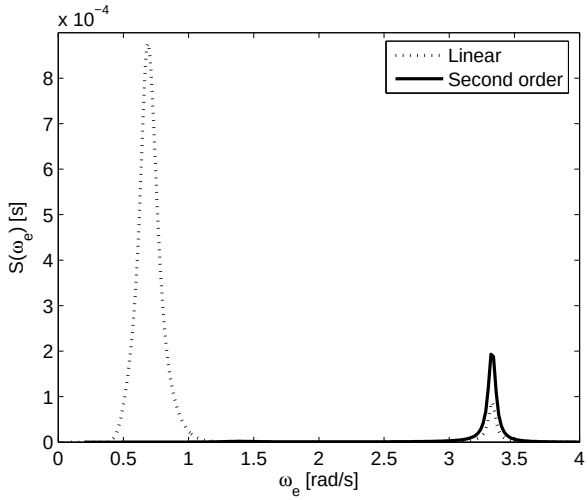

Figure 4.32: *Illustration of spectra for linear response, linear springing and monochromatic second order springing based on Torsethaugen spectrum,* $Bn = 6$ *(*$H_S = 3.5m$ *and* $T_P = 11.9s$*)* $U = 10.9kn$*. The monochromatic second order effect is displayed at the actual vibration frequency (opposite to at the encounter frequency in Figure 4.30).*

Chapter 5

Model test results

The main results from the model tests are provided in this chapter, beginning with the damping in the first section. Section 5.2 deals with the wave amplification in the bow and the added resistance in waves compared to analytical formulations, followed by transfer functions in Section 5.3 and fatigue damage in Section 5.4. Section 5.5 illustrates the relative importance of whipping and springing, while Section 5.6 illustrates the difference between linear and monochromatic sum frequency springing. Finally, a few whipping and springing events are displayed in Section 5.7. Mainly results from ballast 2 condition are covered. Results from other loading conditions and bow shapes are shown in Appendix C, and full scale measurements are described in Chapter 6.

5.1 Damping

The damping ratio was estimated in air and in calm water to investigate the following effects

⋆ Forward speed.

⋆ Rubber sealing and water leakage (in air).

⋆ Effect of mode shape (distinct natural frequencies)

⋆ Springing frequency in air.

⋆ Wall effects due to radiated and reflected waves.

⋆ Mounting gear; Safety ropes, cables, towing and guidance lines.

⋆ Changed number of bearings and design.

The damping ratio was estimated by procedures explained in Section 4.4. The damping contributions from wall reflection, mounting gear and effect of frequency in air were small and regarded as insignificant.

5.1.1 Damping estimates for the 2-node mode from decay tests

The damping was in most cases nonlinear due to insufficient quality (tolerance) and tightening of bearings, loose weights and supports (in air). During the first tests in ballast 1 condition, deficient aft lower bearing was identified in high waves. A second lower bearing was mounted as shown in Figure B.1, and the previous runs were repeated. Figure 5.1 illustrates the effect of using two lower bearings instead of one for the three joints in ballast 1 condition. The damping level and its nonlinearity was reduced (resulting in larger vibration levels). The effect of speed in the model with only one bearing is also shown in Figure 5.1. Apparently, the effect of speed is small. This agrees with Tasai (1974) and Hashimoto et al. (1978), except that they indicated an unexplained jump at zero speed. This jump was not evident from the present measurements.

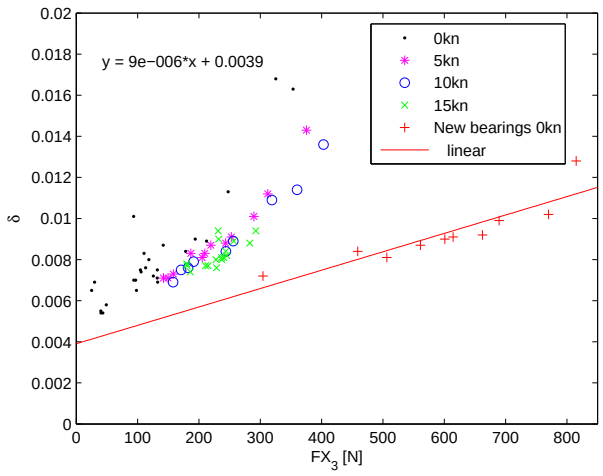

Figure 5.1: *Damping ratio of the 2-node mode from harmonic fits at different speeds in ballast 1 condition. A linear regression (the equation is presented) is applied to the data from the new bearings. The x-axis refers to the axial force, FX_3, which can be converted into a moment at the midship section.*

Figure 5.2 shows a nonlinear damping in air from ballast 1 condition. The estimates are associated with significant uncertainty, and the difference between the damping in air and water appears to be low. The supports contributed to the damping, and the hydrodynamic contribution was therefore difficult to estimate.

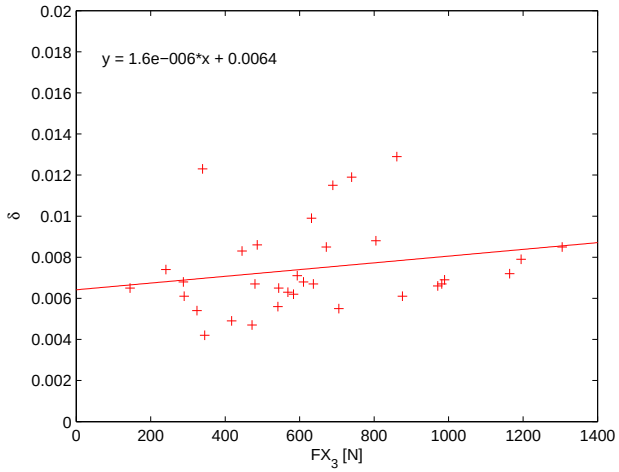

Figure 5.2: *Damping ratio for the 2-node mode in air (on supports) from harmonic fits for ballast 1 condition. Linear regression is performed.*

The rubber sealing and water leakage (small amount of water accumulated between the flexible cuts below the pump) contributed to the damping in water (and in air after the model had been in water). The contribution, illustrated in Figure 5.3, was estimated from tests in air for cargo 1 condition. The rubber sealing and water leakage were of similar importance, and their total contribution was about 0.15%. The tested force range was small, but nevertheless the contribution was significant.

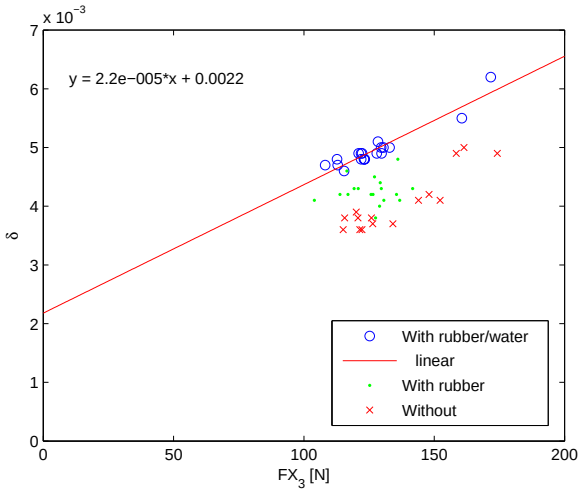

Figure 5.3: *Damping ratio for the 2-node mode from harmonic fits in air for cargo 1 condition. Linear regression is applied to the data with rubber sealing and water leakage.*

Prior to cargo 1 condition, all bearings were modified to include a split and set screws. The purpose was to tighten the bearings to the steel springs (rods). In water the model was pretensioned due to still water sagging or hogging moment, and it was difficult to tighten

the bearings sufficiently well. This tightening was in the subsequent ballast and cargo 2 condition done in air without any pretension, resulting in linear damping. Unfortunately, for cargo 2 condition the bearings were by a mistake adjusted in water, resulting again in a nonlinear damping behavior. Also for ballast and cargo 3 condition improper tightening resulted in nonlinear damping. The nonlinear damping reduced the quality of the results and made the assessment difficult. *Low and linear damping must be ensured prior to tests hereafter, and modification of the flexible joint design should be considered.* Set screws must be used with care, since they produced a nonlinear damping behaviour different than observed in ballast 1 condition.

The damping ratio for ballast 2 condition is presented in Figure 5.4. It is in principle linear with a mean of 1.0% from the left plot. The uncertainty to the mean value is low. The right plot confirms that the damping is speed independent. This contradicts several theories, e.g. (Kaplan et al. 1969; Goodman 1971), and model experiments, e.g.(Hoffman and van Hoof 1976; Troesch 1984), but agrees with model experiments by Achtarides (1979).

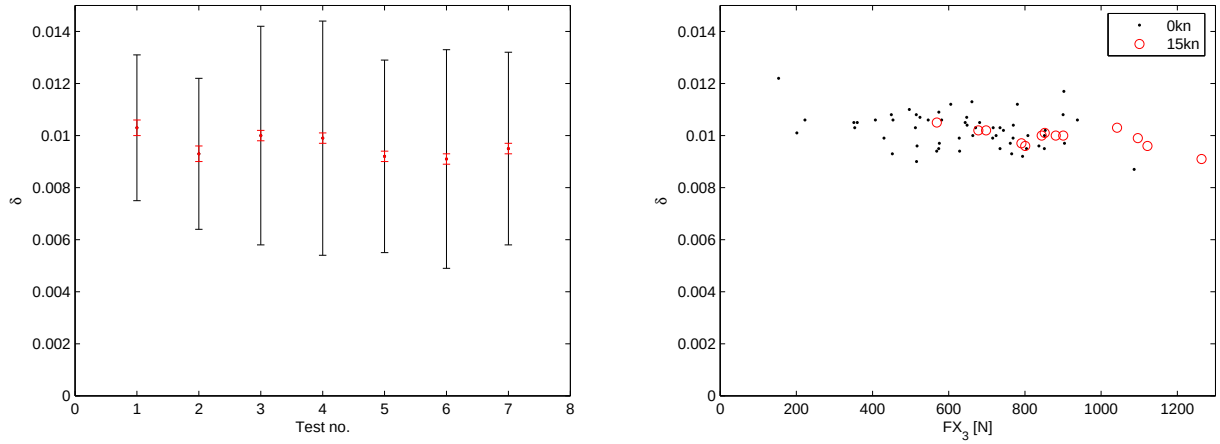

Figure 5.4: *Damping ratio for the 2-node mode obtained by cycle-by-cycle decay with 95% confidence interval of samples and mean (left) and from harmonic fits (right) for ballast 2 condition. Test no. 7 refers to 15kn, while the rest refers to 0kn.*

The damping tests in air after ballast 2 condition were not carried out by the author. The model was hanging in air from two strops, intended to be located at the two node points of the 2-node mode. The results indicated a damping ratio of 0.5%, but the response level was only about $10N$ (too small impulse loading). This damping ratio differs by 0.5% from the damping in water in Figure 5.4. Accounting for the rubber sealing and water leakage, the hydrodynamic damping constituted about 0.35%. This estimate is only an indication of the hydrodynamic contribution, since the response level was low.

Table 5.1 lists the approximate damping values obtained in the different tests. The rather unexpected damping behaviour in water for ballast 3 condition and cargo 2 condition is

illustrated in Figure 5.5. The strong nonlinear contribution was dominated by the insufficient tightening of the bearings.

Table 5.1: *Damping ratio for the 2-node mode in water obtained by different decay tests.*

Load. cond.	δ-range [%]	Load range [N]	Comment
Ballast 1	0.7-1.3	300-800	Weakly nonlinear increasing
Ballast 2	1.0	200-1250	Linear
Ballast 3	3.0-1.2	100-700	Nonlinear, decaying
Cargo 1	1.0-3.0-2.5	200-700-2500	Nonlinear, increasing and then weaker decreasing
Cargo 2	1.0-3.5-2.0	50-200-800	Nonlinear, increasing and then weaker decreasing
Cargo 3	3.5-1.7	100-800	Nonlinear, decaying

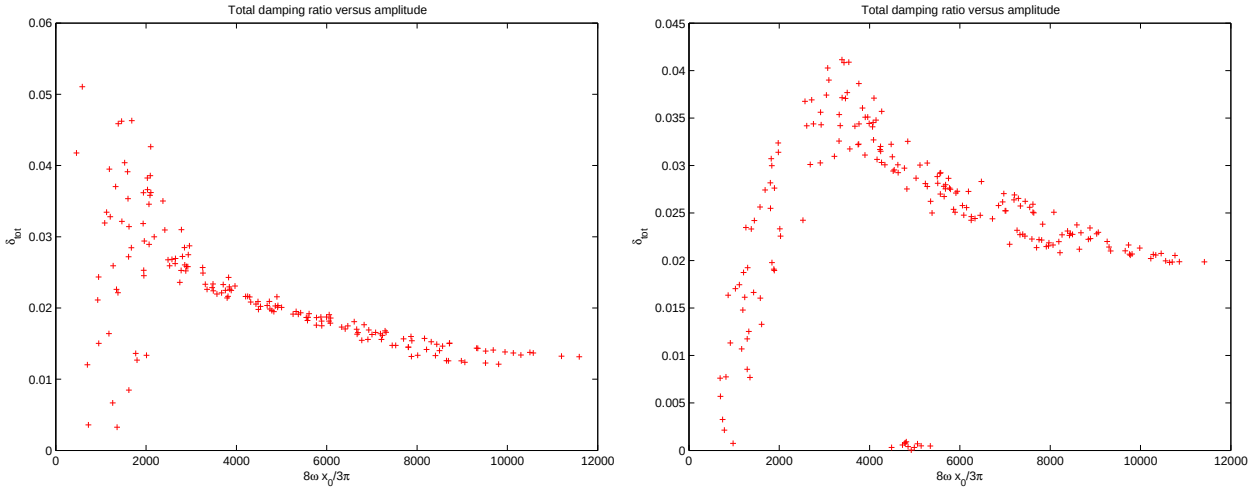

Figure 5.5: *Nonlinear 2-node damping ratio determined by a cycle-by-cycle decay for ballast 3 condition in 15kn (left, run9885) and cargo 2 condition in 13kn (right, run9862). According to Eq.(2.57), the x-axis refers to the vibratory response level, and the slope refers to the equivalent damping coefficient due to the nonlinear damping.*

5.1.2 Spectral method

The damping in irregular sea states was estimated utilizing the spectral method explained in Section 2.3.3. At least twelve sea states times three flexible joints were considered in each combination, and the 95% confidence interval of the sample and mean values were estimated. The natural frequency and JONSWAP high frequency tail factor were included. The results are shown in Table 5.2. The damping ratios for ballast 1 condition were most uncertain, and they were well above the estimates from the decay curves. The uncertainty in the natural frequencies was low, but the confidence interval of the mean value from ballast 1 condition exceeded the other estimates by a factor of two. This indicates a nonlinear stiffness, which explains the relatively high damping estimated for ballast 1 condition. The factor n does not represent a reliable estimate of the high frequency tail

factor, which is typically taken as 4 to 5 in standardized wave spectra, e.g. (DNV 2000). This is illustrated in Table 5.2 by a value of 0.9 estimated in the first row, while it becomes more reasonable by changing the frequency interval. Moreover, if there should be a hump hollow behaviour of the excitation, such behaviour is not captured by the spectral method. The estimated values are therefore not reliable.

Table 5.2: *Damping ratio, natural frequency and high frequency tail factor for the 2-node mode with 95% confidence interval of sample estimates (s.) and mean value (m.) obtained by the spectral method. Fitted frequency interval below/above the natural frequency and number of FFT sample points are indicated. Bold is default values.*

Loading cond.	δ [%] /95% s./95% m.	$\omega_s[rad/s]$ /95% s./95% m.	n /95% s./95% m.
Ballast 1, **2048 -0.5/1**	2.76 /2.44/0.41	3.20 /0.12/0.02	0.9 /4.3/0.7
Ballast 1, 4096 -0.5/1	2.54 /2.42/0.40	3.20 /0.12/0.02	0.9 /4.3/0.7
Ballast 1, 2048 -1/1.5	2.80 /2.71/0.45	3.21 /0.10/0.02	2.2 /3.9/0.7
Ballast 1, 2048 -0.3/0.5	2.08 /1.22/0.21	3.21 /0.12/0.02	2.9 /7.2/1.2
Ballast 1, 4096 -0.3/0.5	1.94 /1.23/0.21	3.21 /0.12/0.02	3.3 /6.7/1.1
Ballast 2	1.39 /0.56/0.06	3.39 /0.08/0.01	4.2 /4.8/0.5
Ballast 2, 4096 -0.3/0.5	1.30 /0.32/0.03	3.39 /0.09/0.01	4.8 /6.1/0.6
Ballast 3	2.14 /0.76/0.09	3.33 /0.04/0.01	4.2 /5.5/0.7
Cargo 1	2.97 /0.82/0.10	2.77 /0.10/0.01	5.0 /5.9/0.7
Cargo 2	3.02 /0.81/0.10	2.95 /0.09/0.01	5.1 /4.7/0.6
Cargo 3	2.68 /0.79/0.10	2.88 /0.04/0.01	5.0 /4.1/0.5

In Table 5.2 the sensitivity of the input parameters to the procedure is illustrated for ballast 1 condition. The frequency range of the fit was by default taken from $0.5rad/s$ below to $1.0rad/s$ above the natural frequency. The default number of sample points in the FFT procedure was 2048. Increasing the number of sample points and using a narrower band produced lower and better estimates. The damping for ballast 2 condition was roughly 30% higher than predicted by the decay test. This was in accordance to Gran (1974), who indicated a 25% increase. Gunsteren (1978) concluded that the method can not be used due to nonstationary response! Based on these findings, the spectral method in case of linear damping and stiffness may only be useful as long as a correction factor of about 0.8 is included in the damping estimates. For nonlinear damping and stiffness it is less useful.

Figure 5.6 shows that the damping increased in higher and longer waves, while the natural frequency decreased. The latter indicates that the stiffness was reduced. Moreover, the variation in the added mass/wet area in larger waves may contribute to explain the decrease and variation in the springing frequency with increasing response level. This reduced natural frequency in higher waves was also observed in the ballast 2 condition, and consequently, the damping ratio from the spectral method was overestimated due to the resulting wider spectral resonance peak.

Due to the nonlinear damping behaviour in ballast and cargo 3 condition shown in Figure 5.5, the low vibration amplitudes were damped out faster than the high vibration amplitudes. If for instance the low vibration amplitudes came from springing and the

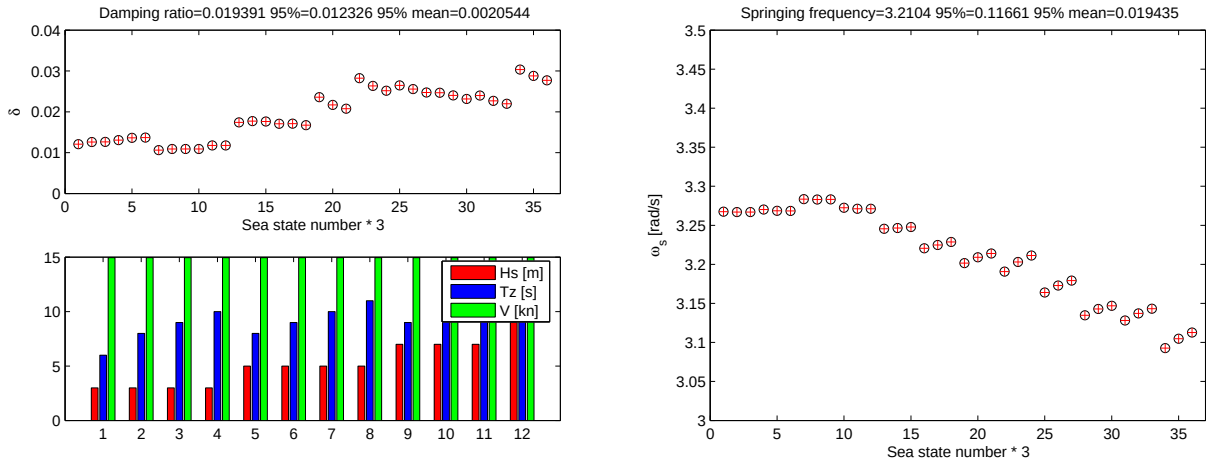

Figure 5.6: *The 2-node damping ratio versus sea states (left) and springing frequency (right) for ballast 1 condition for all three flexible joints.*

larger amplitudes came from whipping, the springing vibration was partly filtered by this damping mechanism. The opposite may be the case for ballast 1 condition.

5.1.3 Damping in higher order modes

The decay tests in ballast 2 condition were assessed to determine the damping of the 3- and 4-node modes. The damping of the 3-node mode ($48.8 rad/s$) was evaluated at the forward quarter length. The cycle-by-cycle method confirmed a speed independent damping. The three methods gave a mean damping ratio of 1.43% with a 95% confidence interval of the mean of 0.12% in average. The fit to the harmonic decay curve displayed a nonlinear decreasing damping for increasing response from about 1.7% at $300N$ to 1.2% at $1100N$. This force was measured by the axial force transducer, and the level was comparable to values in Figure 5.4.

The 4-node mode ($71.0 rad/s$) was evaluated at midship. The estimates from the cycle-by-cycle method became unreliable due to low sampling frequency. The time series were noisy with sharp maxima. A large scatter, also with many low values, were observed. The damping ratio from the two other methods was estimated to have an average mean of 3.23% with a 95% confidence interval of the mean of 0.15%. The fit to the harmonic decay curve showed again a nonlinear decaying trend of damping with increasing response from 3.5% at $300N$ to 3.0% at $700N$.

The amplitudes of the 2-, 3- and 4-node modes were in the same order of magnitude, which are not expected to occur during wave impacts. The damping ratio was frequency dependent, i.e. a function of the mode shape. Strong nonlinear viscous effects, indicated by Hoffman and van Hoof (1976) at higher frequencies, were not evident from these tests.

5.2 Wave amplification and added resistance in waves

5.2.1 Measured and predicted wave amplification in the bow

The analytical estimate of the wave amplification in Section 2.1.2, Eq.(2.5), is compared with the measured relative motion at the bow. The results of ballast 2 condition are shown in the left plot of Figure 5.7. The analytical solution starts where the wave length was equal to the ship length, which implies large ship motions. Above $5rad/s$ the pitch and heave motion were insignificant. In general, the measurements yield somewhat larger values than the analytical linear estimate, but a few lower values are also observed. There are several reasons for the difference.

1. In the regular wave tests, a few of the highest waves struck the flare area causing an artificial increase in the relative motion, since the change to non-vertical side was not accounted for in the calibration of the relative motion sensor. It was relevant for wave heights of $3.5m$ and above, with frequencies supposed to excite springing by sum frequency effects.

2. Some water jets or run ups were observed.

3. In short waves it appeared to be a strong interaction between the steady and unsteady wave field causing breaking front waves and slamming (hypothesis 1), especially for the steeper incident waves. The water spray in particular at the bow quarter exceeded occasionally the deck level, which was $16m$ above the still water level, even though the wave height was less than $2.1m$.

4. Lower/higher speeds than 15 *knots* were also considered for the wave frequencies supposed to excite the linear and second order resonance. This explains a few of the lower/higher values.

A similar difference between analytical estimates and measurements is displayed in the right plot of Figure 5.7, which presents the results for cargo 2 condition. The bow had no flare and the speed was reduced to $13.2kn$. The maximum exceedance of the measured compared to the analytical wave amplification is in the order of 20% for both loading conditions. The uncertainties in the wave amplitudes increase somewhat for the shorter waves as illustrated in Appendix B.5.3, still the linear analytic estimate of the amplification can be considered as a good first approximation for the surface motion which may cause impacts (related to hypothesis 3).

The nonlinear contribution appeared to be moderate, but some sum frequency effects were observed at e.g. the wave lengths supposed to excite springing by sum frequency effects. Figure 5.8 illustrates the sum frequency effect in the spectrum and time series for a wave supposed to excite linear springing. The rise up of water in the bow is more rapid than the decay (third order effects were also present). The sum frequency effect in the bow is larger than observed for the wave elevation amidships.

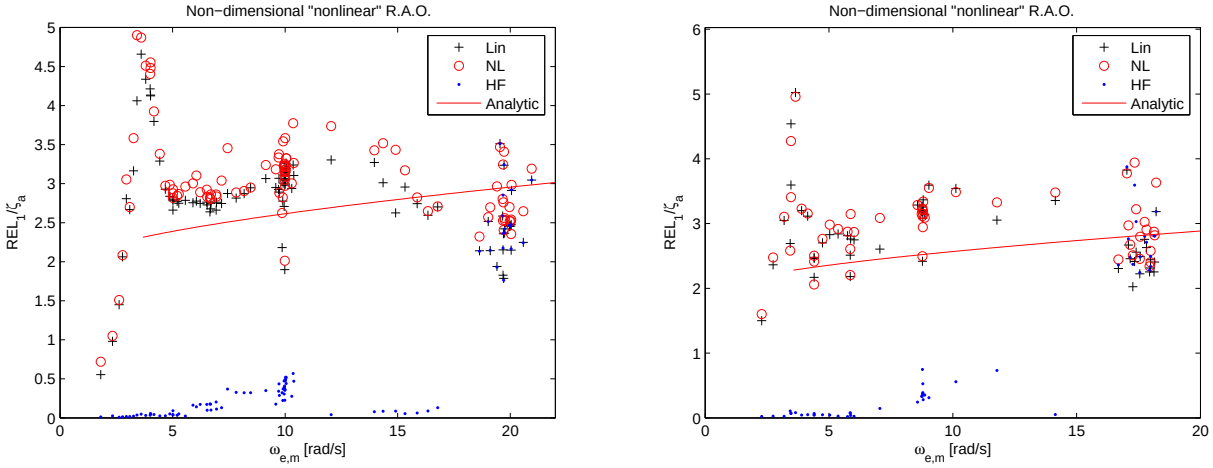

Figure 5.7: *Nondimensional measured relative motion and analytical wave amplification, Eq.(2.5), in the bow of ballast 2 condition in 15kn (left) and cargo 2 condition in 13.2kn (right).*

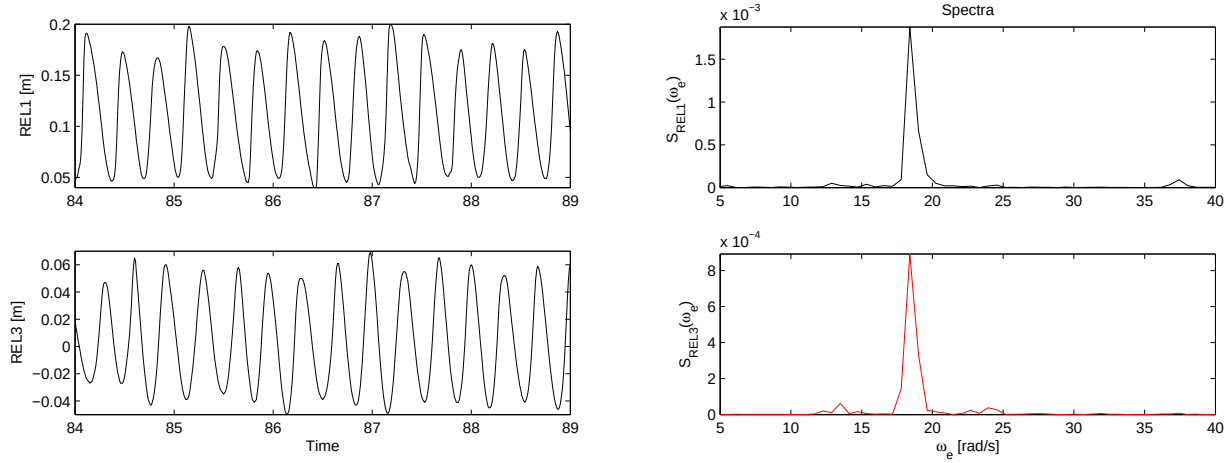

Figure 5.8: *Unfiltered time series (left) and spectra (right) of the relative motion in the bow (upper) and midship (lower) in ballast 2 condition, $H = 2.1m$, $T = 4.2s$ and $U = 15kn$ (run1508).*

5.2.2 Measured and predicted added resistance in head waves

Added resistance in waves is partly related to the relative motion in the bow and stern. In Section 5.2.1 the measured amplification (relative motion) in short waves was found to exceed the analytical estimate. If the measured exceedance compared to the analytical formulation of the amplification was due to bulk water rather than water spray, the measured added resistance would also be expected to exceed the analytical estimate.

The added resistance in waves was predicted by deducting the calm water resistance from

the total resistance. The measured calm water resistance is listed in Table 5.3. No wire was applied to initiate turbulence for bow 2 and 3, and may explain the increased calm water towing resistance compared to bow 1. The calm water towing resistance for bow 3 was higher partly due to larger wet area. It was expected that the calm water towing resistance in cargo condition was higher than in ballast condition due to larger wet area, but the opposite is observed for bow 1. The measured calm water towing resistance in ballast 2 condition was larger than measured in small regular waves, and it was corrected approximately based on the difference obtained from ballast 1 condition ($0.2N$). Ballast and cargo 3 condition did not have transverse lines. The effect of the transverse supporting lines is indicated by comparing the ratio of ballast and cargo 3 condition with the other two bow designs. The effect is significant.

Table 5.3: *Measured calm water towing forces (CWTF). The numbers in parenthesis indicate adjusted values to other speeds assuming a speed square relation. Mean towing forces obtained in small amplitude regular waves are also displayed for comparison.*

Load. cond.	CWTF $[N]$	U $[m/s]$	Comments
Ballast 1	55.4 / 55.6	1.30	run1220 calm water / run1010 in small waves
Cargo 1	20.8 (46.6) / 35.9	0.87	run1433 (adjusted to 1.30) / 1.15 run1301-3; small waves
Ballast 2	61.3 (58) / 58.4	1.30	run9813 (corrected) / run1500-2; small waves
Cargo 2	49.3 (63.0) / 51.4	1.15	run9864 (adjusted to 1.30) / run1700-2; small waves
Ballast 3	66.5 / 67.2	1.30	run9884 / run2323-5; small waves
Cargo 3	62.7 (80.1) / 65.6	1.15	run2222 (adjusted to 1.30) / run2100-1-3; small waves

Figure 5.9 shows the results of ballast and cargo 2 condition. The analytical estimates show some resemblance to the mean value of the measurements, but the uncertainties are considerable. Several factors contributed to the uncertainties.

1. Faltinsen (1990, pp. 146) illustrated that the added resistance in waves was sensitive to the exact bow shape. The analytical formulation was based on a circular cylindrical bow, while the actual bow shape was more elliptic, which will reduce the resistance.

2. Baba (1976) illustrated that the effect of breaking steady waves differed in ballast and cargo condition, indicating that the interaction with the steady potential differed.

3. The added resistance in small short waves was small (e.g. $1N$) compared to the calm water towing resistance (e.g. $50N$), and improper zero setting of the towing force introduced a large uncertainty in the nondimensional added resistance in waves. E.g., $1mm$ surge corresponded to $4N$ assuming a towing spring stiffness of $2000N/m$ at bow and stern.

4. The same uncertainty as in point 3 was introduced in case improper zero setting was carried out prior to calm water testing, used to obtain the calm water towing resistance.

5. The calm water resistance was obtained at a different speed than considered in regular wave tests for cargo 1 condition. The calm water resistance was adjusted by a U^2

relation (speed square) to obtain a value to be used as input to the estimate of added resistance in waves.

6. The transverse supporting lines contributed to the longitudinal forces when the model moved, or when they were not perfectly transverse. They were skipped in ballast and cargo 3 condition without loosing directional stability.

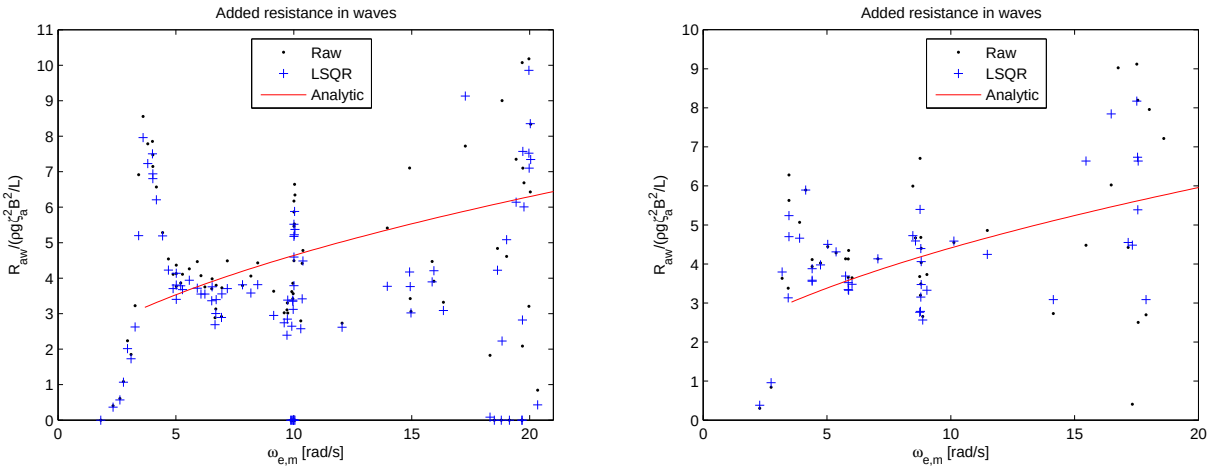

Figure 5.9: *Nondimensional added resistance in waves for ballast (left) and cargo 2 condition (right) in 15kn and 13.2kn.*

The peak value of the nondimensional added resistance in waves due to the rigid body response was about 8.5 for ballast 2 and 6 for cargo 2 condition as seen in Figure 5.9. The assumed nondimensional value in the calculation of the speed reduction in Section 2.1.5 was 8.75. Considering the uncertainties, the discrepancies are considered acceptable.

Figure 5.10 shows the nondimensional added resistance in waves for bow 3 in ballast and cargo condition. The agreement between the analytical solution and measurements for this wedge bow with half apex angle of 36^0 was improved as seen in Figure 5.21. The rigid body response was similar to the blunt bow with a nondimensional maximum of 10 in ballast and 9 in cargo condition. The maximum may have been affected by wall interaction. Bow 3 had less added resistance in waves, accordingly, the involuntary speed reduction in short waves will be less than compared to the blunt bows.

The measured relative motion exceeded the analytical estimate, but a similar difference was not observed for the added resistance in waves. This fact suggests that the measured exceedance of relative motion was not related to bulk water.

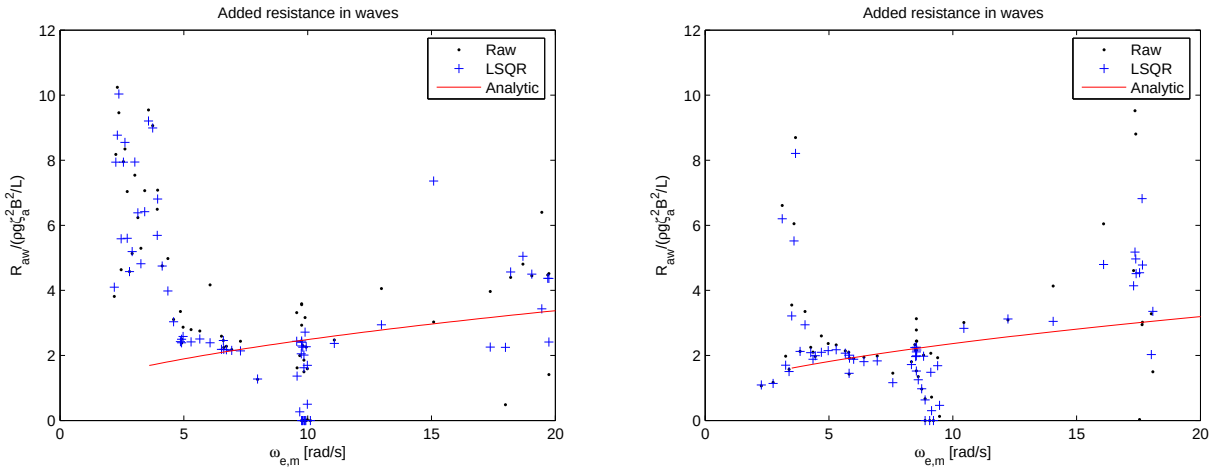

Figure 5.10: *Nondimensional added resistance in waves for ballast (left) and cargo 3 condition (right) in 15 and 13.2kn.*

5.3 Transfer functions

5.3.1 Linear and 'nonlinear' transfer functions

The ballast 2 condition is considered in this section, while the other test results are presented in Appendix C.1. The 'nonlinear' transfer function is compared to the linear and the high frequency contribution. The linear transfer function refers to a response that is proporsional to the wave amplitude, while the 'nonlinear' transfer function may have perturbations proporsional to the wave amplitude squared etc., but it is still made nondimensional with respect to the linear wave amplitude (at the encounter frequency). The high frequency contribution is mainly the result of the filtered vibration response. The linear (Lin), 'nonlinear' (NL) and high frequency (HF) part are illustrated for the heave and pitch motion in $15kn$ in Figure 5.11. The high frequency contribution to the nonlinear response is small, but some flexible response is observed in heave at the first and second harmonics, due to the location of the motion sensors. In high and long waves, the ship motions were influenced only slightly by nonlinear forces. In heave, the apparently nonlinear effects in short waves were due to poor resolution ($1mm$) of the measured heave motion and possible disturbances.

The shear force transfer functions are presented in Figure 5.12, the bending moments in Figure 5.15, the accelerations in Figure 5.16 and the pressures in Figure 5.17. In general, the higher harmonics are visible, and the first, second and third order resonance are pronounced. The higher harmonics have significant contribution from the high frequency response, which occur between 19 and $22rad/s$. The higher harmonics are also observed outside resonance, e.g. for the shear force at cut 5 between 6 and $10rad/s$. The second harmonic relates to the hypothesis of second order contribution from bow reflection (hypothesis 4). The higher order harmonics with high frequency vibration response relates

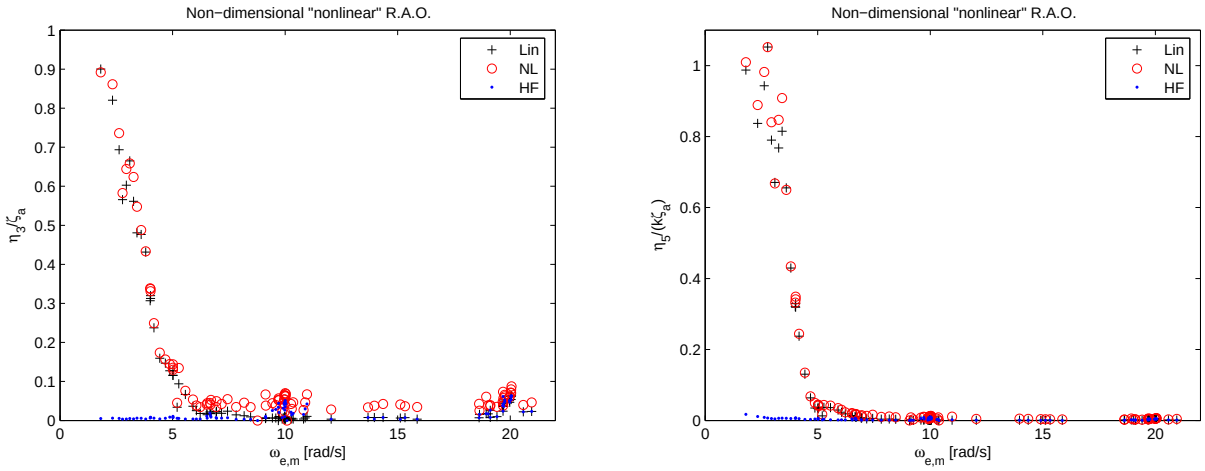

Figure 5.11: *'Nonlinear' transfer function of heave (left) and pitch (right) in ballast 2 condition. 'Nonlinear' refers to the peak process of the total signal made nondimensional as in linear theory.*

mostly to the bow impact hypothesis. It should be noted that for e.g. the monochromtic sum frequency effect (second order) the displayed 'nonlinear' response refers to different incident wave heights. Thereby, for the same frequency the 'nonlinear' response amplitude will vary.

The relative contribution of the springing in the shear forces in Figure 5.12 is higher in the aft than in the fore ship, due to higher flexible response and lower rigid body response. At the forward cross section between the first and second harmonic, the difference between the linear and 'nonlinear' response exceeds the high frequency contribution, indicating the importance of the second harmonic from hypothesis 4. Figure 5.13 presents the time series and spectra of the shear forces at the aft and forward cut in short regular waves. The second and third harmonics do not coincide with the resonance frequencies, and they are pronounced despite the small incident waves. The nonlinearities in the forward cut exist even though the geometry at water line is close to vertical. The observation agrees with the excitation forces measured in short waves by Moeyes (1976). He indicated a small nonlinear behaviour in the bow of a tanker, but also at some wall-sided midbody sections. The second order effect in the aft ship is also pronounced in Figure 5.13, but it is unclear if this is caused by the inertia as an overall effect, or by the second order effects due to nonlinear geometry in the stern part. From Figure 5.14, the pressure in the bow area has a stronger second order effect than measured in the pressure at the stern. This indicates that the second order contribution to the shear force in the stern part is at least not significantly contributed by sum frequency effects from excitation pressure locally.

The relative importance of the linear and second order effect at resonance compared to the rigid body response peak are displayed for the three quarter lengths in Figure 5.15. The rigid body response at the forward quarter length is about 2/3 of the midship moment,

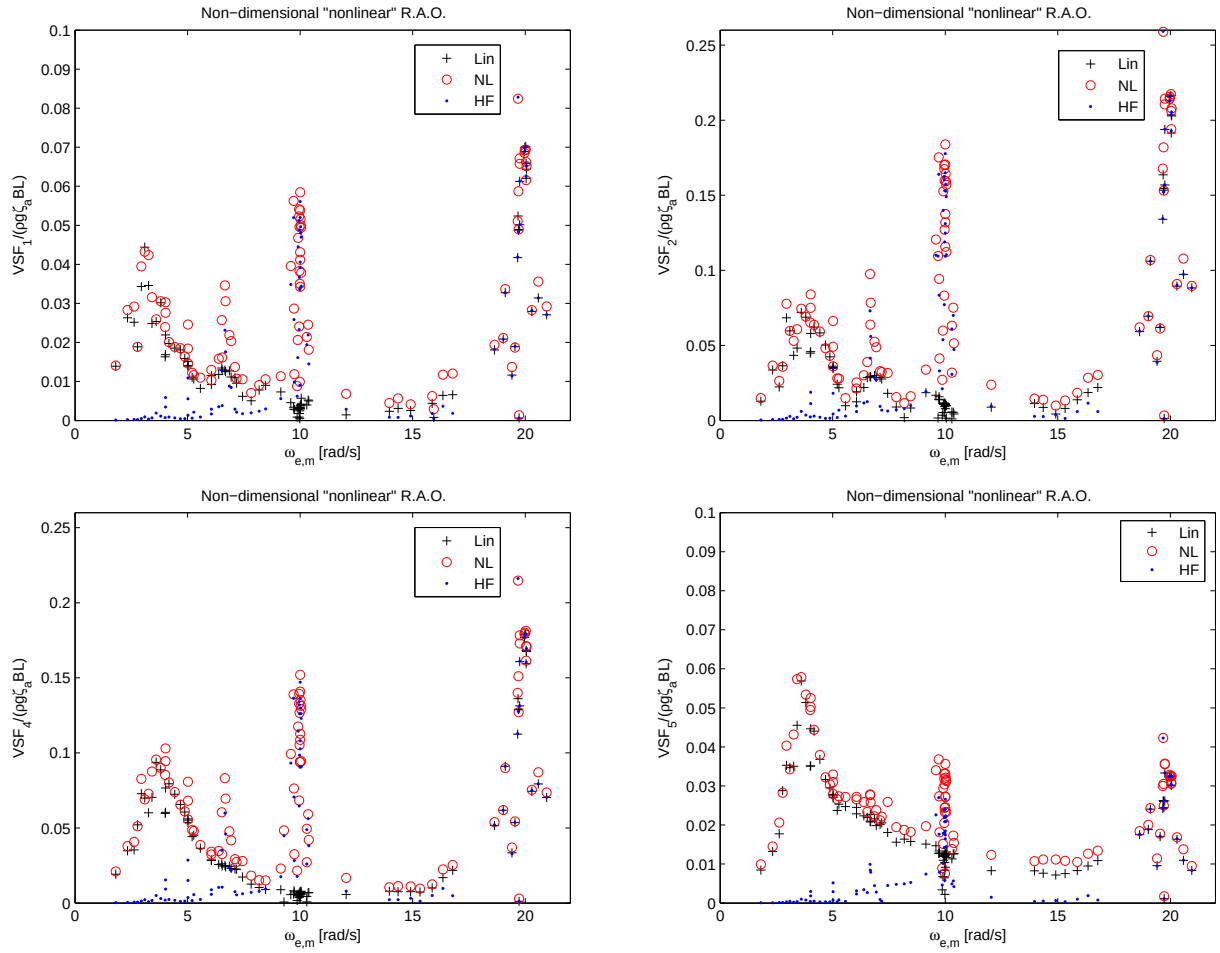

Figure 5.12: *'Nonlinear' transfer function of shear forces from aft (upper left) to fore (lower right) in ballast 2 condition.*

while the linear springing response is about 1/3 compared to the midship section. For the aft quarter the ratio compared to amidships is apparently about 1/3 for both the rigid body response peak and the springing peak. The relative importance of the 2-node springing is then indicated to be about equal at the aft and midship section, while it is lower at the forward quarter length. This has to do with the envelope of the rigid body response along the ship compared to the 2-node bending moment distribution. The former is due to traveling wave loads passing through the ship, while the latter comes from a stationary vibration mode.

The pressure from the rigid body response increases towards the bow, while the vibration pressure decreases in Figure 5.17. The excitation pressure at the resonance is not significantly larger in the resonance area than outside, hence the measured pressures at linear and sum frequency resonance were apparently a consequence of the vibration, rather than a cause of it, and the sum of the radiation and restoring pressures appeared to be large. The

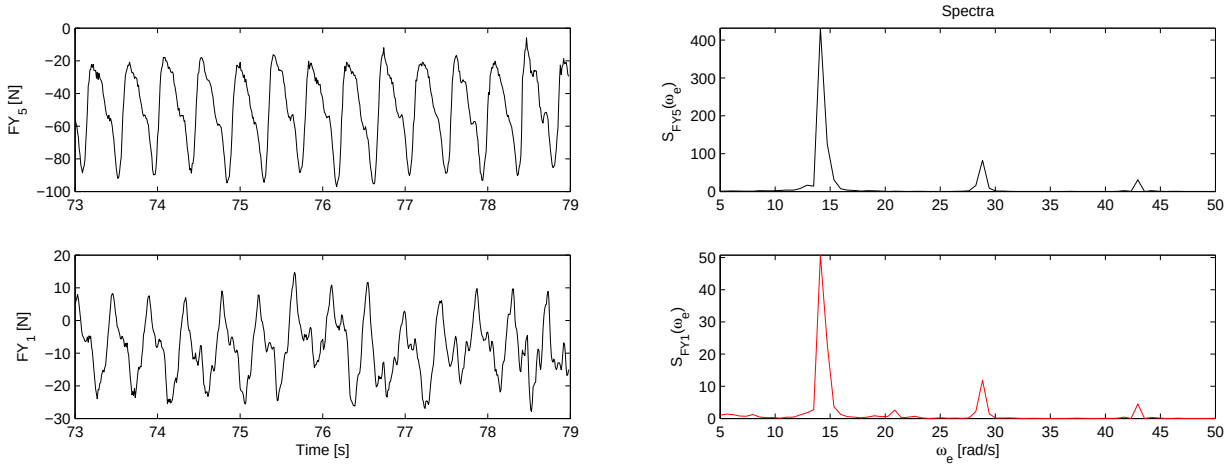

Figure 5.13: *Time series and spectra of shear forces at forward (upper) and aft (lower) cut in ballast 2 condition (run1550, 15kn, $H = 2.1m$, $T = 5.09s$).*

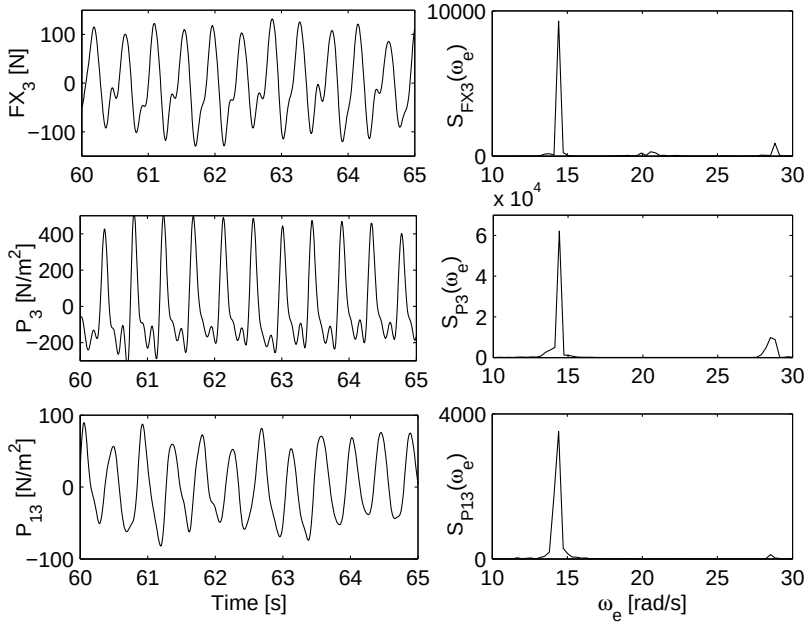

Figure 5.14: *Time series and spectra of moment at midship (row 1) pressure at stem (row 2) and pressure below stern at centre line (row 3) in regular waves (run1550, 15kn, $H = 2.1m$, $T = 5.09s$).*

restoring pressure can be roughly estimated by ρg times the vertical acceleration divided by the frequency squared in regular waves. This constitute only a part of the difference between the total pressure in resonance and outside resonance, hence the dominating part of the difference is due to radiation pressure, which in general is small, but was not small in the presences of wave induced vibrations. The 'nonlinear' and linear pressure differ in

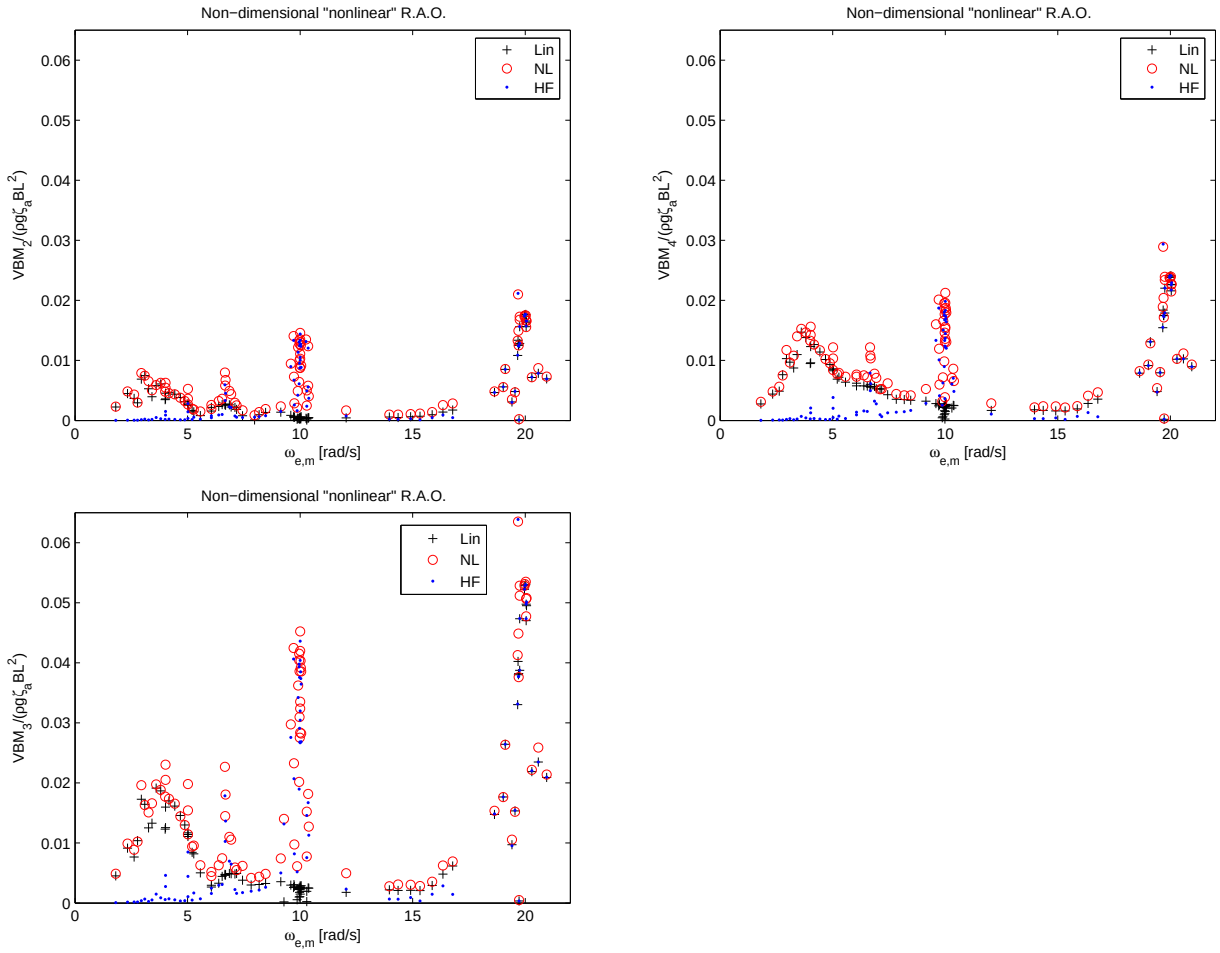

Figure 5.15: *'Nonlinear' transfer function of bending moments in ballast 2 condition. Upper left= Aft, upper right= Forward and lower= Midship.*

general at high frequencies and low pressures (outside resonance). In between the linear and second order resonance, the factor is close to two. The second order excitation pressure from reflection contributed (hypothesis 4), but the low pressures were also affected somewhat by poor resolution. Figure 5.18 presents the time series and spectra of the pressure in the stem and below the bow. The pressures are not sinusoidal as the incident waves. Higher harmonics are present and the fourth harmonic coincides closely with the 3-node resonance in this case. The second, but also the third harmonics, are significant. The non-sinusoidal behaviour of the stem pressure seems to be apparent also in the low bottom pressures, even though the quality of the bottom pressure is poor.

A method employed to separate the excitation pressure from the remaining pressure failed. It was based on evaluation of pressure from decay tests in calm water, and 'deducting' this from the total pressure in the regular wave tests. The remaining part was expected to be the excitation pressure, but the method was not found reliable.

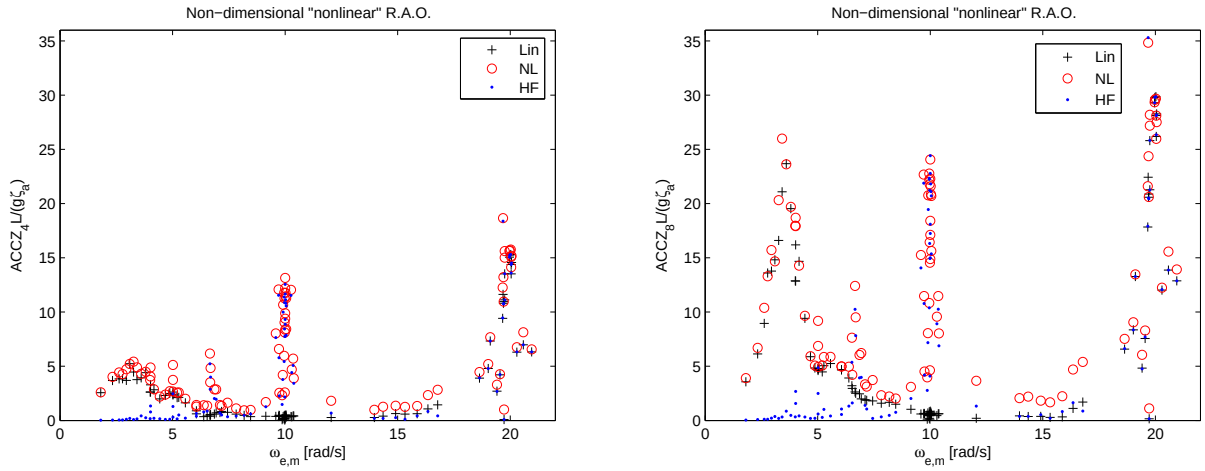

Figure 5.16: *'Nonlinear' transfer function of vertical acceleration at midship (left) and bow (right) in ballast 2 condition.*

The vertical acceleration in Figure 5.16 displays the relative importance of the acceleration due to resonance and due to the rigid body motions. In this case, actually the relative importance is more important amidships, where there is the contribution from pitch is close to zero.

The behaviour of the linear and second order resonance versus speed were investigated. The midship bending moment is displayed in Figure 5.19. The second order resonance remains high for a considerable change in the speed, while the linear part is more sensitive to speed. The second order resonance is still significant at zero speed. The quality of the vibration response was, however, observed to be poor, i.e. the vibration was not very regular at low speeds due to disturbances and reduced wave quality. The reduction in the linear part was partly due to deficient wave quality, and only a moderate speed reduction was possible. It was difficult to measure a quantity that proved the importance of the hypothesis 1 related to the interaction of the steady wave field. The results, however, suggest that the linear springing is more sensitive to speed than the second order springing excitation. This may be caused by two effects: A) The second order excitation may be more localised to the bow region and not affected by oscillations along the hull, and B) the linear springing excitation may be more affected by the steady wave interaction. The hump-hollow behaviour versus speed was indicated by Hoffman and van Hoof (1976) in high speeds. This was not evident here, in particular not for the sum frequency effect, suggesting again that it is a local effect. Few repetitions, wide frequency spreading of the regular waves, inaccurate estimates of the resonance peaks at varying speed, and low speed introduce uncertainties. The sensitivity to speed in these model tests contradicts the findings by Slocum and Troesch (1982), who indicated that the linear springing was less sensitive to speed. Still, due to the pronounced difference in the current model tests, the sum frequency effect is still considered to be less sensitive to speed compared to linear springing in this case.

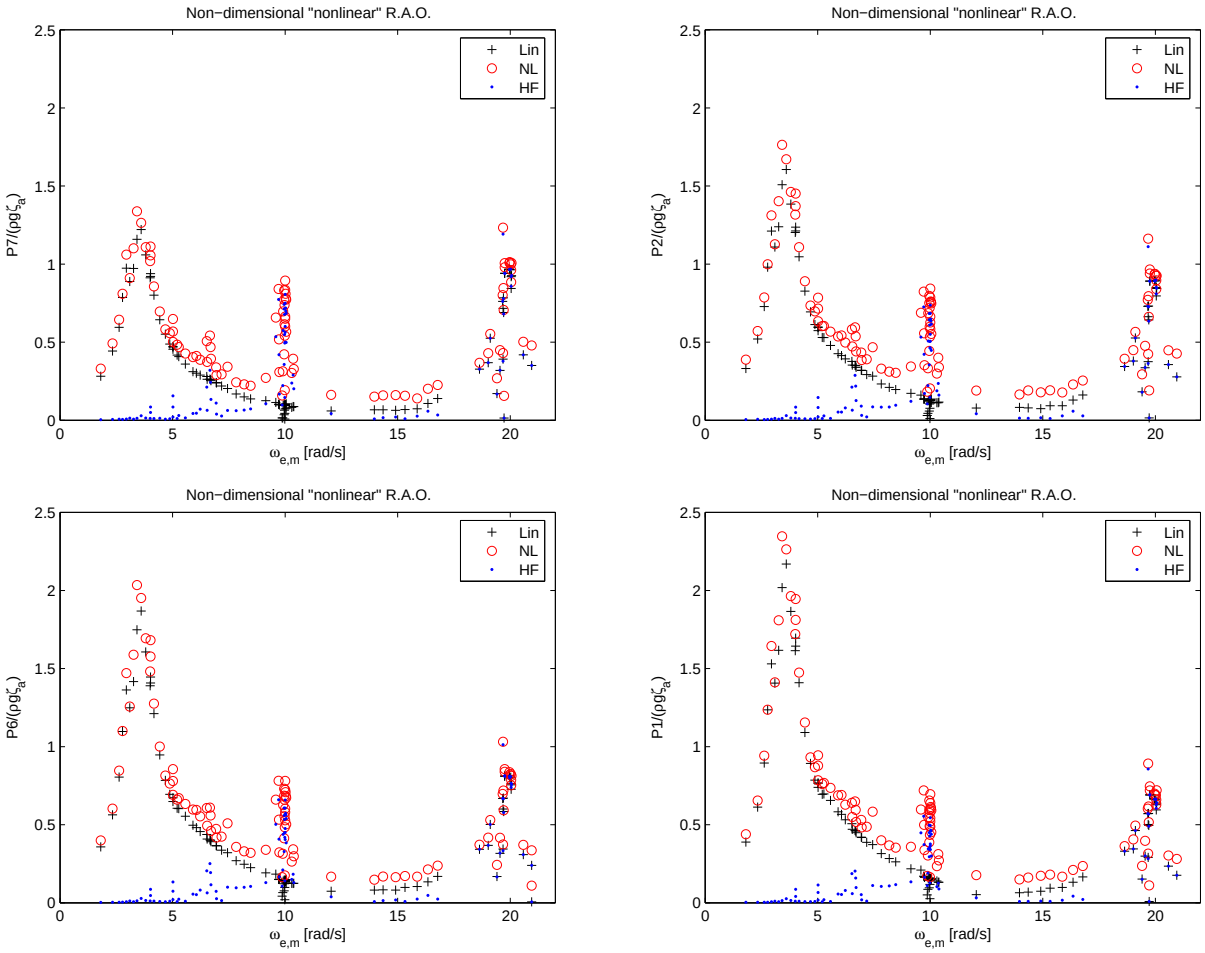

Figure 5.17: *'Nonlinear' transfer function of bottom CL pressures in ballast 2 condition. Upper left=0.92L_{pp}, upper right=0.95L_{pp}, lower left=0.96L_{pp}, lower right=0.97L_{pp}.*

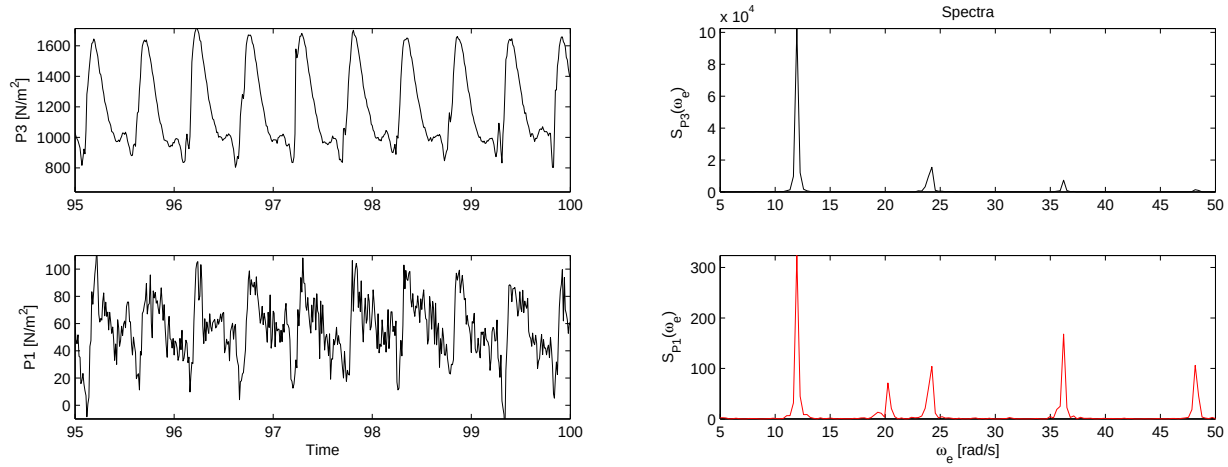

Figure 5.18: *Time series and spectra of stem (upper) and bottom (lower) CL pressure of ballast 2 condition (run1551, 15kn, $H = 2.1m$, $T = 5.75s$, outside resonance). Stem pressure is taken at FP, 10m above BL, while bottom pressure is taken at $0.97L_{pp}$ outside resonance.*

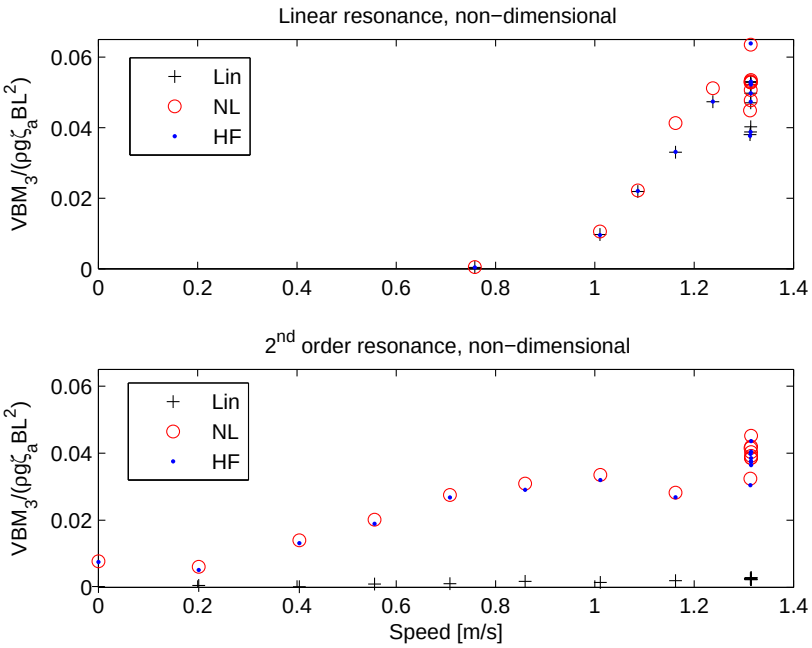

Figure 5.19: *Nondimensional bending moment amidships in ballast 2 condition at linear (upper) and second order (lower) resonance versus speed. $H = 2.1m$ is used for the second order excitation.*

5.3.2 Measured second order transfer functions

Many wave frequency combinations can cause sum frequency excitation. The sum frequency resonance response as a function of the frequency difference of the bichromatic waves was investigated. Results for ballast and cargo 2 condition are presented in this section, while result plots for other loading conditions are presented in Appendix C.2.

Figure 5.20 presents the nondimensional second order transfer function of the bending moment at the midship section, $|H(\omega_{1,e}, \omega_{2,e})|$. The sum frequency responses from the least square fit and from the standard deviation of the filtered time series are similar. The peak process of the raw time series, which includes the encounter response, gives higher estimates. The maximum encounter and sum frequency response appear to add up to the maximum nonlinear response. The sum frequency response of the filtered time series is considered in the following.

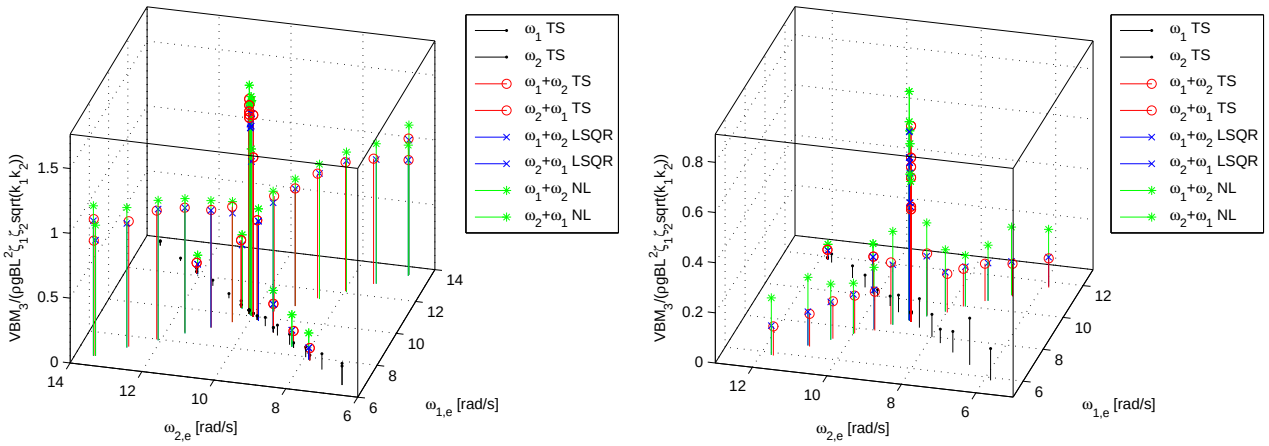

Figure 5.20: *Nondimensional second order transfer function for ballast 2 condition (left) and cargo 2 condition (right) in 15 and 13.2kn. The methods to obtain the various responses, TS (time series), LSQR (least square fit) and NL (nonlinear), are outlined in Section 4.6.3.*

The nondimensional response was larger in ballast 2 than in cargo 2 condition, but the damping differed. The damping ratio in ballast 2 condition was 1%. By correcting the response level of the bichromatic waves in cargo 2 condition, corresponding to a reduction in the damping ratio from about 1.8% to 1%, the nondimensional level increased from 0.1 to 0.2, which was still lower than in ballast 2 condition. Similarly, the monochromatic peak in cargo 2 condition corresponded to a damping ratio of 2.5%, and adjusted down to 1%, the nondimensional value became 2.0, which was higher than in ballast 2 condition.

The bichromatic response is apparently constant in Figure 5.20. The trend of $|H(\omega_{1,e}, \omega_{2,e})|$ away from the diagonal, $|H(\omega_{1,e}, \omega_{1,e})|$, differs slightly in ballast and cargo 2 condition. For

a small frequency difference of the bichromatic waves, the springing response became beat shaped when the model ran into the periodic wave clusters. The nondimensional response was based on the time series covering both the beats and the 'dead zones'. This behaviour in combination with the change of damping at different vibration level may explain the difference in ballast and cargo 2 condition close to the monochromatic peak.

The nondimensional second order bending moment for the monochromatic and bichromatic waves are compared in Table 5.4. Since the damping varied, a correction has been made to the measured response, which was corrected to a damping ratio of 1% for comparison with ballast 2 condition. The damping, taken from Table 5.1, was estimated at different response levels in Figure 5.20, Figure C.5 and Figure C.6. Typical response levels are indicated together with the corresponding damping and the corrected nondimensional second order bending moment in Table 5.4. The nondimensional second order transfer function should be basically independent of the wave heights squared, but for reference, the wave heights of the bichromatic waves are included in parenthesis in Table 5.4. For the monochromatic peak the wave heights in most cases was twice the individual wave heights of the bichromatic waves. The following observations are made:

- The monochromatic level is higher in ballast than in cargo condition except for bow 2.
- The difference of the monochromatic response for bow 2 indicates that the draft does not play an important role, but the draft appears to be more important for the bichromatic waves.
- The difference in the monochromatic response for bow 1 and 2 may be caused by the submerged bulb, which may reduce the sum frequency bottom pressure.
- The whipping contribution from the stem flare in cargo 1 condition appears to be small (when compared to cargo 2 condition without stem flare).
- The monochromatic response of bow 3 is smaller due to reduced reflection, but the effect does not vanish. This may partly be explained by the fact that the steady wave pattern around the pointed bow was more elliptic, and because of interaction with the steady pattern still some waves were reflected back as illustrated in Figure 5.21.
- In general, the bichromatic response is higher in ballast than in cargo condition. The difference is small except for bow 2.
- The bichromatic response for bow 1, 2 and 3 in ballast or cargo condition displays only a moderate difference, except in ballast 2 condition.

Uncertainties were introduced due to the nonlinear damping, nonlinear stiffness in ballast 1 condition and inaccurate resonance conditions away from the diagonal. Second order incident waves may also contribute, but this effect should be small as the incident waves are not very steep.

Table 5.4: *Nondimensional second order bending moment for different bow designs for bichromatic (B) and monochromatic (M) waves. The numbers in parenthesis for the bichromatic waves refer to the wave heights in full scale.*

Load. cond.	B Resp. [N]	B δ [%]	B $\overline{VBM}$	M Resp. [N]	M δ [%]	M $\overline{VBM}$
Bal. 1	250 (2x0.7m)	0.7	0.4	400-550	1.0	1.2
Cargo 1	150 (2x1.0m)	1.0	0.2	300-400	1.6	1.0
Bal. 2	600-1000 (2x1.05m)	1.0	1.0	1500	1.0	1.6
Cargo 2	100 (2x1.05m)	1.8	0.2	400-700	2.5	2.0
Bal. 3	700-800 (2x1.75m)	1.2	0.4	800-1600	1.0	0.9
Cargo 3	175 (2x1.75m)	3.3	0.3	500-700	1.9	0.6

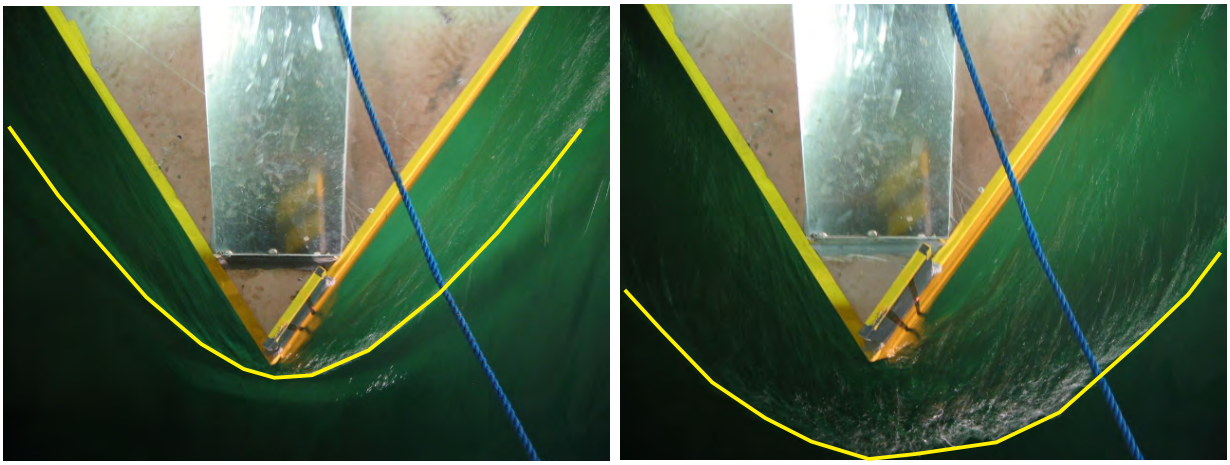

Figure 5.21: *Pictures of bow reflection (including radiation) for bow 3. The half apex angle is roughly* 36^0.

The constant level of the sum frequency response away from the diagonal was earlier identified by Slocum (1983). The current monochromatic peak deviates from his finding. The ratio of the monochromatic to bichromatic response is (only) 1.6 in ballast 2 condition, but this ratio may depend on the ship design and sea conditions.

5.4 Wave and high frequency fatigue damage

Cumulative fatigue damage for longitudinal details in deck was calculated by Rainflow counting on the total and wave frequency pass filtered signal, which gave the total and wave frequency (WF) damage. The latter is also referred to as *wave damage*. The difference constituted the high frequency damage (HF) also referred to as *vibration damage*. A SCF of 2.0 was assumed with a two slope SN-curve for welded details protected from corrosive environment. Reduction in the fatigue damage due to the mean stress effects was disregarded. The vibration level was not corrected for the varying damping ratios measured in the six combinations of bow shapes and loading conditions.

5.4.1 Base case - vessel in selected sea states at full speed

The vessel was run in head sea at 15 and 13.2kn in ballast and cargo condition. The wave and vibration damage were determined from twelve sea states, shown in Figure 5.22 and Table B.10.

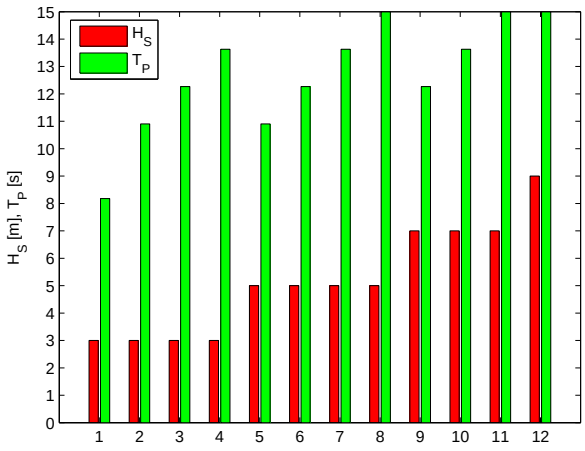

Figure 5.22: *Numbering of the twelve sea states (H_S=left and T_P=right) tested at full speed and used in the wave calibration.*

Figure 5.23 displays the relative importance of the midship wave and vibration damage, which were normalized by the total damage. Their sum is normalized as one for each sea state. The vibration damage contributes more in ballast than in cargo condition. The results differ only moderately with respect to bow geometry. *Bow 3 has less contribution from the vibration in sea states with short and low waves*, while in more severe sea states the difference is small. The reflection causing sum frequency excitation is reduced for the sharp pointed bow, while in more severe sea states whipping may contribute. The damping behaviour may also reduce the springing response for bow 3. Despite the geometry of bow 3 differs considerably from the blunt bows, no drastic change is observed in the relative magnitude of the overall vibration damage. In general, for a given wave height the vibration contribution reduces for increasing periods, while at a given peak period the vibration contribution increases for increasing wave heights. The latter indicates the increasing importance of nonlinear forces.

The fatigue damage ratios at the two quarter lengths are compared to the midship section in Figure 5.24 for ballast and cargo 2 condition. The aft and forward quarter length display the same trend as the midship section, but the relative importance is slightly changed, but not necessarily reduced at the aft quarter. This is consistent with observations and comments made to Figure 5.15 in Section 5.3.1.

Figure 5.23: *Ratio of WF (top) and HF (bottom) damage to total fatigue damage for midship section at full speed. Left= Ballast, right= Cargo. Row 1= Bow 1, row 2= Bow 2, row 3= Bow 3.*

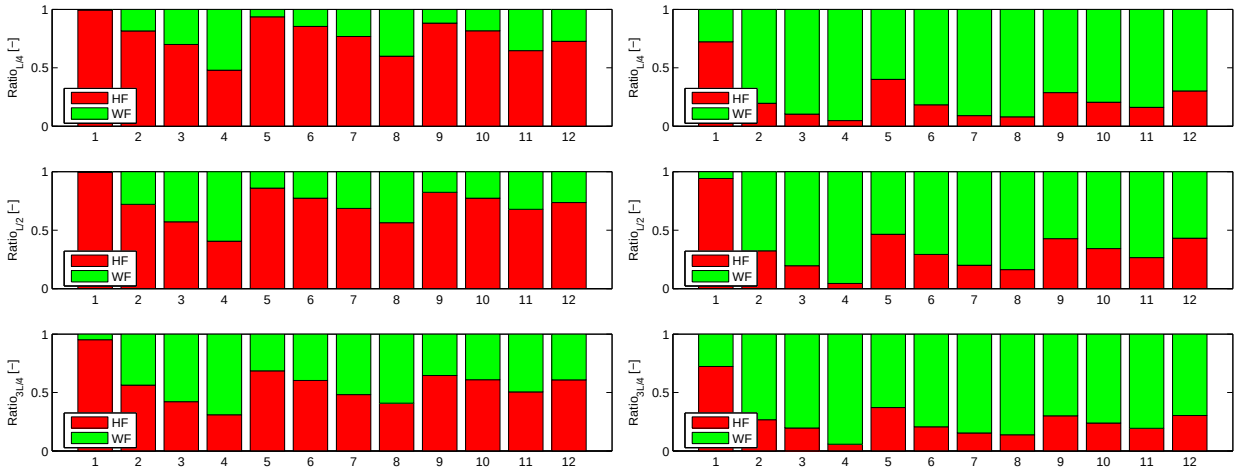

Figure 5.24: *Ratio of WF (top) and HF (bottom) damage to total fatigue damage at aft (row 1), midship (row 2) and forward (row 3) quarter length at full speed. Left= Ballast 2, right= Cargo 2 condition.*

The absolute value of the half hour fatigue damages at the three cross sections of ballast and cargo 2 condition are presented in Figure 5.25. The wave damage increases moderately from ballast to cargo condition, except at the aft quarter length which displays a higher increase. Even though the vibration damage is smaller in cargo than in ballast condition, it is still pronounced in the more severe sea states in cargo condition. Moreover, the vibration and wave damage increase rapidly with increasing wave height.

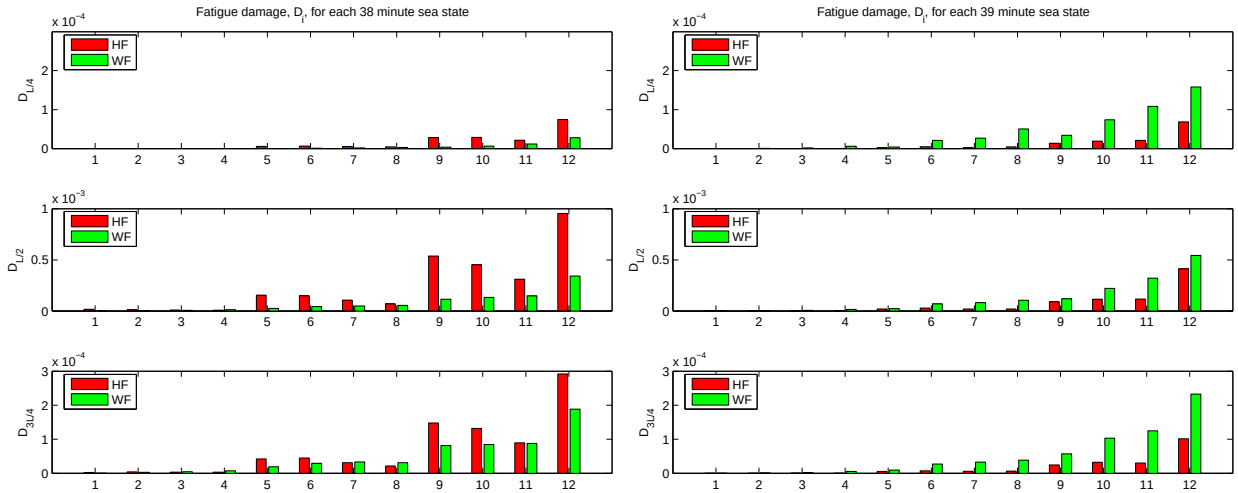

Figure 5.25: *HF (left) and WF (right) fatigue damage at full speed. Row 1= aft, row 2= midship, row 3= forward quarter length; Left = Ballast 2, right= Cargo 2 condition.*

The fatigue damage of the individual sea states was combined with the probability of occurrence in different trades. The fatigue damage in each sea state, assuming 10 years head

sea North Atlantic trade in ballast or cargo condition, is presented in Figure 5.26 for the three bows. The selected sea states have a total probability of occurrence of 26.8%. The 5 and $7m$ significant wave heights contribute more than the 3 and $9m$ waves.

The total fatigue damage from the twelve sea states is summarized in Table 5.5. The vibration damage in head sea at full speed constitutes roughly 1/4 of the total damage in cargo condition, and 2/3 in ballast condition. Ballast 2 condition has higher fatigue damage from the vibration, which may be explained by smaller damping and larger springing excitation. The wave damages in ballast and cargo condition are insensitive to the bow design accounting for the different ship length. The increase in wave damage from ballast to cargo condition is about 70%.

Table 5.5: *Cumulative fatigue damage for the vessel during 10 years head sea North Atlantic trade covering 27% of the sea states. The fatigue damages are based on full speed and SCF of 2.0 for coated details in deck at midship section.*

Fatigue damage	Cargo 1	Ballast 1	Cargo 2	Ballast 2	Cargo 3	Ballast 3
HF	0.5849	2.0101	0.6657	2.9617	0.5754	1.7744
WF	1.7039	1.0107	1.7029	1.1081	1.9457	1.0640
Total	2.2888	3.0208	2.3686	4.0698	2.5211	2.8384
HF contribution [%]	26	66	28	73	23	63

A first estimate of the fatigue life in North Atlantic trade considering bow 2 gave 1.4 years accounting for the probability of the sea states and 33% harbour time. Head sea was assumed in ballast condition for 33.5% of the time, and following sea was assumed in cargo condition the remaining time. In cargo condition the vibration damage was disregarded, and the wave damage in head sea was assumed to represent the wave damage in following sea. The contribution from the vibration damage constituted 51%. The North Atlantic *tanker trade* with prevailing following seas in cargo condition plus accounting for the mean stress effect in deck reduces the total damage and the vibration contribution compared to the *iron ore trade*.

5.4.2 Effect of speed reduction and wave environment

At full speed in the North Atlantic iron ore trade, the vibration damage was dominating. The realistic speed depends on the sea state, and the speed was estimated in Section 3.2. The involuntary speed reduction was considerable, and the speeds in Table 3.4 has been assumed in the following.

The fatigue damage at midship section in 19 North Atlantic head sea states with and without speed reduction is presented in Figure 5.27 based on ballast 2 condition (left plot). The vibration damage is reduced considerably in the more severe sea states due to the speed reduction. Only a small change is evident in the wave damage, which is influenced

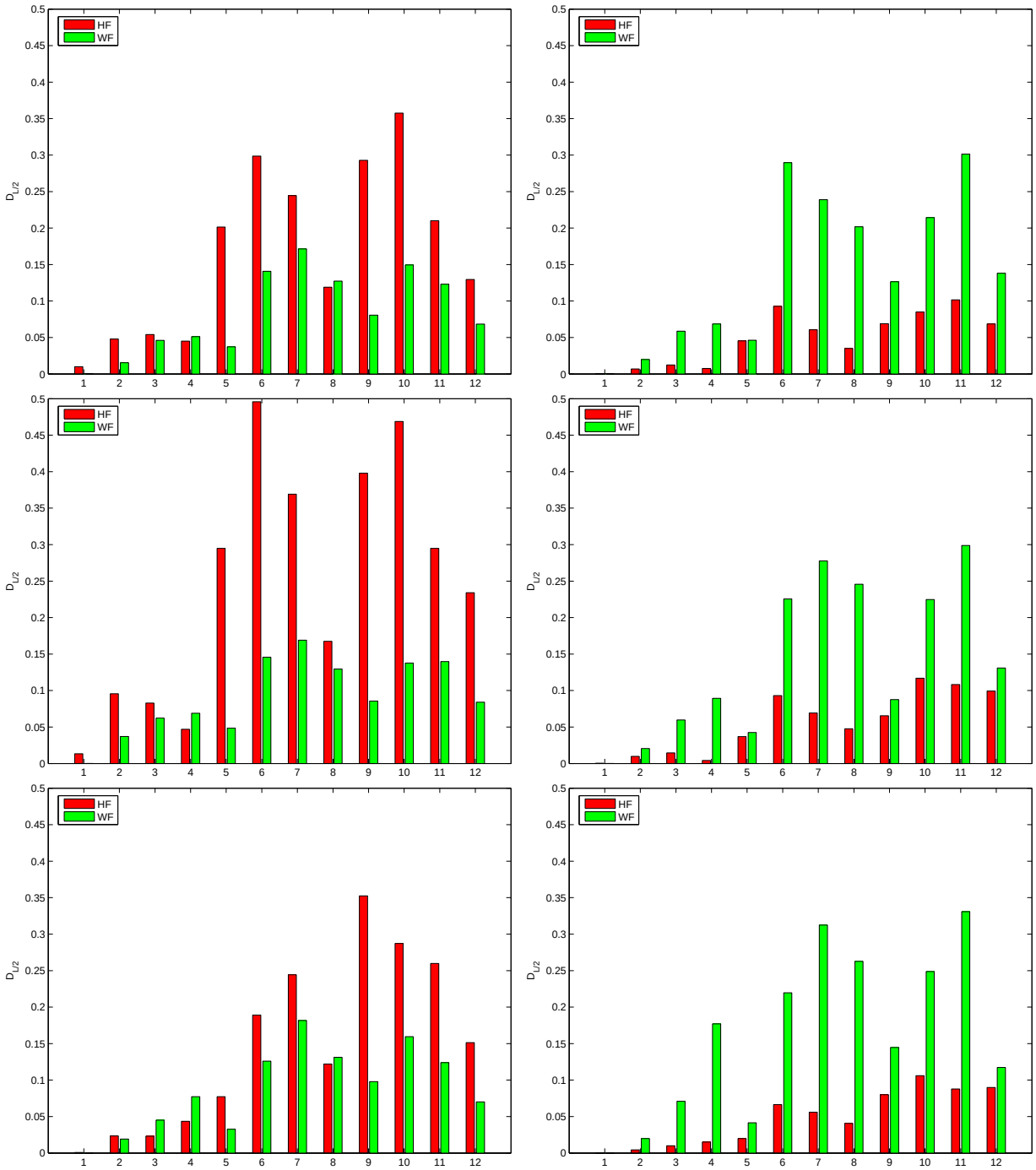

Figure 5.26: *HF (left) and WF (right) fatigue damage at midship section assuming 10 years head sea North Atlantic trade. Left column= Ballast, right column= Cargo condition, row 1= Bow 1, row 2= Bow 2, row 3= Bow 3.*

by wall effects at small speeds and for long wave periods. The small change represents, however, a reduction as expected, since the number of encountered cycles per time unit is

reduced. Therefore, the overall effect of the wall effects does not appear to be significant. The significant wave height that dominates the contribution to fatigue damage is reduced to $5m$, and the vibration damage is still pronounced.

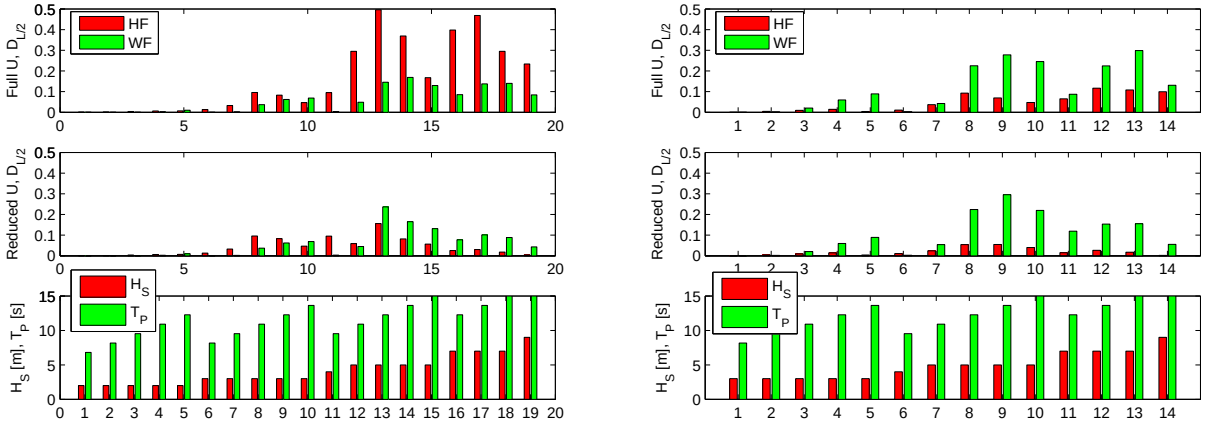

Figure 5.27: *Pairs of HF (left) and WF (right) fatigue damage in head sea North Atlantic trade for midship section of ballast 2 (left) and cargo 2 (right) condition. Row 1= Full speed, row 2= Reduced speed, row 3= Sea states.* $U = 10, 5, 0kn$ *in* $5, 7, 9m$ H_S.

The $9m$ sea state in ballast 2 condition was also tested at 15, 10, 5 and $0kn$, resulting in a standard deviation HF stress of 38.0, 20.1, 9.1 and 3.6MPa, respectively. The following curve, $3.6 + 0.26 \cdot U^{1.8}$ is a good fit, indicating that the vibration increases with the speed to the power of slightly less than 2. Considering the uncertainties, the slope is in some agreement with the factor of 2, which has been indicated in the literature, (Bell and Taylor 1968), but the vibration is still present at zero speed in agreement with (Gran 1974).

The effect of the speed reduction are presented in the right plot of Figure 5.27 for cargo 2 condition in 14 sea states. The same trends are observed as for ballast 2 condition, but the relative reduction in the vibration damage for the dominating sea states of $5m$ significant wave height appear as smaller than in ballast condition. The change in speed is however smaller, from 13.2 to $10kn$, and the vibration is small to begin with.

Table 5.6 presents a summary of the wave, vibration and total fatigue damage at full and reduced speed in the six combinations of loading conditions and bow shapes. Both the North Atlantic and World Wide trade are considered. The number of sea states and their probability of occurrence vary. The calculations were based on the same assumptions as in the previous Section 5.4.1. Several observations are made

- ⋆ The speed reduction reduced the vibration contribution in the order of 25 to 50%.
- ⋆ The contribution from vibration damage was about 15% in cargo and 40% in ballast condition in North Atlantic head sea trade.

- ⋆ The fatigue life for bow 2 with realistic speed, estimated in the same way as in Section 5.4.1 for North Atlantic trade, increased from 1.4 to 3.6 years. The vibration contribution reduced from 51 to 19%.
- ⋆ The tested sea states in ballast 3 condition had twice the probability of occurrence compared to ballast 1 condition, still the vibration contribution was not significantly altered.
- ⋆ The total fatigue damage was reduced significantly in World Wide trade compared to North Atlantic trade. By considering bow 2 and the same head sea conditions as in the North Atlantic, the fatigue life was increased from 3.6 to 6.6 years in the World Wide trade (a different heading profile in the World Wide trade may further increase the fatigue life).
- ⋆ The contribution from vibration damage increased in World Wide trade compared to North Atlantic trade. Considering bow 2, the vibration contribution increased from 19 to 25%.

The fatigue damage, fatigue life and vibration contribution in the North Atlantic trade were derived in the following way (for bow 2 with no HF damage in following sea in cargo condition):

$$\begin{aligned} D &= \frac{1.8953 \cdot 2 \cdot 0.335}{0.526} + \frac{1.451 \cdot 2 \cdot 0.335}{0.307} = 5.58 \\ \frac{20}{D} &= 3.6 \text{ years} \\ \frac{D_{HF}}{D}100 &= \frac{\frac{0.8185}{0.526} \cdot 2 \cdot 0.335}{D}100 = 19\% \end{aligned} \tag{5.1}$$

The cut off frequency for noise in full scale was set at $2.0Hz$, which means that the 2-, 3- and 4-node modes were included in the estimate of the HF damage. To estimate how much the 3- and 4-node mode affected the HF damage, the cut of frequency was taken at $1.0Hz$ in ballast 2 condition. This reduced the HF damage with less than 1% amidships and less than 6% at the quarter lengths at full speed. The effect at reduced speed was slightly smaller. It is seemingly not necessary to consider the higher order modes in the fatigue assessment of blunt ships when it comes to wave induced vibrations. If confirmed also for extreme loads, the sampling frequency and necessary storage capacity can be reduced.

5.4.3 Effect of changed trim

Lopes and Troymann (1989) reported a reduction in the springing stress of 10-15% by increasing the amount of ballast water in the fore peak tank. The sea states were possibly not stationary during this operation.

The effect of changed trim was explored in ballast 2 condition at full speed. $100kg$ was placed in the bow, resulting in an increased draft of $1.6m$ at FP, including increased mean

Table 5.6: *HF, WF and total fatigue damage in North Atlantic and World Wide trade for all combinations at full and reduced speed. The probability of occurrence of the tested sea states, and the contribution from the vibration damage are presented. 10 years of head sea trade was assumed in each combination. Extrapolation of results are based on direct time extrapolation of only the tested sea states.*

	North Atlantic			World Wide		
Combination	Full speed	Reduced speed	Probability [%]	Full speed	Reduced speed	Probability [%]
Ballast 1 HF	2.0101		26.8	0.9180		18.3
Ballast 1 WF	1.0107		26.8	0.4147		18.3
Ballast 1 Total	3.0208		26.8	1.3327		18.3
HF contribution[%]	67			69		
Cargo 1 HF	0.6003	0.2873	30.7	0.2626	0.1584	24.5
Cargo 1 WF	1.7100	1.4329	30.7	0.6851	0.6103	24.5
Cargo 1 Total	2.3103	1.7202	30.7	0.9477	0.7687	24.5
HF contribution[%]	26	17		28	21	
Ballast 2 HF	3.1095	0.8185	52.6	1.6042	0.6654	59.3
Ballast 2 WF	1.1277	1.0769	52.6	0.4977	0.5059	59.3
Ballast 2 Total	4.2371	1.8953	52.6	2.1018	1.1713	59.3
HF contribution[%]	73	43		76	57	
Cargo 2 HF	0.6811	0.2795	30.7	0.2830	0.1500	24.5
Cargo 2 WF	1.7076	1.4510	30.7	0.6726	0.6175	24.5
Cargo 2 Total	2.3887	1.7305	30.7	0.9556	0.7675	24.5
HF contribution[%]	29	16		30	20	
Ballast 3 HF	2.1585	0.9952	69.1/69.7	0.9412	0.5324	59.2/58.2
Ballast 3 WF	1.4599	2.1577	69.1/69.7	0.6407	0.9224	59.2/58.2
Ballast 3 Total	3.6184	3.1530	69.1/69.7	1.5819	1.4548	59.2/58.2
HF contribution[%]	60	32		59	37	
Cargo 3 HF	0.5791	0.2582	30.7	0.2205	0.1253	24.5
Cargo 3 WF	1.9493	1.8211	30.7	0.7765	0.7846	24.5
Cargo 3 Total	2.5283	2.0793	30.7	0.9970	0.9099	24.5
HF contribution[%]	23	12		22	14	

draft of about $0.35m$. The change was expected to increase the flare forces and reduce the bottom excitation, and the change in the vibration would indicate the dominating source. Four sea states were considered, corresponding to the steepest sea states tested at 2, 3, 4 and $5m$ significant wave height.

Figure 5.28 shows the ratio of the fatigue damage from the original draft to the increased draft at FP. The WF and HF damage ratios are displayed in pairs. In general, the ratios

are above one with one exception, which refers to the smallest sea state. The smallest sea state, $H_S = 2m$ and $T_Z = 5s$, with increased bow draft was run soon after a larger sea state, $H_S = 5m$ and $T_Z = 8s$, and the WF damage became affected by swell from the previous sea state.

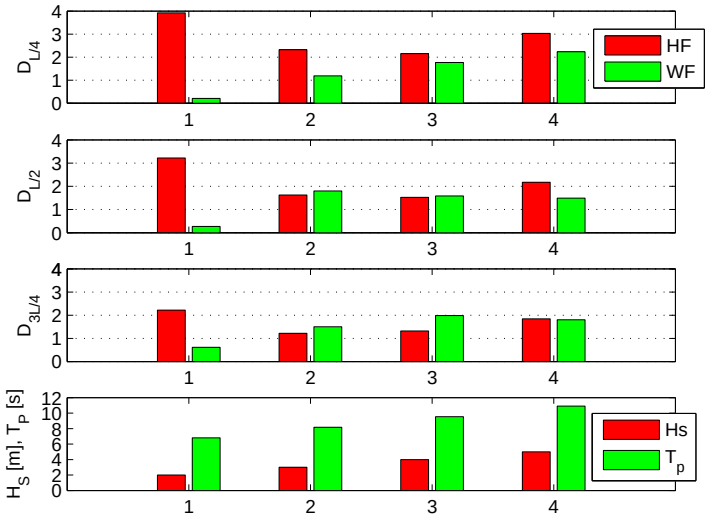

Figure 5.28: *WF (right) fatigue damage ratio of original to increased forward draft and HF (left) fatigue damage ratio, D, of original to increased forward draft in ballast 2 condition at aft (L/4), midship (L/2) and forward (3L/4) cross section. 4 sea states were considered as indicated on the abscissa axis: 1) $H_S = 2m, T_Z = 5s$, 2) $H_S = 3m, T_Z = 6s$, 3) $H_S = 4m, T_Z = 7s$ and 4) $H_S = 5m, T_Z = 8s$.*

The vibration damage ratio indicated that the bottom excitation reduced more than the increase of the flare force for increased forward draft. The WF damage was also reduced for increased draft/forward trim. To illustrate their relative magnitudes, the increase of the flare forces in the highest sea state of $H_S = 5m$ and $T_P = 10.9s$ was estimated according to the simplified analysis in section 3.1. By increasing the draft at FP with $1.6m$, the standard deviation nominal stress in deck of the vibration response increased from $0.8MPa$ to $1.4MPa$, while the measured stress reduced from $10.8MPa$ to $7.3MPa$. The reduction in the springing stress was therefore significant, and the whipping contribution was relatively small in this sea state (and the simplified calculations certainly lack the important excitation source). The measured vibration stresses from the original and increased forward draft are presented in Figure 5.29. The whipping events also appeared to be reduced, indicating that the excitation sources were located at the bottom (bilge) flare rather than at the stem/bow flare.

Even though only a few sea states were considered, the finding suggests that *changing the operational condition slightly may be effective in order to reduce unacceptable fatigue loading* of such ships designs. Fuel consumption is another matter.

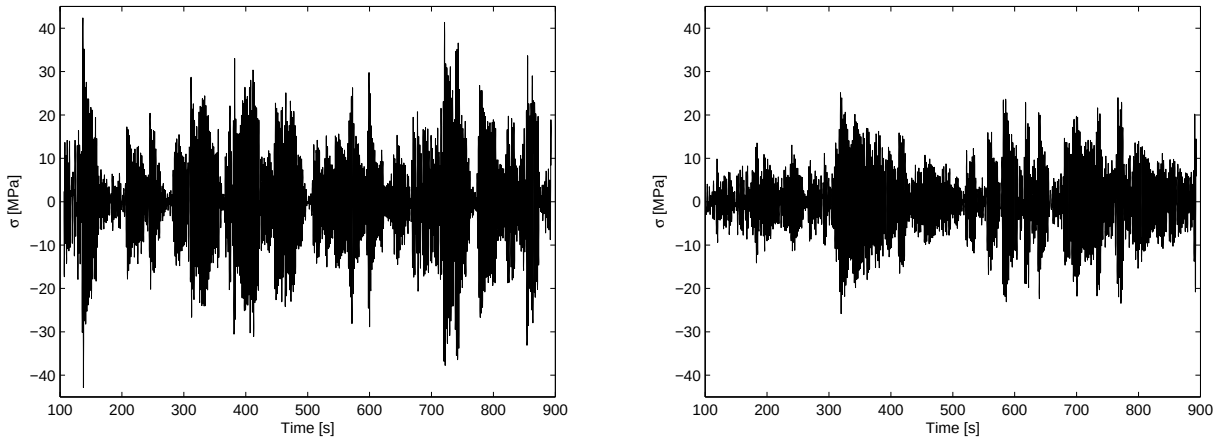

Figure 5.29: *Nominal vibration stress in deck amidships for original (left, run1600) and increased draft at FP (right, run1660). $H_S = 5m$, $T_P = 10.9s$ and $U = 15kn$.*

5.4.4 Wave conditions along the tank and the disturbance from the vessel

The waves in irregular sea states were calibrated as described in Appendix B.5.4. The presence of the large vessel caused scattering, and the continuous runs performed in irregular seas implied disturbances and residual waves in the subsequent runs. The effect of the disturbance was estimated by comparing the measured waves during the model tests with the measured waves during the wave calibration. The difference was expressed in terms of the wave spectrum parameters in Eq.(2.78), such as the significant wave height, peak period, peakness-, shape- and tail factor.

Table 5.7 presents the results from ballast 2 condition, which was tested in 33 sea states shown in Table B.12. The spectrum parameters were determined for all sea states and three wave probes. The mean and 95% confidence interval of the mean were presented as the ratio of the measured to the requested value for both the raw and the smoothed spectra. Values were derived both from a nonlinear fit to the spectra and from spectral moments. Comparison was made with wave calibration results in Table B.11, which was derived from the twelve sea states in Table B.10.
The wave height of the wave probe in front of the vessel, WP3, in Table 5.7 is increased by 10%. It is about 6-7% above the requested value, while the peak period is still as requested. The peakness factor is as requested, and the uncertainty is still significant. The tail factor, n, is increased slightly compared to the wave calibration tests, while the shape factor, m, is somewhat reduced below the requested value.

It was observed that the vibration response had a tendency to increase towards the wave maker, and moreover to be higher for the first run than for subsequent runs in each sea state, indicating that the 3D wave disturbance in subsequent runs actually reduced the

Table 5.7: *JONSWAP parameters from tested sea states in ballast 2 condition with 95% confidence interval of the mean value. Values were obtained from nonlinear fit to raw and smoothed (sm.) wave spectra and from spectral moments. Results are presented as the ratio of the measured to requested value.*

Parameter	Mean (raw)	95% mean (raw)	Mean (sm.)	95% mean (sm.)
H_S fit WP3	1.063	0.022	1.067	0.024
H_S moment WP3	1.072	0.022		
H_S fit WP1	1.125	0.022	1.132	0.024
H_S moment WP1	1.154	0.023		
H_S moment WP2	1.058	0.025		
T_P fit WP3	0.994	0.007	0.997	0.007
T_P fit WP1	0.979	0.008	0.977	0.007
γ fit WP3	1.017	0.094	0.733	0.055
γ fit WP1	0.937	0.086	0.657	0.042
n fit WP3			1.032	0.008
m fit WP3			0.973	0.006
n fit WP1			0.995	0.007
m fit WP1			0.988	0.004

vibration level. This is illustrated in the merged HF response for 3 runs in the first plot of Figure C.16. The observation indicated a reduced energy of short waves along the tank, and reduced quality in continuous runs. The fatigue damage at midship section for ballast 2 condition was determined based on the runs in the first and second half of the tank, the second half being closest to the wave maker. The WF and HF damage from the second half divided by the first half of the tank are displayed in Figure 5.30 for the sea states at full speed. The first two sea states have a HF ratio of more than 10, and the HF damage close to the wave maker is higher in 18 of 19 sea states. The HF damage in ballast 2 condition at full speed in North Atlantic head sea trade increased by 12% from 3.11 in Table 5.6 to 3.49 based on the second half of the tank, confirming that the HF damage was underestimated based on runs along the whole tank length. The linear springing response was the one being most affected and reduced due to lack of stationarity along the tank for the high frequencies.
In Appendix C.3 the JONSWAP parameters obtained from the other loading conditions and bow shapes are presented without any significant new findings. In general, the sea states were acceptable, except for the linear springing excitation.

5.4.5 Extrapolation of results by the response surface method.

The fatigue damage from the individual sea states was extrapolated to cover the whole scatter diagram according to the procedures outlined in Section 2.8.1. No correction for varying damping was made.

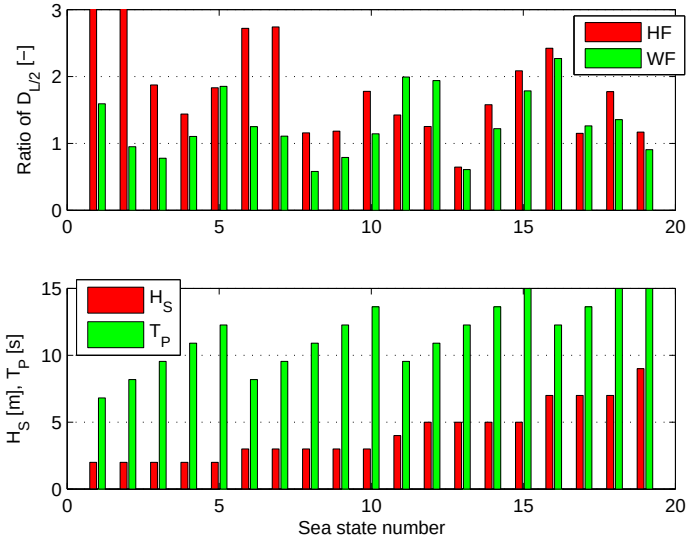

Figure 5.30: *The midship HF (left) and WF (right) fatigue damage ratio between the second half and the first half of the tank for ballast 2 condition in sea states at full speed.*

Polynomial expressions were fitted to the hourly WF and HF damage from the tested sea states. The fitted fatigue damage of the individual sea states were combined with the probability of occurrence from the scatter diagram. The results are shown in Figure 5.31 for North Atlantic and Figure 5.32 for World Wide head sea wave environment for ballast 3 condition at realistic speeds. The dominating sea states (peak) of the HF damage cover a smaller number of sea states than the peak of the WF damage. The peak of the HF damage in North Atlantic corresponds to significant wave heights of 4-5m with zero up-crossing periods of 9-10s. The peak of the WF damage is located at 5-6m and 10-11s. In World Wide head sea trade, the peaks of the HF and WF damage were moved towards lower wave heights and periods.

In full speed the peak of the HF damage of ballast 3 condition in head sea North Atlantic trade was moved towards higher sea states with significant wave heights of 6-7m and zero up-crossing periods of 10-11s, while the location of the WF peak was insensitive to speed. This is shown in Figure 5.33. The speed affected also the total damage and vibration damage. The wall effects were present in particular at low speeds. Considering the dominating sea states, the wall effect was more important for the WF damage than the HF damage, since the speed reduction and peak periods were lower for the dominating sea states contributing to the HF damage.

In Figure 5.31 39 sea states with realistic speed were utilized. Results based on 14 sea states, similar to those run in other combinations, are presented in Figure 5.34 for ballast 3 condition in the North Atlantic head sea wave environment. The total fatigue damage was

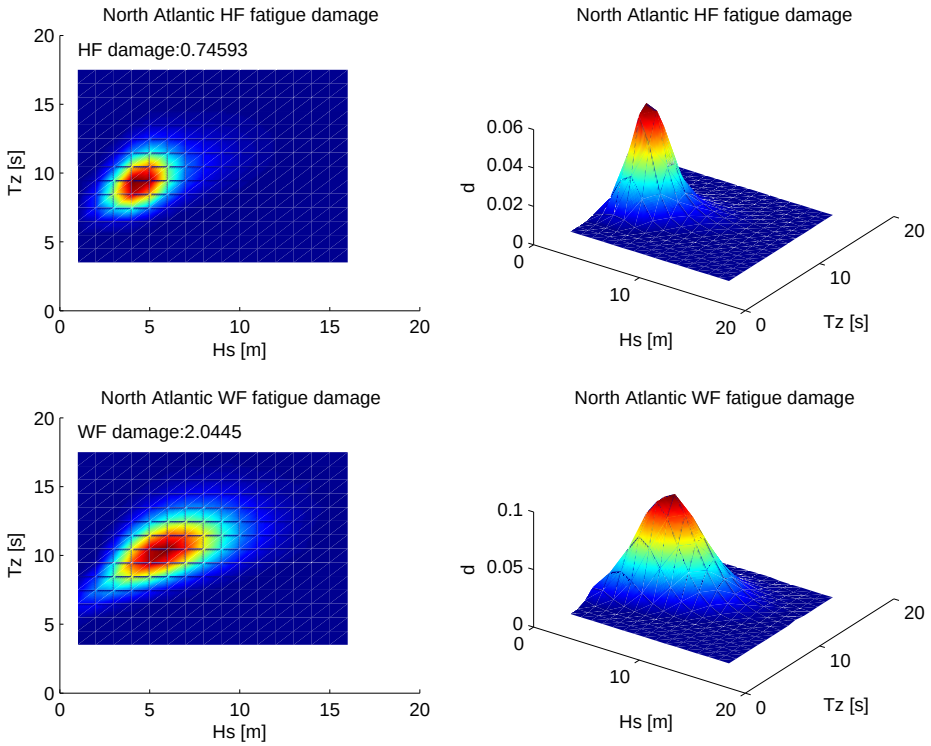

Figure 5.31: *Midship HF (upper) and WF (lower) fatigue damage for ballast 3 condition in North Atlantic head sea wave environment at realistic speeds. 39 sea states were considered.*

increased by 8%, and the contribution from HF damage was reduced by 2% by considering more sea states.

The difference in location of the dominating sea states in ballast and cargo condition was small. The dominating sea states of the HF damage were moved towards higher wave periods in cargo condition, which may indicate that whipping, due to more heave and pitch in longer waves, was more dominant. The WF damage was located at the same position. Results for realistic speeds in other combinations are shown in Appendix 5.4.5.

Table 5.8 presents the results for the HF and WF damage in full and realistic speed in North Atlantic and World Wide head sea wave environment. For ballast 3 condition results based on 39 (All) and 14 sea states can be compared. The damages represent 7 year continuous trade without port time in the respective combinations. Assuming 30% port time, the damage in ballast and cargo condition can be summarized to produce the cumulative damage for a 20 years service. As noted Table 5.8 includes the fatigue damage from all sea states, while Table 5.6 only includes the extrapolated fatigue damage based on the tested sea states only. The former table will then indicate higher fatigue damages, and for fatigue life estimates from the latter table the percentage of the tested sea states has to be

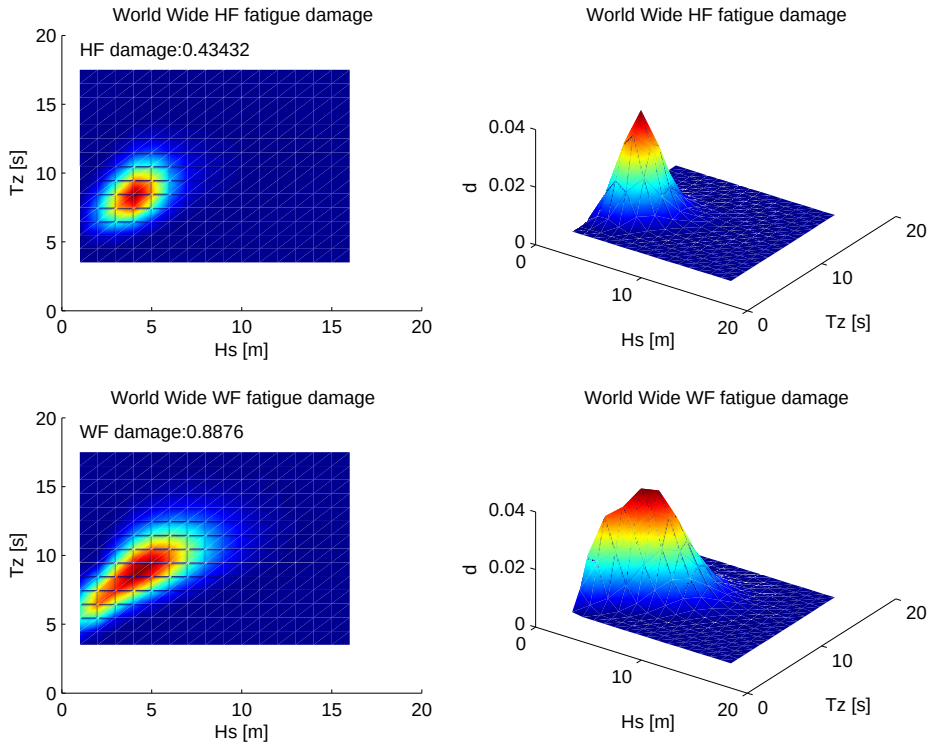

Figure 5.32: *Midship HF (upper) and WF (lower) fatigue damage for ballast 3 condition in World Wide head sea wave environment at realistic speeds.*

accounted for (direct time extrapolation).

From Table 5.8 different observations were made

- ⋆ Full speed gave too conservative HF damage, but also higher WF damage.
- ⋆ World Wide environment gave higher relative HF damage than North Atlantic.
- ⋆ Ballast condition gave higher relative vibration damage than cargo condition (contributed by lower damping).
- ⋆ The increased ship length for bow 3 increased the WF damage in cargo condition, but not in ballast condition.
- ⋆ The HF damage of bow 3 was reduced compared to bow 2, but it was not significantly reduced compared to bow 1.
- ⋆ The difference in the HF damage between bow 1 and 2 in ballast was caused by different damping, but possibly also by slightly different excitation due to the bulb.
- ⋆ The fatigue life for bow 2 in North Atlantic bulk trade was estimated to 2.9 years, which is comparable to 3.6 years obtained by the simple time extrapolation in Section 5.4.2.

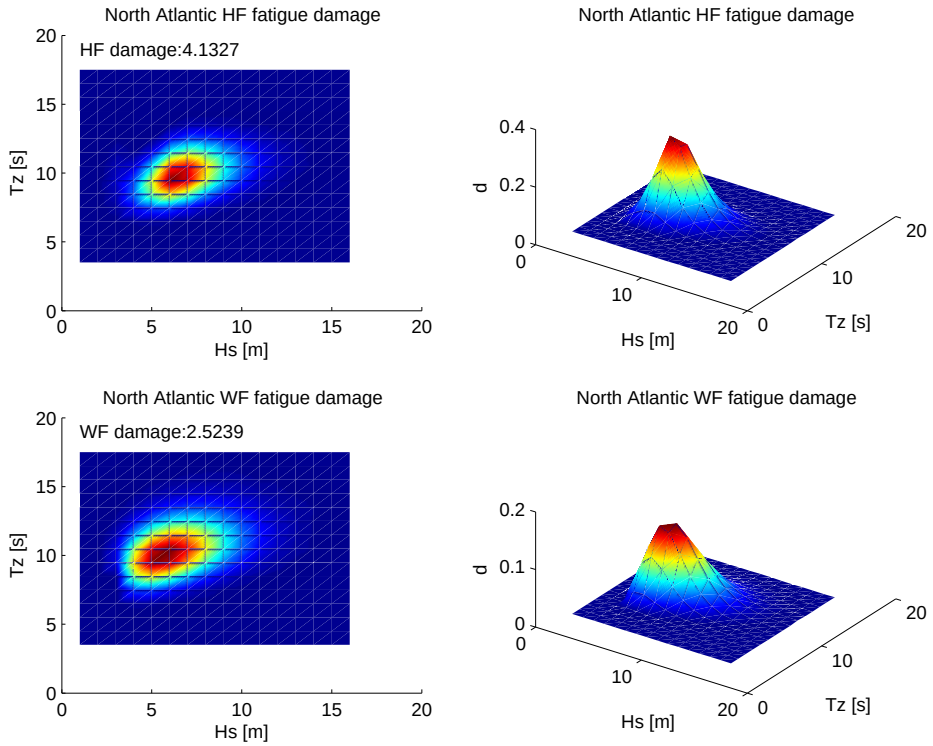

Figure 5.33: *Midship HF (upper) and WF (lower) fatigue damage for ballast 3 condition in North Atlantic head sea wave environment at full speed.*

The contribution from the HF part was reduced by 1% to 18% compared to the simple time extrapolation.

⋆ The fatigue life in the World Wide trade was 5.9 years, twice the fatigue life in the North Atlantic. The HF contribution was 29%.

For bow 3 the estimated fatigue life was 2.8 years in the North Atlantic. Accounting for the reduced length from 304 to 294m, assuming the stress was proportional to the length squared and that the fatigue life was inverse proportional to the stress in the power of 3, the corrected fatigue life became 3.4 years. The HF damage contribution was 10%. The pointed bow was not an effective design to reduce the vibration damage relative to bow 2, considering the difference in damping.

Some features of the testing tend to underestimate the relative importance of the vibration.

1. The damping in the model tests was too high (e.g. reducing the damping to approximately half for a container vessel increased the ratio of the vibration damage to wave damage by about 40% for a typical sea state according predictions performed by Drummen et al. (2006)).

2. The springing response reduced with increased distance from the wave maker.

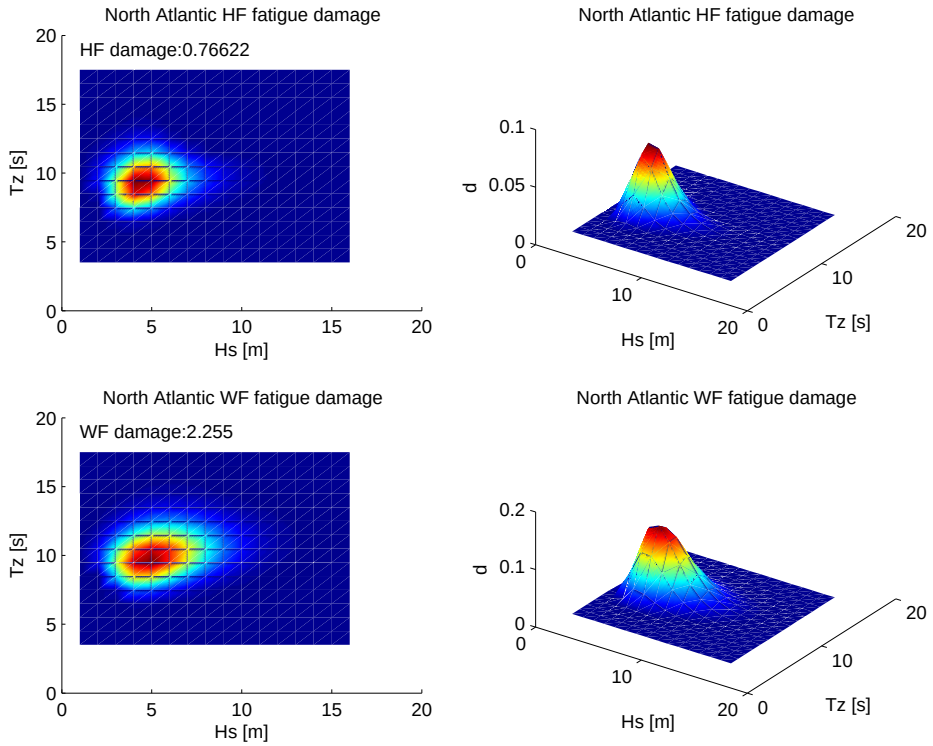

Figure 5.34: *Midship HF (upper) and WF (lower) fatigue damage for ballast 3 condition in North Atlantic head sea wave environment at realistic speeds. 14 sea states were considered.*

3. Subsequent runs in a single sea state resulted in lower springing response.

4. The low number of selected sea states resulted in slightly higher HF damage contribution.

Other factors not considered in the test program were

1. Storhaug et al. (2003) showed that the contribution from the HF damage was reduced for corrosive environment considering a single slope SN-curve.

2. Storhaug et al. (2003) showed that the decrease of the vibration stress from head to beam sea was less than the decrease of the stress from the conventional wave loading.

3. Routing tending to reduce the occurrence of high wave heights, will increase the relative contribution from vibration. Good seamanship may reduced the vibration damage when this is a concern when in adverse weather, while the contribution may be increased when other issues are of more importance, e.g. to void excessive roll.

4. Head sea cargo condition, representing following seas, reduced the vibration contribution due to too high wave damage mainly caused by lower encounter periods.

Table 5.8: *Overview of 7 year midship HF and WF fatigue damage for the different bow and loading combinations in full (FS) and realistic speed (RS) for World Wide (WW) and North Atlantic (NA) head sea wave environment. Extrapolation of results are based on the response surface method covering all sea states.*

Condition	HF NA	WF NA	HF WW	WF WW	Tot. NA	Tot. WW	% HF contr. NA	% HF contr. WW
Ballast 1, FS	4.10	2.41	1.94	0.86	6.51	2.80	63	69
Ballast 2, FS	6.51	2.67	3.03	0.93	9.18	3.96	71	77
Ballast 3, FS	3.92	2.46	1.58	0.90	6.38	2.48	61	64
Ballast 3, FS, All	4.13	2.52	1.68	0.92	6.65	2.60	62	65
Cargo 1, FS	1.69	4.61	0.67	1.46	6.30	2.13	27	31
Cargo 2, FS	2.29	4.90	0.97	1.57	7.19	2.54	32	38
Cargo 3, FS	1.91	5.30	0.74	1.85	7.21	2.59	26	29
Ballast 2, RS	1.24	2.22	0.98	0.98	3.46	1.96	36	50
Ballast 3, RS	0.77	2.26	0.44	0.99	3.03	1.43	25	31
Ballast 3, RS, All	0.75	2.05	0.43	0.89	2.80	1.32	27	33
Cargo 1, RS	0.58	3.46	0.32	1.42	4.04	1.74	14	18
Cargo 2, RS	0.62	3.41	0.32	1.45	4.03	1.77	15	18
Cargo 3, RS	0.57	4.38	0.30	1.82	4.95	2.12	12	14

5. Storhaug et al. (2003) indicated also some small vibration levels in following seas.

The 18% contribution from the HF damage can be considered as a lower limit for the iron ore trade in the North Atlantic for this vessel design.

5.5 Relative importance of whipping and springing

A procedure to identify whipping was outlined in Section 4.8. It is applied to the ballast 2 condition in the following.

The total, whipping and springing standard deviation stress in deck are presented as a function of the sea state in Figure 5.35. The estimates in sea states with reduced speeds were biased, since the springing criterion used to define the occurrence of whipping was based on full speed. Disregarding the cases with reduced speed, whipping occured in all sea states, but it became comparable to springing first around $4m$ significant wave height. Whipping was then comparable to springing in the dominating sea states for the HF damage displayed in Section 5.4.5.

The slope between two local peaks of the filtered 2-node response was used to indicate whipping events. The probability of a slope to indicate whipping is presented in Figure 5.36 based on the moment. The probability of whipping appears to increase with increasing

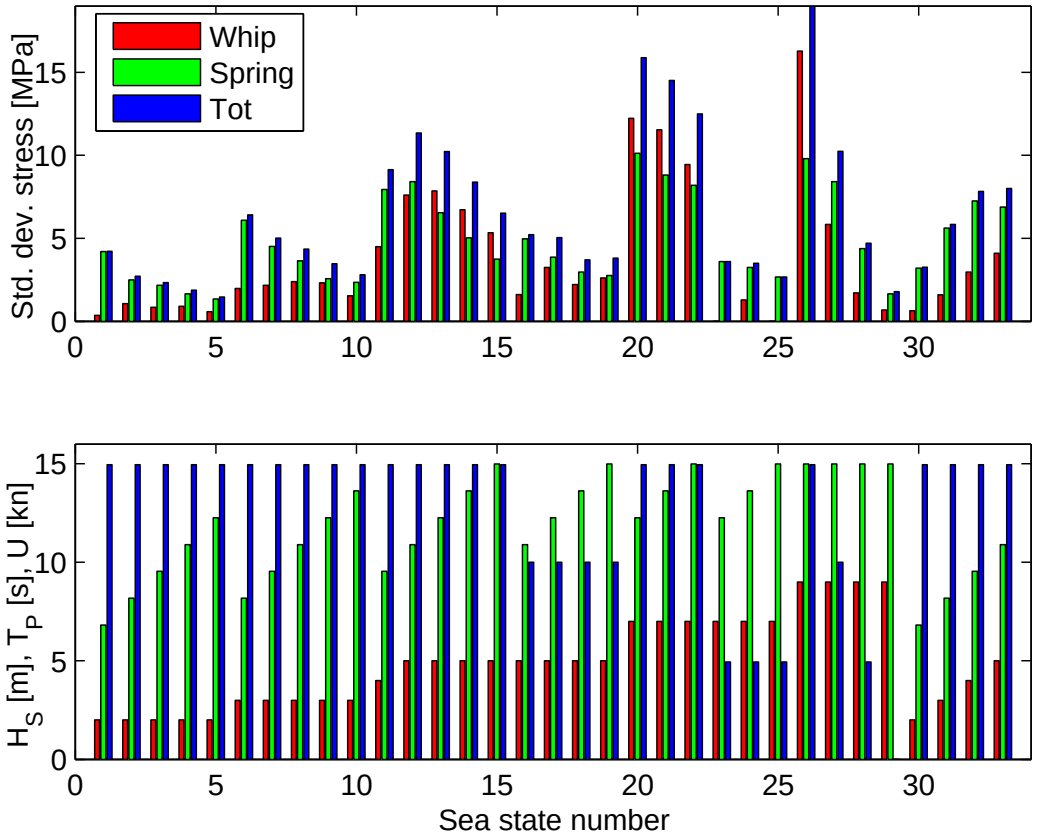

Figure 5.35: *St.dev. of total (right), whipping (left) and springing (middle) nominal stress in deck amidships of ballast 2 condition shown versus H_S (left), T_P (middle) and U (right).*

wave heights and possibly also with increasing peak periods. For the sake of interpretation, the probability of whipping for $5m$ significant wave height was about 0.03 (3 out of 100 vibration cycles indicate whipping; 1 vibration cycle has a duration of 2 seconds in full scale, i.e. 3 events during 200 seconds). This means that every minute there was a whipping event at full speed in full scale. The peak periods of the tested sea states were between 11 and $15s$. In full speed the encounter peak period was about $10s$, and a whipping event occured then for every sixth wave in average. This is about 5-6 times the rule of thumb criterion for voluntary speed reduction, which is related to the encounter waves rather than the whipping response, e.g.(Faltinsen 1990, pp. 282).

A few factors may influence the capability of the method to detect whipping.

- The whipping events may occasionally have contribution from springing.
- Low whipping response may occur without being identified.

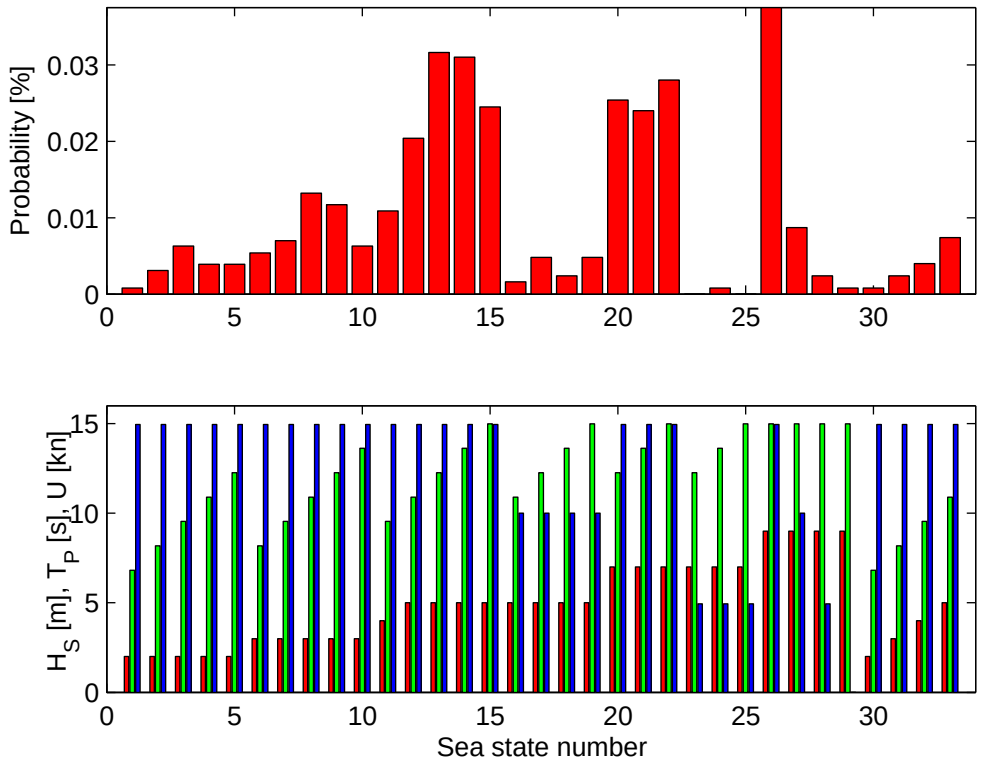

Figure 5.36: *Probability of whipping from individual slope estimates in ballast 2 condition at midship section shown versus H_S (left), T_P (middle) and U (right).*

- The frequency range in the filtering process was chosen rationally, and changing it affects the results.
- Other responses may be more suitable to identify whipping, e.g. acceleration.
- The method required transfer function values, which were input to the criterion.
- The linear and second order springing values should be obtained in realistic speeds.
- The criterion was based on long crested sea and may be too strict for short crested sea.
- The bichromatic sum frequency response was disregarded.

Despite these factors, the results suggest that both whipping and springing ought to be included in theoretical investigations. It indicates that the impacts related to hypothesis 3 is of equivalent importance as springing.

5.5.1 Acceleration levels used to indicate whipping

In hull monitoring systems, vertical accelerations in the bow may be used to identify bow impacts. When the acceleration exceeds a predefined criterion, a warning should tell the captain to take action. The rules for hull monitoring, (DNV 2005e; ABS 1995), do not provide well defined criteria. ABS figures the following criterion: When three times the standard deviation of the acceleration exceeds $0.4g$, bow impacts occur. This criterion is compared to the model test results in the following.

The translatory accelerations in the model tests do not need to be scaled to full scale. The ABS's criterion was compared to the accelerations from ballast 2 condition. Figure 5.37 presents the total, three times the total and the HF standard deviation of the vertical bow acceleration. The high pass filtered acceleration included higher modes in this case. In addition, single maximum amplitudes versus three times the total standard deviation are shown. The speed, significant wave height and peak period are included to characterize the operational condition.

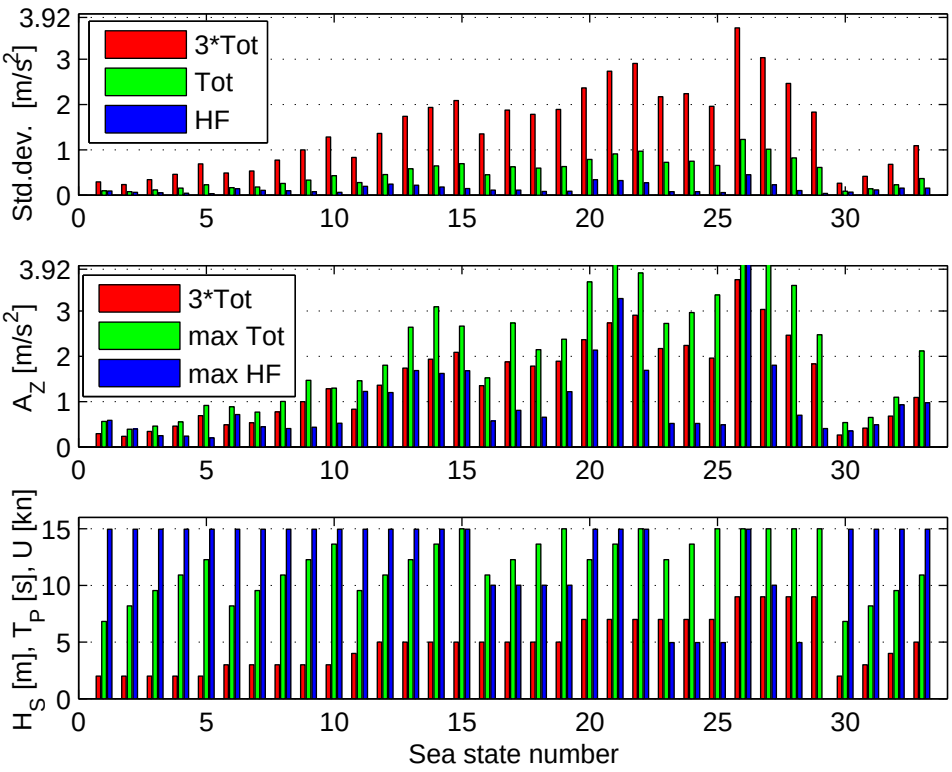

Figure 5.37: *3 times the total (left), total (middle) and HF (right) standard deviation of measured bow acceleration in ballast 2 condition for the different sea states characterized by H_S (left), T_P (middle) and U (right). In row 2 the maximum total (middle) and HF (right) amplitude are compared to 3 times the total standard deviation (left).*

The criterion was not exceeded in any of the sea states, but it was no doubt that bow impacts and whipping did occur. In the highest sea state at full speed, a value close to $3.92m/s^2$ was reached with a maximum single amplitude exceeding the acceleration of gravity. *It may be possible for the measured acceleration to exceed the acceleration used in design without providing an alarm.* For the highest sea state the ratio between the maximum total amplitude and three times the standard deviation was relatively high, but it was reduced drastically with speed. Figure 5.38 confirms bottom exit followed by bottom slamming for a relatively large bottom area. The nominal stress in deck was about $150MPa$, which is high, and the contribution from whipping was significant. This was a conventional flat bottom impact, which gave a significant increase of the vibration cycle in sagging. The slamming peaks are ahead (in time) of the acceleration, which again is ahead of the bending stress amidships. Note also the clustering of the large responses.

A better choice may be to relate the criterion to amplitudes rather than the standard deviation, and base the criterion on some fraction of the design value with an appropriate safety margin to account for the stochastic nature of such extreme events. Moreover, a high ratio between the maximum acceleration amplitude and three times the standard deviation may actually be an indication of severe bottom impacts. The local loading due to the impacts is another matter.

5.6 Linear versus monochromatic second order springing

The measured transfer function was used as input to a basic method, which predicted the difference between monochromatic second order springing and linear springing. The method was outlined in Section 4.9. The results from this method, in terms of standard deviation of the HF nominal stress in deck at midship section, is considered in the following based on ballast 2 condition.

Results from Torsethaugen and PM (wind based) wave spectra are compared in Figure 5.39, and the predictions were based on realistic speeds provided in Chapter 6. The estimated significant wave height and peak period from the two spectra differ as displayed in the lower plots. The trend of the linear and monochromatic second order HF stress differs as well.

The maximum linear HF stress, located at Beaufort 5 to 7, is roughly $3MPa$ in terms of nominal standard deviation stress. The nonlinear contribution is increasingly important above Beaufort 5. The nonlinear HF stress reaches a plateau at $5MPa$ for PM, while Torsethaugen displays an increasing trend exceeding the PM predictions.

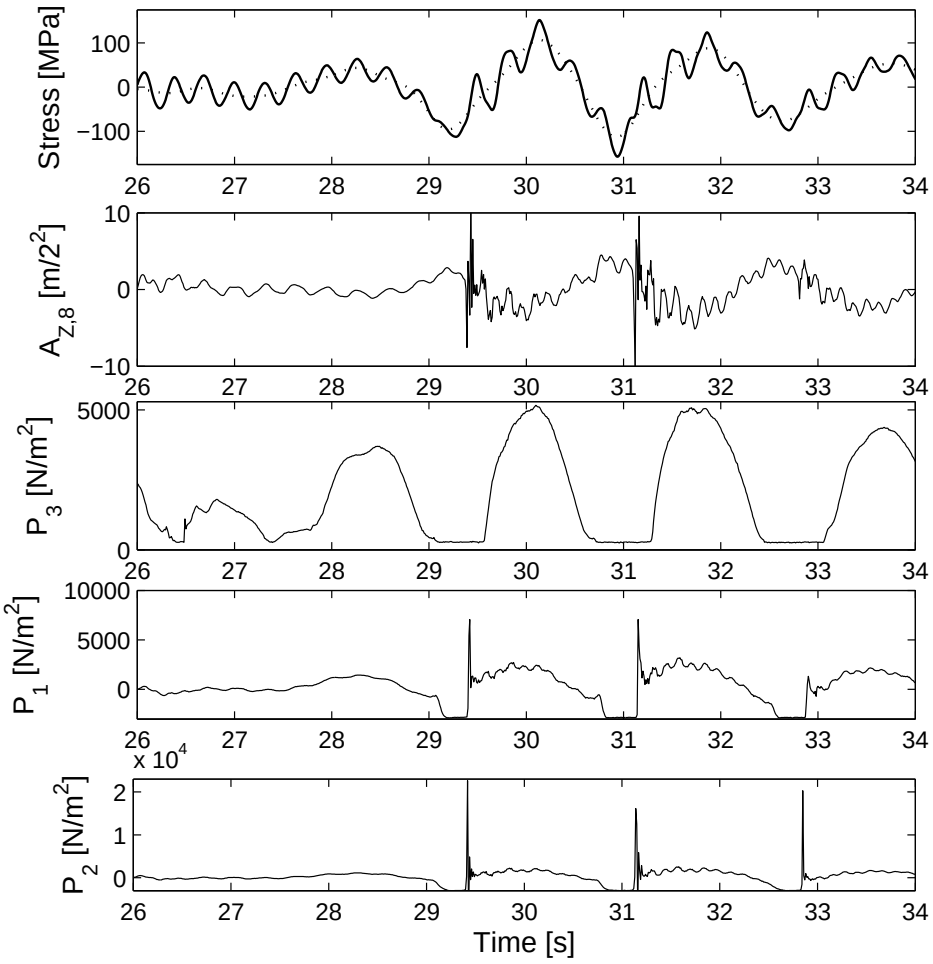

Figure 5.38: *Full scale nominal stress in deck (sagging upwards), vertical bow acceleration (positive downwards) and bottom pressures at stem, 0.972 and 0.945L_{PP} in ballast 2 condition at full speed; $H_S = 9m$, $T_P = 15s$ (run1630). Model time scale.*

The model tests in ballast 2 condition was performed based on different sea states and speeds as shown in Figure 5.40. Some conditions are comparable to those in Figure 5.39. Torsethaugen with Beaufort 7 is similar to sea state 13 and 14. The former predicts a standard deviation stress of $5.5MPa$, while the latter gives 4 to $5MPa$. Torsethaugen with Beaufort 9 predicts $6.5MPa$, while sea state 19 gives $2MPa$. The former is based on $5kn$ higher speed. Torsethaugen with Beaufort 5 predicts $3MPa$, while sea state 3 gives $2.5MPa$.

Perfect agreement between predictions and model tests were not expected, since

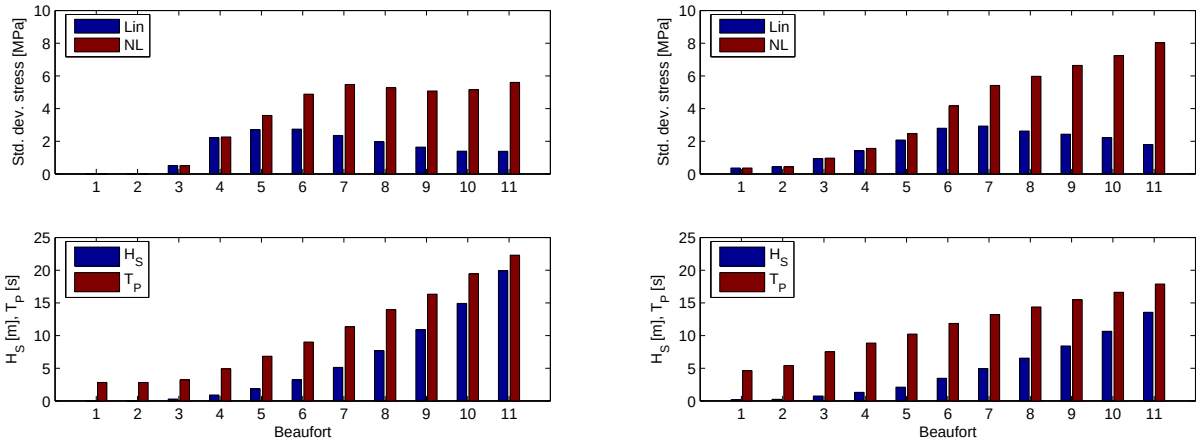

Figure 5.39: *Pairs of linear (left) and second order monochromatic (right; including linear) HF standard deviation nominal stress versus Beaufort strength. PM (left plot) and Torsethaugen (right plot).*

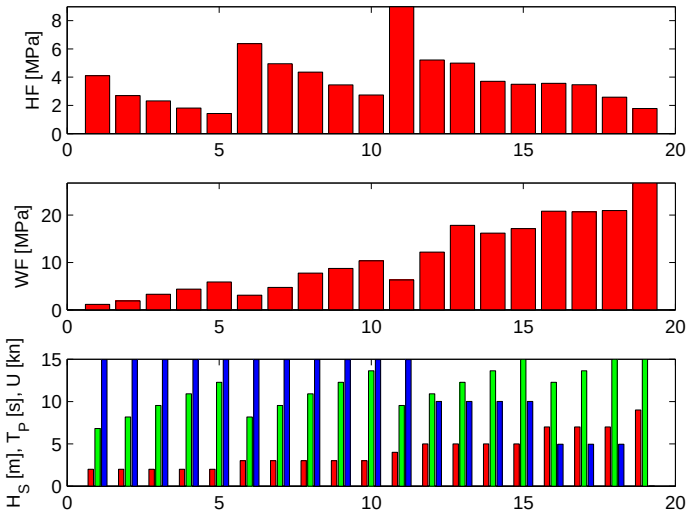

Figure 5.40: *Measured nominal standard deviation HF and WF stress in ballast 2 condition at reduced speed in different sea states characterised by H_S (left), T_P (middle), U (right). JONSWAP wave spectrum with a $\gamma = 2$ is used.*

1. The measurements include whipping, which contributes according to Section 5.5.

2. The predictions lack second order response from bichromatic waves displayed in Section 5.3.2.

3. The input transfer function values in the predictions were based on full speed.

4. The spectra differ.

The predictions illustrate that the linear springing dominates in low wind speeds, while nonlinear effects dominate in higher winds speeds. For the sea states dominating the vibration damage, *the sum frequency springing is considered of similar to higher importance than the linear springing*, thereby comfirming the importance of hypothesis 4. Moreover, the high frequency tail behavior of the wave spectra differs and affects the level of the HF response and the trends for increasing wind strength. The importance of sum frequency effects contradicts (Slocum 1983), who only indicated a moderate (30%) importance in a single sea state.

5.7 Illustration of vibration events

Section 5.6 illustrated the relative importance of linear and second order springing, while Section 5.5 confirmed the contribution from whipping. The excitation sources causing whipping were not well explained in Section 5.5. A few measured time traces are displayed in the following to indicate the excitation sources for bow 2 in ballast and cargo condition. The selected time traces consider 'extreme' whipping events. Bow 3 differs considerably from bow 2, and plots of whipping events for ballast and cargo 3 condition are shown in Appendix C.5.

Figure 5.41 presents whipping events from ballast 2 condition at full speed in small sea states ($3m$). The left plot of the figure refers to a sea state with a peak period of $8.2s$, while the right plot refers to a peak period of $13.6s$. Section 5.5 indicated that similar whipping events occured once every hundred springing cycle. The different rows display the total and wave pass filtered midship stress (sagging=positive), the relative motion in the bow (zero at still water level in zero speed), the pitch motion (bow up=positive), the pressure below the bow and the stern (zero at calm water in zero speed). Note that acceleration is not shown in these figures as in Figure 5.38, since the acceleration does not necessarily involve strong bottom slamming events in these cases.

For clarification, some details are provided to ease the interpretation of the displayed time traces for ballast and cargo 2 condition.

- ⋆ Bow 2 in ballast condition was without bulb, but with stem flare. The bottom (bilge) flare ended $15cm$ above BL in the region 20 to $60cm$ aft of FP.
- ⋆ The stem flare was removed in cargo 2 condition.
- ⋆ The draft at FP in ballast and cargo condition was $32cm$ and $51cm$.
- ⋆ The stem flare and deck level started $21cm$ and $45cm$ above the still water line in ballast condition.

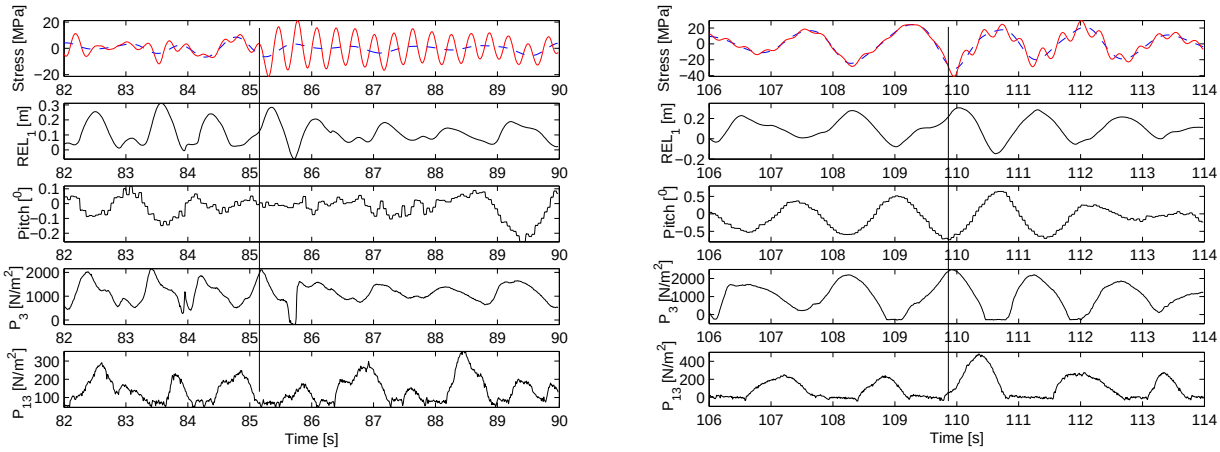

Figure 5.41: *Whipping events in ballast 2 condition in $H_S = 3m$, $U = 15kn$. Left: $T_P = 8.2s$ (run 1582), right: $T_P = 13.6s$ (run 1594). Row 1= Total (continuous) and wave pass filtered (dashed) midship stress, row 2= Relative motion in bow, row 3= Pitch, row 4= Stem pressure, row 5= Stern pressure.*

- ⋆ The measured relative motion in cargo 2 condition was limited to a height of $18.5cm$ above the still water line corresponding to $7.5cm$ below deck level.
- ⋆ A pitch angle of 1^0 corresponds to a motion of $7.3cm$ in the bow.
- ⋆ The CL bow pressure, P_3, was measured $29cm$ above BL at FP.
- ⋆ The CL bottom pressure, P_1, was measured $23cm$ aft of FP.
- ⋆ The CL bottom pressure, P_5, was measured $11cm$ aft of FP.
- ⋆ The stern pressure, P_{13}, was measured in the stern flare $5.6cm$ above the still water line.
- ⋆ The value of $100N/m^2$ corresponds to a water head of $1cm$.
- ⋆ The vertical line represents the possible initiation of whipping.

Returning to the left plot of Figure 5.41. The relative motion in the bow increases, and the water hits the stem flare. The initiation of whipping does not agree in time with the possible stem flare force. The bow pressure decays earlier than the relative motion, indicating that the measured relative motion may include water spray/run up. The pitch motion is small, and the relative motion is solely due to the motion of the water. The stern pressure, P_{13}, is moving in and out of the water, and no slamming is observed in the stern area. The positive stern pressure does not correlate well with the time of the impact. The wave elevation in the stern is small compared to the relative motion in the bow, but the flare in the stern is more pronounced. The first strong vibration amplitude occurs in hogging, and correlates to some extent with both the decay in the bow pressure and the decay of

the stern pressure. It is likely that the contributing force was a downward pull at the bow, since the troughs of the stern pressure are not correlated with changes in the vibration response. The example illustrates that it is not easy to reveal the excitation source from measurements by visual inspection of the responses.

The right plot of Figure 5.41 presents a similar time trace in longer waves. In this case, the bow has maximum draft (negative pitch) at the start of the impact. The pressure at the bow agrees well with the pitch motion, and the pressure decay starts at the same instant as the first half vibration cycle in hogging. Again, the maximum pressure is reached about $0.1s$ before the maximum relative motion. The pressure at stern is increasing at the time of the impact in this case, and the hogging cycle indicates that the impact was due to a downward pull in the foreship only. The vibration amplitude is less than in the short waves.

Figure 5.42 presents whipping events from ballast 2 condition in high sea states ($9m$, $15s$). The left plot assumes full speed, while realistic speed of $5kn$ is considered on the right side. The left plot of Figure 5.42 presents a large whipping event. The pitch is positive and the bow is still going up at the initiation of the impact. The bottom pressure, $P1$, has a rapid increasing suction pressure at the start of the whipping event, resulting in a hogging cycle. Subsequently, flat bottom impact with slamming occurs, and an increase of the following vibration cycle in sagging is observed. The stern pressure and the observed slamming at $68.5s$ does not affect the vibration response. The source of the current whipping event is regarded as a conventional flat bottom impact, but it has contributions from both the *exit* and entry phase as illustrated in Figure A.15.

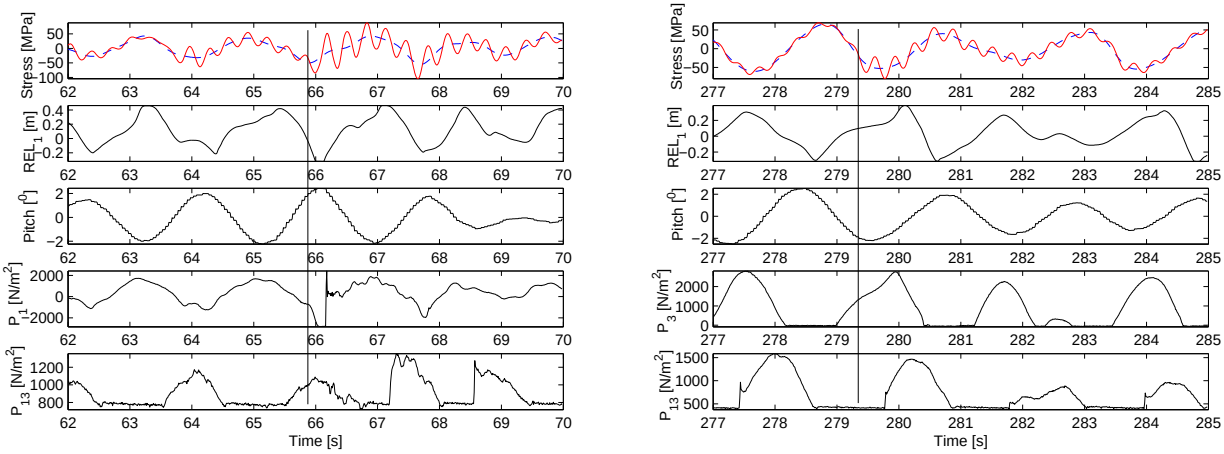

Figure 5.42: *Whipping events in ballast 2 condition in $H_S = 9m$, $T_P = 15s$. Left: $U = 15kn$ (run 1629), right: $U = 5kn$ (run 1636). Row 1= Total (continuous) and wave pass filtered (dashed) midship stress, row 2= Relative motion in bow, row 3= Pitch, row 4= Bottom/stem pressure at bow, row 5= Stern pressure.*

The right plot of Figure 5.42 presents a whipping event in realistic speed when the bow is going down. The pressure probes are going in and out of the water and the pitch motion is significant, indicating large relative motions both at the stern and bow. Small slamming events occur in the aft ship at this speed, but do not appear to produce significant whipping. It is no clear explanation for the initiation of the whipping towards hogging.

A couple of vibration events from cargo 2 condition in realistic speeds are presented in Figure 5.43. The left plot refers to a sea state with a significant wave height of $3m$ and peak period of $8.2s$, while the sea state to the right refers to $5m$ and $15s$. In the left plot of Figure 5.43, the pitch motion is small, while the relative motion and stem pressure display rapid fluctuations. The upper limit of the relative motion is exceeded at $91.5s$, but the water surface did not reach the deck level. The relative motion is far from the non-vertical bilge area, and the stern pressure is small. The period of the relative motion oscillation is about $0.7s$ both at 92 and $96s$, and the stem pressure at $92s$ displays a rapid oscillation, which is not reflected in the relative motion. This represents apparently springing excited by sum frequency effects.

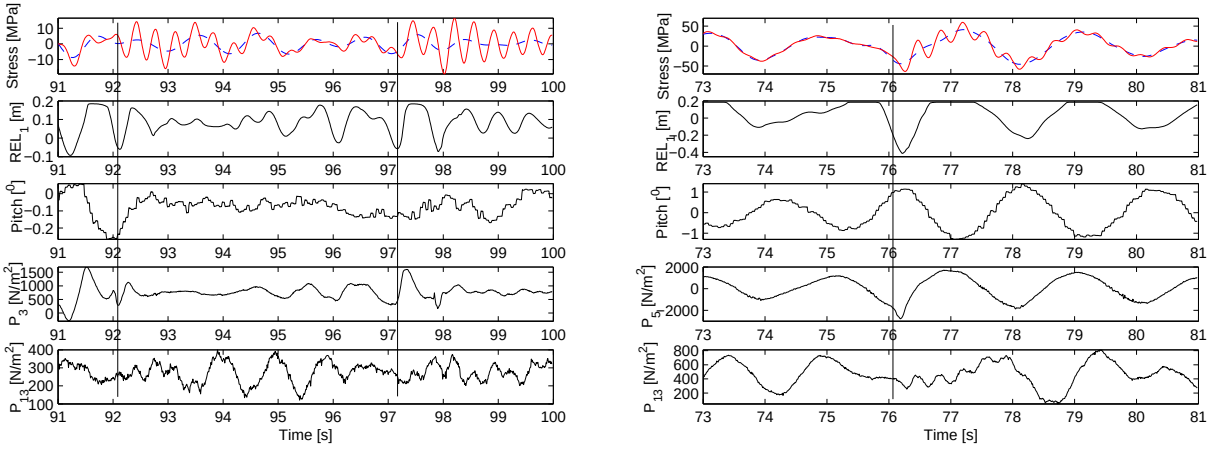

Figure 5.43: *Vibration events in cargo 2 condition. Left:* $H_S = 3m$, $T_P = 8.2s$, $U = 15kn$ *(run 1746), right:* $H_S = 5m$, $T_P = 15s$, $U = 10kn$ *(run 1798). Row 1= Total (continuous) and wave pass filtered (dashed) midship stress, row 2= Relative motion in bow, row 3= Pitch, row 4= Bottom/stem pressure at bow, row 5= Stern pressure.*

The right plot of Figure 5.43 presents a whipping event. The whipping starts when the bow is in the up-pitching cycle and and moves upwards, while the relative motion moves downwards. The bottom pressure, $P5$, displays a change in the suction pressure at the initiation of the impact. It occurs prior to the radiation pressure from vibration, observed in the stern pressure. The minimum surface level is $11cm$ above the BL at the stem, but even lower at the bow quarter due to the steady wave elevation. The estimated difference was $5cm$ in $10kn$, and the water surface at the bottom flare may move down to about $6cm$

above BL. The whipping appears to come from water moving down at the bottom flare area at bow quarter and then moving up again with duration comparable to the vibration period. This may cause a dynamic amplification up to a factor of three according to Figure A.15 for a sinusoidal full period impact.

Figure 5.44 presents another whipping event in cargo 2 condition. The significant wave height is $9m$ with a peak period of $15s$. The left plot represents full speed, while the right plot represents zero speed, which includes voluntary speed reduction. The left plot shows actually a flat bottom impact also in this loading condition. The whipping starts first with a half cycle in hogging. The second cycle in sagging is not significantly increased indicating that the suction force in this case was more important than the subsequent slamming.

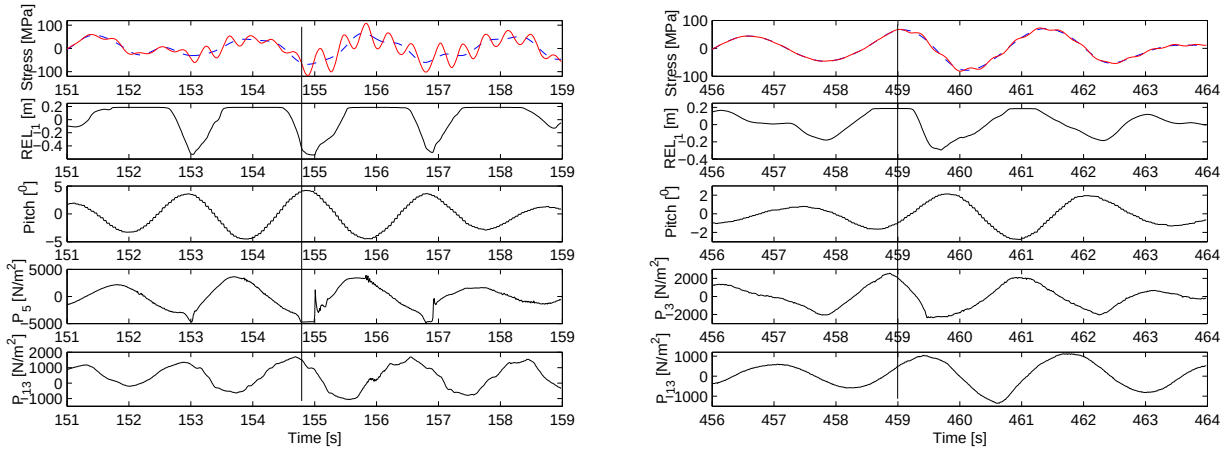

Figure 5.44: *Whipping events in cargo 2 condition in $H_S = 9m$, $T_P = 15s$. Left: $U = 15kn$ (run 1786), right: $U = 0kn$ (run 1787). Row 1= Total (continuous) and wave pass filtered (dashed) midship stress, row 2= Relative motion in bow, row 3= Pitch, row 4= Bottom/stem pressure at bow, row 5= Stern pressure.*

In the right plot of Figure 5.44, representing zero speed, no flat bottom impact is observed. The pitch angle is negative and a high wave caused water on deck. There is a rapid change in the stem pressure, which may explain the vibration, but more likely it was caused by impacts against the 'superstructure'. The vibration was about $8.5MPa$ in amplitude, which constitutes a small contribution to the WF stress. From observations, the bow design without a stem flare gave much more water on deck.

In this section significant vibration events have been illustrated, supporting hypothesis 3 related to impacts and hypothesis 4 related to sum frequency excitation due to bow reflection. It should be noted that the impact related to hypothesis 3 is related to bottom flare impacts in ballast condition rather than bow flare impacts. The first vibration cycle often occurs in hogging due to a downwards pull. This is in agreement with Saunders

(1965), who explained it by rapid loss of buoyancy, and it is also observed in time series presented by Bell and Taylor (1968). Later publications do in general not reflect these type of excitation sources.

Chapter 6

Full scale measurements

Full scale measurements of the iron ore carrier was carried out by DNV, and a workshop was initiated where measurements were made available. The evaluation of the measurements have so far resulted in three publications, (Storhaug et al. 2003; Moe et al. 2005; Storhaug et al. 2006). The ship's geometry is identical to the model with bow 1, which again is similar to bow 2. Full scale measurements of the response for the vessel in head sea $\pm 30^0$, are compared to ballast 2 condition. Damping, involuntary speed reduction in waves, stress versus sea states, whipping response and fatigue damage are presented in the following sections. Focus is given to the wave induced response after strengthening made in 2000, because the wave radar was adjusted after strengthening to produce more reliable wave height estimates, (Moe et al. 2005). Vidic-Perunovic (2005) did also assess measurements from the large iron carrier with respect to bi-directional sea states and vibration response. Unfortunately, the period before the wave radar was adjusted was chosen.

6.1 Damping and springing frequencies

The damping ratio was estimated for a large number of records measured onboard the ship. Measurements from other ships were assessed as well. The spectral method was used to obtain the damping ratio as described in Section 2.3.3 and Section 4.4.2. In most cases it was applied to half hour records.

Figure 6.1 presents estimates of the damping ratio in ballast and cargo condition after strengthening the vessel. The damping appears to be linear in ballast condition, and linear to weakly nonlinear in cargo condition. The possible nonlinear contribution may come from the iron ore cargo. The mean damping ratios are 0.80 and 0.86% in ballast and cargo condition, confirming a small difference. The 95% confidence intervals of the sample values

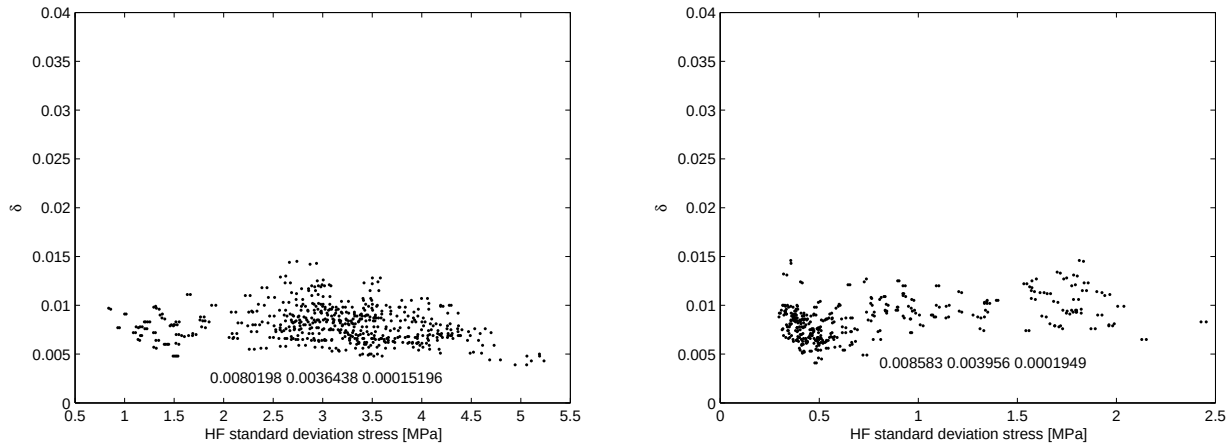

Figure 6.1: *Damping ratios as a function of HF standard deviation nominal stress in ballast (left) and cargo condition (right) from the measurement period of June 04 to May 05.*

are significant, while the 95% confidence intervals of the mean are small.

The 2-node natural frequency was estimated simultaneously with the damping ratio. The natural frequency estimates in ballast and cargo condition are presented in Figure 6.2. The mean springing frequencies are $3.63 rad/s$ in ballast and $3.23 rad/s$ in cargo condition. The uncertainty is twice as large in cargo condition due to slightly different cargo conditions, but in general the uncertainty is insignificant.

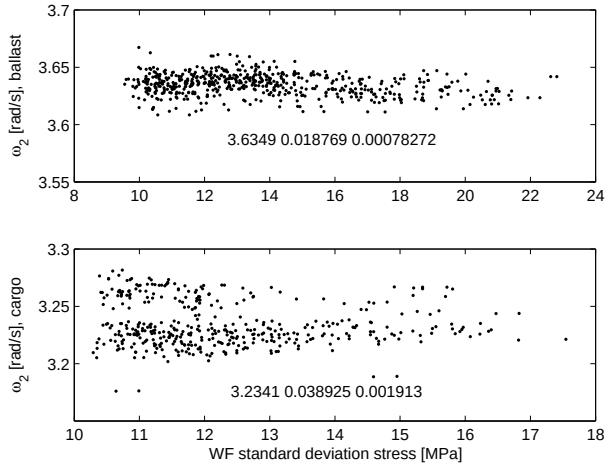

Figure 6.2: *The natural 2-node frequency as a function of the WF standard deviation stress in ballast (upper) and cargo condition (lower) for the measurement period of June 04 to May 05.*

The natural frequency in Figure 6.2 appears to be insensitive to the WF response level. The expected change of the natural frequency, due to the changed wet area and added mass in high and long waves, is not evident. The constant frequency as a function of the WF stress level differs from the decay in higher sea states observed in model tests and displayed in Figure 5.6. The decay in model test was explained by a combination of higher WF responses in long crested sea and somewhat nonlinear stiffness.

The same procedure was employed on 30 records before strengthening in ballast and cargo condition. In addition a few other ships were considered. An overview of the ships is given in Table 6.1.

Table 6.1: *Overview of ships considered in damping assessment.*

Ship name	L_{pp} [m]	T [m]	B [m]	Ship type
Ship 1, 'The ship'	294	18	53	Ore carrier
Ship 2	300	18.3	50	Bulk carrier
Ship 3	300	18.3	50	Bulk carrier
Ship 4	280	17.1	48	Bulk carrier
Ship 5	281	17.4	48	Ore carrier
Ship 6	285	12.2	32.2	Container vessel

The results of the damping estimates are given in Table 6.2. The average damping in cargo condition is about 10% higher than in ballast condition. The damping for ship 1 is also higher after strengthening, which increased the natural frequency by 10%. The natural frequencies of the ship before strengthening were used as basis for the model tests. The difference between the damping before and after strengthening may be affected by the low number of records considered before strengthening. However, the increased damping after strengthening may also be caused by an increase in the structural damping, while the increased natural frequency will tend to reduce the linear hydrodynamic damping. The damping of the container ship (ship no. 6) is noticeably higher than the damping estimated for the bulk carriers.

It was not easy to obtain good damping estimates from the spectral method. Half hour records rather than 5 minutes records were preferred as a basis, and the response spectrum fit was based on a high resolution with 4096 FFT samples and a narrow interval of 0.3 to $0.5 rad/s$ below and above the natural frequency. With reference to Section 5.1.2, a reduction factor should be included for the spectral method due to effects, which will widen the spectral vibration peak (e.g. varying natural frequency due to change of added mass in waves).

In Figure 6.3 the damping ratio is estimated based on the decay curve from a whipping event in ballast condition after strengthening. The damping is 0.51%, and the average of several such events was 0.50%, while the spectral method predicted 0.80%. The ratio of

Table 6.2: *Spectral estimates of damping ratio for different ships and loading conditions*

Ship no., remark	δ	ω_2 [rad/s]	Loading cond.
1, before strengthening	0.70	3.32	Ballast
1, before strengthening	0.70	2.91	Cargo
1, after strengthening	0.80	3.63	Ballast
1, after strengthening	0.86	3.23	Cargo
2, June-Oct.-03	0.69	3.23	Ballast
2, June-Oct.-03	0.87	2.78	Cargo
3, 5 min. time traces, April-03-July-04	0.61	3.23	Ballast
3, 5 min. time traces, April-03-July-04	0.67	2.75	Cargo
4, Jan-Dec.-03	0.96	3.62	Ballast
4, Jan-Dec.-03	1.12	3.16	Cargo
5, Nov-04-May-05	0.81	3.94	Ballast
5, Nov-04-May-05	0.70	3.51	Cargo
6, April-June-02, Feb-April-05	1.52	3.92	Cargo and 'ballast'

0.625 suggests strongly that a correction factor is necessary based on the damping estimates from the spectral method. The whipping events were normally disturbed by wave action after the initial whipping events, and it was not easy to find many good quality whipping responses as input to the damping evaluation. A practical way is to drop the anchor, but then any speed effect on the damping will not be detected. The latter may be especially important for container vessels.

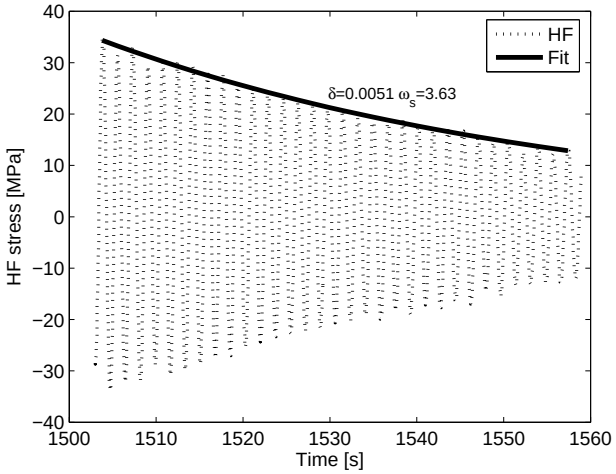

Figure 6.3: *Damping estimated from the decay curve of the high pass filtered stress after a whipping event, 04.12.15.23:30 on starboard side.*

The damping estimates in Table 6.2 may be multiplied with a factor of about 0.8 suggested by Gran (1974). An average value of the damping ratio for the bulk carriers, disregarding

the effect of loading conditions, is then 0.63%. The ratio of 0.625 from the ship in ballast condition suggests an even lower average value of 0.49%. Such large blunt ships are therefore expected to have a damping ratio in the range of 0.5 to 0.6%.

Limited data are available for the container vessel. The higher damping for the container vessel may be explained by contribution from the container stacks with its twisting locks and lashing system, and possible from higher hydrodynamic damping due to forward speed effects. The difference in damping between container vessels and other types of vessels should be investigated further in order to obtain realistic damping values for future numerical predictions. In case the estimated damping level for the container vessel is representative for such ships, this high damping may be beneficial from a fatigue point of view compared to the bulk carriers.

6.2 Measured speeds in different sea states

The wave induced vibration level is sensitive to speed. In order to check if the predicted speeds in Section 3.2 and the speeds applied in the model tests were reasonable, a comparison is made with full scale measurements.

The speed was measured in full scale by a GPS, which measured the speed over ground and disregarded the current or drift. The speed as a function of the significant wave height after strengthening is presented in Figure 6.4. The speed reduction in head sea is similar in ballast and cargo condition, and the speed reduction in following sea is also similar in ballast and cargo condition. The behaviour in head and following sea differs, but a noticeably speed reduction is observed also in following sea probably due to the relative motion effect. The uncertainty in predicted significant wave height is about 10% according to Miros (2003) assuming proper X-band radar setting. Moe et al. (2005) confirmed good agreement between measured wave heights and alternative data after strengthening, so the 10% uncertainty is reasonable in this case.

The measured speed may be compared to the speeds applied during the model tests, given in Table 3.4, and the predicted speeds by the simplified theory, given in Table 3.3. The applied speeds were 15, 10, 5 and $0kn$ in 3, 5, 7 and $9m$ significant wave height. The corresponding full scale measured speeds were 13.8, 9.6, 5.3 and $4.5kn$ in ballast condition, and the predicted speeds were 14.2, 11.2, 7.4 and $6.3kn$. The predictions were somewhat high compared to the measurements, which may be explained by the assumed propulsion efficiency factor in the predictions, and possible drift/current in the full scale measurements. The simplified method was however useful to make a first estimate of the speed reduction for the purpose of model tests. The applied speeds during the model testing were reasonable, except for the highest sea state where the applied speed was too low. The full scale measurements suggest that the voluntary speed reduction is not an issue,

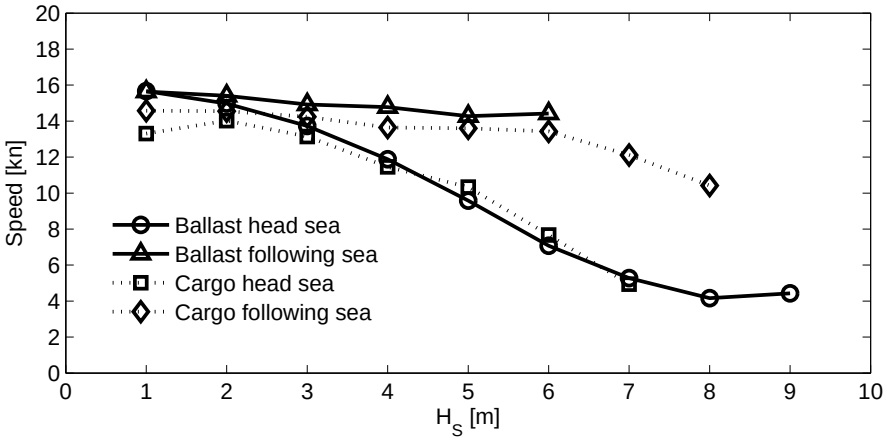

Figure 6.4: *Measured full scale speed in head and following sea in ballast and cargo condition versus measured significant wave height. Extension of Figure 30 in Moe et al (2005).*

and that all available power is basically used at all times. The vessel speed in head seas for even higher extreme sea states is however still an issue for further investigation (rarely measured, but when measured it is available through the VDR(voyage data recorder) for a certain period of time on "all" ships).

6.3 Wave induced stress in different sea states

The standard deviations of the WF and HF nominal stress as a function of the measured significant wave height are presented in Figure 6.5 for ballast condition in head sea $\pm 15^0$. The measured HF and WF stresses were obtained from the period after strengthening, but they were multiplied with 1.39 to represent the stress levels during the period before strengthening. The 1.39 factor denotes the difference in the section modulus at the measurement position at the deck level before and after strengthening. The nominal stress level in Figure 6.5 can then be compared to the stress obtained from the model tests. The WF stress increases as a function of the significant wave height. The HF stress increases up to $4m$, where it appears to reach a constant level. This is partly a consequence of the speed reduction in higher waves. A change in the dominating excitation sources may be an alternative reason, however, since this trend was also predicted in Figure 5.39 just based on the speed reduction, the speed reduction appears to be the main cause of the behaviour. It is noted that Stiansen et al. (1978) presented similar trends as shown in Figure 6.5 from measurements onboard three Great Lakes bulk carriers. There was however some variation depending on vessel size, and the current trend resembles the trend for the largest of the three vessels with almost the same length ($1000ft$), but more shallow draft.

In Table 6.3, the results in Figure 5.40 are compared with those in Figure 6.5. The most

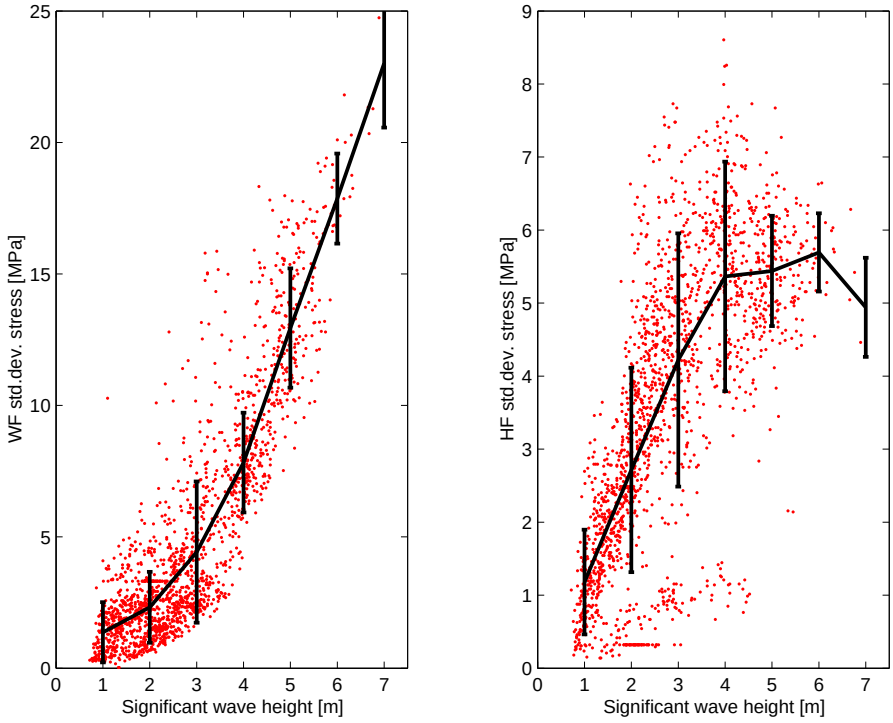

Figure 6.5: *WF and HF std. dev. nominal stress versus H_S in head sea $\pm 15^0$ for ballast condition 'before' strengthening. The stress is derived based on the period after strengthening, but it is multiplied with a factor of 1.39 to represent the nominal stress before strengthening. The standard deviations within half meter intervals are displayed.*

probable zero up-crossing periods from the North Atlantic scatter diagram are indicated in bold numbers, (DNV 2000). The HF stress is obtained from the strengthened vessel with the natural frequency that is 10% higher than prior to strengthening. According to Moe et al. (2005) the corrected standard deviation HF stress (multiplied with 1.39) was maximum $0.8MPa$ lower than prior to strengthening. The WF stress from short term statistics was also calculated by WASIM simulations, (DNV 2004), which were based on full speed, ballast condition, long crested head sea and the same sea conditions as considered in the model tests.

Table 6.3: *Comparison of head sea WF and HF std. dev. nominal stress in MPa from ballast 2 condition (MS), full scale measurements (FS) and WF stress from WASIM (WA). The most probable T_Z periods are indicated in bold. Sea states refers to numbering in Figure 5.40.*

H_S	WF FS	HF FS	Sea state	WF MS	HF MS	$T_Z[s]$	WF WA
2	2.3	2.7	1-5	1.2/1.9/3.3/4.4/5.9	4.1/2.7/2.3/1.8/1.4	5/6/7/**8**/9	0.6/1.3/2.4/4.0/5.3
3	4.1	4.2	6-10	3.1/4.7/7.8/8.7/10.3	6.4/5.0/4.4/3.5/2.7	6/7/8/**9**/10	1.9/3.6/5.9/8.0/9.1
4	7.8	5.4	11	6.3	9.0	7 (**9**)	4.8 (10.6)
5	12.9	5.4	12-15	12.2/17.8/16.2/17.1	5.2/5.0/3.7/3.5	8/**9**/**10**/11	9.9/13.2/15.2/15.8
7	23.0	4.9	16-18	20.8/20.7/21.0	3.6/3.5/2.6	9/**10**/**11**	18.6/21.3/22.1

The HF stresses obtained in the model tests for the most probable wave periods in Table 6.3 are significantly below the full scale average values (when accounting for 0.5-0.8MPa addition in the full scale values). The model was run in 15kn in 4m significant wave height with a zero up-crossing period of 7s, while the most probable values were 12kn and 9s. The HF stress from the model tests is not representative for this sea state. The full scale results were also affected by wave energy spreading.

The WF response obtained from the model tests in Table 6.3 are in some agreement with the WASIM simulations. The difference is explained by wall effects and disturbance from residual waves in the smallest sea states with short peak periods. In the highest sea state it is fair agreement in the WF stress from the full scale, model scale and WASIM results, while in lower sea states the full scale WF stress is lower. This may again be due to more wave energy spreading in lower sea states.

The ratio between the WF and HF stress in full scale was less than in the model tests, both because the HF stress in the full scale was higher and the WF stress in full scale was lower. This will increase the overall vibration damage contribution in full scale compared to the model tests.

Figure 6.6 presents standard deviation of the WF and HF stress versus significant wave height for cargo condition. The WF stress is similar in magnitude as the WF stress from ballast condition. The HF stress increases with wave height, but it reaches a plateau already at 3m significant wave height. The vibration stress at the plateau is about 60% of the similar plateau in ballast condition. The vibration level in head sea for cargo condition is still significant. The number of half hour records indicated by dots in Figure 6.6 confirms that head seas within $\pm 15^0$ occured occasionally in cargo condition, even though the prevailing condition was following seas, (Storhaug et al. 2003).

6.4 Prediction of whipping events from measurements

A method to identify whipping from the envelope process of the vibration response was outlined in Section 4.8. In Section 5.5 the method was shown to detect whipping in most of the sea states tested. The same method is applied for a number of full scale records of the vessel (ship 1) in the following.

The criteria for identifying whipping were corrected compared to the model tests to account for

- A damping ratio of 0.64% in full scale, rather than 1% from model tests.
- Wave periods exciting linear and second order springing were based on the relative direction of the primary sea, rather than pure head sea.

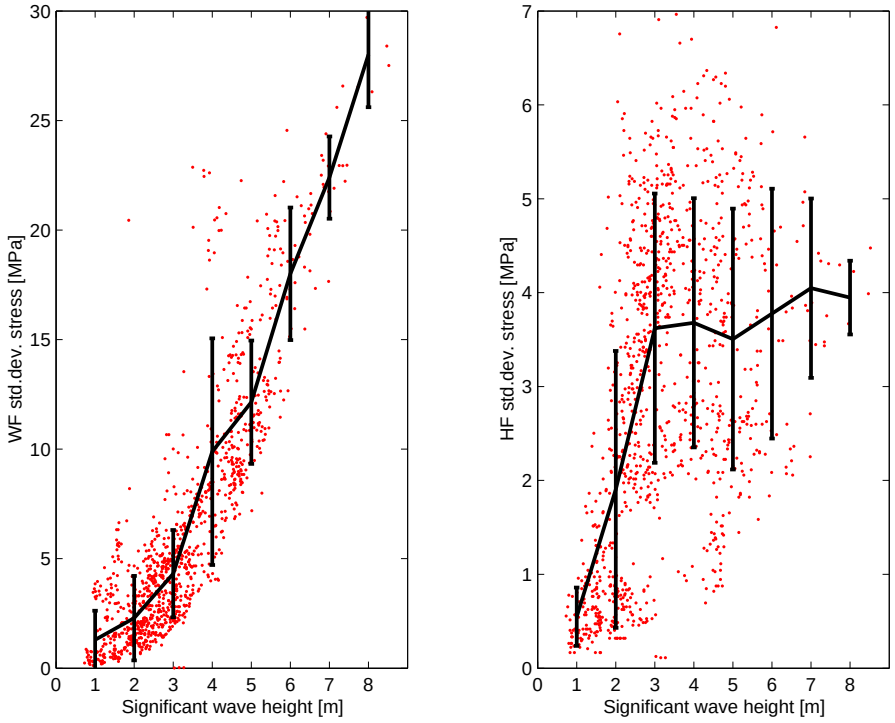

Figure 6.6: *WF and HF std. dev. nominal stress versus H_S in head sea $\pm 15^0$ for cargo condition obtained after strengthening, but multiplied with 1.39 to represent the period before strengthening. The standard deviations within half meter intervals are displayed.*

- A section modulus of $73.8m^3$ at the measurement position, rather than $53.9m^3$.

Characteristic data from a few records are listed in Table 6.4. The heading, β, indicates that the vessel was running slightly off head seas with a significant wave height of about 4.4-5m and a speed of 9.7-11.9kn. All data were obtained during the same day, and they represent sea states and response levels, which give the main contribution to the fatigue damage, (Moe et al. 2005). The peak period of the response, $T_{P,r}$ (corrected based on speed and heading), is compared to the peak period from the wave measurements, T_P. The peak period of the response, considering the shape of the transfer function of the bending moment, was expected to give an alternative estimate of the peak period of the waves, although tending to produce higher response periods than wave periods, when the wave period is lower than the peak period of the transfer function. The response peak period is consistently larger than the measured peak period from the waves. Due to the significant discrepancy by 24% in average between the two estimates, and that the standard deviation of response periods is 43% higher than from the wave radar, the measured wave periods may be somewhat deficient. This was also indicated by Moe et al. (2005), who illustrated a limited variation of the peak periods within a small range of wave heights compared to the North Atlantic scatter diagram. It should be mentioned that the North Atlantic scatter diagram is also related to significant uncertainties.

Table 6.4: *Overview of some records from ballast condition after strengthening (not corrected).*

YY.MM.DD.Hour	H_S $[m]$	$T_P/T_{P,r}$ $[s]$	Bn	U $[m/s]$	β $[^0]$	HF/WF Std.dev. stress [MPa]
05.01.10.09:00	4.5	10.9/13.1	5	6.1	353	3.6/10.8
05.01.10.10:00	4.5	10.9/14.1	5	5.9	344	2.8/10.6
05.01.10.11:00	4.5	10.9/14.6	5	5.4	339	2.8/11.4
05.01.10.12:00	4.7	11.0/14.5	5	5.3	336	2.6/11.4
05.01.10.12:30	4.8	11.4/15.7	5	5.1	338	3.0/11.8
05.01.10.14:00	5.0	12.0/15.2	5	5.0	348	3.0/12.1
05.01.10.18:00	4.4	11.9/13.3	5	5.1	349	3.0/10.2
05.01.10.19:00	4.5	12.2/14.9	5	5.5	347	3.1/11.6
05.01.10.20:30	4.7	12.4/13.4	5	5.3	348	3.3/10.5
05.01.10.21:30	4.9	12.0/13.9	5	5.6	339	3.1/10.9

The method predicts whipping in two of the ten sea states (at 14:00 and 18:00). Figure 6.7 presents the high pass filtered 2-node nominal vibration stress and the corresponding slopes. Several whipping events seem to be present, but only one whipping event was detected. The vibration stress level was about 30% of the wave frequency stress for these sea states.

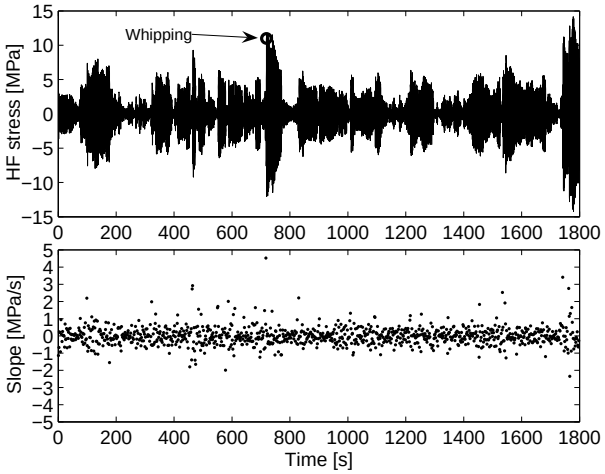

Figure 6.7: *The HF stress time series with indication of whipping events and slopes in ballast condition after strengthening, 05.01.10.18:00 on starboard side.*

Figure 6.8 presents the corresponding cumulative probability distribution of the slope process. The criterion on the positive slopes is apparently a bit strict.

A few records with higher HF responses are listed in Table 6.5. In general, these records were taken from higher sea states with lower speeds. There is still a discrepancy between

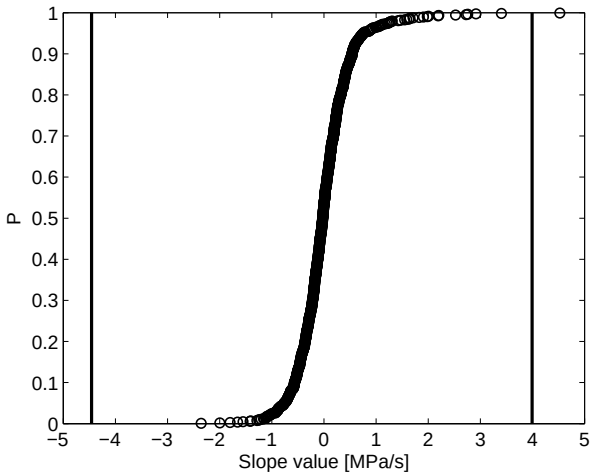

Figure 6.8: *The cumulative probability distribution, P, of the slope process versus the criteria for stress in ballast condition after strengthening, 05.01.10.18:00 on starboard side.*

the measured peak period and the peak period from the response. In this case the variation of the periods are similar, but the average ratio of the response peak period (corrected for heading and speed) and the wave radar peak period of 1.19 is still high.

Table 6.5: *Overview of some records from ballast condition after strengthening (not corrected).*

YY.MM.DD.Time	H_S $[m]$	$T_P/T_{P,r}$ $[s]$	Bn	U $[m/s]$	β $[^0]$	HF/WF std.dev. stress [MPa]
04.12.15.22:30	5.7	10.8/14.5	8	3.0	4	4.7/14.8
04.12.15.23:30	6.1	11.5/13.2	8	2.8	11	5.2/10.2
04.12.16.03:00	7.2	13.1/14.1	8	3.3	34	4.6/11.1
04.12.16.06:00	7.2	13.3/16.2	8	2.7	18	4.6/17.1
04.12.16.07:00	6.9	13.7/11.3	8	3.2	20	4.3/10.6
04.12.16.08:30	6.8	13.7/13.5	8	2.9	9	4.0/14.6
04.12.16.09:30	6.4	12.1/14.7	8	3.0	22	4.3/20.1
04.12.16.10:00	6.4	13.6/14.0	8	3.3	22	4.1/17.4
04.12.16.14:30	4.9	12.1/14.8	8	4.9	354	4.2/10.5
04.12.16.16:30	4.6	9.1/16.6	8	4.3	339	4.3/16.5
04.12.16.18:00	5.2	9.1/12.0	7	3.7	331	5.1/12.3
05.01.14.05:00	5.8	13.7/14.9	6	3.5	16	4.3/14.7
05.01.14.05:30	5.4	13.4/17.5	6	4.3	21	4.5/13.2
05.01.14.09:00	5.4	11.3/14.7	6	4.4	20	4.2/12.5
05.01.14.09:30	5.5	12.1/15.3	6	4.2	24	5.1/14.1
05.01.14.13:00	5.9	13.7/13.6	6	3.8	31	4.1/15.0
05.01.14.18:00	6.6	14.3/14.8	6	3.3	35	4.1/14.2

Whipping was detected in three of these 17 sea states (23:30, 14:30, 05.01.14.09:30), while some apparent whipping events were not identified as in Figure 6.9 (the slope was high but just below the criterion). The whipping criteria appear to be too strict, explained by the

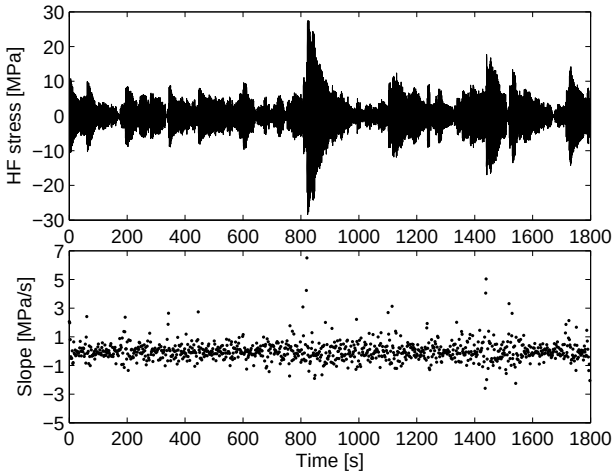

Figure 6.9: *The HF stress time series with no indication of whipping events and slopes in ballast condition after strengthening, 04.12.15.22:30 on starboard side.*

following uncertainties

1. The measured peak period may be too low, resulting in too high calculated wave heights for linear and second order resonance.

2. The criteria were based on transfer function values from model tests at full speed, while significant speed reduction was observed in the different sea states.

3. The criteria were based on transfer function values from model tests in head sea, while in many cases the direction was slightly off head sea.

4. The criteria were based on transfer function values from model tests in long crested seas, while significant spreading was present in the different sea states, e.g. (Storhaug et al. 2003).

The criteria need to be improved in order for the method to be useful for prediction of whipping events in full scale measurements.

To reduce the uncertainty related to point one, the response peak period was given as input instead of the wave peak period. Whipping was then detected in eight of 17 sea states (instead of three). From the detected whipping events an artificial whipping process was established and compared to the total vibration process, as illustrated in Figure 6.10 for a single sea state. The standard deviation of the artificial whipping process was $2.0MPa$, while the total measured HF process gave $4.5MPa$. The corresponding cumulative probability distribution compared to the criteria is presented in Figure 6.11. It still appears that

the criteria are a bit too strict, hence other effects such as speed and spreading needs to be accounted for as well.

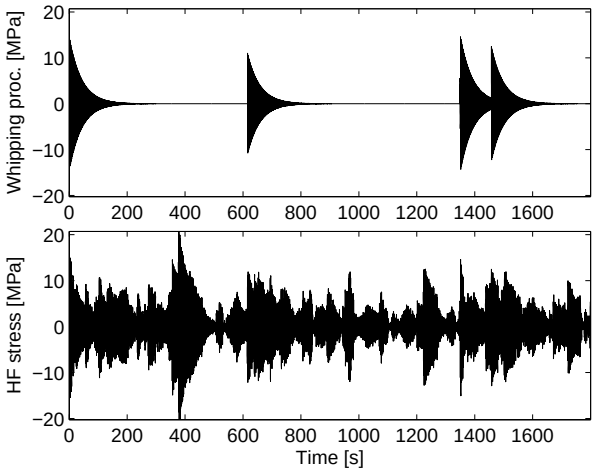

Figure 6.10: *The HF stress time series compared to an artificial whipping process based on the detected whipping events in ballast condition after strengthening, 05.01.14.05:30 on starboard side.*

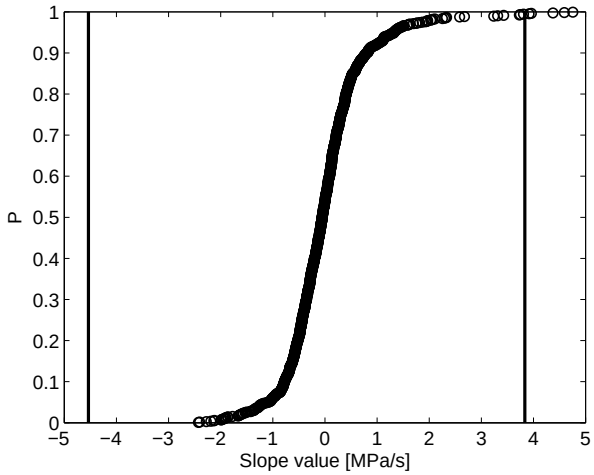

Figure 6.11: *The cumulative probability distribution, P, of the slope process versus the criteria for stress in ballast condition after strengthening, 05.01.14.05:30 on starboard side.*

A strict criterion was applied to detect whipping, and still whipping was detected. This indicated that the whipping process was of similar importance as the springing process also in full scale.

A whipping event is illustrated in Figure 6.12. It is observed that the first large vibration half cycle occurs in hogging, which agrees with the model tests. Moreover, the vibration contribution to the total stress level is evident, and the total stress amplitude in hogging reaches almost 60MPa in this sea state of 5 meter significant wave height. The nominal stress level in deck is 6% higher, and the ship after strengthening refers to a section modulus far beyond rule minimum. Therefore, a nominal stress level of about 90MPa in deck may be expected in this sea state on a similar ship with more standard optimized scantlings. This is considerable, and the effect of the wave induced vibrations on the extreme loading should be evaluated further. The importance of whipping occurring during the hogging cycle due to a downwards force should also be further assessed, and numerical predictions should be able to reproduce this effect before they can be considered as reliable.

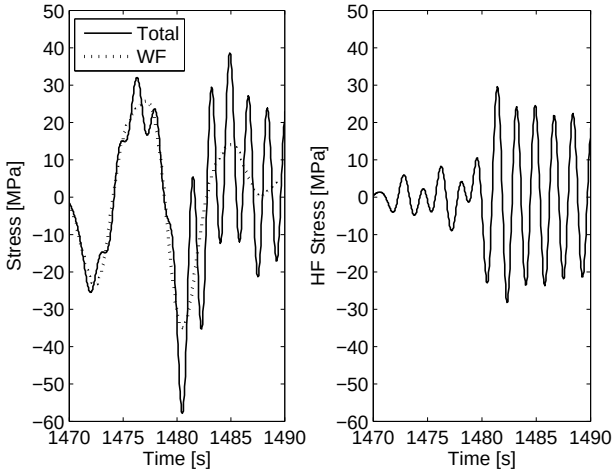

Figure 6.12: *A whipping event after strengthening, 04.12.15.23:30 on starboard side. Positive stress is sagging (compression in deck). Cut off frequency of WF response at 0.08 and 0.3Hz.*

6.5 Wave and vibration frequency fatigue damage

Rainflow counting was applied to calculate the fatigue damage from the stress records obtained from full scale measurements. The calculation procedure was basically the same as for the model tests, and did not introduce new uncertainties. A few selected results of interest are presented in the following. Further details may be found in (Moe and Holtsmark 2005; Moe et al. 2005; Storhaug et al. 2006).

The measured total fatigue damage, wave and vibration damage for the vessel before strengthening are presented in Table 6.6 in addition to the number of half hour recordings. The vibration damage constituted 61% of the damage in ballast condition and 13% damage in cargo condition. The ship encountered head seas in ballast and following seas in cargo

condition most of the time, which explained the lower contribution in cargo condition.

Table 6.6: *Measured fatigue damage from half hour recordings in the period July 1999 to June 2000 before strengthening in North Atlantic trade. Taken from (Moe and Holtsmark 2005).*

Load. cond.	No. of rec.	Tot. damage	Wave damage	Vibration damage
Ballast	3069	0.0515	0.0199	0.0316
Cargo	2827	0.0280	0.0243	0.0037

The time in ballast, cargo condition and port was roughly 33% each in this North Atlantic iron ore trade. A time extrapolation based on the recordings suggested a fatigue life of 6.3 years, which was roughly twice the fatigue life predicted based on the model tests in head seas. The difference was explained by the effect of wave headings, wave energy spreading, routing and the annual variations encountered in the full scale measurements. The routing was indicated to reduce the fatigue damage to half, (Storhaug et al. 2006). The model experiments and full scale measurements were then in satisfactory agreement considering the sensitivity of fatigue life estimates to the various sources of uncertainties.

The fatigue damages based on the period after strengthening are presented in Table 6.7 for a period of more than 4 years. The annual damage before strengthening is 4.1 higher than the annual damage after strengthening based on the number of recordings. Moe et al. (2005) indicated that the annual variations was moderate (maximum about 1.5 times minimum for both ballast and cargo condition) from the measurement period after strengthening, hence the annual variations for a trading ship may be somewhat less than expected for a stationary FPSO. The sectional modulus increased from $52.7m^3$ before strengthening to $73.2m^2$ after strengthening at the measuring position. The ratio of 1.39, representing the difference in stress level for the same bending moment, to the power of 4 is 3.7. The power of 4 was estimated by (Storhaug et al. 2006) for relevant stress levels and the two-slope SN-curve. The expected ratio of 3.7 is in fairly good agreement with the measured ratio of 4.1, considering the natural annual variations of the wave climate. The vibration damage constitutes 52 and 18% of the total damage in ballast and cargo condition, respectively. The total contribution of vibration damage considering all records drops from 44% to 40%, and the change considering the 10% increase of the natural frequency is small. I.e. the springing level was possibly reduced after strengthening, but 10% more vibration cycles counteracted the reduction of the vibration damage. Increasing the strength was not effective to reduce the relative contribution from vibration, but it reduced the nominal stress level and thereby the overall fatigue damage.
Fatigue damage for ship 5 in Table 6.1 was calculated at a position with section modulus of $70.6m^3$. The ship operated in different trades such as North Atlantic, Europe-Brazil and Europe-South Africa. The resulting fatigue damage from one and a half years of measurements are presented in Table 6.8. The vibration damage constitutes 65 and 33% of the

Table 6.7: *Measured fatigue damage in North Atlantic for measurement period October 2000 to May 2005 after strengthening. Taken from (Moe and Holtsmark 2005).*

Load. cond.	No. of rec.	Tot. damage	Wave damage	Vibration damage
Ballast	12679	0.0531	0.0255	0.0275
Cargo	12079	0.0290	0.0235	0.0053

total damage in ballast and cargo condition, and 55% overall. The contribution exceeds that from ship 1. One reason is that ship 5 operated in less severe trade, which is also reflected in less total fatigue damage. Moreover, (Storhaug et al. 2006) showed that during the same period in North Atlantic trade, ship 5 vibrated relatively more than ship 1, when the stress level was corrected with respect to their dimensions. This may be caused by slightly different bow shape, *less operation draft* for ship 5 and different encountered sea states. In any case, the full scale measurements reveal a considerably higher contribution to the fatigue damage from wave induced vibrations than indicated from the model tests in head seas.

Table 6.8: *Measured fatigue damage for measurement period November 2003 to May 2005 for ship 5 in all trades. Taken from (Moe and Holtsmark 2005).*

Load. cond.	No. of rec.	Tot. damage	Wave damage	Vibration damage
Ballast	5508	0.0062	0.0021	0.0040
Cargo	5195	0.0027	0.0018	0.0009

The vibration damage constitutes 18% of the total damage in cargo condition in Table 6.7, which also indicates that the ratio of the wave damage between the cargo and ballast condition is close to 0.9. The model tests indicated that the ratio of the wave damage between the cargo 2 and ballast 2 condition in head sea was 1.4 (average of ratio at full and reduced speed). The large observed difference between 0.9 and 1.4 is mainly a consequence of the number of cycles encountered in following seas compared to head seas. Accordingly, the prediction of the vibration contribution in the North Atlantic iron ore trade based on the model tests was underestimated compared to the full scale measurements for several reasons.

1. HF stress in ballast condition was higher in full scale than in model scale, mainly due to lower damping in full scale and low wave energy in the high frequency tail in the model tests.

2. The WF stress in ballast condition was lower in full scale than in model scale, due to wave energy spreading and possibly due to slightly off head seas to reduce pounding.

3. The cargo condition contributed to the vibration damage in full scale, but the vibration damage contribution was neglected in the predictions based on the model tests under the assumption of following seas.

4. The wave damage from cargo condition in head seas in the model experiments exceeds the wave damage in following seas by roughly 50% due to the number of cycles encountered.

5. See also reasons listed in Section 5.4.5.

The wave (WF) and vibration (HF) half hour damage as a function of significant wave height for the ballast condition of the ship (ship 1) after strengthening is presented in Figure 6.13. The relative importance of the vibration is reduced for increasing wave heights mainly due to the speed reduction. Moreover, the wave damage as a function of the wave height is apparently linear at higher wave heights. Assuming that the wave frequency stress is proportional to the significant wave height, a more rapid growth would be expected. The number of encountered cycles are however reduced in higher head waves, the peak periods of the encountered sea states influence the wave frequency stress level and Figure 6.13 covers all encountered headings. With reference to the latter, it has been said that the captain tries to avoid running straight into the waves in higher sea states to reduce the hull girder loading (reduce pitching and pounding and accept some small roll instead), which are displayed onboard by the monitoring system. This has so far not been documented by assessing the higher sea states more thoroughly, but it is indicated in Table 6.4 and Table 6.5.

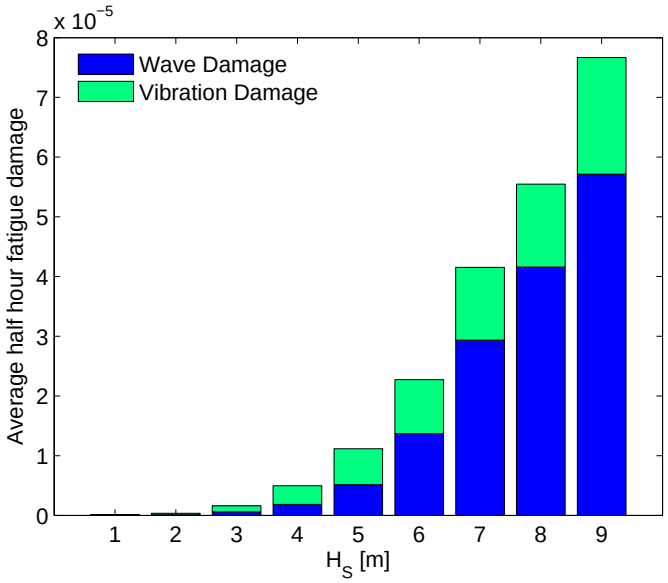

Figure 6.13: *Avarage half hour WF and HF (top) damage as function of the significant wave height in ballast condition after strengthening covering all headings. Taken from (Moe et al. 2005).*

The total contribution to fatigue damage is presented in Figure 6.14 for ballast condition after strengthening. A significant wave height of $5m$ is the most important wave height for the total fatigue damage in this trade. This agrees well with the model experiments in Section 5.4.5.

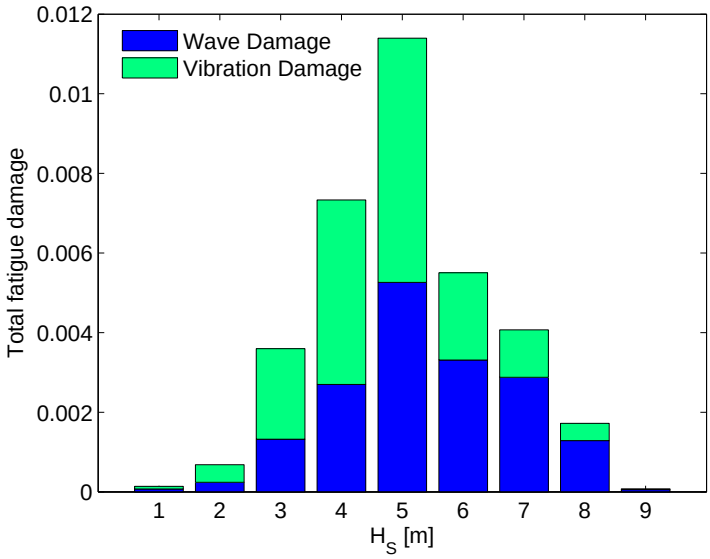

Figure 6.14: *Total WF and HF (top) damage as function of the significant wave height in ballast condition after strengthening covering all headings. Based on 13695 half hour records during a 4 year period. Taken from (Moe et al. 2005).*

Chapter 7

Conclusions and recommendations

7.1 Brief summary

This study was carried out in the following phases

1. Literature study.
2. Participation in a workshop.
3. Definition of hypotheses (based on activities 1 and 2 and other efforts).
4. Testing some of the hypotheses through simplified analysis.
5. Testing of the hypotheses through model experiments.
6. Comparison of model and full scale measurements, and
7. Conclusions and suggestions for further work.

The literature study was summarized in a number of findings and observations related to full scale measurements, model tests and springing and whipping theories.

The purpose of the workshop was to compare the predicted vibration response from four state-of-the-art computer codes with measured vibration response in order to identify the dominating excitation source. The computer codes were representative for the various existing software, and the comparison was made based on ballast condition simulated in 10 different sea states.

For blunt ships in particular, four hypotheses were defined. The force distribution along the hull implied by these hypotheses are antisymmetric, e.g. due to wave reflection in the bow but not in the stern. They may increase the generalized force and thereby increase the vibration. The *first* hypothesis was related to the steady potential and wave elevation around the bow (hull) in forward speed. This includes instabilities and interaction between the steady and unsteady potential. The *second* hypothesis was related to water surface motion in the bow area due to reflected waves and forward speed. The *third* hypothesis included impact forces due to the former two, and the *fourth* hypothesis was associated with second order sum frequency excitation due to bow reflection. The decay of the sum frequency pressure with draught and the extent below the bottom for a vessel of finite extent and forward speed were main issues.

The first three hypotheses were incorporated into a simplified computer code to assess the importance of whipping due to excitation on a half conical stem flare in ballast and cargo condition. Linear springing from undisturbed incident waves was included. The sensitivity to speed, wave period and wave height in regular and irregular waves was investigated. Moreover, a simplified procedure was employed to estimate the speed reduction in different sea states.

Prior to the model tests, the wave quality in the towing tank was evaluated to ensure that it was possible to produce linear and second order springing in short waves.

A large four-segmented flexible model of the iron ore carrier was made. The towed model had flexible joints at the three quarter lengths, and Froude scaled springing frequency was achieved by adjustable bearings. Various responses were measured. The model tests were carried out in ballast and cargo condition in regular and irregular waves. The effects of speed, wave height and wave period were investigated on three different bow shapes, the original, the original without bulb and flare, and a sharp wedge shaped bow with vertical stem. The effect of trim was briefly considered. The results were assessed to determine the damping, linear and second order transfer functions and fatigue damage from conventional wave loading and vibration. Moreover, different procedures were employed to distinguish the linear and second order contribution, and to separate whipping from springing.

Finally, results from full scale measurements were compared with model test results to indicate the validity of the model tests.

7.2 Conclusions

Separate conclusions were derived from the different phases of the study as outlined in the following. The most important ones are finally summarized in Section 7.2.6.

7.2.1 Literature studies

The following conclusions were derived from the literature investigation.

⋆ Wave induced vibrations have been observed (frequently) in ships, and whenever an attempt has been made to measure them, the measurements have confirmed the presence of wave induced vibrations. The question is not related to whether vessels vibrate or not, but to the level and consequence of the vibration.

⋆ Important parameters affecting the magnitude of vibration are dimensions, natural periods, nominal stress level (strength standard and steel type), draft, bow shape (stern shape and midship shape), damping, speed, heading, sea condition (spreading, peak period, wave height and tail behaviour) and trade.

⋆ The springing investigations were mostly related to blunt ships, while the whipping investigations were related to slender ships such as container ships with significant flare. Most of the full scale measurements were related to blunt ships, and some of the extreme whipping events were actually measured on these ships. *Public* literature of measured full scale vibration damage of high speed vessels, slender ships or offshore ships was not identified.

⋆ The full scale vibration damage has been underestimated in previously published literature. The vibration damage was estimated based on the filtered high frequency response, rather than the difference between the total fatigue damage and the filtered wave damage.

⋆ The elasticity of the hull girder tends to reduce the wave bending moment in the wave frequency regime. This will be beneficial from a fatigue point of view.

7.2.2 Workshop; Introductory assessment of full scale measurements

The following main conclusions were made based on the assessment of the first year of measurements from the iron ore carrier.

⋆ Bottom exit was not detected during the measurements.

⋆ Wave induced vibrations were basically continuous.

⋆ The wave induced vibration increased for increasing Beaufort strength, and wind was a better measure for the vibration level than the measured waves.

⋆ The difference of the vibration response for head and beam seas was small, while the vibration response in following sea was much smaller.

⋆ The vibration level in ballast condition was larger than in cargo condition for similar head sea conditions.

- ⋆ The vibration damage constituted 44% of the total fatigue damage in deck amidships.
- ⋆ For this iron ore trade, the ship encountered prevailing head seas in the ballast condition on the westbound leg and following seas in the eastbound cargo leg.
- ⋆ The accuracy of the wave radar measurement system was questioned. The high frequency tail was most deficient.
- ⋆ The nonlinear damping method gave lower predicted damping ratio (0.44%) than the spectral method.
- ⋆ It was the first time the fatigue damage from wave induced vibrations from full scale measurements was handled in a proper manner, i.e. taking the difference between the total damage and the wave frequency damage by Rainflow counting.

Comparison with numerical predictions was the main part of the workshop. A number of people were involved. The main conclusions were

- ⋆ The four computer codes failed to predict the high measured vibrations, and the observed trend in the full scale measurements was not captured.
- ⋆ The dominating excitation source was either missing or not accurately described.
- ⋆ The computer codes were sensitive to the location of the natural frequency compared to the humps and hollows in the excitation (from cancellation effects), in particular from the strip theory programs.
- ⋆ It was the first time the fatigue assessment from full scale measurements was documented utilizing a wave radar for the purpose of determining the sea conditions.

The sea states applied in the numerical predictions was later shown to be overestimated by a deficient wave measurement system during the period before strengthening. Consequently, this fact is expected to increase the difference between the measurements and the predictions by the four programs.

7.2.3 Investigation by simplified theoretical methods

The theoretical investigation consisted of defining the hypotheses, testing three of the hypotheses in a simplified computer code, estimating the speed reduction, and assessing different structural representations of the hull's flexibility. In the following the results obtained for the large iron ore carrier are described.

The surface elevation of the steady wave generated by the ship was $3m$ at $15kn$ at the stagnation point and about minus $1m$ at the bow quarter. The amplification factor of the incident head waves at the stem exciting linear and second order springing was about

three at full speed (and two at zero speed). These effects may consequently imply more whipping excitation.

The steady wave elevation, the wave amplification at the bow and the impacts on the stem flare were included in the simplified predictions of whipping. Linear springing by undisturbed wave pressure was also included. A homogeneous ship was considered, and the following conclusions were derived based on ballast and cargo condition in head seas.

- ⋆ The stem flare impacts contributed insignificantly to vibration in ballast condition.
- ⋆ The stem flare impacts contributed to vibration in cargo condition, and appeared to be much more important than the linear springing for sea states, which contributed significantly to the fatigue damage. The stem flare impacts did only partly explain the measured vibration level.
- ⋆ The bow exit force exceeded occasionally the entry force, and the conventional slamming force might be only a minor part of the maximum force.
- ⋆ The vibration was confirmed to be sensitive to speed, and realistic estimates of the speed in different sea states were necessary.

The simplified method used to estimate the speed reduction was robust. The results were not sensitive to the total efficiency coefficient of the propulsion side. It predicted a significant speed reduction in relevant head sea conditions, e.g. 4-5kn reduction in 5m significant wave height.

An analytical expression for the natural frequency and deformation shape of a homogeneous beam including shear deformation was derived. The effect of realistic shear deformation on the natural frequency was in the order of 6% for the 2-node vibration mode, which was in perfect agreement with FE representation of the beam. Other effects such as axial end pressures due to waves as well as rotational mass and damping on the mode shape and frequency can be disregarded. A stiffness formulation of the segmented model with rotational springs was also proven to be in agreement with results from the model tests.

An estimate of the wave heights that will excite springing from linear excitation and sum frequency effects was made as a function of the Beaufort strength. The mean wave height is in the range of 1-2m for Beaufort 6-8, which contributed significantly to the total fatigue damage. The waves causing the sum frequency effect was in the order of half a meter higher than the waves causing linear springing.

A simple analytical solution of the dynamic response from a sinusoidal (a full period) impact was derived, and it illustrated that the dynamic response amplification can be up to 3 rather than 2 from conventional slamming (transient impulse like) impact load.

Predictions of linear springing require an accurate description of the oscillating loads along the hull and the deflection shape of the 2-node mode. Reliable linear springing predictions require a 3D hydrodynamic model, which includes the interaction between the steady and unsteady velocity potential. The springing predictions from sum frequency effects localized to the bow due to reflection of waves, or whipping predictions due to the excitation in the bow or stern will be less sensitive to the vibration shape. For linear springing using 3D theory, the antisymmetric mode shape and antisymmetric distribution of oscillating loads along the hull will make the numerical predictions less sensitive to the hump-hollow behaviour of the excitation versus the natural frequency, since the difference between humps and hollows will be reduced compared to 2D strip theory. 2D strip theory is thereby not considered as applicable for springing predictions of blunt vessels.

7.2.4 Model experiments

The wave calibration measurements confirmed the following features:

- ⋆ The wave frequency was as requested, but the amplitude deviated from the requested value. All waves must be measured.
- ⋆ The short waves had poor quality, and a large model was desirable to capture linear springing. The length with good quality was less than $80m$, and decreasing for increasing wave amplitude. The effective tank length for stationary springing response was less.
- ⋆ The measured irregular sea state parameters were as requested (H_S was slightly low), but the high frequency tail of the wave spectrum was uncertain.

The model was unconventionally large and cumbersome to handle. This resulted in a number of consequences.

- ⋆ In ballast condition the mass moment of inertia of each segment was too high, affecting the 3- and 4-node mode shapes. The stiffness of the three flexible joints were adjusted to achieve the requested Froude scaled 2-node springing frequency.
- ⋆ The same stiffness in all three joints was found suitable based on numerical predictions. The segmented model gave in any case somewhat high frequencies for the 3- and 4-node mode shapes.
- ⋆ The calibration revealed a significant uncertainty in the rotational stiffness.
- ⋆ The flexible joints, in particular the bearings, were not produced with satisfactory quality, and they gave both slightly nonlinear stiffness and nonlinear damping, which varied for the different combinations of bow shape and loading condition. The damping ratios were between 1 and 3.5%.
- ⋆ In one of the six combinations, i.e. ballast 2 condition, a linear damping ratio of 1.0% was achieved.

⋆ Disturbance of the wave pattern due to reflection from the walls were detected in the response at full speed in cargo condition, while in ballast condition the rigid body response peak of the bending moment transfer function was captured. Wall effects affected the rigid body response in lower speeds and irregular waves with long periods, but the effect on the overall fatigue damage was small.

The damping was an important factor influencing the springing level and the decay of the whipping cycles. The findings from ballast 2 condition confirmed that:

⋆ The damping was insensitive to speed.

⋆ Nonlinear hydrodynamic viscous effects were small and not detectable.

⋆ The rubber sealing and water leakage contributed with a damping ratio of about 0.15%.

⋆ The structural damping ratio was about 0.5%.

⋆ The hydrodynamic linear damping was about 0.35%, and cannot be disregarded in neither model or full scale.

⋆ The damping in the 2-node mode in air was insensitive to the frequency.

⋆ The damping increased with the number of nodes; 1.4% and 3.3% for the 3- and 4-node modes, respectively.

⋆ The spectral method predicted about 30% higher damping than the decay curves in the model tests and 60% higher in full scale.

⋆ The natural frequency decayed in higher sea states due to nonlinear stiffness and possibly due to changes in the average wet length and added mass.

⋆ The exponent n in the spectral method (used to predict the damping) was not representative of the high frequency tail behaviour of the wave spectrum neither for the model nor the full scale measurements.

The following results were obtained in the regular wave tests

⋆ The linear, second (sum frequency) and third order ($3 \cdot \omega_e = \omega_s$) resonance were easily excited in ballast condition, but the third order was less easily exited in cargo condition.

⋆ The linear springing peak in the bending moment transfer function exceeded the rigid body response peak by a factor of three in ballast condition in a speed of 15kn. The sum frequency springing response level was also higher than the rigid response peak.

⋆ The linear springing peak was sensitive to speed.

⋆ The sum frequency springing peak reduced slowly with speed, and it was still present at zero speed. Hump-hollow behaviour is expected in linear springing from the integration along the ship according to the generalised force in Eq.(2.23), since resonance is achieved at different wave lengths at different speeds. No hump-hollow behaviour was observed for the sum frequency effect, and this indicates that the dominating sum frequency effect was localized to the bow.

⋆ The hump-hollow behaviour in the bending moment transfer function was observed, but the hollows were far from zero.

⋆ The analytical surface motion in the bow at forward speed was slightly smaller than estimated from measurements in short waves, as explained by small run up not accounted for in the analytical estimate.

⋆ The added resistance in waves at forward speed agreed fairly well with the analytical short wave approximation. The measurements were sensitive to proper zero setting and measured calm water resistance. The nondimensional peak due to maximum rigid body motions in heave and pitch was in fair agreement with assumptions made in the involuntary speed reduction assessment.

The sum frequency transfer function was investigated in more detail. It was necessary to correct the response for the different damping levels. Moreover, only a few bichromatic waves were tested. This made it difficult to conclude, but the following was observed:

⋆ The second order transfer function gave an apparently constant springing response for increasing frequency difference of the bichromatic waves, but the monochromatic sum frequency waves gave a local peak above the bichromatic level.

⋆ The monochromatic response was higher in ballast than in cargo condition for 2 out of 3 bows, but the difference was moderate.

⋆ The bichromatic response was higher in ballast than in cargo condition, and the relative difference was larger than for the monochromatic waves.

⋆ Apparently, the bulb reduced the monochromatic response slightly.

⋆ The monochromatic response was reduced only moderately by using the wedge bow 3 in stead of the blunt bow.

Tests in irregular sea states were conducted at full and reduced speed. The following conclusions were derived:

⋆ At full speed in ballast condition the vibration damage was dominating (2/3 of the total), while it was reduced to 1/4 in cargo condition. The wave frequency damage was higher in cargo than in ballast condition.

- ⋆ There was no significant difference in the vibration damage between the three bow shapes considering the difference in the damping.

- ⋆ The vibration damage was smaller in the first part of the towing tank than in the second, indicating that the energy of the waves exciting linear springing was reduced along the towing tank. The vibration damage was also less in subsequent runs compared to the first run for each sea state due to 3D disturbance of the wave condition.

- ⋆ The vibration damage was confirmed to be sensitive to (the realistic) speed reduction. Considering the North Atlantic ore trade with head seas in ballast condition and following seas in cargo condition the vibration damage constituted 19% of the total at close to realistic speeds. The figure at full speed was 51%. In similar World Wide trade at realistic speed the vibration damage increased from 19 to 26%, but the total fatigue damage decreased to about half.

- ⋆ The effect of trim was investigated in four steep sea states in ballast condition. An increased forward draft of $1.6m$ reduced the vibration and wave damage by about 1/3, hence the reduced bottom forces were more important than the increased flare forces. This was in agreement with the simplified simulations indicating that the stem flare was unimportant in ballast condition.

- ⋆ Fair agreement was found between predictions of standard deviation WF stress by WASIM and the model tests in the different sea states.

An extrapolation procedure was employed to estimate the total fatigue damage from all the cells in a scatter diagram. Empirical relations were fitted to the measurements. The wave and vibration part was considered separately, and the following findings were found:

- ⋆ The dominating seas states for the wave frequency damage for ballast condition in head seas at realistic speeds in the North Atlantic trade were located at a 4-6m significant wave height and 9-11s zero up-crossing period, while for the vibration damage the dominating sea states were located between 3-5m and 8-10s.

- ⋆ For cargo condition the dominating contribution to wave frequency damage were located at the same place as in ballast condition, while the dominating sea states for the vibration damage was located between 4-5m and 9-10.5s.

- ⋆ At full speed, the location for the vibration damage was moved towards higher sea states and periods.

- ⋆ The dominating sea states were located at lower wave heights and periods for less harsh environments (i.e. for World-wide operation).

- ⋆ The locations of the dominating sea states differed only slightly for the different bow shapes.

⋆ For bow 2, the fatigue life in the North Atlantic was estimated to be 2.9 years by the response surface method (compared to 3.6 years from the simplest time extrapolation based on only the sea states tested). 5.9 years was estimated in World-wide trade. The contribution from the vibration damage was reduced from 18% for bow 2 to 10% for bow 3. Considering the higher damping for bow 3, the bow 3 was not an effective design to avoid the vibrations.

A method was developed to separate high whipping response from springing response by considering the envelope process of the 2-node vibration. Such a method is relevant in connection to further development of numerical tools. Based on input values of the springing peak from the linear and second order transfer function a criterion for the maximum slope of the envelope process was defined. A whipping event was detected when the maximum springing slope was exceeded. The method was applied to ballast 2 condition in head seas, and it was evaluated based on the amidship bending moment.

⋆ Whipping was identified in 31 of 33 sea states. The two sea states without whipping corresponded to tests at reduced speeds, and the criterion was not strictly valid. This means that whipping was identified in all valid sea states. The whipping events were also interpreted as whipping based on visual inspection, while some apparently smaller whipping events were not identified.

⋆ The magnitude of the whipping stress was of similar magnitude, in terms of standard deviation stress, as the springing stress already at a $3m$ significant wave height.

⋆ The relative importance of the whipping process increased with peak period and wave height.

⋆ The criterion was based on springing values obtained at full speed, hence it was somewhat strict when used at reduced speed. Still, the method detected whipping also at reduced speeds except in two sea states.

⋆ The probability of whipping per vibration cycle was up to 3%, meaning that a whipping event would occur in average once every minute in full scale.

The measured acceleration may also be used to indicate bow impacts. A criterion was tested in ballast 2 condition. It was based on the standard deviations of the acceleration. The criterion was not exceeded in any sea state, even though the acceleration amplitude was found to exceed the acceleration of gravity in one case. It is proposed that such a criterion should be based on amplitudes, since single important events may be smeared out by considering standard deviations. The ratio of the amplitude to three times the standard deviation was above one in case of flat bottom impacts.

A method was applied to compare the relative importance of the linear springing and the monochromatic sum frequency effect. It was presented as a function of the Beaufort strength, and two wave spectra were considered.

- ⋆ Both the linear and sum frequency excitation contributed.
- ⋆ The sum frequency effect started to dominate from Beaufort strength 6 and above.
- ⋆ The behaviour and magnitude depended on the wave energy spectrum. The Torsethaugen spectrum predicted higher vibration response than the wind based Pierson-Moskowitz in high wind speeds.

Different time series were displayed to reveal whipping and springing events in different situations, e.g.

- ⋆ Often, the first significant vibration half cycle in whipping corresponded to hogging indicating a downward force rather than an upward force.
- ⋆ Whipping occurred both when the water rised high up in the bow, and when the water surface reached the bottom bilge/flare area. The latter gave higher whipping response in both ballast and cargo condition, and it occurred also for bow 3.
- ⋆ Whipping occurred also for the conventional bottom impact, which was detected in realistic speeds in ballast, but not in cargo condition. Still, the first vibration half cycle occurred in hogging, and the next half cycle in sagging could increase in magnitude due to the subsequent slamming. The increase due to the upward force was not always observed, even though slamming pressures in the bow bottom was measured.
- ⋆ Slamming pressures in the aft ship were observed at realistic speeds, but came possibly from wall interaction. These slams did not give significant vibration responses.
- ⋆ Green seas were observed to give vibration, but the magnitude was small. The effect was somewhat unrealistic, since violent slamming occurred when the water struck the vertical superstructure, which was used to prevent the water from entering the model. This occurred in particular in cargo 2 condition when the stem flare was removed.
- ⋆ Violent horizontal slamming impacts were observed for the blunt bows in short small waves and in high forward speed. For regular wave amplitudes below $1m$, the water spray went occasionally above the deck level at the bow quarter in ballast condition. This was apparently caused by the combined effect of steady and unsteady waves and possible instabilities causing breaking waves and subsequent small relative angles between the stem and water surface (high speed camera may be utilized in future tests). The slamming itself was not considered important for the 2-node vibration.

7.2.5 Full scale measurements

Extensive full scale measurements of the large iron ore carrier were carried out by DNV. The measurement periods covered one year before and four year after strengthening in the North Atlantic iron ore trade. The evaluation was summarized in three publications. Recently, further investigation has also been carried out on a container vessel. First a few general comments are made.

⋆ Evaluation of wave data after a certain measurement period is not common practice. Proper calibration/setting/adjustment of the wave radar measurements was necessary to obtain reliable wave heights. Uncertainties were also related to the measured peak period, which was suggested to be compared by the peak period from the measured stress response spectrum for each half hour record.

⋆ The wind should be measured simultaneously with waves. The measured wind speed and angle should be corrected for the forward speed of the vessel, and the wind speed should also be corrected down to $10m$ above the still water level, which is the reference level of the Beaufort scale.

⋆ The time in ballast, cargo condition and in port was 33% each.

⋆ The routing reduced the fatigue damage to half considering the difference between the directional scatter diagram for North Atlantic trade (from the supplier Argoss) and the directional wave scatter diagram measured onboard. Accounting for the effect of routing, the fatigue lives from full scale and model tests were in fair agreement, although the relative importance of vibration damage differed.

⋆ The contributing vibration damage came from the vibration cycles superposed on the wave frequency stress cycles, rather from the high pass filtered damage isolated.

⋆ Based on the assessment of measurements it was found that the total damage based on the two slope SN-curve should be scaled by the ratio of stress level to the power of 4 rather than 3 for the relevant measurements (in case a higher section modulus or SCF were considered).

⋆ The full scale measurements carried out by DNV confirmed that the wave induced vibrations on a container vessel was of similar importance as documented for the ore carrier.

The following conclusions were derived based on the comparison between full scale and model tests.

⋆ The damping ratio in full scale was in the order of 0.5-0.6% for several ships, while the damping in the model tests was 1.0% in ballast 2 condition. The damping was basically linear.

⋆ The damping appeared to be only slightly higher in cargo than in ballast condition and only slightly higher after strengthening than prior to strengthening. The differences in damping ratio appeared to be in the order of 0.1%.

⋆ The damping predictions from the spectral method was well above the damping from whipping decay curves (0.8 versus 0.5% in ballast condition in full scale), and the spectral method should be used with care, i.e. the damping estimates should be corrected.

- ⋆ The measured speed reduction in head sea waves was in fair agreement with the predicted speed reduction from the simplified method. The measured speed reduction did not indicate voluntary speed reduction for this ship, and too low speed ($0kn$) was applied for the highest sea state of $9m$ significant wave height in the model tests.

- ⋆ The standard deviation of the wave frequency stress in head seas in full scale was somewhat below the WASIM predictions and model test results in ballast condition, probably due to wave energy spreading. Cargo condition displayed a similar magnitude of the wave frequency stress as ballast condition as a function of the wave height.

- ⋆ The standard deviation of the vibration stress obtained in the full scale measurements was higher than that of the model tests. The difference was due to lower damping in full scale and less wave energy in the high frequency tail in the model tests.

- ⋆ Whipping was predicted also in full scale. The whipping criterion was valid for pure head sea at full speed, which partly explained the smaller numbers of detected whipping events in full scale. The criterion needs to be refined to detect whipping in full scale accounting for realistic speed and wave spreading.

- ⋆ Prior to the strengthening of the ship, the vibration damage measured in full scale was 44% of the total damage for typical details in deck, compared to 18% according to the model tests. The difference was explained by e.g. smaller wave frequency damage and higher vibration damage in ballast condition in full scale, less wave frequency damage in cargo condition in full scale (encounter period effect), and significant contribution of vibration damage in cargo condition in full scale. The relative importance of the vibration may also increase for a range of off head sea directions in full scale.

- ⋆ The estimated fatigue life based on full scale measurements was 6.3 years, while it was 2.9 years from model tests (with bow 2). In addition to the effects mentioned above, the effect of routing was significant.

- ⋆ After strengthening, the natural period increased by 10% and the total damage decreased by 78% (based on SCF of 2.0). The vibration damage now constituted 40% of the total damage. Considering the annual variations, which were moderate, it can not be concluded that the difference due to the increased natural frequency was significant.

- ⋆ The most important significant wave height for both the wave and vibration damage for the vessel in ballast condition was $5m$. This was in fair agreement with the model tests, which predicted the dominating sea states to be from 4 to $6m$.

- ⋆ The fatigue damage in ballast condition increased rapidly with increased wave height in the full scale measurements, but the relative importance of the vibration damage decreased. This was also the case for the model tests.

- ⋆ Whipping from the model tests was observed to increase the hogging moment of up to 60% increasing the nominal stress level up to almost $100MPa$ at full speed in a sea

state with a significant wave height of $5m$. The importance of this elastic amplification was confirmed in a similar sea state in full scale, indicating $90MPa$ amplitude in a sea state with a significant wave height of $6m$. This suggests that further assessment of extreme events should be carried out, when such high levels are possible already at relative moderate sea states.

7.2.6 Contribution/major findings

A unique set of data related to the effect of wave induced vibrations on the fatigue damage was obtained based on extensive model tests in head seas considering two loading conditions and three bow shapes. New hypotheses were presented intended to increase the understanding and explaining a significant part of the vibration. The results were discussed in relation to published information, and the model test results were actually compared to measured stress results supplemented by wave radar recordings of the same vessel operating in a North Atlantic iron ore trade. Many uncertainties have been emphasized. The major findings are listed in the following.

⋆ Conventional ships experience wave induced vibrations, which contribute to the fatigue damage and extreme loading. Based on this investigation, the fatigue damage contribution from the wave induced vibrations is of similar importance as the fatigue damage caused by the wave frequency response. This is confirmed for blunt ships, and it has also been indicated for more slender vessels.

⋆ Existing prediction tools are not capable of predicting reliable vibration responses for fatigue assessment (and extreme loading) in particular for blunt ships.

⋆ Earlier full scale measurements/publications underestimated the contribution of fatigue damage due to the wave induced vibrations.

⋆ The vibration cycles superimposed on the conventional wave frequency cycles constituted the important contribution in harsh environment.

⋆ Linear theory is found to explain a significant part of the wave amplification measured at the stem line in the bow.

⋆ The added resistance in waves was sensitive to accurate measurements in the total resistance in waves and in calm water. It was confirmed that the linear theory for short waves was in reasonable agreement with the measurements.

⋆ The observations confirmed a significant modification of the waves along the hull giving small relative motion in the aft part, and the important vibration excitation was related to the bow area. The 3D effects must be accounted for to capture both the linear and second order excitation due to short waves.

- ⋆ Detectable whipping was identified in both the model tests and full scale measurements. The model tests indicated that the whipping process in ballast condition was of equivalent importance as the springing process in the fatigue dominating sea states.
- ⋆ Both springing and whipping excitation must be included in reliable numerical predictions of fatigue damage.
- ⋆ The total damping ratio of these large bulk carriers was in the order of 0.5-0.6% in ballast condition, and up to 0.1% higher in cargo condition. The damping from container vessels appeared as distinctly higher possibly due to the structural damping induced by the container stacks. If this is a general finding, this is beneficial for container vessels from a fatigue point of view.
- ⋆ The damping was basically linear and speed independent. The hydrodynamic damping appeared to be the dominating source in full scale based on the blunt vessels.
- ⋆ Increasing the natural frequency of the ship did not effectively reduce the relative importance of the vibration damage.
- ⋆ The involuntary speed reduction of importance for fatigue damage was considerable in the head seas in the North Atlantic trade. Realistic speeds must be estimated and used in reliable predictions of the vibration damage (and the wave frequency damage due to the number of encountered cycles). The involuntary speed reduction behavior in cargo and ballast condition as a function of the significant wave height was similar.
- ⋆ Model tests underestimated the contribution of vibration damage and overestimated the total damage for various reasons. Such tests need refinements to be used directly in design predictions.
- ⋆ The sum frequency effects were of equivalent to more important than the linear springing in the fatigue dominating sea states in the North Atlantic environment.
- ⋆ The most important sum frequency effect for blunt ships appeared to be caused by bow reflection, and the monochromatic sum frequency effect gave higher vibration than the bichromatic sum frequency effect, which had apparently a constant nondimensional resonance level as a function of the frequency difference.
- ⋆ Increasing the forward draft reduced the vibration level significantly, confirming that the bottom forces were more important than the stem flare forces.
- ⋆ The bulb may reduce the monochromatic sum frequency effect slightly, and the draft appeared to affect the bichromatic sum frequency effects more than the monochromatic sum frequency effect.
- ⋆ The stem flare impacts did not contribute significantly to the vibration in ballast condition, but the stem flare impacts contributed in cargo condition. The high whipping

responses originated in particular from rapid surface motion in the bilge area at the bow quarter in particular in ballast condition, but also in cargo condition. The whipping cycles started with its first half cycle in hogging due to a downwards force. This was also shown to be the dominating behavior in bottom impact, which occurred occasionally in ballast condition at realistic speeds in the highest sea state. The combined effect of steady wave elevation (negative) and amplification of the surface motion due to bow reflection increased the probability of bottom bilge flare impacts.

- The whipping was often excited by first a downward pull and then an upward push, which may increase the dynamic amplification with a factor of 3 (rather than 2).
- Whipping was often initiated when the bow was going upwards, but did also occur when the vessel had only small heave and pitch motions in steep and moderate sea states.
- The sharp bow did not result in a considerable reduction in the vibration damage. Strong, but reduced, sum frequency vibration was confirmed as well as whipping excitation in the bilge area at bow quarter. Reducing the springing effect by a drastic change in the bow geometry, was not an effective means to reduce the vibration damage, since the whipping was still present.
- Based on the results of the sharp bow and vibration damage measured on an old design container vessel, vibration damage will contribute also on slender ships with high powering.
- Routing reduced the total fatigue damage, but will increase the relative importance of the vibration damage.
- Routing should not be taken advantage of if the vibration damage is disregarded in the fatigue assessment.

7.3 Suggestions of further work

The objective of the present research was to reveal the important mechanisms causing wave induced vibrations and thereby additional fatigue damage. The findings and experience gained serve as basis for suggestions of further work. A few new questions were raised, and recommendations to increase the likelihood of success in future model tests are provided in the following.

The linear springing, sum frequency effects and whipping were identified as significant sources to the wave induced vibrations. The next step is to capture these effects in numerical simulations. The following efforts are suggested.

- The importance of the interaction between the nonlinear or linear steady and linear unsteady potential should be investigated in forward speed for the purpose of more

accurate linear springing predictions. A 3D code is necessary to capture the modification of the linear excitation along the hull.

- ⋆ The second order free surface condition (and body boundary conditions) should be included in a 3D code with forward speed. To limit the computational effort yet maintain the accuracy, a sub domain in the bow area, where the reflection effect is important, may be utilized, while the remaining mesh can be more coarse. Reflection effects due to different mesh size must be handled properly.
- ⋆ The whipping effect may be based on a 3D 'slamming' approach with a high frequency surface condition applied from zero draft to maximum draft. The time derivative of the added mass times the relative velocity may be determined from the wet panels below the disturbed water surface rather than the undisturbed incident waves often considered. The steady wave elevation ought to be included. The nonlinear effect considering Froude-Kriloff and restoring must also be applied below the disturbed water surface.

The decay of the sum frequency pressure versus the depth and the effective extent below the bottom for a vessel with forward speed were not successfully obtained from the pressure cells. Three approaches, which may be compared, are suggested to be used in further investigation.

- ⋆ A second order perturbation theory for total reflection against an infinite vertical wall moving forward with constant speed may be solved analytically, similar to the linear theory.
- ⋆ A 2D numerical model in the longitudinal direction may be analyzed with second order free surface condition and body boundary condition. A restrained model, which is not pitching or heaving, is a useful approximation for large ships.
- ⋆ Model testing may be carried out to measure the second order pressure of a restrained model (to avoid the high pressures from radiation). An academic bow shape with a small stem/bilge radius is recommended for comparison with the two theoretical approaches given above.

It may be possible to investigate the correlation between waves, bow bottom pressure and bending/vibration response to confirm which effects that contribute most. This may be carried out by Hilbert-Huang transformations or alternatively by Wavelet transformation.

It was confirmed that the real vessel vibrated significantly in head sea, but the vibration did not decay significantly with heading towards beam seas. The effect of wave energy spreading was also disregarded. These effects may be investigated in the ocean basin based on the same model. The pointed bow intended to reduce the reflection effect in head seas may also be less effective in quartering seas. The effect of various spectra is also of interest.

To differ between the linear and second order effects (and other effects), wave spectra may be modified to include or remove different part of the spectra to distinguish between the

important effects in irregular sea states, e.g. the high frequency tail of the spectra may be removed to exclude linear springing, or part of the spectrum may be removed to reduce the sum frequency excitation.

The horizontal forces due to fluctuations in the propeller trust or due to stem slamming were not considered as a contribution to the vertical vibration. It should be confirmed that these effects are small in amore sophisticated manner. The former was not relevant in the present model tests. The latter effect can not be excluded as a contribution to springing, even though the horizontal slamming force attacks the vertical stem close to the neutral axis in ballast condition. This has been indicated as a minor contribution in previous research, but it can be confirmed in model experiments by shifting the neutral axis by a refined flexible joint. For low speed (rpm) engines the half frequency effect due to pitch moment from the engine is also a possible excitation source to be investigated in heavy seas. This is e.g. relevant for large container vessels, but it is normally disregarded. Stern impacts are also a matter of concern, though not believed to be important for the sea states with high forward speed dominating the contribution to the fatigue damage. It may however be an issue in extreme events with lower forward speeds. It is relevant on ships with flat overhanging sterns.

Whipping due to flat bottom impacts was observed at realistic speeds in moderate sea states in ballast condition. Significant increase of the total bending moment due to the flexibility of the hull was observed. The effect of whipping on the extreme loading should be investigated in particular in ballast condition in head seas at realistic speeds. To reduce the influence of wall interaction in a towing tank, MLER waves may be utilized. Alternatively, an ocean basin may be used for this purpose.

The effect of higher modes on the fatigue damage and the maximum whipping response may be determined in order to simplify the model design dependent on ship type and excitation source. E.g. one flexible joint may be used if linear springing is insignificant and the excitation is localized in the bow or stern area.

The sharp pointed bow did not reduce the wave induced vibrations to an insignificant level. Considerable contribution from the vibration damage has also been confirmed for an old design container vessel. Hence, the effect of wave induced vibration on the fatigue damage should also be investigated by measurements (model and/or full scale) on slender ships such as new design container vessels (wider, longer and with more flare), Ro-Ro vessels, car ferries, cruise vessels and LNG vessels, which are all operating with low drafts. Realistic speeds should be considered in different typical seas states, preferably representative for harsh environments. Some of these ships may have limited possibilities for routing, and the effect of routing should be determined. All these ship may operate in hogging condition with tension in deck, hence in particular deck may be vulnerable to fatigue damage. Realistic damping ratios should be estimated by full scale measurements of different types of ships.

Based on the extensive model experiments carried out some practical recommendations are given with respect to the experimental procedures

- ⋆ For the purpose of investigating linear springing, the wave quality along a towing tank must be evaluated. The appropriate length of the tank with good quality waves should also be determined for the irregular sea states.

- ⋆ Based on the quality of the short waves, an optimal model size must be selected to have as much linear springing excitation as possible, but still such that wall effects at the realistic speeds encountered for the most important sea states do not contribute to the total fatigue damage.

- ⋆ Three flexible joints are proposed in order to include a realistic shape for the purpose of linear springing and higher order modes for whipping, but if the 2-node mode is dominant for whipping and nonlinear springing one flexible joint may be sufficient.

- ⋆ The neutral axis should be located as in the full scale ship.

- ⋆ An improved design of the flexible joints should be considered.

- ⋆ The mass distribution of each segment should be realistic, including the mass moment of inertia.

- ⋆ Towing lines at the bow and stern are sufficient, and transverse lines can be skipped as long as the pretension is enough for directional stability. The stiffness should give a surge period above the periods of interest. The towing forces should not affect the bending moment. Alternatively a self propelled model may be useful in order to obtain realistic speed and surge acceleration levels in various sea states, including variations in the same sea state.

- ⋆ Linear (or weak nonlinear) damping and linear bending stiffness should be confirmed prior and after the model tests to confirm the quality of the flexible joints. The damping ratio as low as 0.5 to 0.8% should be achieved. A higher damping may be acceptable, if this is properly documented based on full scale measurements.

- ⋆ Realistic speeds and vibration frequency must be considered.

- ⋆ Moment should be evaluated at 3 quarter lengths.

- ⋆ Using a heavy steel frame inside the model, the stability should be checked for slender vessels.

- ⋆ Calibration of the main sensors must be carried out incluing uncertainty analysis (as for the other main parameters).

⋆ The candidate must participate in all parts of the experiments. The candidate may be the only one who understands the intention of the experiments, and how it should be carried out. Common practise may not be sufficient.

References

ABS (1995). Guide for hull condition monitoring systems. Published by ABS, `http://www.eagle.com`. Updated December 2003.

Achtarides, T. (1979, October). Wave excited two-node vertical resonant vibration (springing) of flexible ships. In *Ocean Energy*, pp. 190–199. Marine Tech.

Achtarides, T. (1983). Design of multisegmented models for springing experiments. In *Prac. Design of Ships and Other Floating Struct.*, pp. 555–562. The 2nd Internl. Sympo. on Practical Design in Shipbuilding, Tokyo & Seoul.

Aksu, S., W. Price, and P. Temarel (1991). A three-dimensional theory of ship slamming in irregular oblique seaways. In *Advances in Marine Structures*, Volume 2, pp. 208–229.

Almar-Næss, A. (1985). *Fatigue Handbook, Offshore Steel Structures*. Tapir.

Antonides, G. (1975, July). A computer program for structural response to ship slamming (slam). Technical Report Report No. 4480, Naval Ship Research and Development Centre, Bethesda, Maryland, 20084 USA.

ASTM (1998). Standard practices for cycle counting in fatigue analysis. Annual Book of ASTM Standards, Section 3, Metals Test Methods and Analytical Procedures, Vol.03.01. Designation: E1049-85 (reapproved 1997), pp. 693-701.

Baba, E. (1976). Wave breaking resistance of ships. In *International Seminar on Wave Resistance*, pp. 75–92.

Belgova, M. (1962). Determination of overall bending moments caused by elastic vibrations of ships. In *Transactions of the Leningrad Institute of Water Transport, 1962*. Issue XXVIII, BSRA Translation No 1599.

Bell, A. and K. Taylor (1968, February). Wave-excited hull vibration. *Shipping World and Shipbuilder*, 412–426.

Bergan, P., P. Larsen, and E. Mollestad (1981). *Vibration of structures (In Norwegian)*. Tapir, Trondheim.

Bertram, V. (1998, August). Numerical investigation of steady flow effects in three-dimensional seakeeping computations. In *22nd Symp. on Naval Hydrodynamics*, pp. 417–431. National academy press.

Bingham, A., J. Hampshire, S. Miao, and P. Temarel (2001). Motions and loads of a trimaran travelling in regular waves. In *FAST*, pp. 167–217.

Birkenes, J. (2000, December). "vessel's name". Technical Note OCT760, DNV.

Bishop, R., W. Price, and P. Temarel (1986). On the hydroelastic response of swath to regular oblique waves. In *Advances in Marine Structures*, London, pp. 89–110.

Bishop, R., R. Taylor, and K. Jackson (1973). On the structural dynamics of ship hulls in waves. *Trans. of The Royal Inst. of Naval Arch. 115*, 257–274.

Brown, W. et al. (1981, March). Performance and seakeeping tests and analysis of a structural loads model of l/b=6 buoyant sidewall ses. Technical Report Rep. no. 2137, Davidson Laboratory.

Buarø, J. et al. (1999, December). *Veres Version 3.18 - Modal- and time-domain modules User's Manual*. MARINTEK.

Castberg, G. and S. Gran (1976, February). Signal processing of long term stress measurements on tt esso bonn. Technical Report Report No. 76-067, DNV.

Chen, Y. (1980, September). Ship vibrations in random seas. *J. of Ship Research 24*(3), 156–169.

Chezhian, M. (2003). *Three-dimensional analysis of slamming*. Ph. D. thesis, Dep. of Marine Tech., NTNU, Trondheim, Norway.

Clarke, J. (1986). Wave loading in warships. In *Advances in Marine Structures*, London, pp. 1–26.

Clauss, G., A. Kauffeldt, and K. Jacobsen (2007, June). Longitudinal forces and bending moments of a fpso. *Offshore Mech. and Artic Eng.*.

Cleary, W., J. Robertson, and R. Yagle (1971). The results and significance of the strength studies on the great lakes bulk ore carrier *Edward L. Lyerson*. In *SNAME Symposium on Hull Stresses in Bulk Carriers*.

Clough, R. and J. Penzien (1993). *Dynamics of Structures*. McGraw-Hill Education.

Coleman, H. and W. Steele (1989). *Experimentation and Uncertainty Analysis for Engineers*. Wiley, John Wiley & Sons, Inc.

DNV (1985). *Vibration Control in Ships*. Veritec Marine Tech. Consultants. General vibration by Noise and Vibration Group in DNV.

DNV (2000, March). Environmental conditions and environmental loads. Classification notes no. 30.5, DNV, Veritasveien 1, N-1322 Høvik, Norway.

DNV (2004, August). *SESAM USER MANUAL Wasim, Wave Loads on Vessels with Forward Speed* (3.2 ed.). DNV. DNV Report No. 2003-0209, rev. 3, 12th of August 2004.

DNV (2005a, July). Fatigue assessment of ship structures. Classification notes no. 30.7, DNV.

DNV (2005b). Guidance note, assessment of the additional fatigue effect of wave induced vibrations of the hull girder. Draft Guidance Note written by DNV, `http://www.dnv.com`. New version based on recent full-scale measurements carried out as a part of a Joint Industry Project.

DNV (2005c, March). *NAUTICUS HULL User Manual, Section Scantling, Hull Section Scantlings Acc. to DNV Rules* (9.5 ed.). DNV. DNV Report No. 96-03110.

DNV (2005d, January). *NAUTICUS User Manual, 3D BEAM* (9.0 ed.). DNV. DNV Report No. 98-0513; `http://www.dnv.com/software/`.

DNV (2005e, January). Part 6 chapter 11, hull monitoring systems. Published by DNV, `http://www.dnv.com`. Rules for Classification of Ships / High speed, Light Craft and Naval Surface Craft.

DNV (2005f, December). *SESAM User Manual, SESTRA, Superelement Structural Analysis* (8.3 ed.). DNV. DNV Report No. 91-7033, rev. 8.

DNV ET AL. (2004, June). Joint tanker project, common structural rules for double hull oil tankers. Published by ABS, DNV and Lloyd's Register, `http://www.jtprules.com`. Rules March 2005 Second Draft.

DOMNISORU, L. AND D. DOMNISORU (1997). The unified analysis of springing and whipping phenomena. In *Trans. of The Royal Inst. of Naval Arch.*, pp. 19–36.

DONG, Y. AND W. LIN (1992). Hydroelasticity and wave loads for a full-form ship with shallow draft. *J. of Ship Research 36*(2), 280–285.

DONOHO ET AL. (1999, October). Wavelab 802 for matlab5.x. Free downloads. Stanford University, USA `http://www-stat.stanford.edu/w̃avelab`.

DRIVEKLEPP, T. (2000, December). *Oblique Water Impact of Two Dimensional Bodies*. M.sc. thesis, Dep. of Marine Tech., NTNU, Trondheim, Norway.

DRUMMEN, I., G. STORHAUG, E. MOE, AND T. MOAN (2006). Experimental and full scale investigation of the importance of fatigue damage due to wave-induced vibration stress in a container vessel. In *Trans. of The Royal Inst. of Naval Arch.*, pp. 61–75. Design & Operation of container ships, 22-23th of Nov., London, UK.

DU, S., Y. WU, AND W. PRICE (1998). Forward speed effect on the structure responses of a ship travelling in waves. In K. ET AL. (Ed.), *Hydroelasticity in Marine Tech.*, pp. 117–131. RIAM, Kyushu University. Proc. of the 2nd int. conf.

DUDSON, E., H. RAMBECH, AND M. WU (2001, September, 4th-6th). Determination of wave bending loads on a 40 knot, long slender open topped containership through

model tests and hydrodynamic calculations with particular reference to the effects of hull flexibility on fatigue life. In *FAST*, pp. 177–190.

Ersdal, S. (2004). *An experimental study of Hydrodynamic Forces on Cylinders and Cables in Near Axial Flow*. Ph. D. thesis, Dep. of Marine Tech., NTNU, Trondheim, Norway.

Ertekin, R., S. Wang, X. Che, and H. Riggs (1995). On the application of the haskin-hanaoka relations to hydroelasticity problems. In *Marine Struct.*, Volume 8, pp. 617–629.

Faltinsen, O. and R. Zhao (1991a). Flow predictions around high-speed ships in waves. In *Mathematical approaches in hydrodynamics, SIAM*.

Faltinsen, O. and R. Zhao (1991b). Numerical predictions of ship motions at high forward speed. In *Philosophical Transactions of the Royal Society, Series A*, pp. 241–252.

Faltinsen, O. and R. Zhao (1997, September). Water entry of ship sections and axisymmetric bodies. Research Report AGARD-R-827, Advisory Group for Aerospace Research & Development (AGARD), North Atlantic Treaty Organization. Proc. of a Fluid Dyn. Panel Workshop on "High Speed Body Motion in Water", National Academy of Sci. in Ukraine.

Faltinsen, O. M. (1976). Lecture notes about sink-source methods and wave-induced loads. Dep. of Marine Tech., NTNU, Trondheim, Norway. Part of the Ph.D. course Hydrodynamic Aspects of Marine Structures 1.

Faltinsen, O. M. (1980). Lecture notes for sea loads and motions of ships (in norwegian). Dep. of Marine Tech., NTNU, Trondheim, Norway.

Faltinsen, O. M. (1990). *Sea Loads on Ships and Offshore Structures*. Cambridge, UK: Cambridge University Press.

Faltinsen, O. M. (2005). *Hydrodynamics of High-speed Marine Vehicles*. Cambridge University Press.

Faltinsen, O. M., K. Minsås, N. Liapis, and S. Skjørdal (1980, October). Prediction of resistance and propulsion of a ship in a seaway. In *Thirteenth Symposium on Naval Hydrodynamics*, pp. 505–529. The Shipbuilding Research Association of Japan, 1981.

Fathi, D. and A. K. Dahl (2000, December). *EmPower 3.0 - User Manual SKIPRO 2001: Empirical and Experimental Determination of Ship Resistance* (3.0 ed.). MARINTEK.

Ge, C. (2002). *Global hydroelastic Response of catamarans due to wetdeck slamming*. Ph. D. thesis, Dep. of Marine Tech., NTNU, Trondheim, Norway.

Ge, C., O. Faltinsen, and T. Moan (2002). Modelling of wetdeck slamming for a catamaran at forward speed. In *Proc. of OMAE'2002*. OMAE-02-28031, June, Oslo, Norway.

Gerritsma, J. et al. (1974). The effects of beam on the hydrodynamic charateristics of ship hulls. In *10th ONR Symp. on Naval Hydrodynamics*. Refined theory by Gerritsma and Beukelman, 1967.

Gerritsma, J. and W. Beukelman (1967, June). Analysis of the modified strip theory for the calculation of ship motions and wave bending moments. Technical Report Report No. 96S, Nederlands Ship Research Centre.

Glinka, G. and J. Kam (1987). Rainflow counting algorithm for very long stress histories. *Int. J. Fatigue 9*(3), 223–228.

Goodman, R. (1971). Wave-excited main hull vibration in large tankers and bulk carriers. In *Trans. of The Royal Inst. of Naval Arch.*, pp. 167–184.

Gran, S. (1974, September). Full scale measurements of wave excited vibrations of a 255 000 dwt tanker in ballast condition (progress report no. 5). Technical Report Report No. 74-41-S, DNV.

Gran, S. (1976, December). Full scale measurement of springing contribution to extreme stress and fatigue in a large tanker. Technical Report Report No. 76-417, DNV.

Gran, S. (1977, May). Springing - a short contribution. Unpublish paper from DNV. Presented on Seminar on Ship Vibrations 8th - pth of June 1977, sponsored by DNV.

Gran, S. (1980, December). Statistical description of wave induced vibratory stresses in ships. Technical Report Report No. 80-1171, DNV.

Gu, M., Y. Wu, and J. Xia (1989). Time domain analysis of non-linear hydroelastic response of ships. In *Prac. Design of Ships and Other Floating Struct.*, Volume 4 of *145*, pp. 1–6. 4th int. symp.

Gu, X. and T. Moan (2002). Long-term fatigue damage of ship structures under nonlinear wave loads. *J. of Marine Tech. 39*, 95–104.

Gu, X., J. Shen, and T. Moan (2003, September). Efficient and simplified time domain simulation of nonlinear responses of ships in waves. *J. of Ship Research 47*(2), 262–273.

Gunsteren, F. v. (1978, October). *Springing of ships in waves*. Ph. D. thesis, Delft University of Tech. (DUT), Delft, Holland.

Hamid, A. (1980+). The study on wave-induced hull vibration of a ship in regular waves. In *NN*, pp. II.b–1 to II.b–11.

Hansen, P., J. Jensen, and P. Pedersen (1995). Long term springing and whipping stresses in high speed vessels. In *FAST '95*, pp. 473–485.

Hansen, P. and A. Thayamballi (1995). Fatigue damage considering whipping arising from slamming. In *OMAE*, pp. 155–163.

Hashimoto, K., M. Fujino, and S. Motora (1978, December). On the wave-induced ship-hull vibration springing caused by higher-order exciting force. *J. of the Soc. of Naval Arch. of Japan 144*, 183–194. Written in japanese.

HBM (2004). Catman software. *www.hbm.com*.

He, H., A. Troesch, Y. Shin, and B. Kim (2004, June). Springing analysis of elastic vessels in head and oblique seas including nonlinear effects due to second order diffraction pressures. In *23rd International Conference on Offshore Mech. and Artic Eng.*, Proceedings of OMAE04. ASME. OMAE2004-51518.

Heller, S. and H. Abramson (1959). Hydroelasticity: A new naval science. In *J. Am. Soc. Naval Engr.*, Volume 71, pp. 205–209.

Helmers, J. (2001, March). Incident second order pressure induced by two sinusoidal waves. White paper from DNV.

Hermundstad, O., J. Aarsnes, and T. Moan (1994). Hydroelastic response analysis of high speed monohull. In F. et. al. (Ed.), *Hydroelasticity in Marine Tech.*, NTNU, Norway, pp. 245–259. Balkema, Rotterdam. Proc. of the 1st int conf.

Hermundstad, O., J. Aarsnes, and T. Moan (1999, March). Linear hydroelastic analysis of high-speed catamarans and monohulls. *J. of Ship Research 43*(1), 48–63.

Hoffman, D. (1972, April). Analysis of ship structural loading in a seaway. In *Marine Tech.*, Volume 9, pp. 173–194.

Hoffman, D. and R. van Hoof (1976). Experimental and theoretical evaluation of springing on a geart lakes bulk carrier. *Int. Shipbuilding Progress 23*, 173–193.

Huang, N. et al. (1998). The empirical mode decomposition and the hilbert spectrum for nonlinear and non-stationary time series analysis. In *Proc. The Royal Society London*, Volume A, pp. 903–995.

Hure, D. (1973). Dynamic measurements on a large tanker (in norwegian). *SKIP 12*, 26–31.

Huse, E. (1993). Experimental methods in marine hydrodynamics. UK-93-48, Dep. of Marine Tech., NTNU, Trondheim, Norway.

IACS (2004, July). Joint bulker project, iacs common structural rules for bulk carriers. Published by IACS, `http://www.jbprules.com`. Rules April 2005 Second Draft.

Jensen, J. (1993, September). *Non-linear wave load predictions for marine structures*. Ph. D. thesis, Dep. of Ocean Eng., Technical University of Denmark, DK-2800, Lyngby, Denmark.

Jensen, J. (1996, February). Wave-induced hydroelastic response of fast monohull ships. Paper presented at CETENA Seminar on Hydroelasticity for Ship Structural Design. Genoa, Italy.

Jensen, J. and D. Dogliani (1996). Wave-induced ship hull vibrations in stochastic seaways. In *Marine Struct.*, 9, pp. 353–387. Elsevier Science Limited.

Jensen, J. and P. Pedersen (1979). Wave-induced bending moments in ships - a quadratic theory. In *Trans. of The Royal Inst. of Naval Arch.*, Volume 121, pp. 151–165.

Jensen, J. and P. Pedersen (1981). Bending moments and shear forces in ships sailing in irregular waves. *J. of Ship Research 25*(4), 243–251.

Jensen, J. and J. Petersen (1992). Stresses in containerships. In *Schiffsfestigkeit und Shiffskonstruktion*, Volume 86, pp. 143–150+.

Jensen, J. and J. Vidic-Perunovic (2002). On springing of monohull ships. White paper presented at the Nordic Seminar "DNV Workshop on Fatigue Strength Analysis of Ships". Arranged at Kvaerner Masa Yards in Turku, Finland, January 25-26, 2002.

Jensen, J. and Z. Wang (1998). Wave-induced hydroelastic response of fast monohull displacement ships. In *Hydroelasticity in Marine Tech.*, pp. 411–417.

Jiao, G. and T. Moan (1990). Probabilistic analysis of fatigue due to gaussian load processes. *Probabilistic Eng. Mech. 5*(2), 76–83.

Jullumstrø, E. and J. Aarsnes (1993). Hull loads and response on high speed craft. In *Proceedings, RINA International Conference on High Speed Passanger Craft*, London, UK.

Kagawa, G. et al. (1977). Measurement of wave-induced vibrations on board a ship. In *Technical Bulletin of Mitsubishi Heavy Industry*, Volume 14 of *2*, pp. 107–112. Written in Japanese.

Kaplan, P. et al. (1969, June). An investigation of the utility of computer simulation to predict ship structural response in waves. Second Technical Report of Ship Structure Committee Project SR-174, TR-68-57, SSC-197, Oceanics, Inc. under Dep. of the Navy, U.S. Coast Guard.

Kaplan, P. and T. Sargent (1972, July). Further studies of computer siulation of slamming and other wave-induced vibratory structural loadings on ships in waves. Technical Report of Ship Structure Committee SSC-231, Oceanics, Inc., Plainview, New York.

Kapsenberg, G. and S. Brizzolara (1999). Hydro-elastic effects of bow flare slamming on a fast monohull. In *FAST*, pp. 699–705.

Kawakami, M. and T. Kiso (1976, March). On the wave induced ship hull vibration. In *Trans. of the West-Japan Soc. of Naval Arch.*, 51, pp. 31–40. Written in japanese.

Kawakami, M., J. Michimoto, and K. Kobayashi (1977). Prediction of long term whipping vibration stress due to slamming of large full ship in rough seas. In *Int. Shipbuilding Progress*, pp. 83–110.

Keane, A., P. Temarel, X. Wu, and Y. Wu (1991). Hydroelasticity of nonbeamlike ships in waves. *Phil. Trans. R. Soc. London 334*, 339–355.

Kumai, T. (1972). Wave-induced force exciting hull vibration and its response. In *Trans. of the West-Japan Soc. of Naval Arch.*, 44.

Kumai, T. (1974). On the exciting force and response of springing of ships. In *NN*.

Lacey, P. and H. Chen (1995, January). Improved passage planning using weather forecasting, maneuvering guidance, and instrumentation feedback. In *Marine Tech.*, 3, pp. 1–19.

Lacey, P. and R. Edwards (1993, July). Arco tanker slamming study. In *Marine Tech.*, 3, Long Beach, California, pp. 135–147.

Langen, I. and R. Sigbjørnsson (1979). *Dynamic analysis of structures (In Norewegian)*. Tapir.

Lekkerkerker, J. (1979, September). Wave-induced vibrations of a ship hull with internal damping. In *Proceedings of Euromech. Colloquium 122*, Paris, France, pp. 35–81.

Lewis, E. (1954). Ship model tests to determine bending moments in waves. In *Trans. of The Soc. of Naval Arch. and Marine Eng.*, Volume 62.

Lin, W., Y. Shin, and J. Chung (1997). Nonlinear predictions of ship motions and wave loads for structural analysis. In *OMAE*, Volume 1A, pp. 243–250. ASME.

Little, R., E. Lewis, and F. Bailey (1971). A statistical study of wave-induced bending moments of large oceangoing tankers and bulk carriers. In *SNAME*, pp. 117–168. Presented at SNAME annual meeting in New York, November 11th and 12th 1971.

Lopes, T. and A. Troymann (1989, October). Experimental study of springing vibration in waves. In *Fourth International Symposium on Practical Design of Ships and Mobile Units*, Volume 2, pp. 46.1–46.6. Varna, Bulgaria.

Malenica, S. et al. (2003). Hydroelastic response of a barge to impulsive and non-impulsive wave loads. In *Hydroelasticity in Marine Tech.*, pp. 107–115. University of Oxford. Proc. of the 3rd int. conf.

Mathews, S. and L. Kawerninski (1967). Main hull girder stresses s.s. ontario power. Technical report.

Mathisen, J. (1988). *Analysis of Experiments and a Functional Model for Ship Rolling*. Ph. D. thesis, Brunel University, Uxbridge, Middlesex, UK.

Mathisen, J. (2001, November). Springing analysis routine. DNV Internal memo no.: OCT760/JMAT/76000000-J-1979, rev. 2.

McGoldrick, R. (1935, February). A study of ship hull vibration. Technical Report 395, United States Experimental Model Basin.

McGoldrick, R. (1960, June). Rudder-excited hull vibration on uss forrest sherman (dd 931) (a problem in hydroelasticity). Technical Report 1431, Dep. of the Navy, David Taylor Model Basin.

McGoldrick, R. and V. Russo (1956, July). Hull vibration investigation on ss gopher mariner. Technical Report Report No. 1060, David Taylor Model Basin.

Mei, C. C. (1989). *The Applied Dynamics of Ocean Surface Waves*. Singapore: World Scientific Publishing Co. Pte. Ltd.

Miros (2003). Wavex marine radar wave extractor. *www.miros.no*. Brochure.

MIT (1998). Wamit user manual versions 6.3, 6.3pc, 6.3s, 6.3s-pc. WAMIT, Inc. USA, www.wamit.com.

Moe, E. and G. Holtsmark (2005). Estimation of additional fatigue effect of wave induced hull girder vibrations (draft). Technical Report Report No. 2005-0130, DNV.

Moe, E., G. Holtsmark, and G. Storhaug (2005). Full scale measurements of the wave induced hull girder vibration of an ore carrier trading in the north atlantic. In *Trans. of The Royal Inst. of Naval Arch.* Conference on Design & Operation of bulk carriers, 18-19th of Oct., London, UK.

Moeyes, G. (1976). Measurements of exciting forces in short waves. Technical Report Delft Progress Report no. 2, Shipbuilding and Shipping, pages 87-107, Ship Hydrodynamics Laboratory, Delft University of Tech.

Mürer, C. (1995, August). Dnv hull structural rules, developement, background, motives 1995. Published by DNV. Report DSO-275.

Myrhaug, D. (1998). Hydrodynamic and ocean environment. UK-98-58, Dep. of Marine Tech., NTNU, Trondheim, Norway.

Myrhaug, D. and Kvålsvold (1995, May). Comparative study of joint distributions of primary wave characteristics. *J. of Offshore Mech. and Arctic Eng. 117*, 91–98.

Myrhaug, D. and J. Kvålsvold (1992). Comparative study of joint distributions of primary wave characteristics. In *Offshore Mech. and Artic Eng.*, Volume II, pp. 291–299. ASME. Safety and Reliability.

Naess, A. (1996). A second-order theory for the response statistics of wave induced ship hull vibrations in random seas. In *Marine Struct.*, 9, pp. 389–408. Elsevier Science Limited.

Napa (Napa Ltd founded 1989). Napa, the naval architectural package. Program developed by Napa Ltd, Helsinki, Finland. `http://www.napa.fi`.

Nechita, M. (2001). *Study on a seakeeping computation method of ships considering fully-nonlinear steady wave field*. Ph. D. thesis, Gradyate School of Eng. of Hiroshima University, Higashi-Hiroshima, Japan.

Newland, D. (1993). *An introduction to Random Vibrations, spectral & Wavelet Analysis*. Pearson Education Limited.

Newman, J. N. (1977). *Marine Hydrodynamics*. Cambridge, Massachusetts, USA: The MIT Press.

Nordenstrøm, N. et al. (1970, September). Some notes on observed springing. In *Proceedings of the 4th International Ship Structures Congress, The Society of Naval Architects of Japan*, pp. 105–110. Tokyo.

Ochi, M. and L. Motter (1973, November). Prediction of slamming characteristics and hull responses for ship design. *Trans. of The Soc. of Naval Arch. and Marine Eng. 81*, 144–176.

Ohkusu, M. (1980, May). A review of japanese studies of ship springing. Technical Report Report No. MA-RD-940-80062, Dep. of Naval Architecture & Marine Eng., The University of Michigan, Ann Arbor, MI 48109, USA.

Økland, O. (2002). *Numerical and Experimental investigation of whipping in twin hull vessels exposed to severe wet deck slamming*. Ph. D. thesis, Dep. of Marine Tech., NTNU, Trondheim, Norway.

Økland, O. et al. (2003). Numerical assessment of segmented test model approach for measurements of whipping response. In *FAST 2003*.

Price, W. and Y. Wu (1985). Hydroelasticity of marine structures. In *Theoretical and Applied Mech.*, Netherlands, pp. 311–337. Elsevier Science Publishers B.V.

Price, W. and Y. Wu (1986, January). Hydroelasticity of marine structures. Technical Report Report No. 86001, english version, China Ship Scientific Research Center, CSSRC, P.O. Box 116, Wuxi, Jiangsu, China.

Rüdinger, F. (2003). Identification of springing and wave excitation of ship from stochastic response records. White paper in "DNV workshop of springing 2002".

Salvesen, N., E. Tuck, and O. Faltinsen (1970). Ship motions and sea loads. In *Trans. of The Soc. of Naval Arch. and Marine Eng.*, Volume 78, pp. 250–287.

Saunders, H. (1965). *Hydrodynamics in Ship Design*. SNAME.

Sauvalle, G. (1960). Measures extensometirques sur la coque du mineralier, jean schneider. In *ATMA*.

Schetzen, M. (1980). *The Volterra and Wiener theories of nonlinear systems*. Wiley-Interscience, John Wiley & Sons.

Schlacter, G. (1989). Hull girder loads in a seaway including nonlinear effects. *Schifftechnik 36*, 169–180.

Schlick, O. (1884). On the vibration of steam vessels. In *RINA Transaction and Annual Report*.

Sele, H. O. (2001, May). *Springing of Ships (In Norwegian)*. M.sc. thesis, Dep. of Marine Tech., NTNU, Trondheim, Norway.

Senjanovic, I., S. Tomasevic, and J. Parunov (2001). Analytical solution of pontoon transient vibration related to investigation of ship whipping due to slamming. In *Int. Shipbuilding Progress*, Volume 48 of *4*, pp. 305–331.

Shiffman, M. and D. C. Spencer (1951, November). The force of impact on a cone striking a water surface (vertical entry). In *Communications on Pure and Applied Mathematics*, Volume 4.4, New York, USA, pp. 379–417. New York University Institute for Mathematics and Mech.: Interscience Publishers, Inc.

Skjørdal, S. (1974). Vibration measurements on m/s 60000 dwt. bulk (in norwegian). Technical Report Report No. 74-96-C, DNV.

Skjørdal, S. (1978, January). *A rational strip theory approach for the evaluation of springing*. Ph. D. thesis, Dep. of Marine Tech., NTNU, Trondheim, Norway.

Skjørdal, S. and O. Faltinsen (1980, June). A linear theory of springing. *J. of Ship Research 24*(2), 74–84.

Slocum, S. (1983, August). *Theoretical evaluation of nonlinear springing excitation and response*. Ph. D. thesis, The University of Michigan, College of Eng., The Dep. of Naval Architecture and Marine Eng., Ann Arbor, Michigan 48109, USA. Report no. 273.

Slocum, S. and A. Troesch (1982, September). Non-linear ship springing experiments. Technical Report MA-RD-940-80056, report 266, February 1983, Dep. of Naval Arch. and Marine Eng., College of Eng., The Univ. of Michigan.

Søding, H. (1975, March). Springing of ships - consideration and computations for the development of a forecasting procedure. In *Sonderforschungsbereich 98*, 7, pp. 1–29. Lehrstuhl und Institut für Entwerfen von Schiffen und Schiffstheorie.

Stansberg, C. (2004, July). Wave field homogeneity in marintek's towing tank i+iii. Technical report, MARINTEK, Trondheim, Norway. Draft report.

Stavovy, A. and S. Chuang (1976). Analytical determination of slamming pressures for high-speed vehicles in waves. *J. of Ship Research 20*, 190–198.

St.Denis, M. and W. Pierson (1953). On the motion of ships in confused sea. In *Trans. of The Soc. of Naval Arch. and Marine Eng.*, Volume 61.

Stiansen, S., A. Mansour, and Y. Chen (1978). Dynamic response of large great lakes bulk carriers to wave-excited loads. In *SNAME Transactions*, Volume 85, pp. 174–208.

Storhaug, G. and E. Moe (2007, October). Measurements of wave induced vibrations onboard a large container vessel operating in harsh environment. *Prac. Design of Ships and Other Floating Struct. 1*.

Storhaug, G., E. Moe, and G. Holtsmark (2006, June). Measurements of wave induced hull girder vibrations of an ore carrier in different trades. In *Offshore Mech. and Artic Eng.*, Hamburg, Germany. ASME.

Storhaug, G., J. Vidic-Perunovic, F. Rüdinger, G. Holtsmark, J. B. Helmers, and X. Gu (2003). Springing/whipping response of a large ocean going vessel - a comparison between numerical simulations and full scale measurements. In *Hydroelasticity in Marine Tech.*, pp. 117–131. Third int. conf.

Strating, J. (1973, May). *Fatigue and Stochastic Loading*. Ph. D. thesis, Delft University of Tech., DUT, Delft, Nederlands.

Takarada, N. et al. (1993, December). R&d of a displacement-type high speed ship. In *FAST*, Volume 1, Yokohama, Japan, pp. 341–359. Proc of the 2nd int. conf. on Fast Sea Transportation.

Tasai, F. (1974). On the calculation methods of wave induced vibrations of ships. In *Trans. of the West-Japan Soc. of Naval Arch.*, 48, pp. 163–180. Written in japanese.

Tasai, F., Y. Yamasaki, K. Kawasumi, T. Kita, and Y. Koga (1971). Investigation on the seakeeping performance of m.t. b-maru. *J. of the Soc. of Naval Arch. of Japan* (42), 99–114. Written in japanese.

Todd, F. (1961). *Ship Hull Vibration*. Edward Arnold (Publishers) LTD.

Tongeren, M. (2002). *Analysis of Springing of Large Ships by a Rankine Panel Method*. M.sc. thesis, Technological University of Delft, Holland.

Torsethaugen, K. (1996). Model for a double peaked wave spectrum. Technical Report STF22 A96204, SINTEF Civil and Environmental Eng., Coastal and Ocean Eng. Includes errata, dated 6th of August 1998 (significant bugs in earlier version).

Troesch, A. (1984, June). Wave-induced hull vibrations: An experimental and theoretical study. *J. of Ship Research 28*(2), 141–150.

Trulsen, K. and H. Krogstad (2001). Empirical mode decomposition of ocean wave records. Dep. of Mathematical Sciences, NTNU, and SINTEF Applied Mathematics, Trondheim, Norway.

Veltcheva, A. (2001, December). Wave and group transformation by hilbert spectrum. *Coastal Eng. J. 44*(4), 283–300.

Vidic-Perunovic, J. (2005, September). *Springing Response due to Bidirectional Wave Excitation*. Ph. D. thesis, Dep. of Ocean Eng., Technical University of Denmark.

Vidic-Perunovic, J. and J. J. Jensen (2004, August). Springing response due to directional wave field excitation. In *9th symp on Practical Design of Ships and Other Floating Structures*, Volume 2, Hamburg, Germany, pp. 869–875.

Walderhaug, H. (1991, Spring). Resistance, propulsion and manouvering (in norwegian). UK-91-26, Dep. of Marine Tech., NTNU, Trondheim, Norway.

Wang, L. (2001). *Probabilistic analysis of nonlinear wave-induced loads on ships*. Ph. D. thesis, Dep. of Marine Tech., NTNU, Trondheim, Norway.

Watanabe, I. and H. Sawada (1985, December). Effects of elastic responses to the longitudinal bending moment in two-directional irregular waves. *J. of the Soc. of Naval Arch. of Japan 158*, 1–12.

Watanabe, I. and C. Soares (1999). Comparative study on the time-domain analysis of non-linear ship motions and loads. In *Marine Struct.*, pp. 153–170.

Watanabe, Y. (1968). On a cause of whipping. In *Report of the West-Japan Ship Structure Committee*, 6. Written in Japanese.

White, F. M. (1999). *Fluid Mech.* WCB McGraw-Hill.

Winterstein, S. et al. (1994). Springing and slow-drift responses: Predicted extremes and fatigue versus simulations. In *BOSS-94*.

Wirshing, P. (1981). Probability based fatigue design criteria for offshore structures. Technical Report API-PRAC 80-15, The University of Arizona.

Wist, H. (2004). *Statistical properties of successive ocean wave parameters*. Ph. D. thesis, Dep. of Marine Tech., NTNU, Trondheim, Norway.

Wu, M. (2002, May). *LATWAB - A Computer Program for Linear Static Response and Dynamic Eigenmode Analysis of Non-Prismatic Thin-Walled Beams, Version 1.0* (1.0 ed.). MARINTEK. Flexible input to VERES.

Wu, M., J. Aarsnes, O. Hermundstad, and T. Moan (1996). A practical prediction of wave-induced structural responses in ships with large amplitude motion. In *Proc. 21st Symp. of Naval Hydrod.*, pp. 438–452.

Wu, M. and O. Hermundstad (2002). Time-domain simulation of wave-induced nonlinear motions and loads and its applications in ship design. In *Marine Struct.*, pp. 561–597.

Wu, M., O. Hermundstad, and T. Moan (1993). Hydroelastic analysis of ship hulls at high forward speed. In *FAST*, Yokohama, Japan, pp. 699–711.

Wu, M. and T. Moan (1996, June). Linear and nonlinear hydroelastic analysis of high-speed vessels. *J. of Ship Research 40*(2), 149–163.

Wu, Y. et al. (1991, December). Two eng. approaches to hydroelastic analysis of slender ships. Technical Report Report No. 91004, english version, China Ship Scientific Research Center, CSSRC.

Xia, J., Z. Wand, and J. Jensen (1998). Non-linear wave loads and ship responses by a time-domain strip theory. In *Marine Struct.*, 11, pp. 101–123.

Xia, J. and Z. Wang (1997). Time-domain hydroelasticity theory of ships responding to waves. *J. of Ship Research 41*(4), 286–300.

Xia, J., Z. Wang, X. Gu, J. Shen, and Y. Wu (1995). Numerical simulations of the wave-induced non-linear bending moment of ships. In *OMAE*, Volume 2, pp. 147–153. ASME.

Yagle, R. (1963). Long term strain measurements aboard a great lakes ore carrier. In *SNAME*.

Yamamoto, Y., M. Fujino, and T. Fukasawa (1978, June). Motion and longitudinal strength of a ship in head sea and the effects of non-linearities. *J. of the Soc. of Naval Arch. of Japan 143*, 91–100.

Zhao, R. and O. Faltinsen (1998). Water entry of arbitrary axisymmetric bodies with and without flow separation. In *22nd symp on Naval Hydrodyn.*, pp. 652–664.

Appendix A

Theory

A.1 Potential theory

Hydrodynamic theory for the purpose of calculating global loads on ships in an engineering context assumes, in general, potential theory, which is based on an incompressible and inviscid liquid with irrotational flow. The velocity vector, $\mathbf{V}(x, y, z, t)$, can be expressed by the velocity potential, Φ, as

$$\mathbf{V} = \nabla\Phi \tag{A.1}$$

The assumption of irrotational liquid states that the curl of the velocity field is zero

$$\overline{\omega} = \nabla \times \mathbf{V} = 0 \tag{A.2}$$

The assumption of incompressible liquid with constant density gives a simple relation for conservation of mass stating that the divergence of the velocity field is zero

$$\nabla \cdot \mathbf{V} = 0 \tag{A.3}$$

The additional assumption of invicid liquid is related to lack of shear forces on a liquid element.

Combining the definition of the velocity potential and the zero divergence yields Laplace equation. It expresses the conservation of the mass in the liquid domain based on the velocity potential. This is the governing equation in potential theory, and it must be satisfied in the whole liquid domain.

$$\nabla^2\Phi = 0 \tag{A.4}$$

Laplace equation does not have much meaning in practice unless boundary conditions are applied, and these may be highly nonlinear. Before considering the boundary conditions, it is necessary to introduce Bernoulli's equation, which can be expressed as

$$p + \rho g z + \rho \frac{\partial \Phi}{\partial t} + \frac{1}{2}\rho \mathbf{V} \cdot \mathbf{V} = C \tag{A.5}$$

where z is the distance from the still water line (positive upwards). The equation relates the hydrodynamic and "hydrostatic" ($-\rho g z$) pressure to the velocity field and velocity potential. C is a constant.

The boundary condition at the free surface states that a particle on the surface will remain on the surface. This is referred to as the kinematic free surface condition and can be written

$$\frac{\partial \zeta}{\partial t} + \frac{\partial \Phi}{\partial x}\frac{\partial \zeta}{\partial x} + \frac{\partial \Phi}{\partial y}\frac{\partial \zeta}{\partial y} - \frac{\partial \Phi}{\partial z} = 0 \text{ on } z = \zeta(x, y, t) \tag{A.6}$$

It is nonlinear, since both the wave elevation, ζ, and the velocity potential are unknown.

Bernoulli's equation is used to express the second free surface condition referred to as the dynamic free surface condition. The insignificant surface tension is neglected. The dynamic free surface condition states that the pressure on the surface is identical to the atmospheric pressure, p_a, which is normally assumed to be constant (zero) and consequently disregarded.

$$g\zeta + \frac{\partial \Phi}{\partial t} + \frac{1}{2}(\nabla \Phi \cdot \nabla \Phi) = 0 \text{ on } z = \zeta(x, y, t) \tag{A.7}$$

The second free surface condition is also nonlinear. It may be convenient to merge the two surface conditions into one written as

$$\frac{Dp}{Dt} = 0 \text{ on } z = \zeta(x, y, t) \tag{A.8}$$

where $\frac{D}{Dt}$ is the material (substantial) derivative giving the change of pressure when following a liquid particle on the surface.

The body boundary condition on the hull surface is generally defined as

$$\frac{\partial \Phi}{\partial n} = \mathbf{U} \cdot \mathbf{n} \tag{A.9}$$

where $\mathbf{n}$ is the normal vector on the hull, pointing into the liquid volume. The boundary condition states that there is zero flux through the hull. The $\mathbf{U}$ defines the velocity vector of the vessel in its rigid and flexible modes. The coordinate (reference) system is normally body fixed, which means that the velocity potential includes the free stream velocity representing the vessel's speed. The bottom (or wall) boundary condition is handled in a similar

manner.

The last conditions are the far field conditions and radiation conditions (in the time domain). These imply that waves created by a moving ship or by reflection from the ship radiate away from the ship, and the disturbance from the ship approaches zero when the distance from the ship goes to infinity.

The Laplace equation with boundary conditions can be solved by various methods. The boundary element method (BEM) is the basis of the programs WASIM, VERES, SINO and SOST, which were used by Storhaug et al. (2003). The governing equation is the Green's theorem, which is written

$$\phi(x,y,z,) = -\frac{1}{4\pi}\int\int_S (\psi\frac{\partial\phi}{\partial n} - \phi\frac{\partial\psi}{\partial n})dS \tag{A.10}$$

where ψ is a source and $\frac{\partial\psi}{\partial n}$ is a dipole. The term ϕ becomes the strength of the dipole and the term $\frac{\partial\phi}{\partial n}$ becomes the strength of the source.

To solve Green's theorem, the surfaces are divided into segments with a certain distribution of the singularities. The strength is solved by letting the field point approach each of these segments and by using the boundary condition. Further description of basic potential theory and liquid mechanics can be found in many text books, e.g. (Faltinsen 1976; Newman 1977; Mei 1989; Faltinsen 1990; White 1999).

A.1.1 Calculation of high frequency added mass

The added mass, represented by the high frequency asymptote, was used to estimate the natural frequencies of the flexible modes. A 2D BEM theory was derived to calculate the sectional added mass. This is briefly explained in the following.

The asymptotic high frequency added mass in heave was solved by a double body approximation in heave in infinite liquid. The wet surface up to the still water was mirrored about the still water line. The surface was divided up into straight elements. On each element a linear distribution of dipoles and sources were assumed. The 2D the Green's theorem is written

$$\phi(q) = -\frac{1}{2\pi}\int_S (\phi(p)\frac{\partial\ln(Z(p,q))}{\partial n(p)} - \ln(Z(p,q))\frac{\partial\phi(p)}{\partial n(p)})dS(p) \tag{A.11}$$

where Z is the complex notation of the distance between the field point q and the body coordinate p. The use of complex sources and dipoles was found convenient in 2D.

The source and dipole expressions were integrated for each element in its local coordinate system. Thereafter, the local coordinate system was transformed into the global coordinate

system. The boundary condition defines the strength of the source as

$$\frac{\partial \phi(p)}{\partial n(p)} = \mathbf{U} \cdot \mathbf{n} = \dot{\eta}_3 \mathbf{n}_3 \tag{A.12}$$

where the velocity potential is the unknown. Letting q approach p on each end of each element, a set of linear equations were established and could be solved for the unknown strength of the dipole. Continuity of the strength from element to element had to be ensured. The equation to be solved is written

$$(\mathbf{D} + 2\pi\mathbf{I})\phi = \mathbf{S}\frac{\partial \phi}{\partial n} \tag{A.13}$$

where $\mathbf{D}$ is the matrix expression for the unit dipoles, $\mathbf{S}$ is the matrix for the unit sources and $\mathbf{I}$ is the unit diagonal matrix. ϕ and $\frac{\partial \phi}{\partial n}$ are vectors with $N+1$ unknowns for the N elements. The method is further described in Appendix A.1.2, since the formulation differs slightly from what is often encountered in the literature.

A.1.2 Detailed numerical implementation of 2D BEM

A linear strength distribution for dipoles and sources was chosen, as illustrated in Figure A.1. The singularity strength at element i is expressed as

$$\sigma(\overline{x}) = \frac{\overline{x}}{ds}\phi_i + \frac{ds - \overline{x}}{ds}\phi_{i+1} = B + A\overline{x} \text{ for } 0 \leq \overline{x} \leq ds \tag{A.14}$$

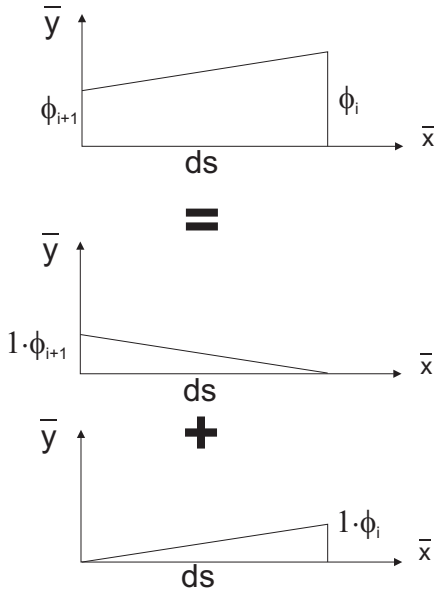

Figure A.1: *Strength distribution of singularities for an element in the local coordinate system. ϕ_{i+1} and ϕ_i are singularity strengths for the dipole.*

The integral for the source is written

$$F_S(Z) = \int_0^{ds} (B + A\overline{x}) \ln(Z - \overline{x}) d\overline{x} =$$
$$B[-(Z - \overline{x}) \ln(Z - \overline{x}) - \overline{x}]_0^{ds} + A[\frac{1}{2}(\overline{x}^2 - Z^2) \ln(Z - \overline{x}) - \frac{1}{4}(Z - \overline{x})^2]_0^{ds} \quad \text{(A.15)}$$

Similarly, the integral for the dipole is written

$$F_D(Z) = -\int_0^{ds} (C\overline{x} + D) \frac{i}{Z - \overline{x}} d\overline{x} =$$
$$iD \ln(\frac{Z - ds}{Z}) + iC[ds + Z \ln(\frac{Z - ds}{Z})] \quad \text{(A.16)}$$

where C is similar to A, and D is similar to B, but in general with different values. The complex function $F(Z) = \phi + i\psi$ describes both the velocity potential and the stream function in 2D. The velocity field was found from $\frac{dF(Z)}{dz} = u - iv$. For the source this becomes

$$\frac{dF_S(Z)}{dz} = -B \ln(\frac{Z - ds}{Z}) - A[Z \ln(\frac{Z - ds}{Z}) - ds] \quad \text{(A.17)}$$

while for the dipole it becomes

$$\frac{dF_D(Z)}{dz} = i[\frac{1}{Z - ds} - \frac{1}{Z}](D + CZ) + iC \ln(\frac{Z - ds}{Z}) \quad \text{(A.18)}$$

For the same strength distribution $A = C$ and $B = D$, the potential of the dipole can be related to the velocity of the source as

$$F_D(Z) = -i\frac{dF_S(Z)}{dz} \quad \text{(A.19)}$$

The velocity fields for a unit source and dipole strength are shown in Figure A.2 and A.3. The dipole distribution looks like two end vortices, which can be shown.

When arranging segments to define the geometry, it was necessary to convert the global coordinate system into a local coordinate system. These coordinate systems are shown in Figure A.4. The $Z = X + iY$ in the global system is converted to the $\overline{z} = \overline{x} + i\overline{y}$ in the following way

$$\overline{z} = \frac{(Z - Z_{i+1}) \cdot (Z_i - Z_{i+1})^*}{ds} \quad \text{(A.20)}$$

The * denotes the complex conjugate.

The numbering convention in Figure A.5 was chosen for a closed geometry. The geometry stretched out along the X axis is displayed in Figure A.6. If the geometry of the hull and

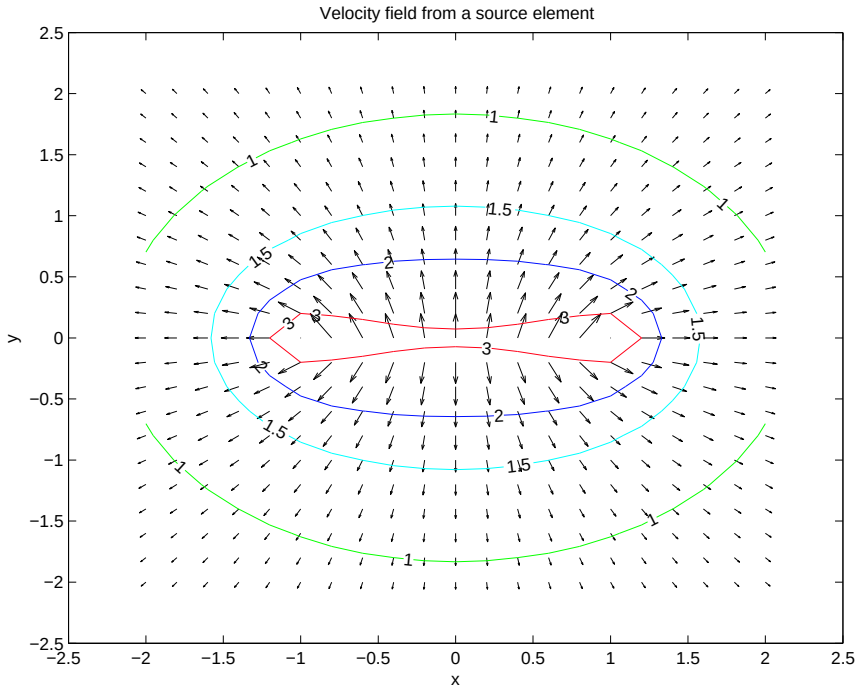

Figure A.2: *Velocity field for a segment stretching from (-1,0) to (1,0) with unit source distribution.*

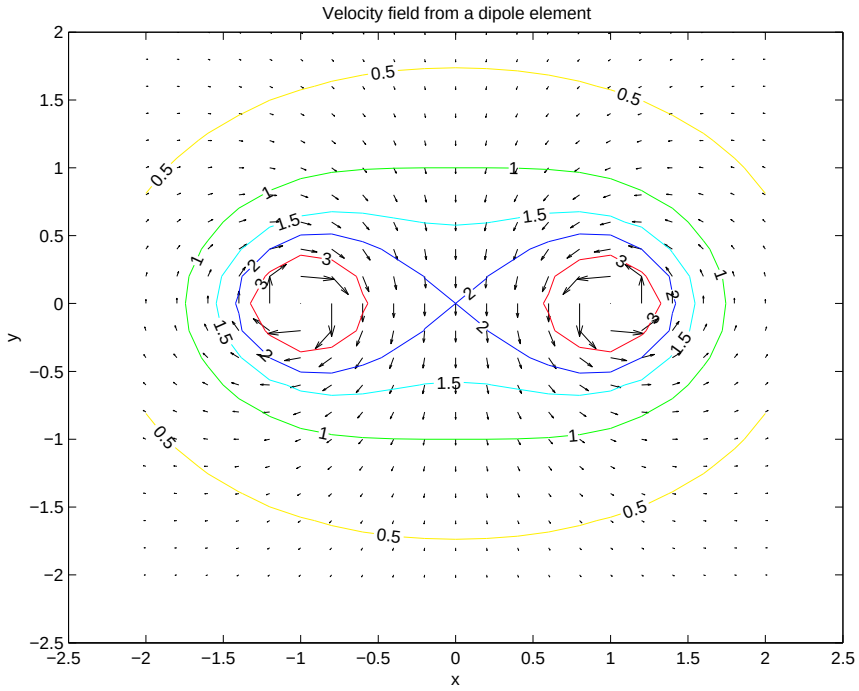

Figure A.3: *Velocity field for a segment stretching from (-1,0) to (1,0) with unit dipole distribution.*

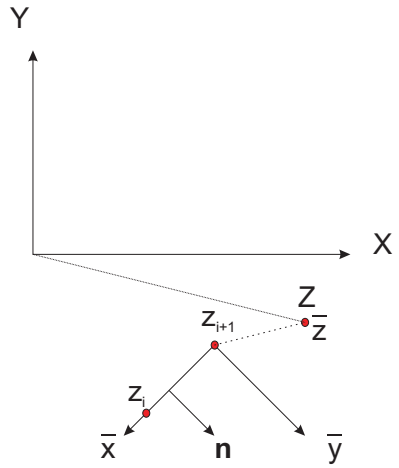

Figure A.4: *Local and global coordinate system with numbering of element ends in the global system.*

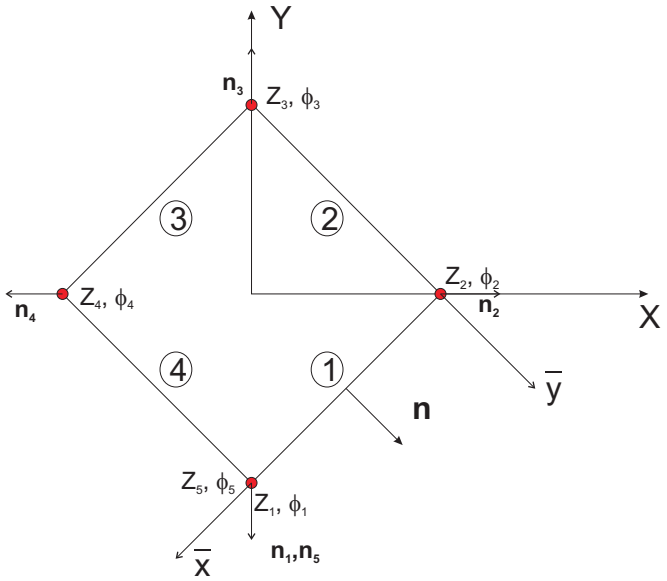

Figure A.5: *Local and global coordinate system with numbering of elements and specification of unknowns*

surface is divided into discrete elements, the system will follow the numbering in Figure A.6, while for a closed geometry continuity is required, hence $Z_5 = Z_1$, $\mathbf{n}_5 = \mathbf{n}_1$ and $\phi_5 = \phi_1$.

The discrete equation, which must be solved, is written

$$2\pi\phi(q) + \sum_{i=1}^{4} \phi(p) F_{D,i} = \sum_{i=1}^{4} \frac{\partial \phi(p)}{\partial n(p)} F_{S,i} \tag{A.21}$$

where the velocity potential is replaced by

$$\phi = \overline{\phi} \dot{\eta}_3 \tag{A.22}$$

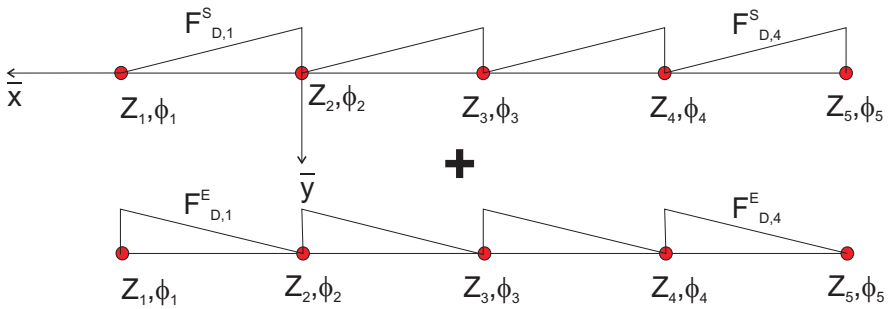

Figure A.6: *Geometry stretched out showing unit singularity distribution, which should be multiplied with the unknown strengths, ϕ_i. Note the local coordinate system. The lower row denotes distribution with unknown strengths at the End, while the upper row denotes distribution with unknown strengths at the Start.*

Hence, $\overline{\phi}$ is the unit velocity potential per m/s heave motion. Similarly, the body boundary condition is expressed as

$$\frac{\partial \phi}{\partial n} = \mathbf{V} \cdot \mathbf{n} = \dot{\eta_3} n_3$$
$$\frac{\partial \overline{\phi}}{\partial n} = n_3 \tag{A.23}$$

For simplicity, ϕ hereafter means $\overline{\phi}$. By letting q approach Z_1 at $Z_{1'} = Z_1 + \epsilon \mathbf{n_1}$, where ϵ is a small number, the following equation can be established

$$\begin{aligned} 2\pi\phi(Z_{1'}) + \phi_1 F^E_{D,1}(Z_{1'}) + \phi_2 F^S_{D,1}(Z_{1'}) + \phi_2 F^E_{D,2}(Z_{1'}) + \phi_3 F^S_{D,2}(Z_{1'}) \\ + \phi_3 F^E_{D,3}(Z_{1'}) + \phi_4 F^S_{D,3}(Z_{1'}) + \phi_4 F^E_{D,4}(Z_{1'}) + \phi_1 F^S_{D,4}(Z_{1'}) = \\ F^E_{S,1}(Z_{1'}) n_{3,1} + F^S_{S,1}(Z_{1'}) n_{3,2} + F^E_{S,2}(Z_{1'}) n_{3,2} + F^S_{S,2}(Z_{1'}) n_{3,3} \\ + F^E_{S,3}(Z_{1'}) n_{3,3} + F^S_{S,3}(Z_{1'}) n_{3,4} + F^E_{S,4}(Z_{1'}) n_{3,4} + F^S_{S,4}(Z_{1'}) n_{3,1} \end{aligned} \tag{A.24}$$

Superscript E denotes *End* where $A = C = \frac{1}{ds}$ and $B = D = 0$, while superscript S denotes *Start* where $A = C = \frac{1}{ds}$ and $B = D = 1$. Subscript D denotes the dipoles, while subscript S denotes the sources. E.g., $F^E_{D,1}(Z_{1'})$ means the dipole distribution at element 1 with unknown strength at *End* of the element evaluated at field point $Z_{1'}$.

It should be understood that it is the real part of the source and dipole distributions, which were used in the expression above. The normal component in the heave direction was found as the imaginary part of the normal, which depended on two adjacent elements. The normal is found as

$$\mathbf{n}_i = \frac{\frac{-i(Z_i - Zi-1)}{ds_{i-1}} + \frac{-i(Z_{i+1} - Zi-1)}{ds_i}}{abs(\frac{-i(Z_i - Zi-1)}{ds_{i-1}} + \frac{-i(Z_{i+1} - Zi-1)}{ds_i})} \tag{A.25}$$

If this is done for all four points, there are four linear equations with four unknowns, and this is written as a matrix system

$$(\mathbf{D} + 2\pi\mathbf{I})\phi = \mathbf{S}\mathbf{n}_3 \tag{A.26}$$

It was solved by using the arithmetic matrix operator "\" in MATLAB, and the whole program to calculate added mass of a geometry defined from bottom centre line to the side at the water line was less than 40 lines long.

The theory was extended to time domain analysis, including discrete elements on the water surface. Numerical beaches were used on the surface far away from the body. The CPU time was found unacceptable in the linear case with 100 sections of roughly 400 elements each solved with a time step of 0.1 seconds for a period of 3 hours. By using Fortran or coupling MATLAB and FORTRAN, the CPU time may be reduced. Moreover, for comparison with towing tank experiments, the CPU time in MATLAB can be reduced by considering head sea and symmetry conditions, and only half of the body and surface elements need to be included. This can be investigated further.

A.1.3 Example of added mass

The method was compared to the analytical formulation of the high frequency added mass for a circular cylinder

$$a_{33}^{2D} = \rho\pi r^2 \tag{A.27}$$

where r is the radius. The error in percent of the exact added mass was expressed versus the number of elements, as illustrated in Figure A.7. A log-log scale is used, and a straight line represents the error. This indicates that there were no numerical problems, but the geometry represented by the straight segments is an approximation. 8 segments on a quarter of the cylinder gave an error of 1%, hence, this can be considered as a minimum number of elements for a simple shape.

Towards the bow and stern the 3D effects are pronounced. To illustrate the order of magnitude, Figure 4.8 in (Newman 1977) is considered. The overall added mass of an ellipsoid is normalised by the displaced mass. The length is $2a$ and the maximum width is $2b$, and the mass becomes $M = \frac{4}{3}\pi\rho ab^2$. The nondimensional values are shown versus the ratio $\frac{b}{a}$. A ratio of zero corresponds to a 2D case, and the nondimensional added mass in heave becomes 1.0. For real ship dimensions, the ratio is approximately $\frac{b}{a} = \frac{1}{6}$. The nondimensional value becomes 0.93, indicating an overall 3D effect of 7%. The sections at the ends experience more 3D effects than amidships, hence a 7% reduction is a lower limit towards the ends. The distribution of added mass influences the natural springing frequency, but as a first approximation a reduction in the added mass of 7% can be assumed.

A.2 Amplification of incident short waves

The theory by Faltinsen et al. (1980) is briefly outlined. Firstly, the encounter frequency, ω_e, needs an explanation. Either the ship is moving with a velocity U, or the current is moving with the same speed. In either case, the ship will oscillate with the meeting

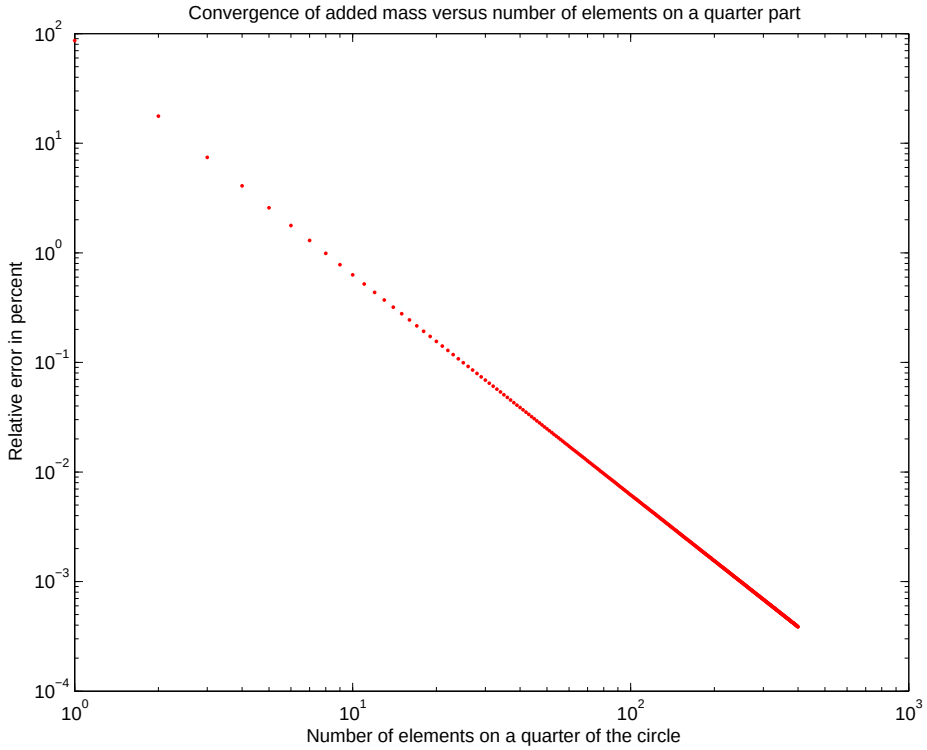

Figure A.7: *Convergence of high frequency added mass using 2D BEM method for a circular cylinder versus number of elements on a quarter part.*

frequency (frequency of encounter), ω_e, and not the wave frequency, ω. The relation between these two is

$$\omega_e = |\omega + kU\cos(\alpha)| = |\omega + \frac{\omega^2}{g}U\cos(\alpha)| \tag{A.28}$$

where α is the heading angle. In head sea $\alpha = 0$, and the encounter frequency is larger than the wave frequency, and visa versa in following sea. The encounter frequency is assumed positive.

The speed U is assumed small, and only the incident flow and the stationary potential, ϕ_s, are considered. Using the boundary condition on the ship, it can be shown that $\phi_s = O(U)$, where ϕ_s is of the same order of magnitude as U. From Bernoulli's equation, the steady wave elevation $\zeta_s = O(U^2)$. The linear kinematic free surface condition by Taylor expansion becomes

$$\frac{\partial \phi_s}{\partial z} \mid_{z=0} = 0 \tag{A.29}$$

where the rest of the terms is of order U^3. It represents a rigid wall, i.e. the velocity field at the surface is horizontal in the xy-plane. If the waves are assumed small compared to the

ship, and the ship side is vertical and infinitely long, the ship side will give total reflection of the incident waves. The total potential can be written in the local coordinate system as

$$\Phi = V(x_0, y_0) \cdot s + \phi_I + \phi_D \tag{A.30}$$

where ϕ_D is the velocity potential of the diffracted (or reflected) waves, and V is the local tangential velocity in the local coordinate system illustrated in Figure A.8. The resulting velocity potential is based on an incident wave and incident velocity potential of

$$\begin{aligned} \zeta_I &= \zeta_a \sin(k_0 x \cos(\alpha) + k_0 y \sin(\alpha) + \omega_e t) \\ \phi_I &= \frac{g\zeta_a}{\omega_0} e^{k_0 z} \cos(k_0 x \cos(\alpha) + k_0 y \sin(\alpha) + \omega_e t) \end{aligned} \tag{A.31}$$

in the global coordinate system. The local and global coordinate systems are shown in Figure A.8. Note that the global coordinate system differs from (Faltinsen et al. 1980). x_0, y_0 is the origin of the local coordinate system. Transforming the incident waves into

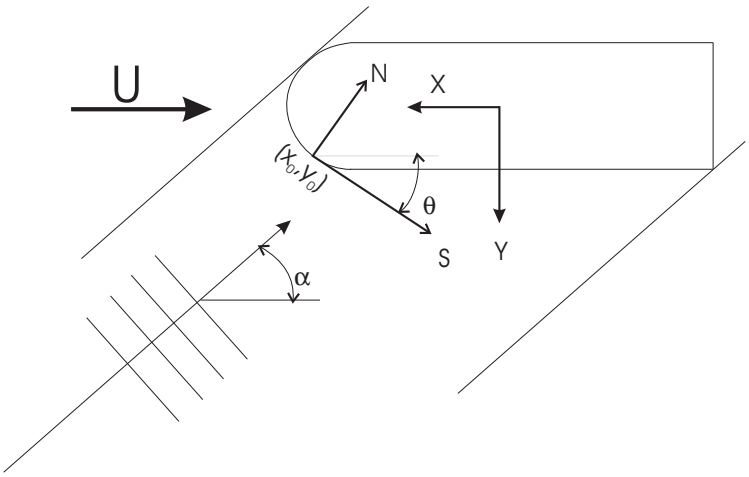

Figure A.8: *Global and local coordinate system for short waves. The capital N and S correspond to small n and s in the equations.*

the local coordinate system gives

$$\begin{aligned} \zeta_I = \zeta_a \sin(k_0 n \sin(\theta + \alpha) + k_0 s \cos(\theta + \alpha) + k_0 x_0 \cos(\alpha) + k_0 y_0 \sin(\alpha) + \omega_e t) \\ \phi_I = \frac{g\zeta_a}{\omega_0} e^{k_0 z} \cos(k_0 n \sin(\theta + \alpha) + \\ k_0 s \cos(\theta + \alpha) + k_0 x_0 \cos(\alpha) + k_0 y_0 \sin(\alpha) + \omega_e t) \end{aligned} \tag{A.32}$$

The solution is expressed as ((Faltinsen et al. 1980) but with some different signs).

$$\begin{aligned}\Phi &= \phi + Vs \\ &= -\frac{g\zeta_a}{\omega_0}e^{k_0 z}\sin(k_0 s\cos(\theta+\alpha) - k_0 n\sin(\theta+\alpha) + \alpha_0 + \omega_e t) \\ &\quad -\frac{g\zeta_a}{\omega_0}Be^{k_1 z}\sin(k_0 s\cos(\theta+\alpha) + k_2 n + \alpha_0 + \omega_e t) \\ &\quad +Vs \end{aligned} \tag{A.33}$$

where

$$\begin{aligned}\alpha_0 &= k_0 x_0\cos(\alpha) + k_0 y_0\sin(\alpha) \\ B &= \frac{2k_1}{k_1+k_0}\frac{k_0}{k_2}\sin(\theta+\alpha) \\ k_1 &= \frac{(\omega_e - Vk_0\cos(\theta+\alpha))^2}{g} \\ k_2 &= \sqrt{k_1^2 - k_0^2\cos^2(\theta+\alpha)}\end{aligned}$$

From the total potential the surface elevation may be calculated through Bernoulli's equation again

$$p + \rho g z + \rho\frac{\partial\Phi}{\partial t} + \frac{\rho}{2}\vec{V}\cdot\vec{V} = p_a + \frac{1}{2}\rho U^2 \tag{A.34}$$

The constant on the right hand side comes from the far field condition at the surface. Considering the surface, ζ, where $p = p_a$, Taylor expand to $z = 0$ and keeping only the linear terms, the total elevation becomes

$$\zeta = \frac{U^2 - V^2}{2g} - \frac{1}{g}(\frac{\partial\phi_I}{\partial t} + \frac{\partial\phi_D}{\partial t}) - \frac{1}{g}V(\frac{\partial\phi_I}{\partial s} + \frac{\partial\phi_D}{\partial s}) \tag{A.35}$$

The linear wave elevation is written

$$\begin{aligned}\zeta &= \frac{U^2 - V^2}{2g} + \frac{\omega_e}{\omega_0}\zeta_a(\sin(a) + B\sin(b)) \\ &\quad -\frac{k_0 V}{\omega_0}\cos(\theta+\alpha)\zeta_a(\sin(a) + B\sin(b))\end{aligned} \tag{A.36}$$

where

$$\begin{aligned}a &= k_0 s\cos(\theta+\alpha) - k_0 n\sin(\theta+\alpha) + \alpha_0 + \omega_e t \\ b &= k_0 s\cos(\theta+\alpha) + k_2 n + \alpha_0 + \omega_e t\end{aligned}$$

If the behaviour at the stem is considered for head sea waves, then $y_0 = 0$, $\alpha = 0$ and $\theta = \frac{\pi}{2}$. This simplifies the expression to

$$\zeta = \frac{U^2}{2g} + \zeta_a\frac{\omega_e}{\omega_0}(\cos(-k_0 n + k_0 x_0 + \omega_e t) + \frac{2}{\frac{k_1}{k_0}+1}\cos(k_1 n + k_0 x_0 + \omega_e t)) \tag{A.37}$$

Transforming back to the global coordinate system using $n = x_0 - x$ (remembering that we consider head sea) gives

$$\zeta = \frac{U^2}{2g} + \zeta_a \frac{\omega_e}{\omega_0}(\cos(k_0 x + \omega_e t) + \frac{2}{\frac{\omega_e^2}{\omega_0^2} + 1}\cos(-k_1 x + (k_0 + k_1)x_0 + \omega_e t)) \tag{A.38}$$

where

$$k_1 = \frac{\omega_e^2}{g} \text{ and } k_0 = \frac{\omega_0^2}{g}$$

At zero speed the expression represents a standing wave.

At the stem $x = x_0$ and the amplification of the dynamic wave motion relative to the incident wave finally becomes

$$\frac{\zeta}{\zeta_a} = \frac{\omega_e}{\omega_0}(1 + \frac{2}{\frac{\omega_e^2}{\omega_0^2} + 1}) \tag{A.39}$$

This expression has been used for comparison with experimental data.

A.3 Added mass for a cone

Added mass for a cone was expressed by Faltinsen and Zhao (1997) for small deadrise angles, while Shiffman and Spencer (1951) expressed it for any deadrise angle. The latter was used in the whipping assessment in Section 3.1, and the approximate added mass formulation will be outlined in Section A.3.1, since this reference can be difficult to obtain.

A.3.1 Added mass for a cone at any deadrise angle

The stem angle or bow flare angle may be in the range of 40 to 60^0. An analytically formula, derived by using expressions for an ellipsoid, is presented. The dimension of the ellipsoid was varied depending on the actual submergence of the cone as illustrated in Figure A.9. The velocity potential around the ellipsoid was used at each instance of the submerged cone.

The added mass with respect to the vertex angle, θ, is written (considering only a half cone a factor of 0.5 is used)

$$A_{33} = \frac{1}{2}k\rho\tan^3(\frac{\theta}{2})h^3 \tag{A.40}$$

$$k = k_w - k_s \ , \ k_w = k_E \cdot w^3 \ , \ k_E = \frac{2\pi}{3}\gamma\frac{\mu}{2-\mu} \ , \ \gamma = \frac{h}{c}$$

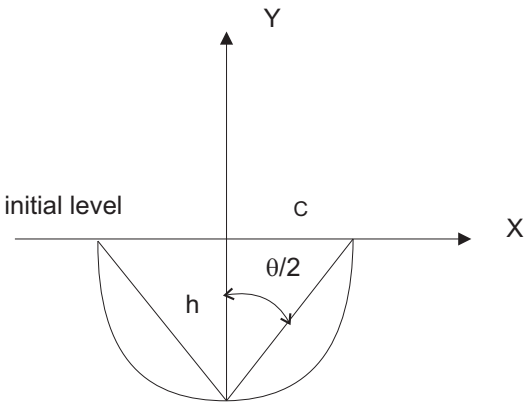

Figure A.9: *Approximation of the cone by an ellipsoid at each time instance.*

w is a wetting factor due to pile up of water, while k_s is a free surface correction where also the square of the velocity on the free surface is no longer neglected. μ, w and k_s are dependent on the ratio γ in the following way

$$\mu = \begin{cases} \frac{2\gamma}{(1-\gamma^2)^{1.5}}[\frac{\sqrt{1-\gamma^2}}{\gamma} - acos(\gamma)] & 0 < \gamma < 1 \\ \frac{2}{3} & \gamma = 1 \\ \frac{2\gamma}{(\gamma^2-1)^{1.5}}[acosh(\gamma) - \frac{\sqrt{\gamma^2-1}}{\gamma}] & \gamma > 1 \end{cases} \tag{A.41}$$

$$w - 1 = \begin{cases} \frac{2\gamma}{(2-\mu)(1-\gamma^2)^{1.5}}[\frac{2(1-\gamma)}{\sqrt{1-\gamma^2}} - acos(\gamma)] & 0 < \gamma < 1 \\ \frac{1}{\gamma} & \gamma = 1 \\ \frac{2\gamma}{(2-\mu)(\gamma^2-1)^{1.5}}[acosh(\gamma) - \frac{2(\gamma-1)}{\sqrt{\gamma^2-1}}] & \gamma > 1 \end{cases} \tag{A.42}$$

$$k_s = \begin{cases} \frac{\pi}{3}w^2\gamma\{\frac{\log(\frac{1}{\gamma}) - \frac{1-\gamma^2}{2}}{[\frac{acos(\gamma)}{\sqrt{1-\gamma^2}-\gamma}]^2} - \frac{1}{2}\} & 0 < \gamma < 1 \\ \frac{\pi}{3}(\frac{9}{8})^2\frac{1}{16} & \gamma = 1 \\ \frac{\pi}{3}w^2\gamma\{\frac{\log(\frac{1}{\gamma}) - \frac{1-\gamma^2}{2}}{[\frac{acosh(\gamma)}{\sqrt{\gamma^2-1}-\gamma}]^2} - \frac{1}{2}\} & \gamma > 1 \end{cases} \tag{A.43}$$

The k-factors and wetting factor for different vertex angles are shown in Figure A.10. The change of the added mass is calculated as (with θ being constant for the cone)

$$\frac{dA_{33}}{dt} = \frac{dA_{33}}{dh} \cdot \frac{dh}{dt} = V_R \cdot \frac{3}{2}k\rho \tan^3(\frac{\theta}{2})h^2 \tag{A.44}$$

The draft including water pile up is written

$$H = wh \tag{A.45}$$

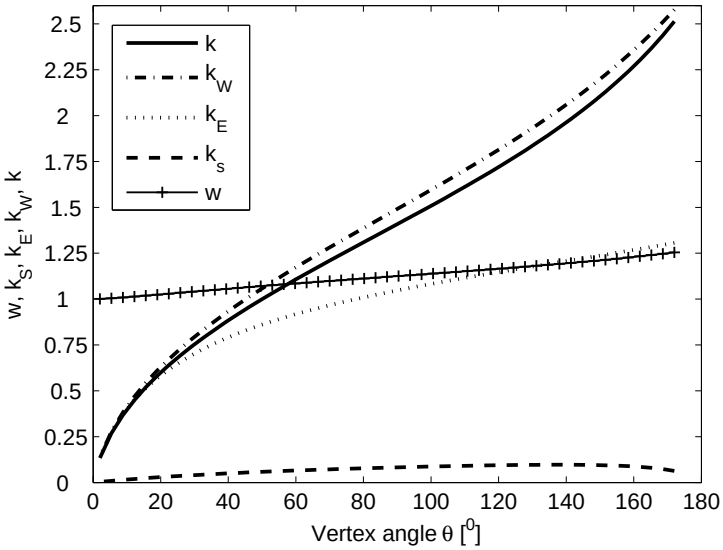

Figure A.10: *k-factors and wetting factor versus vertex angle.*

while the effective width is written

$$c_1 = wh\tan(\frac{\theta}{2}) \tag{A.46}$$

The volume becomes

$$\Omega = \frac{1}{2}\cdot\frac{\pi c_1^2 H}{3} = \frac{\pi}{6}w^3\tan(\frac{\theta}{2})h^3 \tag{A.47}$$

The "hydrostatic" pressure has been considered up to the undisturbed free surface without pile up.

A.4 Resistance components

Various resistance components were used in prediction of speed reduction in irregular sea states. A part of the resistance components, which are related to resistance in calm water, are explained in the following.

A.4.1 The wave making resistance, C_w

This component considers the wave making resistance, which is in the order of 5 to 10% of the total calm water resistance for a blunt ship in calm water at $Fn \approx 0.15$, with reference to Figure 10 in (Baba 1976). It includes wave pattern resistance created by the stern and bow as well as wave breaking resistance created by the bow. A bulb may reduce the latter and adjusting the length may reduce the former.

According to Walderhaug (1991) pp. 2.55, this component can be written simplified for a large variation of ships as

$$1000C_w = 0.0032(LCB - 10C_B + 30)(\frac{B}{T})^{3/2}\frac{1 + 2000Fn^{10}}{\overline{M}C_B^{2.3}}(10Fn)^{6C_B} \quad (A.48)$$

$$\overline{M} = \frac{L_{WL}}{\bigtriangledown^{1/3}}$$

as long as the flow separation at the stern is small. The block coefficient C_B, the Froude number Fn, the length L, draft T and distance of centre of buoyancy forward of midship LCB are all based on the actual water line.

A.4.2 The viscous resistance, C_V

This is the main resistance part in calm water for a large ship, (Fathi and Dahl 2000), and the total viscous resistance is written

$$C_V = (1 + k_0)(C_F + \Delta C_F) \quad (A.49)$$

where the friction coefficient for a flat plate is

$$C_F = \frac{0.075}{(\log_{10}(Rn) - 2)^2} \quad (A.50)$$

and the roughness allowance is

$$\Delta C_F = (110.31(H_\mu \cdot V)^{0.21} - 403.33)C_F^2 \quad (A.51)$$

with a hull surface roughness $H_\mu = 150$. The form factor, k_0, is estimated by

$$k_0 = 0.6\varphi + 145\varphi^{3.5} \quad (A.52)$$

$$\varphi = \frac{C_B(L_{WL})}{L_{WL}}\sqrt{(T_{AP} + T_{FP})B}$$

The method is referred to as the form factor method.

A.4.3 The air resistance, C_{AA}

The air resistance is small and calculated as

$$C_{AA} = 0.001\frac{A_T}{S} \quad (A.53)$$

where A_T is the transverse projected area, (Fathi and Dahl 2000).

A.4.4 The resistance due to base drag, C_{BD}

This is due to the transom stern effect, and Walderhaug (1991) pp. 2.30 expressed this as

$$C_{BD} = 0.029\sqrt{\frac{1}{C_F}(\frac{S_B}{S-S_B})^3} \tag{A.54}$$

where S_B is the transverse area of the transom stern below still water line. This contribution is small for the actual ship in cargo condition and zero in ballast condition. The contribution may be included in the form factor method.

A.5 Solving the beam equation

The mode shapes are found from solving the eigenvalue problem of the structure (Euler beam equation in Eq.(2.20)). Once the eigenvalues are known the eigenvectors can be derived. For a homogeneous beam the mode shapes in head sea may be expressed as

$$\begin{aligned}
\Psi_1(x) &= 1 \text{ , heave} \\
\Psi_2(x) &= 2\frac{x}{L} \text{ , pitch} \\
\Psi_i(x) &= \frac{cos(\beta_i x)}{2cos(\beta_i \frac{L}{2})} + \frac{cosh(\beta_i x)}{2cosh(\beta_i \frac{L}{2})} \text{ i=3,5,7...} \\
\Psi_i(x) &= \frac{sin(\beta_i x)}{2sin(\beta_i \frac{L}{2})} + \frac{sinh(\beta_i x)}{2sinh(\beta_i \frac{L}{2})} \text{ i=4,6,8...} \\
\beta_i &\approx \frac{\pi}{2L}(2(i-2)+1) \\
\omega_{1,2} &= \sqrt{\frac{c}{m+a_r}} \\
\omega_i &= \sqrt{\frac{EI}{m+a_f}\beta_i^4} \text{ for } i > 2
\end{aligned} \tag{A.55}$$

The n mode shapes represent heave, pitch and $n-2$ flexible modes (i=3 is the 2-node mode). The added mass differs for the flexible modes and the rigid body motions. The former can be approximated by the high frequency asymptotic value, while the latter is frequency dependent.

The beam equation can be solved by introducing separation of variables. The equation is

multiplied with a mode shape and integrated over the length.

$$(m+a_i)\int_{-L/2}^{L/2}\Psi_i(x)\Psi_j(x)dx\ddot{q}_i(t)+b\int_{-L/2}^{L/2}\Psi_i(x)\Psi_j(x)dx\dot{q}_i(t)$$
$$+EI\int_{-L/2}^{L/2}\Psi_i^{IV}(x)\Psi_j(x)dxq_i(t)+c\int_{-L/2}^{L/2}\Psi_i(x)\Psi_j(x)dxq_i(t)$$
$$=\int_{-L/2}^{L/2}P(x,t)\Psi_j(x)dx \tag{A.56}$$

The property of orthogonal modes is utilized

$$\int_{-L/2}^{L/2}\Psi_i(x)\Psi_j(x)dx=\begin{cases}0 & \text{if } i\neq j\\ L & \text{if } i=1\\ \frac{L}{3} & \text{if } i=2\\ \approx\frac{L}{4} & \text{if } i>2\end{cases} \tag{A.57}$$

Similarly,

$$\int_{-L/2}^{L/2}\Psi_i^{IV}(x)\Psi_j(x)dx=\begin{cases}0 & \text{if } i\neq j\\ 0 & \text{if } i=1,2\\ \approx\beta_i^4\frac{L}{4} & \text{if } i>2\end{cases} \tag{A.58}$$

The load per meter, $P(x,t)$, consists of the local bow impact load, but also the harmonic oscillating pressure along the ship. The impact load is assumed to act only locally, and the final equations for the principal coordinates may be expressed as

$$\ddot{q}_1(t)+2\delta_r\omega_1\dot{q}_1(t)+\frac{B}{m+a_r}q_1(t)=\frac{1}{(m+a_r)L}[F_s(t)+\int_{-L/2}^{L/2}P_h(x,t)dx]$$
$$\ddot{q}_2(t)+2\delta_r\omega_2\dot{q}_2(t)+\frac{B}{m+a_r}q_2(t)=\frac{3}{(m+a_r)L}[F_s(t)+\int_{-L/2}^{L/2}P_h(x,t)\frac{2}{L}xdx]$$
$$\ddot{q}_i(t)+2\delta_i\omega_i\dot{q}_i(t)+\frac{EI}{m+a_f}\beta_i^4q_i(t)\approx\frac{4}{(m+a_f)L}[F_s(t)+\int_{-L/2}^{L/2}P_h(x,t)\Psi_i(x)dx] \tag{A.59}$$

where $L=L_{pp}$ and the width of the ship at water line is B.

A.5.1 Assumptions made in the simplified procedure

The generalized harmonic force, $F_h(t)$, was based on the dynamic pressure under the incident wave

$$F_{h,i}(t)=\rho gB\int_{-L/2}^{L/2}\sum_{j=1}^{m}\zeta_{a,j}e^{-k_jT}\cos(k_jx+\omega_et+\epsilon_j)\Psi_i(x)dx \tag{A.60}$$

$T = T_{FP}$ is the draft of the ship floating without trim. The irregular sea was represented by linear superposition. The phase angle $\epsilon =< 0, 2\pi >$ was randomly chosen. The diffraction force was neglected, and the radiation forces were represented by approximate values of hydrodynamic added mass and damping forces tabulated in (Faltinsen 1990).

The impact force outlined in Section 2.1.3 was based on the added mass from a half cone as described in Appendix A.3.1. The water level above the apex of the cone was estimated based on the relative distance between the water surface and the vertical vessel motion at the bow. The wet draft h of the cone is estimated as

$$h = max \begin{cases} 0 \\ \zeta + \zeta_s + T_{FP} - z_c - \sum_{i=1}^{n} q_i(t)\Psi(x = L_{pp}/2) \end{cases} \tag{A.61}$$

0 refers to the water surface being below the apex of the cone. z_c is the distance from base line to the cone's apex. The summation term refers to the vertical motion of the ship at FP.

The relative velocity is calculated as

$$V_R = \sum_{i=1}^{n} \dot{q}_i(t)\Psi(x = L_{pp}/2) - \frac{\partial \zeta}{\partial t} - U \cdot \sum_{i=1}^{n} q_i(t)\Psi^I(x)|_{x=L_{pp}/2} \tag{A.62}$$

while the acceleration is written

$$\frac{\partial V_R}{\partial t} = \sum_{i=1}^{n} \ddot{q}_i(t)\Psi(x = L_{pp}/2) - \frac{\partial^2 \zeta}{\partial t^2} - U \cdot \sum_{i=1}^{n} \dot{q}_i(t)^I(x)|_{x=L_{pp}/2} \tag{A.63}$$

The last terms in the expressions of relative velocity and acceleration represent the angle of attack term.

The velocity and acceleration of the surface profile due to the incident and reflected wave considering forward speed in head sea were given by

$$\begin{aligned} \frac{\partial \zeta}{\partial t} &= -\zeta_a \frac{\omega_e^2}{\omega_0}(\sin(k_0 x + \omega_e t) + \frac{2}{\frac{\omega_e^2}{\omega_0^2} + 1} \sin(-k_1 x + (k_0 + k_1)x_0 + \omega_e t)) \\ \frac{\partial^2 \zeta}{\partial t^2} &= -\zeta_a \frac{\omega_e^3}{\omega_0}(\cos(k_0 x + \omega_e t) + \frac{2}{\frac{\omega_e^2}{\omega_0^2} + 1} \cos(-k_1 x + (k_0 + k_1)x_0 + \omega_e t)) \\ & \qquad\qquad k_1 = \frac{\omega_e^2}{g} \text{ and } k_0 = \frac{\omega_0^2}{g} \end{aligned} \tag{A.64}$$

and in these cases $x = x_0 = L_{pp}/2$ considering the location of the bow.

A.5.2 Numerical scheme applied in the simplified procedure

The equation of motion was solved in time using a Newmark-β scheme. The procedure is illustrated for one mode, hence the subscript $_i$ is omitted. The initial condition is given by

$$\dot{q}_0 = 0 \ , \ q_0 = 0 \text{ and } \ddot{q}_0 = \frac{f}{L(m+a)}(F_{s,0} + F_{h,0}) \text{ at } t = 0 \tag{A.65}$$

where $f = 1$ for $i = 1$, $f = 3$ for $i = 2$ and $f = 4$ for $i > 2$. At subsequent time steps the acceleration is calculated from the equation of motion

$$\ddot{q}_j = \frac{f}{L(m+a)}(F_{s,j} + F_{h,j}) - 2\omega\delta\dot{q}_j - \omega^2 q_j \tag{A.66}$$

The Newmark-β scheme can be expressed in general form (where subscript j refers to time step no. j)

$$\begin{aligned} \dot{q}_{j+1} &= \dot{q}_j + (1-\gamma)dt\ddot{q}_j + \gamma dt\ddot{q}_{j+1} \\ q_{j+1} &= q_j + dt\dot{q}_j + (\frac{1}{2} - \beta)dt^2\ddot{q}_j + \beta dt^2\ddot{q}_{j+1} \end{aligned} \tag{A.67}$$

To achieve a stable system $\gamma = \frac{1}{2}$ and $\beta = \frac{1}{4}$ were used. This corresponds to the case of linear acceleration and does not include an artificial damping of the response. The third formula comes from the equation of motion.

$$\ddot{q}_{j+1} = \frac{f}{L(m+a)}(F_{s,j+1} + F_{h,j+1}) - 2\omega\delta\dot{q}_{j+1} - \omega^2 q_{j+1} \tag{A.68}$$

The three last equations may be written in an explicit form

$$\begin{aligned} q_{j+1} = \frac{f}{c_j(m+a)L}[F_{s,j+1} + F_{h,j+1}] + \frac{1}{c_j}[a_j + 2\omega\delta b_j] \\ \dot{q}_{j+1} = \frac{\gamma}{\beta dt}q_{j+1} - b_j \\ \ddot{q}_{j+1} = \frac{1}{\beta dt^2}q_{j+1} - a_j \\ \text{where } c_j = \frac{1}{\beta dt^2} + 2\omega\delta_i\frac{\gamma}{\beta dt} + \omega^2 \\ b_j = \frac{\gamma}{\beta dt}q_j + (\frac{\gamma}{\beta} - 1)\dot{q}_j \\ a_j = \frac{1}{\beta dt^2}(q_j + dt\dot{q}_j + (\frac{1}{2} - \beta)dt^2\ddot{q}_j) \end{aligned} \tag{A.69}$$

The procedure was as follows:

1. Calculate the impact force and harmonic force at time step j, $F_{s,j}, F_{h,j}$
2. Calculate the acceleration for time step j, $\ddot{q}_j$

3. The initial conditions for deflection and velocity at time step j is known, $q_j, \dot{q}_j$
4. Calculate the harmonic force at time step j+1, $F_{h,j+1}$. This is straight forward since the motion does not influence this term in linear theory.
5. Assume that the impact force at time step j+1 is equal to the impact force at time step j, $F_{s,j+1} = F_{s,j}$
6. Calculate the deflection, velocity and acceleration at time step j+1, $q_{j+1}, \dot{q}_{j+1}, \ddot{q}_{j+1}$
7. Based on these quantities at time step j+1 the relative deflection, relative velocity and relative acceleration can be calculated, hence the updated impact force at time instant j+1 is calculated, $F_{s,j+1}$
8. Finally the deflection, velocity and acceleration at time step j+1 are calculated once again, $q_{j+1}, \dot{q}_{j+1}, \ddot{q}_{j+1}$
9. The loop is ended and the procedure is applied to the next time step.

The procedure above includes one iteration on the impact force, and this was considered as sufficient.

A.6 Finite beam element formulation

The basic beam element is illustrated in Figure A.11. At each end it has two degrees of freedom. The stiffness matrix, (Langen and Sigbjørnsson 1979), for the element is written

$$\mathbf{c} = \begin{bmatrix} \frac{12EI}{\ell^3(1+\alpha)} & -\frac{6EI}{\ell^2(1+\alpha)} & -\frac{12EI}{\ell^3(1+\alpha)} & -\frac{6EI}{\ell^2(1+\alpha)} \\ -\frac{6EI}{\ell^2(1+\alpha)} & \frac{(4+\alpha)EI}{\ell(1+\alpha)} & \frac{6EI}{\ell^2(1+\alpha)} & \frac{(2-\alpha)EI}{\ell(1+\alpha)} \\ -\frac{12EI}{\ell^3(1+\alpha)} & \frac{6EI}{\ell^2(1+\alpha)} & \frac{12EI}{\ell^3(1+\alpha)} & \frac{6EI}{\ell^2(1+\alpha)} \\ -\frac{6EI}{\ell^2(1+\alpha)} & \frac{(2-\alpha)EI}{\ell(1+\alpha)} & \frac{6EI}{\ell^2(1+\alpha)} & \frac{(4+\alpha)EI}{\ell(1+\alpha)} \end{bmatrix} \tag{A.70}$$

where

$$\alpha = \frac{12EI}{GA_S} \text{ and } G = \frac{E}{2(1+\nu)} \tag{A.71}$$

The consistent mass matrix for the element is written

$$\mathbf{m} = \frac{m\ell}{420} \begin{bmatrix} 156 & -22\ell & 54 & 13\ell \\ -22\ell & 4\ell^2 & -13\ell & -3\ell^2 \\ 54 & -13\ell & 156 & 22\ell \\ 13\ell & -3\ell^2 & 22\ell & 4\ell^2 \end{bmatrix} \tag{A.72}$$

Both the mass matrix and stiffness matrix are symmetric.

For a long slender ship a lumped mass system is convenient. For each element half of the mass is placed at each element end. If the rotational mass is neglected, manipulation of the equation system may be necessary to solve the eigenvalue problem. Firstly, the vector of the degrees of freedom is separated into vertical degrees of freedom and rotational degrees of freedom. The stiffness and mass distribution are altered accordingly. The system is written

$$\left(\begin{bmatrix} \mathbf{C}_{11} & \mathbf{C}_{12} \\ \mathbf{C}_{21} & \mathbf{C}_{22} \end{bmatrix} - \omega^2 \begin{bmatrix} \mathbf{M}_{11} & \mathbf{M}_{12} \\ \mathbf{M}_{21} & \mathbf{M}_{22} \end{bmatrix}\right) \cdot \begin{bmatrix} \mathbf{v}_t \\ \mathbf{v}_r \end{bmatrix} = \begin{bmatrix} \mathbf{0} \\ \mathbf{0} \end{bmatrix} \tag{A.73}$$

Utilizing that all mass matrices except $\mathbf{M}_{11}$ is zero, the system is reduced to

$$[(\mathbf{C}_{11} - \mathbf{C}_{12}\mathbf{C}_{22}^{-1}\mathbf{C}_{21}) - \omega^2\mathbf{M}_{11}]\mathbf{v}_r = \mathbf{0} \tag{A.74}$$

The subscript $_t$ and $_r$ refers to vertical and rotational degrees of freedom. Solving this eigenvalue problem for n elements give $n+1$ degrees of freedom and $n+1$ eigenfrequencies. The eigenvalues are found by requiring that the determinant is zero. The eigenvectors are found by introducing the eigenvalues into Eq.(A.74). The eigenvector was made nondimensional by requiring that the aft end of the FE beam model had unit displacement. The rotations are found by

$$\mathbf{v}_r = -\mathbf{C}_{22}^{-1}\mathbf{C}_{21}\mathbf{v}_t \tag{A.75}$$

The elements in the stiffness matrix can be considered as forces per unit displacement. When the displacements are determined, the sectional forces at element i based on the global degrees of freedom are derived as

$$\begin{bmatrix} VSF^i_{End1} \\ VBM^i_{End1} \\ VSF^i_{End2} \\ VBM^i_{End2} \end{bmatrix} = \mathbf{c}_i \cdot \begin{bmatrix} v_{(i-1)2+1} \\ v_{(i-1)2+2} \\ v_{(i-1)2+3} \\ v_{(i-1)2+4} \end{bmatrix} \tag{A.76}$$

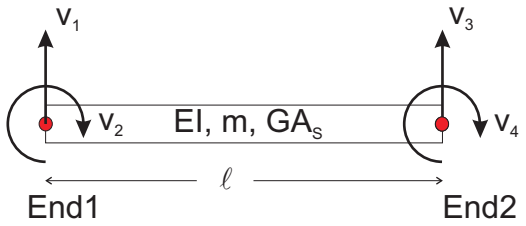

Figure A.11: *Basic beam element with length ℓ, mass per meter m, bending stiffness EI and shear stiffness GA_S.*

A.7 Analytical solution of beam equations

The approach to derive analytical expression for the eigenfrequencies including shear deformation was illustrated in Section 2.2.2. Similar rough approximations were derived for the beam equation including other effects. Axial force, P_x, due to e.g. wave crests in both ends of the ship, modify the beam equation to

$$m\frac{\partial^2 y}{\partial t^2} + \frac{\partial^2}{\partial x^2}(EI\frac{\partial^2 y}{\partial x^2}) + P_x\frac{\partial^2 y}{\partial t^2} = P(x,t) \tag{A.77}$$

with the rough approximation of the natural frequency

$$\begin{aligned} k &= \frac{P_x}{EI} \\ \omega_i &= \omega_{EI}\sqrt{1-\frac{k}{a_1^2}} \end{aligned} \tag{A.78}$$

This indicates that changes in the frequency due to axial forces are rather small for the springing frequency. This may however increase the damping estimates slightly when the width of the springing response peak is considered.

The beam equation with rotational mass becomes

$$\begin{aligned} m\frac{\partial^2 y}{\partial t^2} + \frac{\partial^2}{\partial x^2}(EI\frac{\partial^2 y}{\partial x^2}) - \frac{m_1 r^2}{EI}\frac{\partial^4 y}{\partial x^2 \partial t^2} &= P(x,t) \\ m_1 &= \kappa m \end{aligned} \tag{A.79}$$

where r is the radius of gyration of a vertical slice (cross section) about the y-axis. The κ factor is included to differ between m, which may include added mass and m_1, which does not include added mass. The rough approximation for the natural frequency is

$$\omega_i = \omega_{EI} \cdot \sqrt{\frac{1}{1+a_1^2\kappa^2 r^2}} \tag{A.80}$$

This is also insignificant for the springing frequency, but the importance increases for higher modes.

If external damping is considered, the beam equation is written

$$m\frac{\partial^2 y}{\partial t^2} + \frac{\partial^2}{\partial x^2}(EI\frac{\partial^2 y}{\partial x^2}) + b\frac{\partial y}{\partial t} = P(x,t) \tag{A.81}$$

where b is the linear damping coefficient from external damping such as wave generation damping. Solving the equation confirms that the linear damping has no effect on the mode shape, but the equation for time after using separation of variables is affected.

The beam equation with internal structural damping gives complex and traveling mode shapes. Lekkerkerker (1979) investigated analytically springing based on internal damping, and solved the equations including hydroelastic effects. The force expression and the geometry were simplified. It may be shown that the effect for a lightly damped structure is small, since damped modes are essentially the same as undamped modes.

A.8 Stiffness distribution for a segmented model

A formulation was derived for the stiffness and mass matrix based on a direct approach. The equilibrium of forces was applied directly for each segment. There were two springs in between each element, one vertical spring, k_z, representing shear stiffness and one rotational spring, k_θ, representing the bending stiffness. A segmented model with shear and rotational springs are illustrated in Figure A.12. Continuity was required at the cuts between the segments.

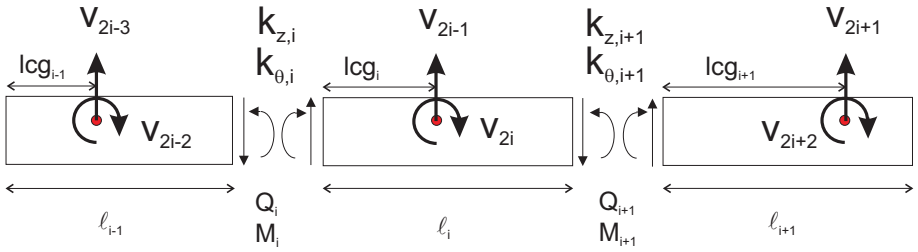

Figure A.12: *Notations for a segmented beam model.*

The local stiffness matrix for element number i, which is connected to element $i-1$ and $i+1$ by springs i and $i+1$ respectively, is written

$$\vec{k}\cdot\vec{v} = \begin{bmatrix} 0 & 0 & 0 & 0 & 0 & 0 \\ 0 & 0 & 0 & 0 & 0 & 0 \\ k_{31} & k_{32} & k_{33}+C_{11,i} & k_{34}+C_{12,i} & k_{35} & k_{36} \\ k_{41} & k_{42} & k_{43}+C_{21,i} & k_{44}+C_{22,i} & k_{45} & k_{46} \\ 0 & 0 & 0 & 0 & 0 & 0 \\ 0 & 0 & 0 & 0 & 0 & 0 \end{bmatrix} \cdot \begin{bmatrix} v_{2i-3} \\ v_{2i-2} \\ v_{2i-1} \\ v_{2i} \\ v_{2i+1} \\ v_{2i+2} \end{bmatrix} \tag{A.82}$$

where the local stiffness factors, k, are

$$\begin{aligned}
k_{31} &= -k_{z,i} \\
k_{32} &= k_{z,i}(\ell_{i-1} - lcg_{i-1}) \\
k_{33} &= k_{z,i} + k_{z,i+1} \\
k_{34} &= k_{z,i} lcg_i - k_{z,i+1}(\ell_i - lcg_i) \\
k_{35} &= -k_{z,i+1} \\
k_{36} &= -k_{z,i+1} lcg_i \\
k_{41} &= -k_{z,i} lcg_i \\
k_{42} &= -k_{\theta,i} + k_{z,i} lcg_i(\ell_{i-1} - lcg_{i-1}) \\
k_{43} &= k_{z,i} lcg_i - k_{z,i+1}(\ell_i - lcg_i) \\
k_{44} &= k_{\theta,i} + k_{\theta,i+1} + k_{z,i} lcg_i^2 + k_{z,i+1}^2(\ell_i - lcg_i)^2 \\
k_{45} &= k_{z,i+1}(\ell_i - lcg_i) \\
k_{46} &= -k_{\theta,i+1} + k_{z,i+1} lcg_{i+1}(\ell_i - lcg_i)
\end{aligned} \tag{A.83}$$

ℓ_i is the rigid body length of element i and lcg_i is the length from aft end to COG of element no. i. The element numbering is going from the stern to bow. When the system stiffness matrix is assembled, element number 1 does not have a flexible connection aft of the stiff segment, hence $k_{z,1}$ and $k_{\theta,1}$ are set equal to 0. Similarly, for the last element n, which has the flexible connection number $n+1$ to the right of the stiff segment, $k_{z,n+1} = k_{\theta,n+1} = 0$. The C coefficients represent the hydrodynamic restoring coefficients due to heave and pitch of segment i, hence C_{21} is the restoring coefficient in pitch due to motion in heave. The local mass matrix is written

$$\vec{M} \cdot \ddot{\vec{v}} = \begin{bmatrix} 0 & 0 & 0 & 0 & 0 & 0 \\ 0 & 0 & 0 & 0 & 0 & 0 \\ 0 & 0 & M_i + A_{11,i} & A_{12,i} & 0 & 0 \\ 0 & 0 & A_{21,i} & I_i + A_{22,i} & 0 & 0 \\ 0 & 0 & 0 & 0 & 0 & 0 \\ 0 & 0 & 0 & 0 & 0 & 0 \end{bmatrix} \cdot \begin{bmatrix} \ddot{v}_{2i-3} \\ \ddot{v}_{2i-2} \\ \ddot{v}_{2i-1} \\ \ddot{v}_{2i} \\ \ddot{v}_{2i+1} \\ \ddot{v}_{2i+2} \end{bmatrix}$$

where A is the added mass.

The segmented beam model was validated against results from Økland (2002), pp. 201-202. The natural frequencies for 2-node and 3-node vibration were calculated based on data from his model tests. The calculated periods were 0.17 and $0.068s$ versus 0.17 and $0.070s$ in his thesis.

A segmented model using a vertical and rotational spring between each segment was also tested. The dimensions of the model were

$$L_{pp} = 294m,\ B = 53m,\ D = 2T = 23.3m,\ I_{ship} = 694m^4$$

An equivalent rotational stiffness was estimated based on considering the static deflection at the middle of the beam, which was simply supported at the ends and exposed to a lateral force at the middle. By requiring the same deflection at the middle, the rotational stiffness becomes

$$k_\theta = 3E\frac{I_{ship}}{L_{pp}} \tag{A.84}$$

This gave a 2-node natural frequency of $0.474Hz$, and the mode shape is illustrated in Figure A.13. $0.474Hz$ was also the exact natural frequency from the analytical solution, which is written

$$\omega = \sqrt{\frac{k_\theta(I_1 + I_2)}{I_1 \cdot I_2}} \tag{A.85}$$
$$I_1 = I_2 = \frac{1}{12}(2\rho BT)(\frac{L_{pp}}{2})^3$$

The mass moment of inertia includes a factor 2 in front of ρ, just because the added mass was assumed equal to the mass.

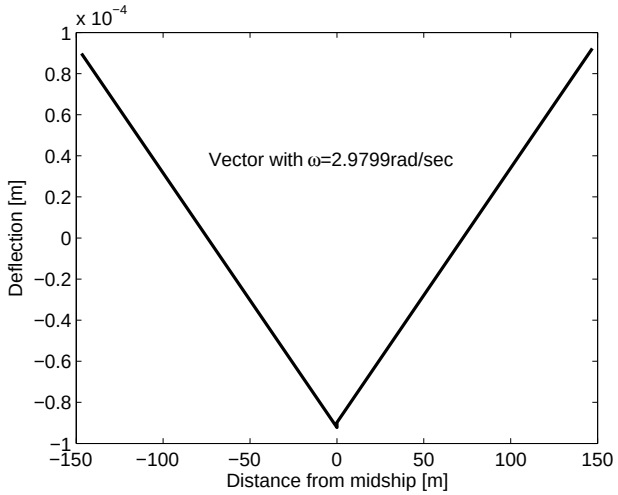

Figure A.13: *Flexible mode of a 2-segmented beam.*

A.9 Different features of the SDOF system

The SDOF system for a harmonic loading with forcing frequency ω_f is written

$$m\ddot{x} + b\dot{x} + cx = F_0 \sin(\omega_p t) \tag{A.86}$$

This system may represent the 2-node springing mode. However, while the force amplitude, F, is assumed constant in the SDOF system, the real excitation on a ship is frequency and

speed dependent, $F(\omega_p, U)$, displaying a hump and hollow behaviour as a function of the frequency.

The solution to the SDOF system consists of summation of the homogeneous and particular solution

$$x(t) = e^{-\delta\omega t}[A\sin(\omega_d t) + B\cos(\omega_d t)] + \frac{F_0}{c}\frac{1}{[(1-\beta^2)^2 + (2\delta\beta)^2]^{\frac{1}{2}}}[(1-\beta^2)\sin(\omega_f t) - 2\delta\beta\cos(\omega_f t)] \tag{A.87}$$

$$\beta = \frac{\omega_f}{\omega}$$

The damping ratio is defined as

$$\delta = \frac{b}{2mc} \tag{A.88}$$

and the damped frequency and natural frequency are expressed as

$$\omega_d = \omega\sqrt{1-\delta^2}$$
$$\omega = \sqrt{\frac{c}{m}} \tag{A.89}$$

The coefficients A and B are determined from the initial conditions $\dot{x}(t=0) = \dot{x}_0$ and $x(t=0) = x_0$. After a while the transient part dies out due to the damping, but the forced vibration remains. The dynamic amplification of the forced excitation relative to the static deflection is written

$$D = |\frac{x_{max}}{x_{static}}| = \frac{1}{[(1-\beta^2)^2 + (2\delta\beta)^2]^{\frac{1}{2}}} \tag{A.90}$$

The damping ratio for the flexible modes is in the order of 1%, hence the system is lightly damped. This will give $\omega_d \approx \omega$ and

$$D_{max} \approx \frac{1}{2\delta} \tag{A.91}$$

The latter gives a resonance amplification of 100 times the static deflection for a damping ratio of 0.5%.

The response to a system initially at rest is written

$$x(t) = \frac{F_0}{c}[e^{-\delta\omega t}(\delta\frac{\omega}{\omega_d}\sin(\omega_d t) + \cos(\omega_d t)) - \cos(\omega_f t)] \tag{A.92}$$

Considering a lightly damped system, the response at resonance excitation is

$$\frac{x(t)}{x_{static}} = \frac{1}{2\delta}(e^{-\delta\omega t} - 1)\cos(\omega t) \tag{A.93}$$

The envelope curve of this process, or rather the slope of the non-oscillating process, is expressed as

$$\frac{1}{2\delta}(1 - e^{-\delta\omega t}) \tag{A.94}$$

This may define the increase of springing when entering a harmonic wave train in the towing tank.

By considering the maximum amplitudes of the homogeneous part decaying with time, an estimate for the damping ratio can be made assuming a lightly damped system

$$\delta = \frac{1}{2\pi n} \ln(\frac{x_i}{x_{i+n}}) \tag{A.95}$$

Another important issue is the behaviour of the response to an impulse loading. An impulse loading is often considered to be an impact with duration less than 25% of the natural period. Whipping is not necessarily an impulse loading. The Duhamel (convolution) integral can be used to calculate the response at time t. This is written

$$x(t) = \frac{1}{m\omega_d} \int_0^t e^{-\delta\omega(t-\tau)} P(\tau) \sin(\omega_d(t-\tau)) d\tau \tag{A.96}$$

for a damped system where $P(\tau)$ is the general loading. The solution of an impulse of the form $\sin(\omega_p t)$ with a duration of $T_p/2 = \pi/\omega_p$ was derived analytically. At time $t = T_p/2$ the resulting displacement and velocity was estimated and used to define the free vibration phase after the end of the impact. The results are presented as the maximum response ratio to the static response $1/c$ versus the nondimensional time in Figure A.14. The nondimensional time is the impact duration, which is $T_p/2$, divided by the natural period, T_s. Similar shapes were presented by Bergan et al. (1981), with a maximum amplification of 2. An example of the time series where the impulse duration is 0.9 times the natural period is displayed in the right plot of Figure A.14. The plot does also show the minimum. The minimum in absolute value is less than the maximum independent of the length of the impact in this case. The time series also illustrates that the largest amplitude is achieved after slightly more than half a cycle, and for short impacts the amplification follows a seemingly straight line. The maximum amplification is about 1.7.

The impact may however have a different shape than the conventional slamming impact similar to the one considered in Figure A.14. Due to the inertia part of the impact load (and possibly other contributions) both a positive and a negative load, or the opposite, may occur as illustrated in Figure 3.2. This was represented by a whole sinusoidal impact $\sin(\omega_p t)$ with a duration of $T_p = 2\pi/\omega_p$. The convolution integral was again solved and the initial conditions for the displacement and velocity was applied at $t = T_p$ for the free harmonic vibration. Figure A.15 presents the results of the amplification both as a maximum and a minimum versus the nondimensional impact time. The amplification may exceed a level of 2 and reach a level of 3 in this case. Moreover, the absolute value

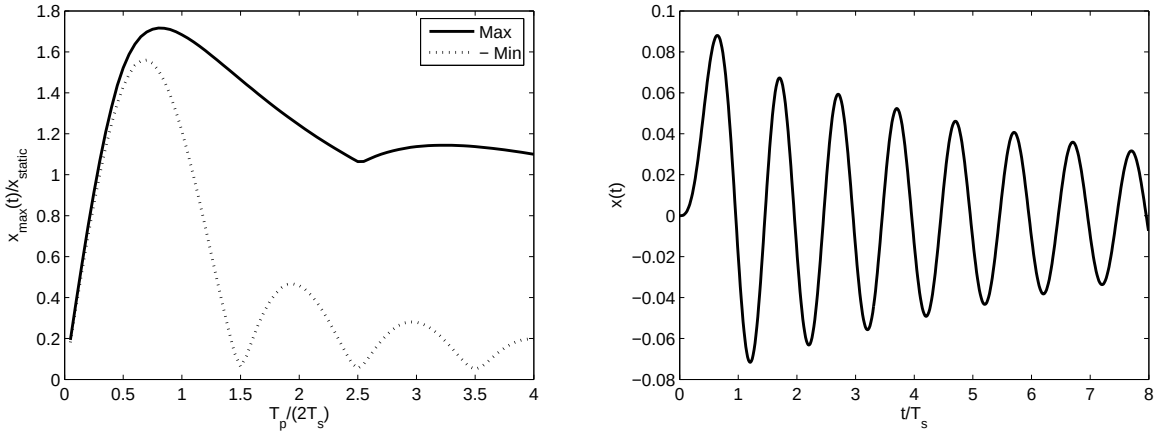

Figure A.14: *Maximum amplification from a half sinusoidal impact with time series illustrated by an impact duration of $0.9T_s$; $\omega_S = 19.7rad/s$, $m = 0.05$ and $\delta = 0.02$.*

of the minimum may exceed the maximum. The absolute amplitude will in any case exceed the static deflection, also in the negative cycle. This is actually the beginning of a resonance case similar to Figure 4.27, and the absolute maximum appears at the second local maximum or minimum instead of the first. A time series is included in the right plot to illustrate this. From the measured time series either two of these impact cases may occur, and the behaviour of the vibratory response may then indicate which loading that occured.

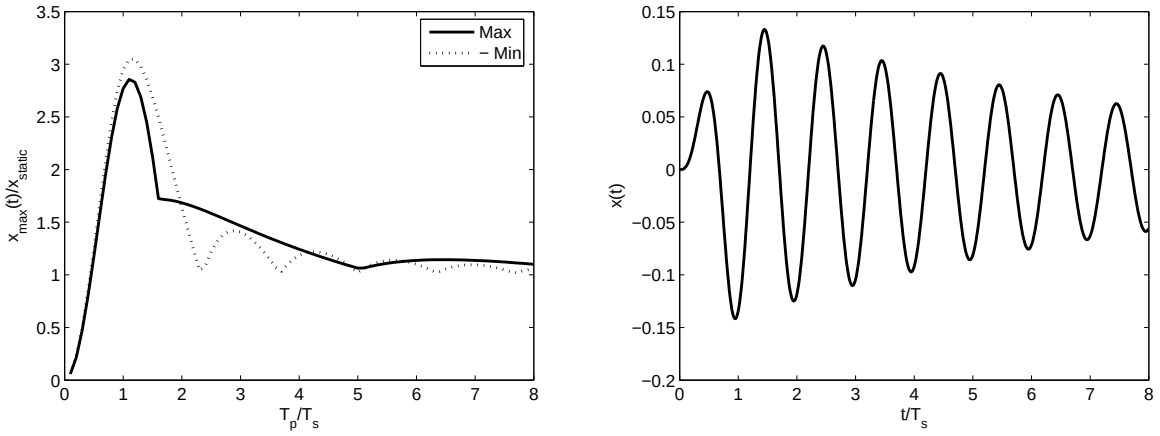

Figure A.15: *Maximum amplification from a whole sinusoidal impact with time series illustrated by an impact duration of $0.9T_s$; $\omega_S = 19.7rad/s$, $m = 0.05$ and $\delta = 0.02$.*

A.10 Estimate of the wave height in a sea state given the period

For the simplified nonlinear estimate of springing, and for the method used to separate whipping and springing, the second order contribution was corrected with respect to the wave amplitude. The refined method was used to estimate the wave height. It was based on the joint probability density function (jpdf) of the wave height and wave period presented in (Myrhaug and Kvålsvold 1992; Myrhaug and Kvålsvold 1995). Their expressions are presented in the following.

The jpdf for the wave height and wave period, $p(h,t)$, is written

$$p(h,t) = p(t|h)p(h) \tag{A.97}$$

where the marginal pdf for the wave height is

$$p(h) = \frac{2.39h^{1.39}}{1.05^{2.39}} exp[-(\frac{h}{1.05})^{2.39}] \tag{A.98}$$

(note that it differs from Rayleigh, which has an exponent of 2 inside the brackets) and the conditional pdf for the period given the wave height is

$$\begin{aligned} p(t|h) &= \frac{\beta(t-0.12\sqrt{h})^{\beta-1}}{\rho^{\beta}} exp[-(\frac{t-0.12\sqrt{h}}{\rho})^{\beta}] \\ \rho(h) &= \begin{cases} 0.78h + 0.26 & \text{for } h \leq 0.9 \\ 0.962 & \text{for } h > 0.9 \end{cases} \\ \beta(h) &= 2atan(2(h-1.2)) + 5 \end{aligned} \tag{A.99}$$

h and t are nondimensional zero down-crossing wave height, H, and period, T. They are made nondimensional as

$$\begin{aligned} h &= \frac{H}{\gamma_H \sqrt{m_0}} \text{ where } \gamma_H = 2.8582 \\ t &= \frac{T}{\gamma_T 2\pi \sqrt{\frac{m_0}{m_2}}} \text{ where } \gamma_T = 1.2416 \text{ and} \\ m_i &= \int_{-\infty}^{\infty} \omega^i S(\omega) d\omega \end{aligned} \tag{A.100}$$

Once the wave spectrum is specified, the mean amplitude is calculated by the following procedure. Firstly, the marginal pdf for the period is calculated as

$$p(t) = \int_{-\infty}^{\infty} p(h,t) dh \tag{A.101}$$

Thereafter, the conditional pdf for the wave height given the wave period is estimated from

$$p(h|t) = \frac{p(h,t)}{p(t)} \tag{A.102}$$

and finally, the conditional mean value for the wave height given the wave period is determined by

$$E(h|t) = \int_{-\infty}^{\infty} hp(h|t)dh \tag{A.103}$$

A plot is shown in Figure A.17. This is the same curve as shown by Myrhaug and Kvålsvold (1992), which verifies the expressions used. The jpdf is shown in Figure A.16.

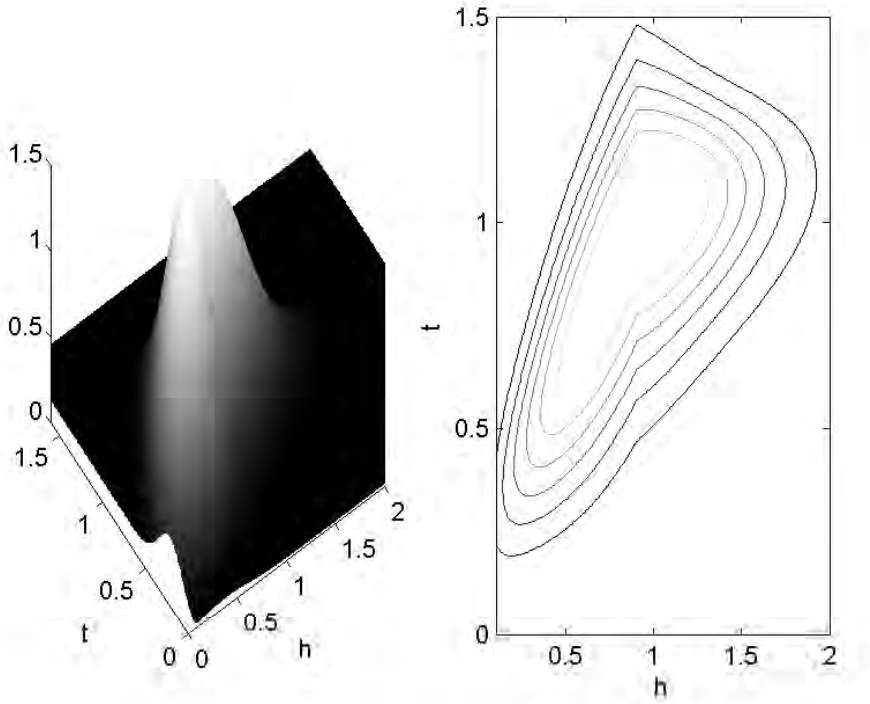

Figure A.16: *Joint probability density function of nondimensional wave height and period.*

This has been used to estimate the wave height for a specific period that excites either resonance by linear or second order excitation. It was printed versus the Beaufort wind scale, however the PM wave spectrum based on wind speed may give unrealistic high waves compared to the Beaufort scale, e.g. $H_S = 19.9m$ in Beaufort 11 with wind speed of $30.6m/s$. A JONSWAP wave spectrum was used instead, but the peak period must then be defined. The relation from DNV (2000) giving $T_Z = 6H_S^{0.3}$ is used with a peakness factor γ of 2. The results were shown in Section 2.6.

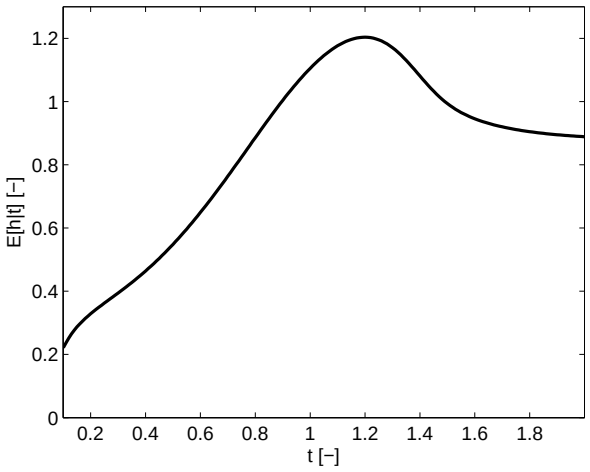

Figure A.17: *Nondimensional conditional mean wave height for a given period in a sea state, ref. Eq.(A.101).*

A.11 The Beaufort scale

The wind speed and wave height for the Beaufort scale are listed in Table A.1. The wind speeds, $U = 0.836Bn^{1.5}[m/s]$, were taken from *www.met.no* and relates to wind $10m$ above the sea surface. The numbers in parenthesis were taken from *www.globalwavestatisticsonline.com* as well as the significant wave heights. The first number refers to probable wave height, while the second refers to the maximum. The corresponding wave height depends on the duration of the wind. Assuming unlimited fetch and $25kn$ wind speed, the wave height (=1.8) increases by a factor of 1.33 by increasing the duration from 3 to 6 hours. For 9 and 12 hours duration the factors are 1.9 and 2.5, (*www.bom.gov.au*).

Table A.1: *Beaufort scale of wind speed and significant wave height.*

Beaufort no. Bn	Wind speed, U $[m/s]$ (kn)	H_S $[m]$
1	0.3-1.5 (1-3)	0.1-0.1
2	1.6-3.3 (4-6)	0.2-0.3
3	3.4-5.4 (7-10)	0.6-1.0
4	5.5-7.9 (11-16)	1.0-1.5
5	8.0-10.7 (17-21)	2.0-2.5
6	10.8-13.8 (22-27)	3-4
7	13.9-17.1 (28-33)	4-5.5
8	17.2-20.7 (34-40)	5.5-7.5
9	20.8-24.4 (41-47)	7-10
10	24.5-28.4 (48-55)	9-12.5
11	28.5-32.6 (56-63)	11.5-16
12	Above 32.6 (64)	Above 14

Appendix B

Experimental set-up procedures and uncertainty analysis

B.1 Model setup

B.1.1 Description of transverse cuts

The five transverse cuts were divided into one stiff cut at each end and three flexible cuts at the quarter lengths. Examples are shown in Figure B.1. The circular steel rod/spring had a diameter of $4.0cm$, and the distance between the locks/bearings were about $31cm$. By adjusting the length between the bearings the springing frequency could be changed. The numbering of the cuts starts from the aft. The design of cut 5 was identical to cut 1, and cut 4 was identical to cut 2. The shear force was not measured at the same location as the bending moment in cut 2 and 4, but about $8cm$ forward of the moment.

B.1.2 Mass properties of the segments

To compare model experiments and numerical calculations, mass, mass moment of inertia and centre of gravity were determined for each of the four rigid segments. Moreover, the mass was measured for segment 1 and 6 for the purpose of shear calculations. The mass was estimated using a weight, while the mass moment of inertia, longitudinal and vertical COG were obtained through a pendulum test using a cradle.

Pendulum tests

Huse (1993) described the pendulum test in principle. The full set of equations were derived in this research to account for the properties and design of the cradle. The procedure

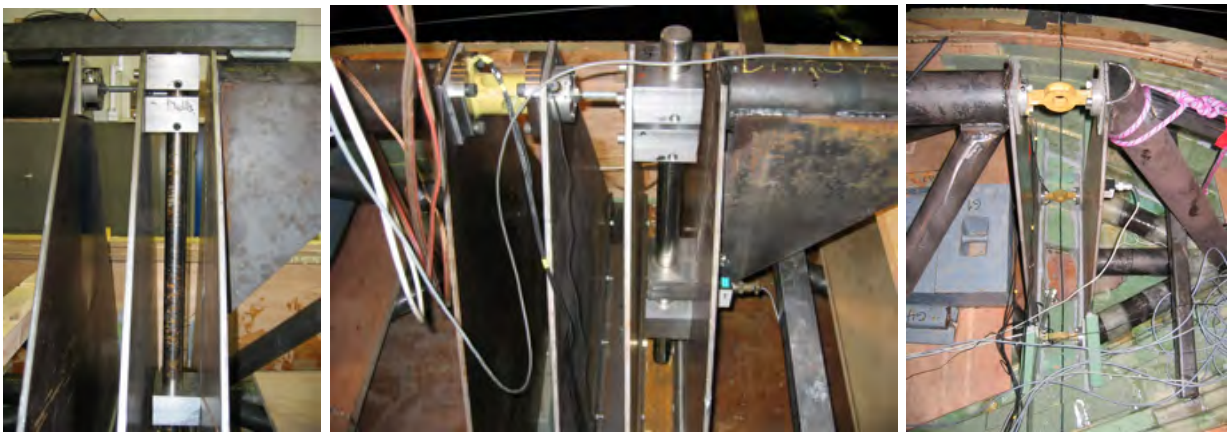

Figure B.1: *The joints at 3 cuts. Left picture = Cut 3 at midship section, middle pic. = Cut 2 at aft quarter (similar to cut 4) and right pict. = Cut 1 at stern (similar to cut 5).*

is briefly described in the following.

The LCG was determined by placing the model on the cradle and balancing it on even keel. The cradle with model was oscillated to determine the period of oscillation. However, both the VCG and the moment of inertia, I, were unknowns. Therefore, two additional weights with known equal masses, m, were placed horizontally a distance a on each side of the knife edge. The knife edge defined the centre point of rotation. The oscillation period was determined again, and the I and VCG could be calculated.

It was necessary to separate the I_m and VCG for the model from the measured total I^t and VCG that included the cradle. The cradle was heavy with a low centre of gravity to ensure short periods and positive distance, h, from the knife edge to the centre of gravity measured downwards. This was a requirement, but high h was also an advantage from an accuracy point of view. 600 to $800kg$ was placed in the bottom of the cradle due to the heavy mass of the model segments.

Firstly, the VCG and mass moment of inertia of the cradle, I_c, are determined.

$$\begin{aligned} h_c &= \frac{8\pi^2 m a^2}{M_c g(T_1^2 - T_0^2)} \\ I_c^t &= \frac{2ma^2 T_0^2}{T_1^2 - T_0^2} \\ I_c &= I_c^t - M_c h_c^2 \end{aligned} \tag{B.1}$$

M_c is the total mass of the cradle, h_c is the distance from the knife edge to the COG being positive downwards, and T_1 and T_0 are the oscillation period with and without the additional weights. The oscillation period was measured by a crystal clock with three significant decimals (milliseconds). Additional weights were hanged a fixed distance, $a = 3.000m$,

from the knife edge. $m = 10kg$ (measured to 10.000 and $9.990kg$ by an accurate weight) or $m = 15kg$ (14.986 and $14.967kg$) on each side were used. $g = 9.81m/s^2$ is the acceleration of gravity.

Secondly, the model was placed on the cradle with the keel at a distance h_{keel} from the knife edge. The pendulum test was repeated following the same procedures and using the same equations. T_1 and T_0 differ from above.

$$\begin{aligned} h &= \frac{8\pi^2 m a^2}{Mg(T_1^2 - T_0^2)} \\ I^t &= \frac{2ma^2T_0^2}{T_1^2 - T_0^2} \\ I &= I^t - Mh^2 \end{aligned} \tag{B.2}$$

where

$$\begin{aligned} M &= M_m + M_c \\ h_m &= h + \frac{M_c}{M_m}(h - h_c) \\ I_m &= I^t - Mh^2 - M_m(h - h_m)^2 - I_c - M_c(h - h_c)^2 \\ VCG &= h_{keel} - h_m \end{aligned} \tag{B.3}$$

The results of interest are I_m and VCG for each stiff segment. I_m is about its COG.

Mass properties

The results are collected in Table B.1. For clarification, LCG was defined from the aft part of the segment, hence from the dry transom stern $15.1cm$ aft of AP for segment 1 as displayed in Figure 4.3. In cargo condition the number in parenthesis indicates when the calculation was based on cradle estimates with 10 or $15kg$ additional mass. This gives an indication of the uncertainty. Rigid segment 1 was based on a slightly different cradle mass, since the segment was supported from tilting.

Pendulum tests for bow 2 in ballast and bow 2 and 3 in cargo conditions were not performed. The intention was to keep the mass distribution identical in the three ballast conditions and in the three cargo conditions. Pendulum test for ballast 3 condition was performed to provide an estimate of the uncertainties, since also the bow geometry was changed. Results for ballast 3 condition are presented in Table B.2. The results are in satisfactory agreement with the ballast 1 condition, considering that the mass distribution and bow geometry differ. A picture of the cradle with segment 4 is shown in Figure B.2.

Uncertainties in the mass properties

No detailed uncertainty analysis was carried out. There were, however, some uncertainties related to the pendulum tests, mass weights, the model mass in water versus in air and

Table B.1: *Mass properties of rigid segments for original ballast and cargo 1 condition.*

Rigid Segment	Segment	M_m[kg]	LCG [m]	VCG [m]	I_m [kgm^2]	m [kg]
Cradle case 1 B.	all	782.1	n.a.	h_c=0.5422	209.4	15
Cradle case 2 B.	1 and 2	784.0	n.a.	h_c=0.5427	210.0	15
1 Ballast	1 and 2	556.2	1.67	0.523	152.4	15
2 Ballast	3	990.5	0.98	0.505	513.1	15
3 Ballast	4	936.9	1.04	0.498	426.5	15
4 Ballast	5 and 6	859.4	0.86	0.496	339.4	15
4 Ballast	5 and 6	859.4	0.86	0.498	331.2	10
1 Cargo	1	133.6				
4 Cargo	6	115.3				
Cradle case 1 C.	all	980.9	n.a.	h_c=0.547	241.1	10
Cradle case 1 C.	all	980.9	n.a.	h_c=0.548	241.0	15
Cradle case 2 C.	1 and 2	982.9	n.a.	h_c=0.546	241.8	15
1 Cargo	1 and 2	849.0	1.73	0.494	170.2	10
1 Cargo	1 and 2	849.0	1.73	0.496	167.3	15
2 Cargo	3	1689.0	1.01	0.491	555.6	10 (10)
2 Cargo	3	1689.0	1.01	0.491	554.8	10 (15)
2 Cargo	3	1689.0	1.01	0.492	546.3	15 (10)
2 Cargo	3	1689.0	1.01	0.492	545.6	15 (15)
3 Cargo	4	1761.0	1.04	0.479	615.4	10 (10)
3 Cargo	4	1761.0	1.04	0.480	614.7	10 (15)
3 Cargo	4	1761.0	1.04	0.480	609.9	15 (10)
3 Cargo	4	1761.0	1.04	0.480	609.2	15 (15)
4 Cargo	5 and 6	1224.5	0.87	0.500	353.0	10 (10)
4 Cargo	5 and 6	1224.5	0.87	0.500	352.3	10 (15)
4 Cargo	5 and 6	1224.5	0.87	0.501	348.4	15 (10)
4 Cargo	5 and 6	1224.5	0.87	0.501	347.6	15 (15)
1 Cargo	1	143.6				
4 Cargo	6	119.0				

Table B.2: *Mass and inertia properties of rigid segments for ballast 3 condition.*

Rigid Segment	Segment	Mass[kg]	LCG [m]	VCG [m]	I_m [kgm^2]	m [kg]
Cradle case 1 B	all	981.3	n.a.	h_c=0.545	240.6	15
1 Ballast	1 and 2	535.0	1.72	0.526	156.6	15
2 Ballast	3	982.6	1.12	0.524	494.1	15
3 Ballast	4	981.0	1.06	0.492	454.0	15
4 Ballast	5 and 6	873.3	0.83	0.517	285.0	15

division of masses between segments.

For each segment about twenty cycles were counted. This was done 5-6 times for each

Figure B.2: *Cradle with segment 4 and with the crystal clock shown in front.*

additional weight (0, 10 and 15kg). The average of the repeated tests was taken to find the oscillation period. The standard deviation was within one millisecond, and the uncertainty was in the order of 0.02%. Moreover, the height from the keel to the knife edge of the pendulum introduced some uncertainty. This was related to the divinycell thickness between the model and the aluminum frame of the cradle. This distance was measured by a folding rule with an inherent uncertainty of $0.5mm$. The thickness of the dyvinicell was about $0.5 \pm 0.2cm$, while the height from the frame to the knife edge was $30.0cm$. The uncertainty was less than 1%. The additional weights were determined by a weight with accuracy within 1 gram. 6 repeated tests with 1 of the additional masses gave for instance all 9990 grams. Their arm, a, was estimated to $3.006m$ with a measuring tape with an inherent uncertainty of $0.5mm$. Basically, the pendulum tests was related to an uncertainty within about 2.5%.

The mass of each segment was weighed with a resolution of $\pm 0.2kg$ with an inherent uncertainty of $0.1kg$. Repeated tests gave the same, but there was no knowledge about the bias. The "$100kg$" ballast weights were weighing between 99.8 to $100.8kg$. The average of

10 weights were 100.225kg, and the expected bias was about 0.2%.

The mass of each segment differed slightly from when it was placed in water with all the equipment. Examples of lacking or added weights were pressure sensors, accelerometers, top frame locks, "Nypos tree", cables (9.5kg), screws, bow flare aluminum foils (3kg), and small weights from the towing arrangement. The total mass was probably maximum 10kg less than in water. The uncertainty may be up to 1%.

The mass at the ends of each segments may be off by about 4kg (half the spring), which gave an addition of up to 4kgm^2. Moreover, the ballast weights were taken out of the model in between each test and also between the model tests and the pendulum tests. The weight positions were marked and pictures were taken to reduce this uncertainty. All together, this introduced an uncertainty of 1 to 2% for the different segments.

A rough estimate of the 95% sample confidence interval of the mass moment of inertia from the Table B.1 is in the order of 2.0%. Totally, it was roughly estimated that the 95% sample confidence interval was less than 6% for the smallest segment and less than 5% for the largest.

For the different loading condition there were differences in the mass distribution. For the bow 2 in cargo condition and bow 3 in both cargo and ballast, plywood was fitted to the deck at the ship side to increase the deck height and to avoid water ingress in larger waves. Water on deck was only allowed on the deck at the bow. The weight of the additional plywood was in the order of 20kg. There were also some differences to the weights placed inside in the different segments, and the weight of the bow segments. Table B.3 shows the amount of free weights located inside each of the stiff segments. The model tests with the different bows ought to be considered as separate loading conditions. Ballast 1 and ballast 3 referred to in Table B.1 and B.2 displays the largest difference.

Table B.3: *Ballast weights inserted into the different segments in the different cases.*

Segment	Ballast 1	Ballast 2	Ballast 3	Cargo 1	Cargo 2	Cargo 3
1 and 2	170	150	130	450	410	400
3	320	300	300	1000	1000	1000
4	300	300	300	1100	1100	1100
5 and 6	250	230	300	610	620	630

Approximate full scale data scaled down

The output from the loading computer onboard the vessel was reviewed, and two representative loading conditions from the loading manual were selected as basis for the model tests. Detailed mass distribution was derived from NAPA (Napa 1989) as input to WASIM (DNV 2004), which was used by Storhaug et al. (2003). The mass distributions for ballast

and cargo condition were scaled down as a reference in the planning process. The full scale data underestimated the mass moment of inertia slightly, since the contribution from the vertical mass distribution was disregarded. The additional ballast weights of more than one ton in ballast condition and three tonnes in cargo condition were placed inside the model to represent the full scale mass moment of inertia, the realistic longitudinal mass distribution and trim. The comparison with the model test conditions are shown in Table B.4.

Table B.4: *Mass properties of rigid segments for real versus model mass ($_m$) distribution.*

Rigid Segm.	Segm.	M $[kg]$	LCG $[m]$	I $[kgm^2]$	M_m $[kg]$	LCG_m $[m]$	I_m $[kgm^2]$
1 Ballast	1,2	602	1.53	164	556	1.67	152
2 Ballast	3	912	1.25	233	991	0.98	513
3 Ballast	4	963	1.09	195	937	1.04	427
4 Ballast	5,6	859	0.90	178	859	0.86	335
1 Cargo	1,2	872	1.64	179	849	1.73	169
2 Cargo	3	1677	1.04	596	1689	1.01	551
3 Cargo	4	1712	1.03	636	1761	1.04	612
4 Cargo	5,6	1285	0.81	305	1225	0.87	350

The comparison displays a large difference in the moment of inertia in ballast condition. Because of the many steel end plates used, the radii of gyration became too large for the segments. For future tests, end plates made of thicker aluminum plates were proposed. The data in cargo condition was in satisfactory agreement. The inaccurate mass moment of inertia in ballast condition may have affected the springing response slightly, but it was expected to be important for the higher order modes.

B.2 Scaling laws and nondimensional properties

B.2.1 Scaling laws

The basic model scaling laws were shown in Section 4.2.3. These were the Froude scaling implying the dispersion relation and the scaling of the sectional stiffness. Scaling of other properties were derived from these based on the length scale, Λ. The subscript $_f$ denotes values in full scale, while $_m$ denotes values in model scale.

Translatory motions η_i as surge ($i = 1$), sway ($i = 2$) and heave ($i = 3$) are scaled as

$$\begin{aligned} \eta_{1,f} &= \eta_{1,m}\Lambda \\ \eta_{3,f} &= \eta_{3,m}\Lambda \\ w_f &= w_m\Lambda \\ \zeta_{a,f} &= \zeta_{a,m}\Lambda \end{aligned} \tag{B.4}$$

w is the deflection or some translatory motion, and ζ_a is the incident wave amplitude. The angular motion as roll ($i = 4$), pitch ($i = 5$) and yaw ($i = 6$) are not scaled. Translatory velocities are scaled as

$$\begin{aligned}
\dot{\eta}_{1,f} &= \dot{\eta}_{1,m}\sqrt{\Lambda} \\
\dot{\eta}_{3,f} &= \dot{\eta}_{3,m}\sqrt{\Lambda} \\
\dot{w}_f &= \dot{w}_m\sqrt{\Lambda} \\
\dot{\zeta}_{a,f} &= \dot{\zeta}_{a,m}\sqrt{\Lambda}
\end{aligned} \tag{B.5}$$

while, rotational velocities are scaled as

$$\dot{\eta}_{5,f} = \frac{\dot{\eta}_{5,m}}{\sqrt{\Lambda}} \tag{B.6}$$

The translatory accelerations are not scaled. Standing in the bow of the model will give the same acceleration as in full scale, but the period differs.

$$\begin{aligned}
\ddot{\eta}_{1,f} &= \ddot{\eta}_{1,m} \\
\ddot{\eta}_{3,f} &= \ddot{\eta}_{3,m} \\
\ddot{w}_f &= \ddot{w}_m \\
\ddot{\zeta}_{a,f} &= \ddot{\zeta}_{a,m}
\end{aligned} \tag{B.7}$$

The rotational accelerations are scaled according to

$$\ddot{\eta}_{5,f} = \frac{\ddot{\eta}_{5,m}}{\Lambda} \tag{B.8}$$

Pressures, p, are scaled based on the hydrodynamic (static) pressure under a wave crest according to linear theory

$$p_f = p_m \frac{\rho_f}{\rho_m}\Lambda \tag{B.9}$$

where ρ is the density of the water.

The vertical bending moment, VBM, and vertical shear force, VSF, are scaled as

$$\begin{aligned}
VBM_f &= VBM_m \frac{\rho_f}{\rho_m}\Lambda^4 \\
VSF_f &= VSF_m \frac{\rho_f}{\rho_m}\Lambda^3
\end{aligned} \tag{B.10}$$

The panel force, FP, follows the same scaling as the pressure when the average pressure is used. The force can be scaled as

$$FP_f = FP_m \frac{\rho_f}{\rho_m}\Lambda^3 \tag{B.11}$$

The total towing force is not easily scaled, since the viscous parts depend on the Reynolds number $R_n = Ux/\nu$ and the rest depends on the Froude number. The viscous part can be manipulated by initiation of turbulence by a small core placed around a transverse bow section. Scaling the added resistance, R_{AW}, in waves can be done by

$$R_{AW,f} = R_{AW,f}\frac{\rho_f}{\rho_w}\Lambda^3 \tag{B.12}$$

The stiffness of the segmented model is represented by rotational stiffness, k_θ, and shear stiffness, k_z. These are scaled in the following way

$$\begin{aligned} k_{\theta,f} &= k_{\theta,m}\frac{\rho_f}{\rho_m}\Lambda^4 \\ k_{z,f} &= k_{z,m}\frac{\rho_f}{\rho_m}\Lambda^2 \end{aligned} \tag{B.13}$$

The damping ratio is nondimensional, and does not have to be scaled.

B.2.2 Nondimensional properties

The results should be made nondimensional wrt. the important physical variables for easy comparison with other results, calculations and in order to check if the results are independent of changes in the important physical variables.

The nondimensional transfer functions may be defined without first scaling the results. E.g. considering the nondimensional transfer function of the pitch angular velocity gives

$$\overline{\dot{\eta}_{5,f}} = \frac{|\dot{\eta}_{5,f}|}{k_f\zeta_{a,f}g/L_f} = \frac{|\dot{\eta}_{5,m}|/\Lambda}{2\pi/(\lambda_m\Lambda)\zeta_{a,m}\Lambda g/(L_m\Lambda)} = \frac{|\dot{\eta}_{5,m}|}{k_m\zeta_{a,m}g/L_m} = \overline{\dot{\eta}_{5,m}} \tag{B.14}$$

where $k = 2\pi/\lambda$ is the wave number, λ is the wave length and g is the acceleration of gravity. The other responses yield the same agreement between transfer functions in model and full scale.

Basically, the motions of interest in relation to the model tests were the two translatory motions heave, surge and the rotational motion pitch. These are made nondimensional in the following way

$$\begin{aligned} \overline{\eta_1} &= \frac{\eta_1}{\zeta_a} \\ \overline{\eta_3} &= \frac{\eta_3}{\zeta_a} \\ \overline{\eta_5} &= \frac{\eta_5}{k\zeta_a} \end{aligned} \tag{B.15}$$

The velocities of a harmonic response is equal to the frequency, ω, times the displacement (with a phase shift). The wave length is made nondimensional by the length between perpendiculars, L_{pp}. The frequency and time, t, are made nondimensional using the dispersion

relation Eq.(4.3).

$$\begin{aligned} \overline{\lambda} &= \frac{\lambda}{L} \\ \overline{\omega} &= \frac{\omega}{\sqrt{g/L}} \\ \overline{t} &= \frac{t}{\sqrt{L/g}} \end{aligned} \tag{B.16}$$

The translatory and rotational velocity are then made nondimensional as

$$\begin{aligned} \overline{\dot{\eta}_1} &= \frac{\dot{\eta}_1}{\zeta_a\sqrt{g/L}} \\ \overline{\dot{\eta}_3} &= \frac{\dot{\eta}_3}{\zeta_a\sqrt{g/L}} \\ \overline{\dot{\eta}_5} &= \frac{\dot{\eta}_5}{k\zeta_a\sqrt{g/L}} \end{aligned} \tag{B.17}$$

while accelerations are made nondimensional based on ω^2 times the displacement, hence

$$\begin{aligned} \overline{\ddot{\eta}_1} &= \frac{\ddot{\eta}_1}{\zeta_a g/L} \\ \overline{\ddot{\eta}_3} &= \frac{\ddot{\eta}_3}{\zeta_a g/L} \\ \overline{\ddot{\eta}_5} &= \frac{\ddot{\eta}_5}{k\zeta_a g/L} \end{aligned} \tag{B.18}$$

Pressure may be difficult to make nondimensional, especially when different physics are involved. The pressure under the wave crest is made nondimensional by use of the hydrostatic pressure height.

$$\overline{p} = \frac{p}{\rho g \zeta_a} \tag{B.19}$$

The physics of the slamming pressure is assumed to be independent of the gravity due to high accelerations, hence it is made nondimensional as

$$\overline{p} = \frac{p}{0.5\rho V_R^2} \tag{B.20}$$

where V_R is the relative velocity between the structure and the wave. In this research the ship had forward speed, different steepness of the waves and 3D geometry with different "deadrise" angles. This made it difficult to find the relative velocity from the measurements. The former method was therefore used.

The vertical bending moment, VBM, is made nondimensional by

$$\overline{VBM} = \frac{VBM}{\rho g \zeta_a B L^2} \tag{B.21}$$

where B is the breadth. Similar the vertical shear force, VSF, is made nondimensional as

$$\overline{VSF} = \frac{VSF}{\rho g \zeta_a B L} \tag{B.22}$$

The force panels were positioned to measure the slamming pressures, but they measured also ordinary wave forces. The force is made nondimensional as

$$\overline{FP} = \frac{4 \cdot FP}{\rho g \zeta_a \pi d^2} \tag{B.23}$$

where the disk diameter, d, in the model tests was $10.0cm$. The forces on the panel was divided by the area and presented as average pressure, p_{av}, for comparison with the pressure from pressure cells.

$$p_{av} = \frac{4 \cdot FP}{\pi d^2} \tag{B.24}$$

The average pressure is made nondimensional in two ways

$$\begin{aligned} \overline{p_{av}} &= \frac{p_{av}}{\rho g \zeta_a} \\ \overline{p_{av}} &= \frac{p_{av}}{0.5 \rho V_R^2} \end{aligned} \tag{B.25}$$

The towing force measured the total force from viscous skin friction, wave resistance in calm water, wave breaking resistance and added resistance in waves. The latter is made nondimensional by

$$\overline{R_{AW}} = \frac{R_{AW} \cdot}{\rho g \zeta_a^2 B^2 / L} \tag{B.26}$$

B.2.3 Measurement devices with locations

Approximate positions of different sensors are listed in Table B.5. The coordinates are given relative to AP, BL and CL with x pointing forward, y pointing to port side and z pointing upwards. The position may vary for the three bows when indicated.

The NYPOS system measured the motions relative to the COG. The program, developed at MARINTEK, calculated the motions of the vessel in 6 DOF. This was based on a ProReflex Motion Capture System with two cameras that captured infrared light from 3 active markers on the "Nypos tree". A separate PC was used for this purpose. COG did not exactly coincide with the COG of either the real ship or the model. However, it was sufficient for evaluating the motions. The "Nypos tree" was placed on the segment aft of

the COG, and deflections introduced small "errors" in pitch and heave. In the extreme case the errors were estimated to 0.3° in pitch and $0.8mm$ in heave based on the relative deflection between the segments.

Digital BM Hottinger Baldwin Messtechnik (HBM) MGC Plus amplifiers were used in combination with the program CATMAN from HBM. CATMAN was modified by MARINTEK to serve their needs. The fixed wave probes were measured by an analog DHI Water and Environment amplifier and converted into a digital signal by an AD-card inserted in one of the digital amplifiers. All channels were sampled at $100Hz$ using a Butterworth low pass filter at $40Hz$. This was insufficient to capture the slamming peaks, but the intention was only to confirm its presence.

The pressures cells measured the absolute pressure. Two types were used with rated pressure of 1.7 and 3.5 bar, respectively. Both were produced by Kulite Semiconductor Products, Inc. The location of the pressure cells on bow 2 is illustrated in Figure B.3. The bow had vertical sides and a natural bottom bilge curvature.

The axial sensors were produced by Entran, and the type ELKM-D2M was used with a limit of 10 and 25kN, respectively. These were ordered based on the maximum expected loads from still water and dynamic bending calculated by VERES for the highest sea state.

For bow 1 and 2, accelerometers produced by Lucas Schaevitz (UK) were used. The type was A433-0001. One of these broke due to hammer decay test, and new accelerometers produced by MARINTEK were used for bow 3.

The inductive transducer measuring the relative position between the segments were also produced by HBM, while the rest of the sensors were manufactured by MARINTEK.

B.3 Uncertainty analysis

In experimental analysis it is necessary to repeat experiments to find the uncertainties, referred to as *precision* error, in the measured quantity. If a specific quantity X is measured N times, the mean value, the standard deviation of the samples and the standard deviation of the mean value are found by

$$\begin{aligned} \overline{X} &= \frac{1}{N}\sum_{i=1}^{N} X_i \\ \sigma &= \sqrt{\frac{1}{N-1}\sum_{i=1}^{N}(X_i - \overline{X})^2} \\ \sigma_{\overline{X}} &= \frac{\sigma}{\sqrt{N}} \end{aligned} \tag{B.27}$$

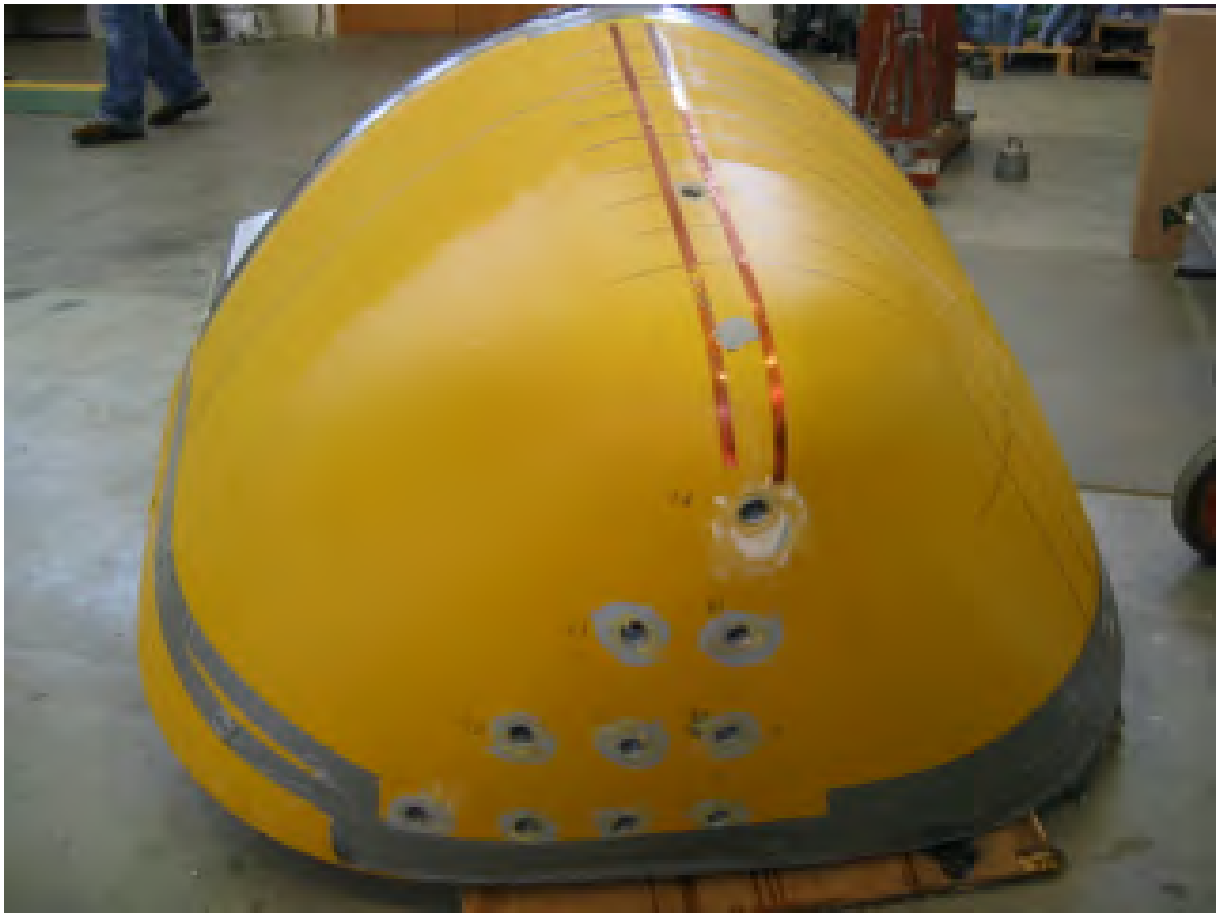

Figure B.3: *Bow 2 run in cargo condition with locations of the pressure probes and relative motion device. The first black horizontal line is located 6m above BL and marked for every second meter upwards.*

The latter assumes a Gaussian parent distribution. For a Gaussian distribution with infinite number of samples, N, the 95% *sample* confidence interval is found within $\overline{X} \pm 1.96\sigma$. However, for a finite number of samples the 95% sample confidence interval is found within $\overline{X} \pm t\sigma$, where the factor t is found from the t-distribution with $N-1$ DOF. The 95% *mean* confidence interval is given in the same manner by $\overline{X} \pm t\sigma_{\overline{X}}$. For N larger than 30, $t = 2.0$ may be used as an approximation.

Wild readings may occur for various reasons. The criterion used herein is referred to as Chauvenent's criterion (Coleman and Steele 1989), which defines an acceptable scatter. It says that points within a probability band of $1 - \frac{1}{2N}$ is kept. This criterion applies the Gaussian distribution instead of the t-distribution also when N is small. After rejecting measurements outside $\overline{X} \pm t_r\sigma$ the mean and standard deviations are finally calculated again, and no more rejections are considered.

The probability band versus number of samples is shown in the right plot of Figure B.4. In the left plot the t-factors for rejection and for the 95% confidence interval are shown. For $N = 1$, 6 and 30 samples the probability band is 0.5, **0.92** and 0.98. The t-factors for rejection become 0.67, **1.73** and 2.39, while for the 95% confidence interval they become 12.7, **2.57** and 2.042. 12.7 is taken from $N = 2$, since the t-distribution for $N = 1$ is not given. Six samples may be a suitable number of tests.

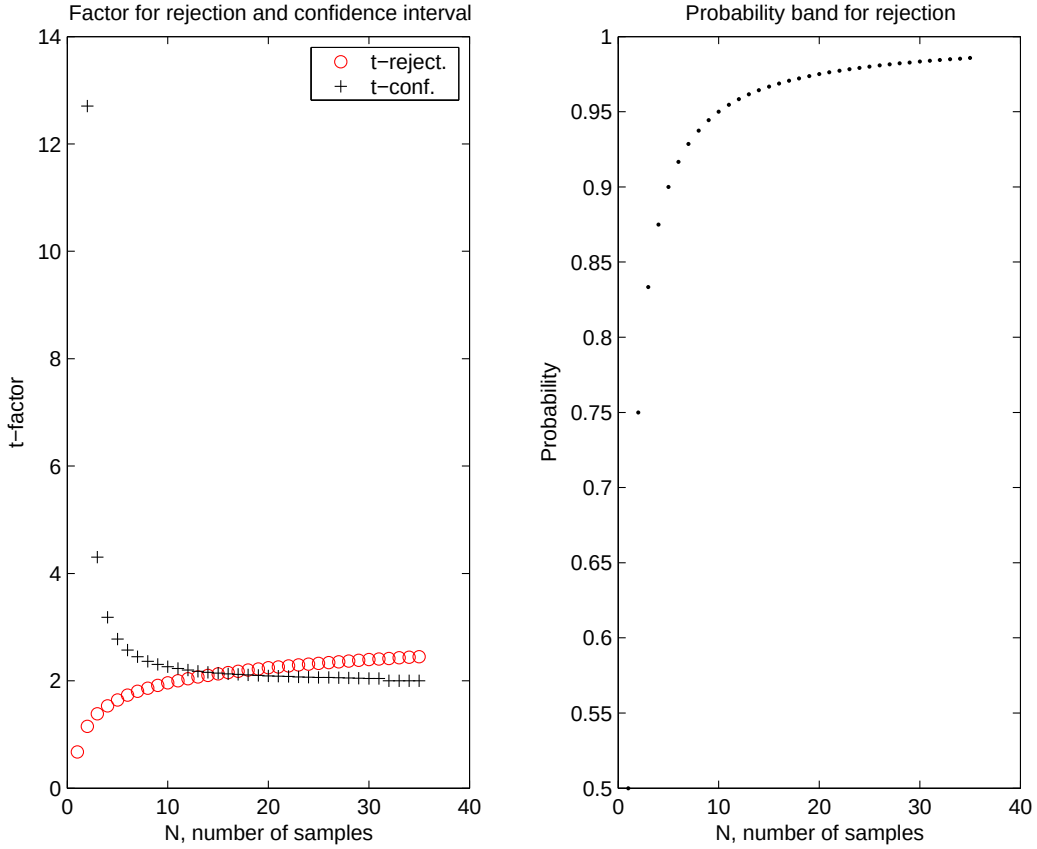

Figure B.4: *The probability band for rejection (to the right), the corresponding t-factors for rejection (to the left) and the t-factors for the 95% confidence interval (to the left).*

Table B.5: *Position of devices.*

Name	Unit	x $[m]$	y $[m]$	z $[m]$	Comment
FX2	N	2.24	0	1.16	Measuring axial force in x-direction, sag=positive
FX3	N	4.34	0	1.16	Measuring axial force in x-direction
FX4	N	6.44	0	1.16	Measuring axial force in x-direction
$FY1_1$	N	1.26	0	1.16	Measuring vertical shear force in z-direction
$FY1_2$	N	1.26	-0.28	0.26	Measuring vertical shear force in z-direction
$FY1_3$	N	1.26	0.28	0.26	Measuring vertical shear force in z-direction
$FY2_1$	N	2.32	0	1.16	Measuring vertical shear force in z-direction
$FY2_2$	N	2.32	-0.55	0.26	Measuring vertical shear force in z-direction
$FY2_3$	N	2.32	0.55	0.26	Measuring vertical shear force in z-direction
$FY4_1$	N	6.52	0	1.16	Measuring vertical shear force in z-direction
$FY4_2$	N	6.52	-0.55	0.26	Measuring vertical shear force in z-direction
$FY4_3$	N	6.52	0.55	0.26	Measuring vertical shear force in z-direction
$FY5_1$	N	7.86	0	1.16	Measuring vertical shear force in z-direction
$FY5_2$	N	7.86	-0.33	0.26	Measuring vertical shear force in z-direction
$FY5_3$	N	7.86	0.33	0.26	Measuring vertical shear force in z-direction
ACCZ1	m/s^2	-0.14	0	0.80	Measuring vertical acceleration, downwards=positive
ACCZ2	m/s^2	1.17	0.1	0.80	Measuring vertical acceleration
ACCZ3	m/s^2	2.01	0.1	0.80	Measuring vertical acceleration
ACCZ4	m/s^2	4.11	0.1	0.80	Measuring vertical acceleration
ACCZ5	m/s^2	6.21	0.1	0.80	Measuring vertical acceleration
ACCZ7	m/s^2	7.77	0.1	0.80	Measuring vertical acceleration
ACCZ8	m/s^2	8.54	0	0.80	Measuring vertical acceleration
P1	N/m^2	8.40/8.17/8.65	0	0.54/0/0	Bow 1/2/3, pressure cell
P2	N/m^2	8.42/7.94/8.50	0	0.40/0/0	Bow 1/2/3, pressure cell
P3	N/m^2	8.48/8.40/8.49	0/0/0.16	0.29	Bow 1/2/3, pressure cell
P4	N/m^2	8.28/8.17/8.43	0/0.08/0	0	Bow 1/2/3, pressure cell
P5	N/m^2	8.55/8.29	0	0.14/0	Bow 1/2, pressure cell
P6	N/m^2	7.96/8.05	0	0	Bow 1/2, pressure cell
P7	N/m^2	7.74	0	0	Pressure cell
P8	N/m^2	8.44/8.05	0/0.08	0.63	Bow 1/2, pressure cell
P9	N/m^2	4.17	0	0	Pressure cell
P10	N/m^2	4.17/8.05	0/0.17	0.29/0	Bow 1/2, pressure cell
P11	N/m^2	1.11/7.94	0/0.09	0	Bow 1/2, pressure cell
P13	N/m^2	0.14	0.02	0.40	Pressure cell
P14	N/m^2	0.00/7.94	0.02/0.17	0.43/0	Bow 1/2, pressure cell
P15	N/m^2	0.13/7.94	0.02/0.26	0.47/0	Bow 1/2, pressure cell
COG	m	4.48/4.51/4.35	0	0.50/0.43/0.49	ballast 1/cargo 1/ bow 2 and 3, used in Nypos
Surge	m	COG			Positive forward
Sway	m	COG			Positive towards starboard
Heave	m	COG			Positive downwards
Roll	°				Positive starboard down
Pitch	°				Positive bow up
Yaw	°				Positive turning to starboard
REL3	m	4.41			Relative motion at "COG"
REL1	m	8.38+	-0.1±		Bow 1, relative motion in bow, skewed
REL2	m	8.29±	0.35±		Bow 1, relative motion at bow side, skewed
REL1	m	8.40			Bow 2, relative motion in bow stem
REL1	m	8.62	0.06		Bow 3, relative motion in bow
WP1	m	5-10	0		Wave probe from wave maker and CL of tank
WP2	m	164	3.3		Wave probe from wave maker and CL of tank
WP3	m	4.0	0		Wave probe from bow of model and CL of tank
WP5	m	-3.6	3.4		Wave probe from bow of model and CL of tank
FP0	N	8.38	0.17	0.57	Lower slamming panel, 10cm diameter
FP1	N	8.42	0.16	0.67	Upper slamming panel, 10cm diameter
FP13	N	0.05	0.06	0.43	Aft slamming panel, 10cm diameter
U	m/s				Speed of towing carriage
TA/TF	N				Towing force ring AP/FP, positive in tension
POS2	mm	2100	76	825	Relative deflection from centre of I-bar, cut 2
POS3	mm	4200	76	823	Relative deflection from centre of I-bar, cut 3
POS4	mm	6300	76	826	Relative deflection from centre of I-bar, cut 4

B.4 Uncertainties and calibration of different sensors

Calibration was divided into two tasks. The *first task* was to calibrate the sensor for a range of different loadings to determine the slope, or response per unit loading. This was done by starting at zero load and then add loads stepwise up to the maximum load, and step down to zero again. A straight line through the points was estimated by a least square fit. It did not indicate the uncertainty in the slope or in the load at high or low load levels. The *second task* was to perform zero setting of the sensors between each run. In practice, after each run there was a waiting time until the water surface was calm. The responses were then measured for a couple of minutes, and the time average was taken representing the new zero point. Subsequently, the new test could be run. When only considering the dynamic behaviour, the mean response was of less importance. However, the mean value was used for different purposes, e.g. to determine added resistance in waves and to determine zero level for nonlinear bending moments.

Uncertainty measures can be obtained in various ways. Calibration certificates may provide such information. Another way is to remove some points along the line and perform a least square fit on the remaining points to estimate the slope. This can be done several times, and the standard deviation and confidence intervals can be established according to Appendix B.3. In the present research, tests were repeated several times. The confidence interval was then based on independent estimates of the slope.

Calibration is normally performed under ideal conditions. For instance, calibration of the axial force sensor was carried out under perfect centric and axial loading. These data were also obtained from the calibration certificate provided. Calibration of the force transducers was performed using small weights (5, 10, 15kg), which confirmed very good linear relationship at low load levels. Since both the shear and axial force transducers were mounted in the model and eccentricities could exist, all shear and axial sensors were calibrated when mounted using small and large loads. This was also done to estimate the rotational stiffness.

The calibration of the axial force versus the applied moment is illustrated in Figure B.5 for the midship section. The data were derived from a single loading and unloading sequence displaying an almost perfectly straight line. The weight measured by an axial sensor was applied by a crane. The governing uncertainty was related to the moment arm.

Figure B.6 shows the calibration of the rotational stiffness, $k_\theta = VBM/\theta$. The rotational stiffness was difficult to determine accurately. The linear regression line did not necessarily go through zero. A quadratic fit in the right plot represents seemingly a better fit through the measured points. The damping tests indicated that the natural frequency varied more with the response level than the full scale measurements. This fact in combination with the linear regression line failing to go through zero support that the stiffness was truly weakly nonlinear. This is possible explained by bearings below required tolerance, mixture of steel and aluminum and redistribution of forces in the flexible connections.

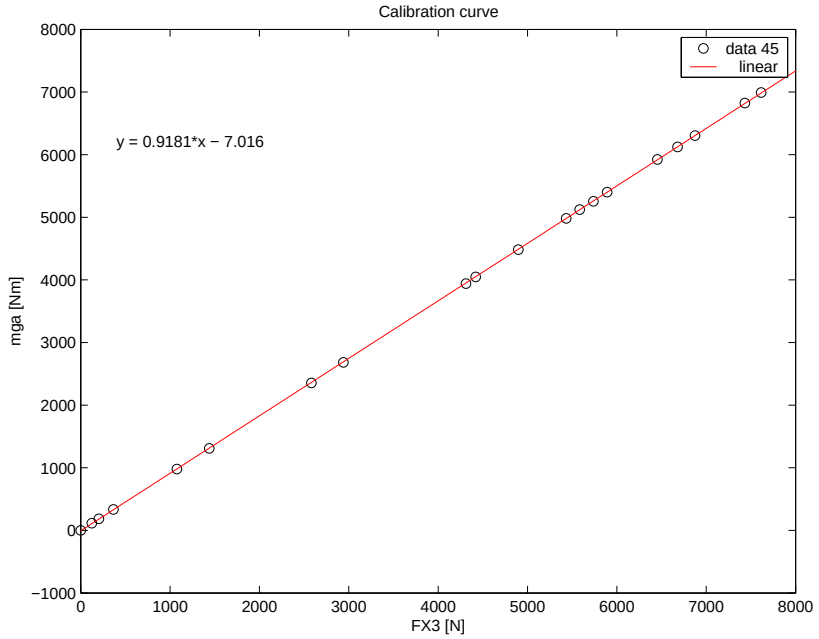

Figure B.5: *Calibration curves for the moment amidships.*

Linear curves as shown in Figure B.5 were established by repeated tests both for high and low load levels with positive and negative loading to establish the uncertainties. Figure B.7 shows the estimated slopes with rejected values for all three axial sensors. The results were merged, since they represent the same design. The expected value was the ratio between the moment, VBM, and the axial forces measured, N. This was equal to the arm from the neutral axis, which was slightly above the I-beam, to the centre of the screw in Figure B.1. The arm was $0.90m$ amidships, which was close to the estimated mean values. Table B.6 presents the uncertainties for the different shear forces, moments and rotational stiffness. $FY5$ denotes the shear force in cut 5. The rotational stiffness is rather uncertain. The data were derived after cargo 1 condition. *The factor of 0.88 was used to define the moment and stress in the subsequent fatigue calculations and for transfer functions.* The factors for the shear forces were generally far from the expected value of 1.0, and confirmed the importance of the calibration in assembled condition. The shear force sensors referred to as guide towers were of slightly different design at the different cuts, hence these results were not merged.

It should be noted that although the axial force sensor is calibrated as explained above, there is a physical bias introduced when the model is placed in water. This is caused by axial forces, that contribute to the measured axial force, which is converted into the vertical bending moment. The vertical bending moment has contribution from axial forces, but the axial force is also a separate global force. The measured "vertical bending moment" therefore contains a contribution from the global axial force. This effect is considered as

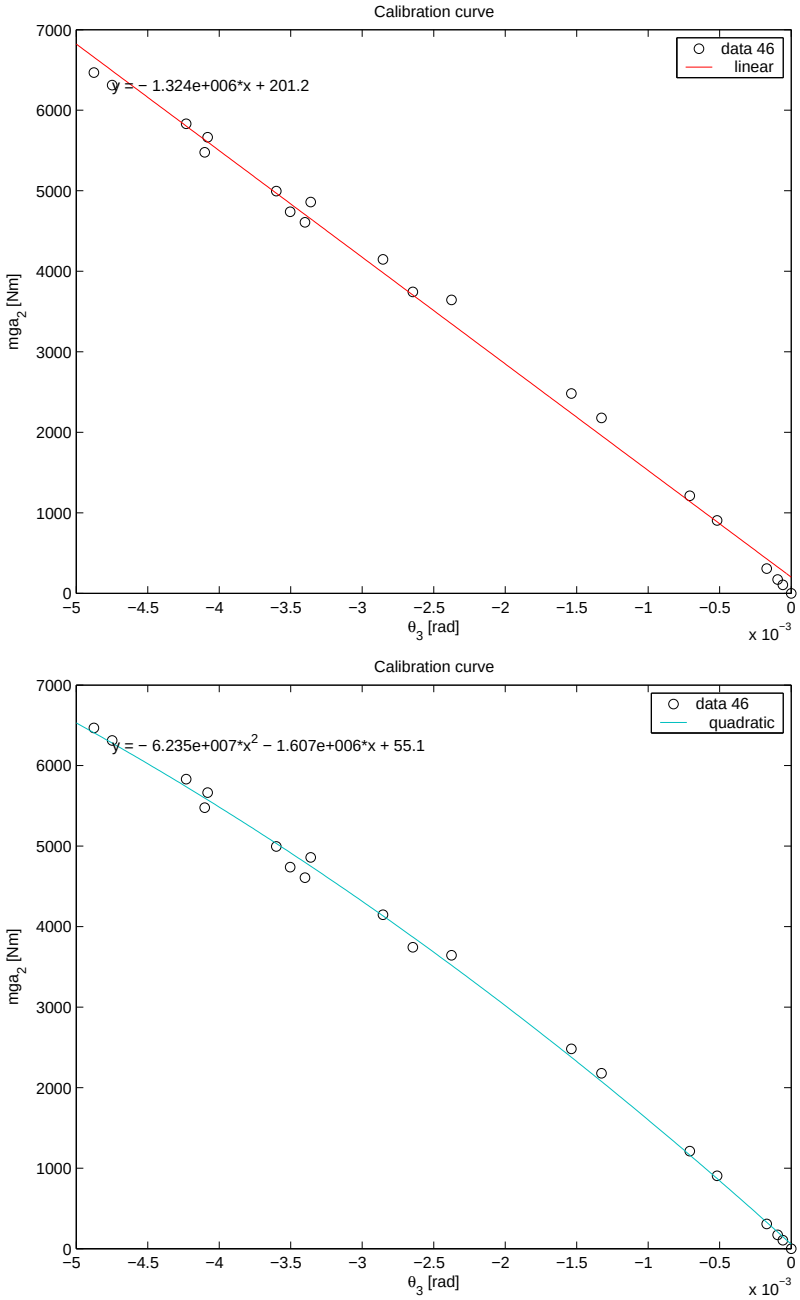

Figure B.6: *Calibration curves for rotational stiffness amidships.*

insignificant for the vibration response, but it will contribute to the nondimensional vertical bending moment. The effect of the axial stress can not be separated with the single axial force sensor in "deck", but two sets of sensors must be used to separate these global loads. This is illustrated in (Storhaug and Moe 2007), which also shows that the axial stress component is small for a container vessel. It should be kept in mind that most (if not all) references on model tests and full scale measurements do not explain or handle

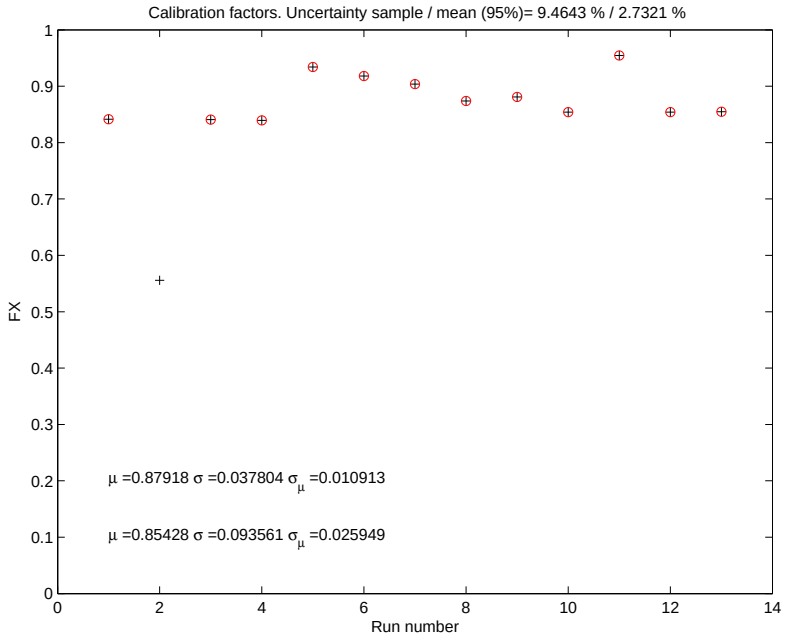

Figure B.7: *Calibration factors for the moment for different sensors and load sequences.*

Table B.6: *Calibration factors; mean value and 95% mean confidence interval in %.*

Response	Mean value (slope)	95%
FY1	1.13	3.0
FY2	1.19	2.0
FY4	0.93	5.3
FY5	0.99	0.2
FX2	0.86	7.5
FX3	0.91	7.1
FX4	0.86	1.7
FX	**0.88**	2.7
$k_{\theta,2}$	0.88E6	53
$k_{\theta,3}$	1.58E6	145
$k_{\theta,4}$	1.23E6	100
k_{θ}	**1.22E6**	22

this properly. Therefore there exist a lot of model experiments which is somewhat biased, hence the reported vertical bending moment is not the true vertical bending moment, but slightly different as in these model tests. From a fatigue consequent point of view, this is not important. This additional effect is also recently illustrated by Clauss et al. (2007).

The expected maximum pressures were estimated in order to define a range to be used by the amplifier. E.g. the maximum pressure was estimated to $70kPa$ for slamming including a safety margin. This was defined as the range. The amplifier operates in the range

of $\pm 10V$. To achieve maximum resolution in the measurements using the amplifier, $10V$ should give $70kPa$. The resolution becomes important at low amplitudes. E.g. with a 16 bits amplifier, used in these experiments, the range from $-10V$ to $+10V$ was divided into $2^{16-1} = 32768$ levels, and the resolution became $4.3Pa$. The use of filters reduced the stepwise behaviour somewhat. Another important uncertainty was related to the numbers written to file. In this case, three significant digits were used in the ASCII files. The pressures were written in Pa, but if it had been written in kPa, the uncertainty would be $0.5Pa$. At the bottom of the ship the pressures were low and in the order of 10-100Pa depending on waves and motions. For these pressures, the resolution became poor. To determine the second order excitation pressure became difficult.

The relative motion sensors as seen in Figure 4.4 was calibrated by fitting the two copper fibers on a vertical plate that was lowered into the water at known depths. A specific distance between the copper fibers was used. Similar pairs were fitted on the model. The hull may not be plane and vertical, and it was difficult to achieve exact the specified distance between the copper fibers. Some uncertainties were then introduced, but a few rough calibrations were performed. E.g. by the water exceeding the upper limit of the copper fibers, the measured relative motion was compared to the distance from still water level to the upper part of the copper fibers. The agreement was within a couple of millimeters or about 1%. The wave probes were calibrated in the same way as the relative motion sensors.

The accelerometers, the local deflection sensors, the slamming panels and the motions by the NYPOS system were calibrated before conducting these experiments, while the towing force sensors were calibrated by hanging known weights from the sensors.

B.5 Calibration of waves prior to model testing

A few questions must be answered before proceeding with springing tests. How sensitive is the springing response to inaccuracies in wave frequency and speed? What is the necessary distance to build up the springing response and to produce enough cycles at a 'maximum' level for subsequent assessment? What is the accuracy of the requested wave frequency, and how far down the tank are the waves of acceptable quality? The answers to these questions will be elaborate in the following.

B.5.1 Sensitivity of springing response

The sensitivity of resonance response to changes in wave frequency and/or speed was illustrated utilizing basic theory. The relation between the wave frequency and the encounter frequency in head sea waves with forward speed was found in Eq.(A.28), and this expression solved for ω_0 was shown in Eq.(2.85). The change of the encounter frequency due to

a change in speed and wave frequency can be expressed as

$$\delta\omega_e = (1 + \frac{2\omega_0}{g}U)\delta\omega_0 + \frac{\omega_0^2}{g}\delta U \tag{B.28}$$

The SDOF system was used to find the necessary change in speed and/or wave frequency causing a drop from resonance to $1/\sqrt{2}$ times the maximum level. This was given by the half-power bandwidth method, Eq.(2.52), which was one way to determine the damping ratio, λ, from the transfer function. It is rewritten

$$2\lambda\omega_s = \omega_2 - \omega_1 \tag{B.29}$$

where ω_s is the natural frequency, and ω_2 and ω_1 is the frequency on each side of the peak that corresponds to the $1/\sqrt{2}$ level.

The change in encounter frequency that gives $1/\sqrt{2}$ times the resonance peak based on a damping ratio can now be written

$$\delta\omega_e = \lambda\omega_s = (1 + \frac{2\omega_0}{g}U)\delta\omega_0 + \frac{\omega_0^2}{g}\delta U \tag{B.30}$$

Considering each component separately, and making them nondimensional gives

$$\frac{\delta\omega_0}{\omega_0} = \frac{\lambda\omega_s}{(\omega_0 + \frac{2}{g}\omega_0^2 U)} \tag{B.31}$$

$$\frac{\delta U}{U} = \frac{g\lambda\omega_s}{\omega_0^2 U} \tag{B.32}$$

The damping ratio is set to 1%, the speed to $7.7m/s$ $(15kn)$ and the natural frequency to $3.33rad/s$ $(0.53Hz)$. The wave frequency which gave resonance in head sea was $1.518rad/s$ $(4.14s)$. The relative change necessary to reduce the response to 70% corresponds to 0.6% in wave frequency or 1.8% in speed, confirming the *significant sensitivity* to both, but that the wave frequency might be critical.

The towing spring were chosen to provide a surge period, T, of about $6s$ ($35s$ in full scale), which was well above the periods of interest. A spring stiffness of $2000N/m$ at each end was used in ballast condition, while $3000N/m$ was used in cargo condition. Considering the surge motion under harmonic resonance condition, the surge velocity can be estimated by

$$\dot{\eta}_1 = \omega\eta_1 = \frac{2\pi}{T}\eta_1 \tag{B.33}$$

A surge motion of $2cm$ gave a maximum additional speed of $\pm 1.6\%$ at full speed. Hence, the surge motion had to be controlled to a minimum, roughly less than $2cm$, to avoid a beat shape of the springing response. The controlling of the surge motion was confirmed necessary from the tests, and if not done properly, the response became beat shaped with

a difference in the two spectrum peaks corresponding to the natural frequency in surge.

A third point was to estimate the necessary distance to build up the response to e.g. $x = 99\%$ of the maximum response. This was estimated based on Eq.(A.94) as

$$s = -U\frac{\ln(1-\frac{x}{100})}{\omega_s \delta} \tag{B.34}$$

Roughly $30m$ was necessary in the model experiments assuming a damping ratio of 1% and service speed. A sufficient number of cycles with a constant and 'maximum' level should also be available from the time series. For linear springing 10 cycles may be regarded as sufficient, and this required a distance of only $4m$, hence *the build up phase was critical*.

B.5.2 Location of wave probes and tested wave conditions

Five wave probes (WP) were used in the wave calibration. Two were fixed, one close to the wave maker and one half way down the tank. Three others were placed on the towing carriage and were moved down the tank with the model speed to cover a spatial distribution of the towing tank. A few measurements were also carried out at fixed positions.

The positions of the wave probes are shown in Table B.7. The wave probes consisted of

Table B.7: *Channels and positions for wave calibration tests.*

Name	Channel	Position
Time	1	
WP1	6	Fixed $10m$ from the wave maker
WP2	7	Fixed $164m$ from the wave maker and 3m from the side wall
WP3	2	Towing carriage, $3m$ in front of vessel
WP4	3	Towing carriage, COG and at centre of the tank
WP5	4	Towing carriage, COG and $2.25m$ from the side wall
SPEED	5	Speed of the towing carriage

two thin cores and one circular column going down into the water. The column generated a wake, which was somewhat disturbing in a visual sense. A foil shaped coumn is preferred.

The regular waves, as listed in Table B.8 in full scale values, were proposed for the springing model tests in ballast condition. The regular waves were chosen to excite linear and higher order effects with three different wave amplitudes.

B.5.3 Results of regular wave tests

The wave amplitude was estimated by three methods. The first method was based on the zero crossing process and local maxima. The second was based on the standard deviation

Table B.8: *Regular wave test proposed for ballast condition.*

Run	T [s]	H [m]	Comment
8002	4.14	0.7	Linear resonance
8003	4.14	1.4	Linear
8004	4.14	2.1	Linear
8005	6.60	1.4	2^{nd} order
8006	6.60	2.1	2^{nd} order
8007	6.60	3.5	2^{nd} order
8008	8.83	2.1	3^{rd} order
8009	8.83	3.5	3^{rd} order
8010	8.83	4.9	3^{rd} order
8011	10.953	2.1	4^{th} order
8012	10.953	4.1	4^{th} order
8013	10.953	9.8	4^{th} order
8014	13.019	2.1	5^{th} order
8015	13.019	4.9	5^{th} order
8016	13.019	11.8	5^{th} order

of the time series, and the third was based on the standard deviation obtained from the spectra. A filter was used in all cases to remove noise and low frequency components. The latter was also partly due to elevation of the track along the tank ($3cm$ difference). The three methods gave in practice identical answers. The uncertainty represented by the 95% sample confidence interval, was based on two times the standard deviation derived from the zero crossing process.

The ratios between the requested input amplitudes in Table B.8 and the measured values are shown in Figure B.8 versus the measured wave frequency for WP1. Waves that will excite first to fifth order resonance were included. Both the mean value (dot) and the 95% sample confidence interval (bar) were presented. The uncertainty increased for higher frequencies, even though the shorter waves were evaluated closer to the wave maker. The uncertainty did not seem to increase for higher waves (the highest waves at second order wave frequencies for WP2 were biased and shouold be disregarded). The uncertainty was higher for the moving wave probes than WP1 close to the wave maker. The WP5 at the side displayed more uncertainty than those at the centre. This may come from wall interaction, especially for the shorter waves. The shortest waves did not reach WP2, because of the time necessary for the short waves to travel $164m$. It was also noted that *the highest waves for linear springing showed a shift in the frequency.* The mean amplitude differed from the ratio of one, and no clear trend was displayed. A wave amplitude different than requested, e.g. by 17% for the longest and highest wave, was found acceptable as long as the wave height was measured, and the model test results were made nondimensional with respect to the measured wave.

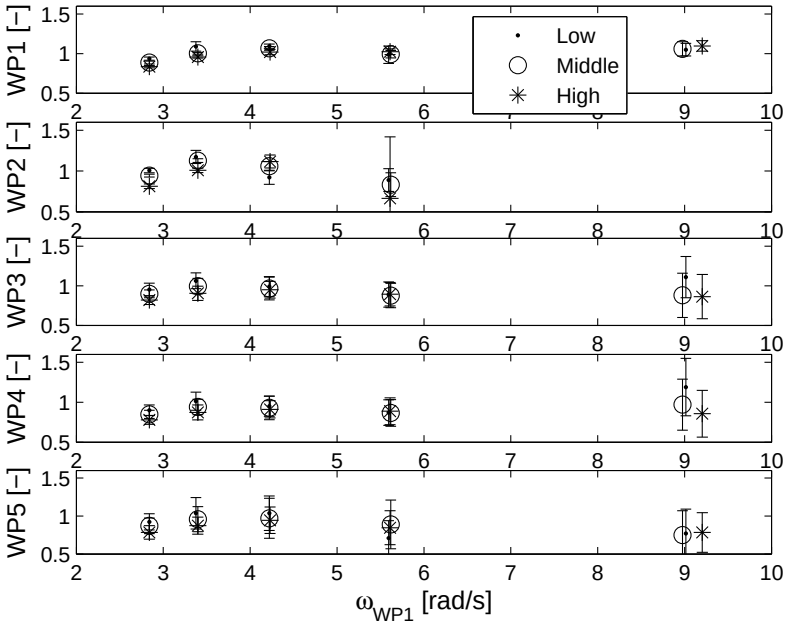

Figure B.8: *Mean wave height value with 95% sample confidence interval (bar) versus input wave height and wave frequency (WP1) for three wave heights.*

Accurate wave frequency is essential. Figure B.9 shows the ratio between the dominating frequency in the wave spectra and the input frequency for the different wave input. For the moving wave probes, the encounter input frequency was used. This was based on the measured speed, which was accurately measured. The speed was set to $1.300m/s$, but the measured velocity of the towing carriage was $1.3093\pm0.0004m/s$ as the 95% mean confidence interval. The ratio was within 1% except the shortest waves for the moving wave probes. WP4 and WP5 results were not shown because they gave identical results as WP3. The discrepancy for the shortest waves may partly come from the resolution of the wave spectra. Only $10.24s$ with acceptable quality were considered for the shortest and highest waves resulting in $N = 1024$ samples. The resolution was $0.628rad/s$ as a maximum according to Eq.(2.75), while down to $0.06rad/s$ for longer waves. The maximum discrepancy from a ratio of one was only about 4%. The resolution indicates an uncertainty of maximum 3.5% for the fixed probes and maximum 1.6% for the moving probes. Taking the resolution into consideration, the wave frequency was in general good.

The mean value of each wave run was considered as an independent estimate, and the uncertainty of a random wave amplitude or wave frequency was estimated based on the 15 individual wave runs. The results are listed in Table B.9. Basically, this shows that the *wave amplitudes were as requested at the wave maker, but were too low at other positions.* Moreover, the frequency was as requested.

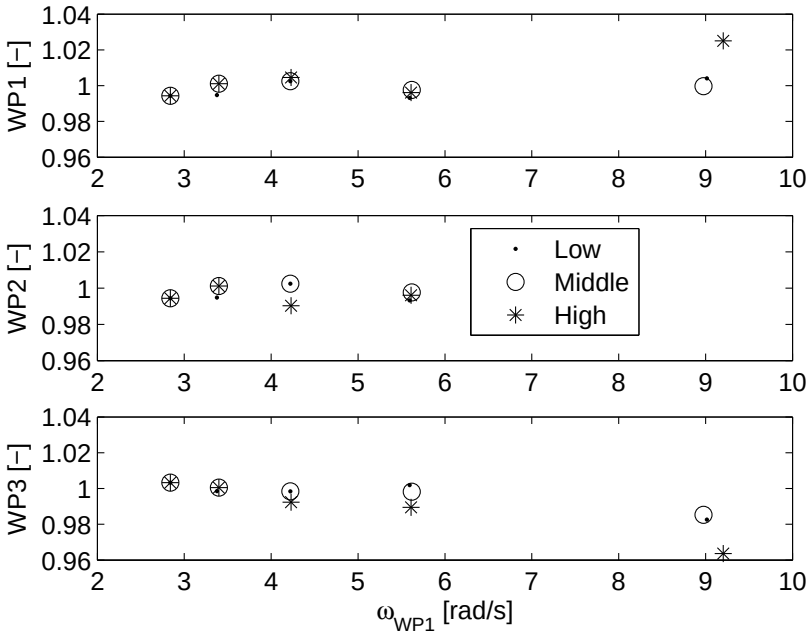

Figure B.9: *Ratio of measured frequency from spectra to input frequency shown for different wave probes and wave heights.*

Figure B.10 illustrates the difficulties with the short waves at fixed positions along the tank. It was observed that between 40 and 60m from the wave maker, the waves became unacceptable. At 60m the regular wave turned into a spectrum, which evolved continuously towards longer wave components possibly by some interaction. It was observed that a damper intended to damp out transverse waves, and located on each side about 40m from the wave maker, initiated disturbances and possibly instabilities. It was decided to remove this damper in the subsequent model tests.

Table B.9: *Ratio of measured parameter to input parameter. Mean of amplitude or frequency with their respective 95% mean confidence interval for the different wave probes.*

Response	Mean	95%
WP1, amplitude	1.012	0.035
WP2, amplitude	0.773	0.223
WP3, amplitude	0.925	0.036
WP4, amplitude	0.900	0.033
WP5, amplitude	0.877	0.055
WP1, frequency	0.999	0.002
WP2, frequency	0.973	0.051
WP3, frequency	0.997	0.004

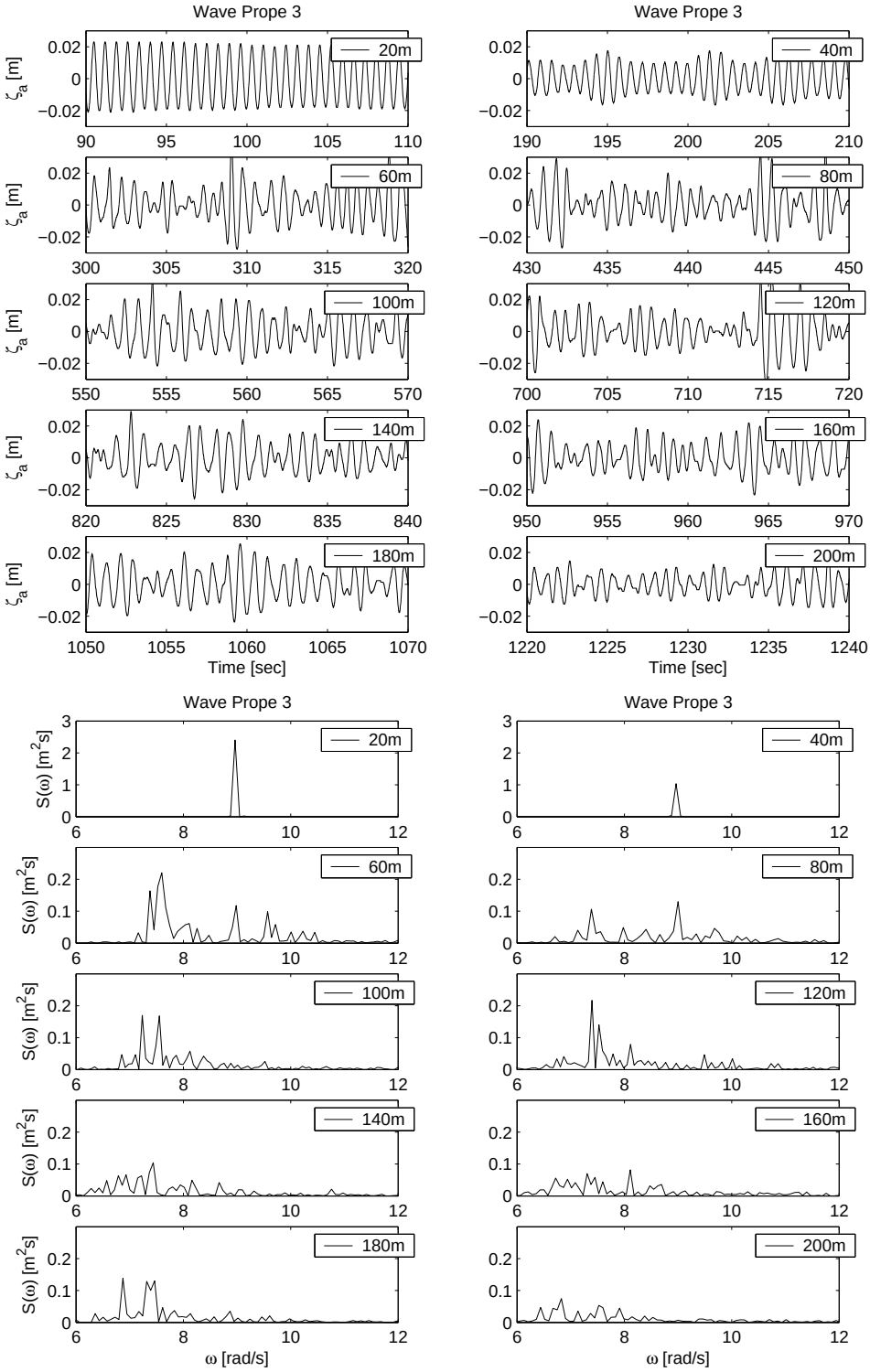

Figure B.10: *Wave amplitudes and spectra at 20m steps from the wave maker for the shortest waves; $H = 1.4m$ (in full scale). Only WP3 was considered.*

B.5.4 Irregular waves

The irregular waves represented by JONSWAP, Eq.(2.78), shown in Table B.10 were defined for the purpose of the springing tests. A peakness factor of $\gamma = 2$ was chosen. This may be a realistic value for waves encountered in open ocean. Higher γ may give breaking waves, which may change the spectrum. A steepness criterion defined by Eq.(2.88) was used as a rule of thumb value to avoid breaking waves. This was satisfied for all sea states, and breaking waves were only observed a couple of times in run 8100 and 8108.

Table B.10: *Irregular sea states considered for wave calibration (at full speed).*

Sea state no.	Run	T_P [s]	H_S [m]	H_S/λ_P
1	8100	8.177	3.0	0.029
2	8101	10.902	3.0	0.016
3	8102	12.265	3.0	0.013
4	8103	13.628	3.0	0.010
5	8104	10.902	5.0	0.027
6	8105	12.265	5.0	0.021
7	8106	13.628	5.0	0.017
8	8107	14.990	5.0	0.014
9	8108	12.265	7.0	0.030
10	8109	13.628	7.0	0.024
11	8110	14.990	7.0	0.020
12	8111	14.990	9.0	0.026

The irregular waves were measured using two sweeps along the tank at full speed ($1.3m/s$). This gave a time trace equivalent to 26 minutes in full scale. The duration was a bit short to establish a reliable spectrum, nevertheless, the measured spectra were compared to the requested spectra for the 12 different sea states.

FFT was used directly on the measured time trace to obtain the spectra. The spectra were spiky, and they were smoothed by the Gaussian Bell in Eq.(2.76). The encounter spectra from the moving wave probes were converted into wave spectra for comparison with the fixed wave probes and input spectra. This gave a finer resolution for the converted spectra. H_S and T_Z were calculated directly from the spectra, while T_P was found at the maximum peak. The smoothed spectra gave more reliable estimates of T_P than the raw spectra. H_S, T_P, γ, n and m were also estimated by a nonlinear fit. This method was less sensitive to cut off frequencies. $n = 5$ and $m = 4$ were tail and shape factors in the JONSWAP spectrum. These were estimated based on previously estimates of H_S, T_P and γ. Fits to both the raw and smoothed spectrum were considered, except for n and m.

The results for the 5 wave probes and 12 sea states were presented as ratios between the estimated and requested input, as illustrated in Figure B.11, B.12, B.13 and B.14 for H_S, T_P, γ and n and m, respectively.

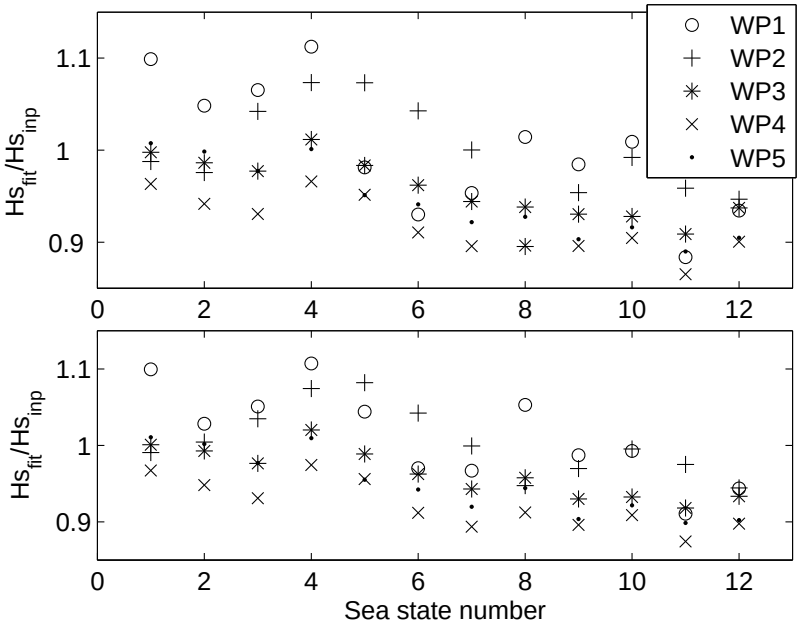

Figure B.11: *Ratio of measured and input H_S for raw (upper) and smoothed fit (lower).*

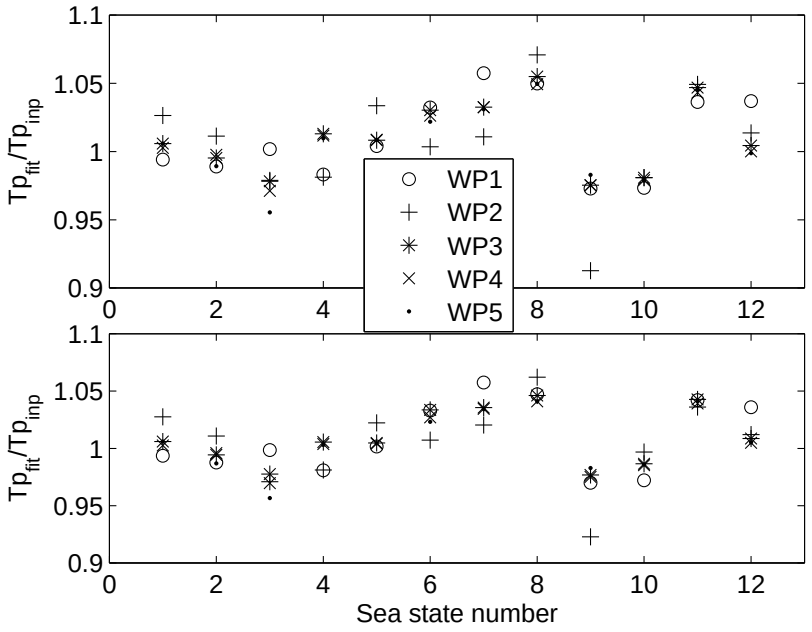

Figure B.12: *Ratio of measured and input T_P for raw (upper) and smoothed fit (lower).*

WP3 was relevant for describing the wave quality located in front of the model. The uncertainties of the different sea state characteristics based on WP3 and also on all wave probes

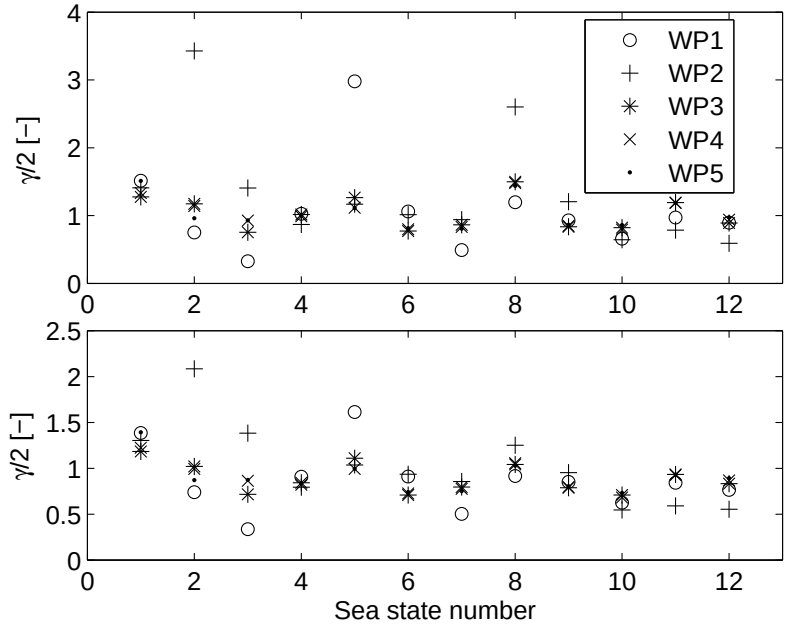

Figure B.13: *Ratio of measured and input γ for raw (upper) and smoothed fit (lower).*

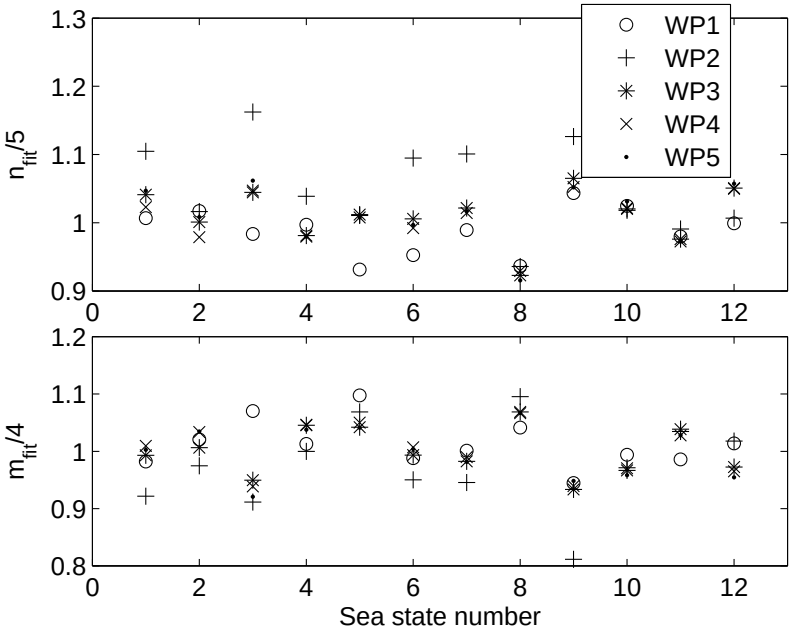

Figure B.14: *Ratio of measured and input n and m for smoothed fit.*

merged are listed in Table B.11. It was evident that the peakness factor should not be estimated based on the smoothed spectrum. This factor had the largest variation, but the mean value was as requested. The JONSWAP tail, n, and shape, m, parameters were as

requested, but the fit method may be somewhat deficient for the n factor when the whole frequency range was considered. *The wave heights were in general too low and the peak periods were in general acceptable.*

Table B.11: *Uncertainty in JONSWAP parameters from fit to raw and smoothed spectrum, and data derived directly from the moments of the smoothed (sm.) spectrum. Results are presented as ratio of measured value to requested input.*

Parameter	Mean (raw)	95% mean (raw)	Mean (sm.)	95% mean (sm.)
H_S fit WP3	0.959	0.020	0.963	0.020
H_S moment WP3			0.953	0.019
H_S fit WP1-5	0.961	0.014	0.967	0.014
H_S moment WP1-5			0.956	0.012
T_P fit WP3	1.011	0.016	1.010	0.015
T_P fit WP1-5	1.011	0.007	1.009	0.007
T_P moment WP3			1.008	0.018
T_P moment WP1-5			0.998	0.011
γ fit WP3	1.030	0.148	0.890	0.100
γ fit WP1-5	1.001	0.069	0.896	0.060
n fit WP3			1.020	0.018
m fit WP3			0.999	0.026
n fit WP1-5			1.011	0.012
m fit WP1-5			1.001	0.012

The results were consistent with the regular wave tests indicating too low wave heights, but with acceptable periods. There were still uncertainties related to how the shorter waves were developing down the tank in absence of wind, but Figure B.10 indicated that the energy was "lost" after roughly $100m$. It was expected that *the contribution from linear springing would be reduced along the tank* in the subsequent model tests. Other effects such as wall interaction, scattering from the model, wave-wave interaction, reflection from the beach and depth changes may also influence subsequent results. In any case, *the wave heights must be measured during the experiments.*

B.6 Sea states considered in the fatigue assessment

Table B.12 presents all sea states investigated for different combinations of bow design, loading condition and speed. The sea states were defined by the significant wave height, H_S, and the zero-upcrossing period, T_Z. The latter was converted to peak period, T_P, for input to the wave maker based on the Eq.(2.83).

Table B.12: *Overview of sea states run for combination of loading conditions and bow designs. The notation T refers to runs with additional trim by placing 100kg on the bow, giving an increased draft of 1.6m. In case two speeds are indicated, the higher was used in the ballast and the lower in cargo condition.*

H_S/T_Z	U [m/s]	Ballast	Cargo	Ballast 2	Cargo 2	Ballast 3	Cargo 3
2/5	1.3			1639,1640,1641			
2/5 T	1.3			1663,1664,1665			
2/6	1.3			1642,1643,1644			
2/7	1.3			1645,1646,1647			
2/8	1.3			1648,1649,1650			
2/9	1.3			1651,1652,1653			
3/6	1.3/1.15	1100,1101,1102	1357,1358,1359	1582,1583,1584	1745,1746,1747	2350,2351,2352	2147,2148,2149
3/6 T	1.3			1654,1655,1656			
3/7	1.3/1.15		1405,1406,1407	1585,1586,1587	1748,1749,1750	2353,2354,2355	2150,2151,2152
3/8	1.3/1.15	1110,1111,1112	1360,1361,1362	1588,1589,1590	1751,1752,1753	2356,2357,2358	2153,2154,2155
3/9	1.3/1.15	1120,1121,1122	1363,1364,1365	1591,1592,1593	1754,1755,1756	2359,2360,2361	2156,2157,2158
3/10	1.3/1.15	1130,1131,1132	1366,1367,1368	1594,1595,1596	1757,1758,1759	2362,2363,2364	2159,2160,2161
4/7	1.3/1.15		1408,1409,1410	1597,1598,1599	1760,1761,1762	2365,2366,2367	2162,2163,2164
4/7 T	1.3			1657,1658,1659			
5/8	1.3/1.15	1140,1141,1142	1369,1370,1371	1600,1601,1602	1763,1764,1765	2368,2369,2370	2165,2166,2167
5/8 T	1.3			1660,1661,1662			
5/8	0.87		1372,1373	1612,1613	1791,1792	2395,2396	2193,2194
5/9	1.3/1.15	1150,1151,1152	1374,1375,1376	1603,1604,1605	1766,1767,1768	2371,2372,2373	2168,2169,2170
5/9	0.87		1377,1378	1614,1615	1793,1794	2397,2398	2195,2196
5/10	1.3/1.15	1160,1161,1162	1379,1380,1381	1606,1607,1608	1769,1770,1771	2374,2375,2376	2171,2172,2173
5/10	0.87		1382,1383	1616,1617	1795,1796	2399,2400	2197,2198
5/11	1.3/1.15	1170,1171,1172	1384,1385,1386	1609,1610,1611	1772,1773,1774	2377,2378,2379	2174,2175,2176
5/11	0.87		1387,1388	1618,1619	1797,1798	2401,2402	2199,2200
7/9	1.3/1.15	1180,1181,1182	1389,1390,1391	1620,1621,1622	1775,1776,1777	2380,2381,2382	2177,2178,2179
7/9	0.43		1392	1633	1788	2392	2190
7/10	1.3/1.15	1190,1191,1192	1393,1394,1395	1623,1624,1625	1778,1779,1780	2383,2384,2385	2180,2181,2182
7/10	0.43		1396	1634	1789	2393	2191
7/11	1.3/1.15	1250,1251,1252	1397,1398,1399	1626,1627,1628	1781,1782,1783	2386,2387,2388	2183,2184,2185
7/11	0.43		1400	1635	1790	2394	2192
9/11	1.3/1.15	1260,1261,1262	1402,1403,1404	1629,1630,1631	1784,1785,1786	2389,2390,2391	2186,2187,2188
9/11	0.87			1637,1638			
9/11	0.43			1636			
9/11	0		1401	1632	1787	2300	2189
4/8.5	1.3					2403,2404,2405	
4/9.5	1.3					2406,2407,2408	
4/10.5	1.3					2409,2410,2411	
2/7.5	1.3					2412,2413,2414	
2/8.5	1.3					2415,2416,2417	
2/6.5	1.3					2418,2419,2420	
6/9.5	0.65					2421,2422	
6/8.5	0.65					2440,2441	
6/10.5	0.65					2442,2443	
6/7.5	0.65					2444,2445	
5/6.5	0.87					2446,2447	
7/11.5	0.43					2448	
3/11	1.30					2449,2450,2451	
4/11.5	1.30					2452,2453,2454	
5/11.5	0.87					2455,2456	
6/11.5	0.65					2457,2458	
8/9.5	0.22					2459	
8/10.5	0.22					2460	
7/7.5	0.43					2461	
6/6.5	0.65					2462,2463	
4/5.5	1.30					2464,2465,2466	
2/9.5	1.30					2467,2468,2469	
9/7.5	0					2470	
9/9.5	0					2471	
12/10.5	0					2472	

B.7 Modes shapes, sectional properties and mass distribution of the real ship

The 2 and 3-node vertical mode shapes in one ballast condition were provided by DNV, and numerical values are presented in Table B.13.

Distributions of bending stiffness and shear stiffness were derived for 10 cross sections along

Table B.13: *Measured mode shape in full scale in ballast condition.*

Position forward of midship $[m]$	Nondimensional 2-node	Nondimensional 3-node
-150.0	1.0	-1.0
-133.0	0.83	-0.75
-119.4	0.71	-0.60
-104.1	0.54	-0.40
-98.5	0.47	-0.28
-87.2	0.35	-0.13
-75.9	0.25	0.03
-65.1	0.14	0.14
-53.9	0.02	0.23
-42.6	-0.09	0.28
-31.8	-0.15	0.28
-20.5	-0.22	0.24
-9.2	-0.27	0.16
1.6	-0.29	0.06
12.9	-0.29	-0.06
24.2	-0.28	-0.16
35.0	-0.25	-0.23
46.3	-0.17	-0.28
57.5	-0.10	-0.24
68.4	-0.02	-0.23
79.6	0.08	-0.12
90.9	0.18	-0.02
101.7	0.28	0.10
113.0	0.40	0.27
124.3	0.53	0.38
136.3	0.62	0.53
150.7	0.71	0.65

the ship. This was input to the continuous FE beam model. A few simplifications were made

1. Linear interpolation was used between the cross sections.

2. The structure was assumed to be 100% efficient and continuous without small openings (except manholes).

3. The effective flanges were disregarded.

4. Gross scantlings (as built) were assumed.

5. The effective shear area was based on the projected vertical side and bulkhead structure.

The sectional properties are provided in Table B.14, and they were obtained from the DNV Program NAUTICUS Section Scantlings. For clarification, I_h is the sectional area moment of inertia about the horizontal neutral axis, I_v is about the vertical neutral axis at CL, A is the total cross sectional area, A_v is the vertical projected area without stiffeners and z_{na} is the position of the neutral axis above BL. A_v was assumed to represent the effective shear area A_s.

Table B.14: *Sectional properties derived for the real ship.*

Distance from AP $[m]$	I_h $[m^4]$	I_v $[m^4]$	A $[m^2]$	A_v $[m^2]$	z_{na} $[m]$
17.0	185	191	3.39	1.30	15.91
44.5	437	1108	5.41	1.97	12.59
68.9	533	1640	5.89	1.88	11.85
81.1	603	1818	6.31	1.90	11.90
146.9	689	2021	6.78	1.92	11.83
204.3	665	1989	6.71	2.00	11.73
227.8	593	2008	6.37	1.84	11.12
253.2	498	1845	5.97	2.00	10.71
263.5	445	1485	5.56	1.95	11.05
285.7	270	399	3.92	1.46	14.02

The mass distribution as point masses based on the ballast condition is provided in Table B.15 with FP and BL as references. More detailed mass distribution was used in the numerical predictions.

Table B.15: *Point mass distribution for ballast condition. Total mass is 14663Ttonnes.*

Mass [*tonnes*]	Distance from FP [m]	Distance above BL [m]
229.2	2.74	13.85
372.9	9.10	14.70
472.8	16.52	14.76
4053.8	23.70	13.45
4631.1	30.48	13.42
9563.4	41.32	13.42
10843.2	55.81	13.01
7245.8	67.62	12.77
3693.7	88.02	13.05
11412.0	98.74	12.65
11443.0	113.13	12.65
11642.6	127.39	12.67
4461.9	138.33	12.88
6667.5	158.97	12.82
11396.2	170.61	12.67
11090.4	184.80	12.34
7842.2	199.33	9.43
1358.6	212.83	13.25
7545.1	229.07	14.21
8365.4	242.38	14.23
6088.0	255.62	14.50
2099.3	267.72	14.80
1515.3	274.18	14.38
1272.4	281.99	15.61
631.3	-0.29	15.45
29.1	298.69	13.85
670.7	0.62	13.85

Appendix C

Miscellaneous results

This appendix contains additional material about results presented in Chapter 5.

C.1 Linear and 'nonlinear' transfer functions

The heave motion transfer function amplitudes for the different combinations are presented in Figure C.2. The trend for longer waves differs in ballast and cargo condition, while the different bow shapes do not affect the transfer functions significantly. The trend for the longer waves is surprising. This is affected by wall interaction and the placement of the 'Nypos tree'. A few wild readings for the nonlinear estimates are also observed for the bow 2 in cargo conditions.

The pitch transfer function amplitudes are presented in Figure C.3. The trend differs for ballast and cargo condition, and again they display a peculiar behaviour for longer waves. The wall interaction were obviously important.

The transfer function amplitudes of the midship bending moments are shown in Figure C.4. The rigid response peak of the cargo condition shows an odd behaviour due to the wall interaction. The rigid body response peaks of the ballast condition are as expected, but for bow 3 the nonlinear and linear estimates differ considerably at low frequencies. The nonlinear estimates left of the peak must be disregarded, since they were obtained from four-component waves rather than a regular wave train. This is why only the linear plots were shown for heave and pitch of ballast 3 condition in Figure C.2 and Figure C.3. Except for bow 1 in ballast condition the nonlinear effect is small. Bow 1 in ballast condition was run in higher regular waves than the other runs, explaining the significant nonlinearities,

also contributed by wave induced vibrations.

The wall interaction caused difficulties for lower speeds in particular for cargo condition, which displayed unexpectedly high nondimensional values for the rigid response peak. This possibly affected the relative importance of the wave damage somewhat. Moreover, the longest waves were possibly disturbed by the change in draft $80m$ from the wave maker (deeper close to the wave maker). The draft changed from 10 to $5m$. Figure C.1 presents the measured wave and the corresponding full scale stress along the tank. The wave was measured by wave probe 3 in front of the model, moving with a speed of $1.15m/s$. The requested wave length was $17.8m$, and waves with length exceeding $10m$ may be affected. This corresponded to encounter frequencies below $3.2/3.3rad/s$ in cargo/ballast condition at full speed. A change in the measured amplitude is visible around $60s$, which corresponds to the location of the changed draft. The amplitude close to the wave maker is almost 40% higher than far from the wave maker. A similar change is not observed in the stress amplitude. This will subsequently influence the nondimensional results depending on the length of the time selected time trace.

C.2 Second order transfer functions

Figure C.5 presents the nondimensional second order transfer function for the bending moment at the midship section, $|H(\omega_1, \omega_2)|$, for ballast 1 and cargo 1 condition, while Figure C.6 presents the same for ballast 3 and cargo 3 condition.

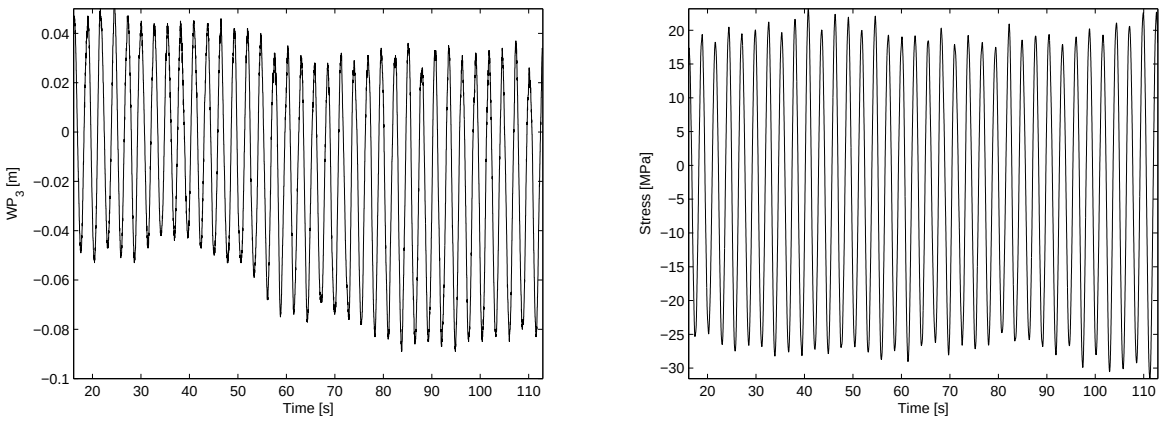

Figure C.1: *Variation of measured raw wave amplitude in front of the model, ($T = 20s$, $H = 3.5m$, $V = 1.15m/s$), and the corresponding midship deck stress. 60s corresponds to the change in draft 80m from the wave maker.*

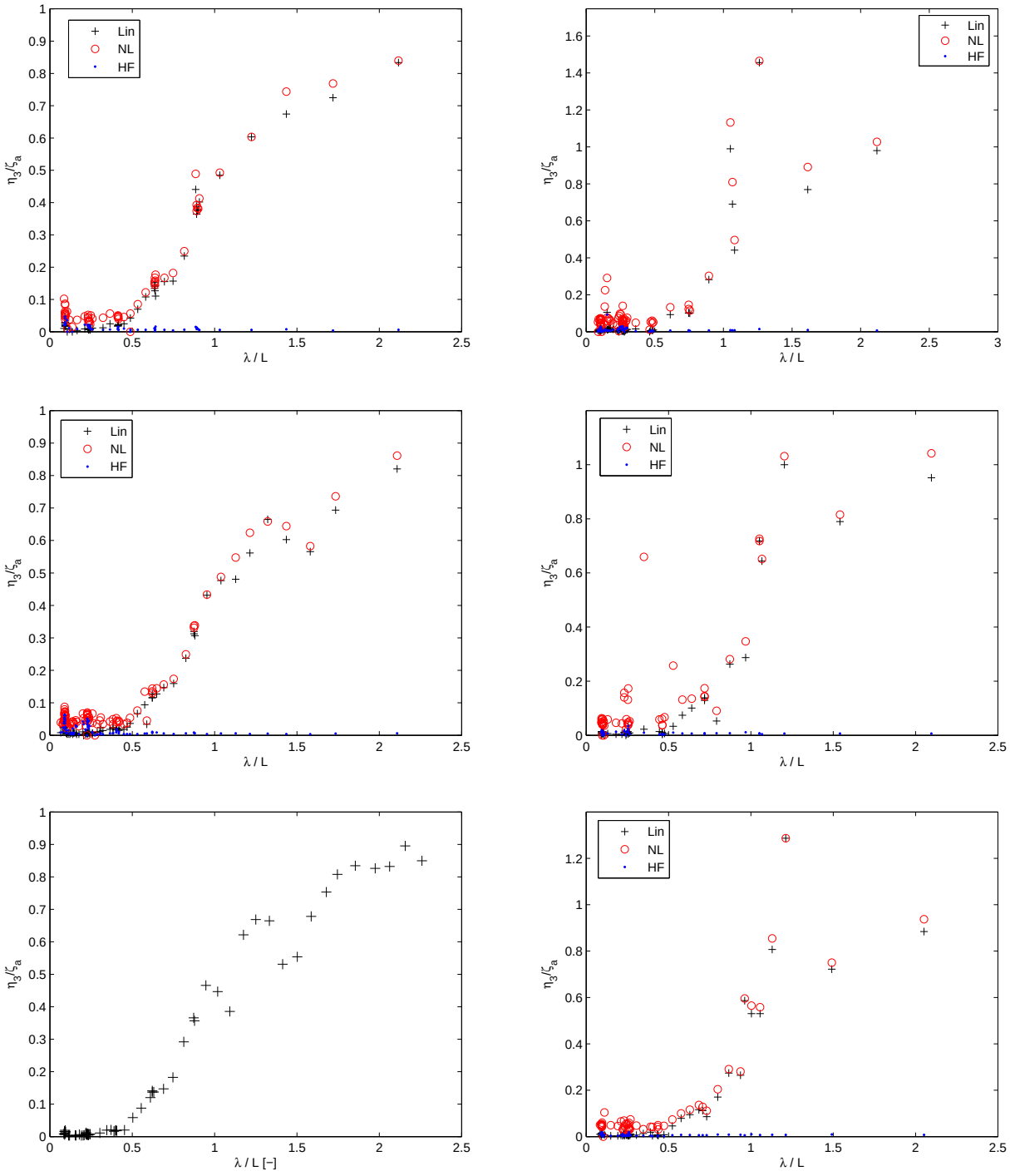

Figure C.2: *Nondim. heave transfer function for ballast (left column) and cargo condition (right column) in 15 and 13.2kn. Row 1= Bow 1, row 2= Bow 2, row 3= Bow 3.* $L = L_{PP}$

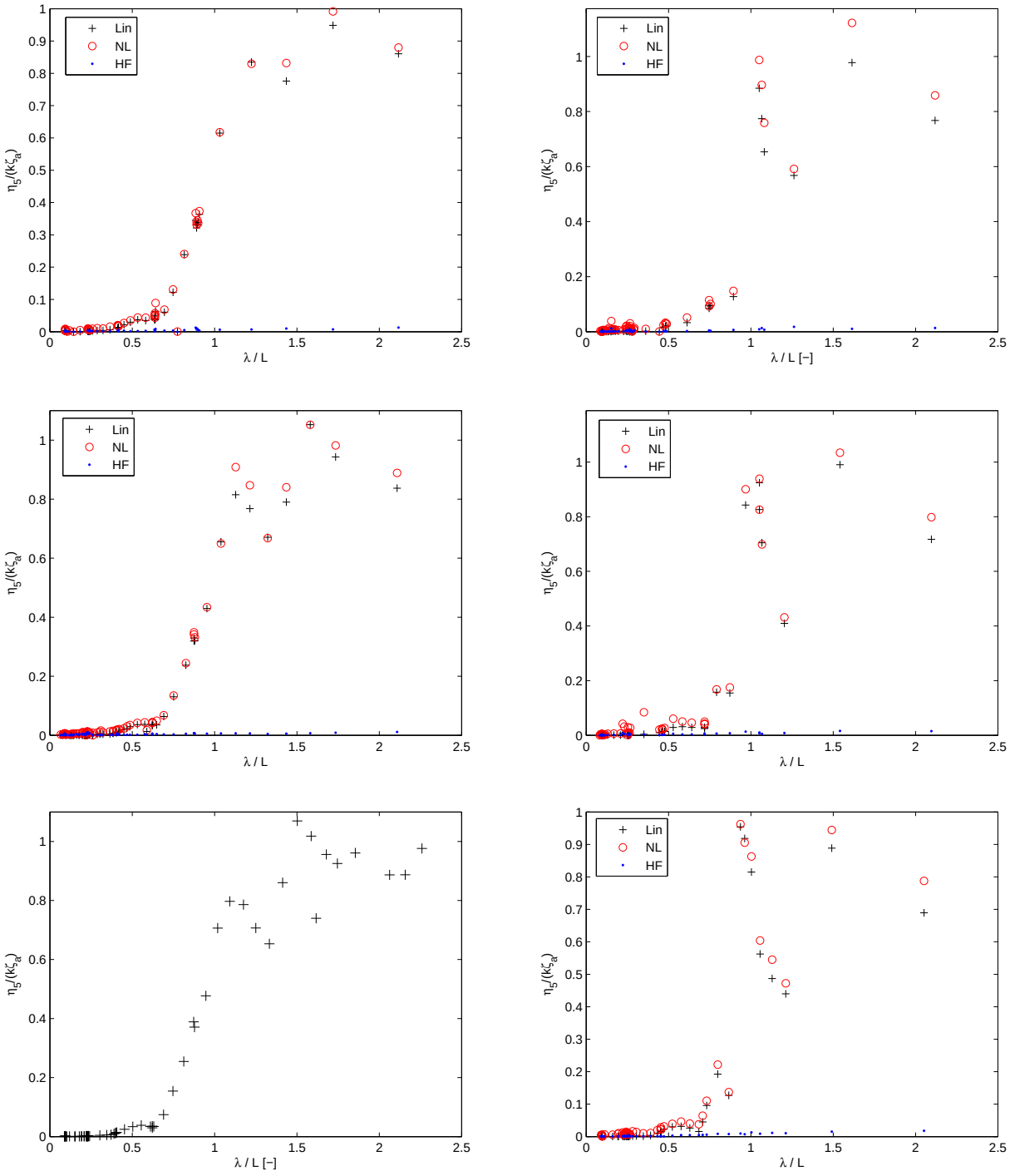

Figure C.3: *Nondim. pitch transfer function for ballast (left column) and cargo condition (right column) in 15 and 13.2kn. Row 1= Bow 1, row 2= Bow 2, row 3= Bow 3.*

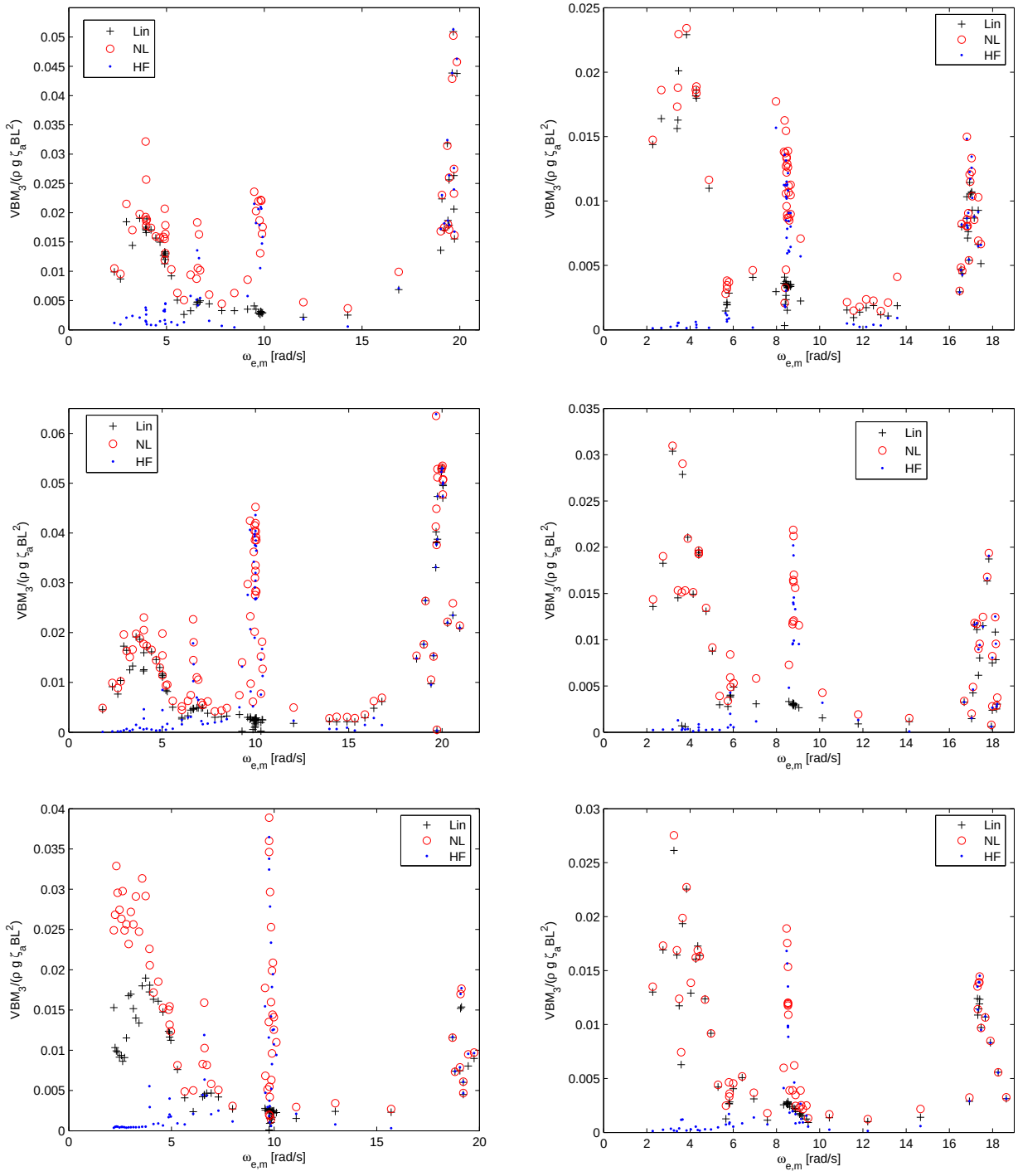

Figure C.4: *Nondim. midship moment transfer function amplitude for ballast (left column) and cargo condition (right column) in 15 and 13.2kn. Row 1= Bow 1, row 2= Bow 2, row 3= Bow 3.*

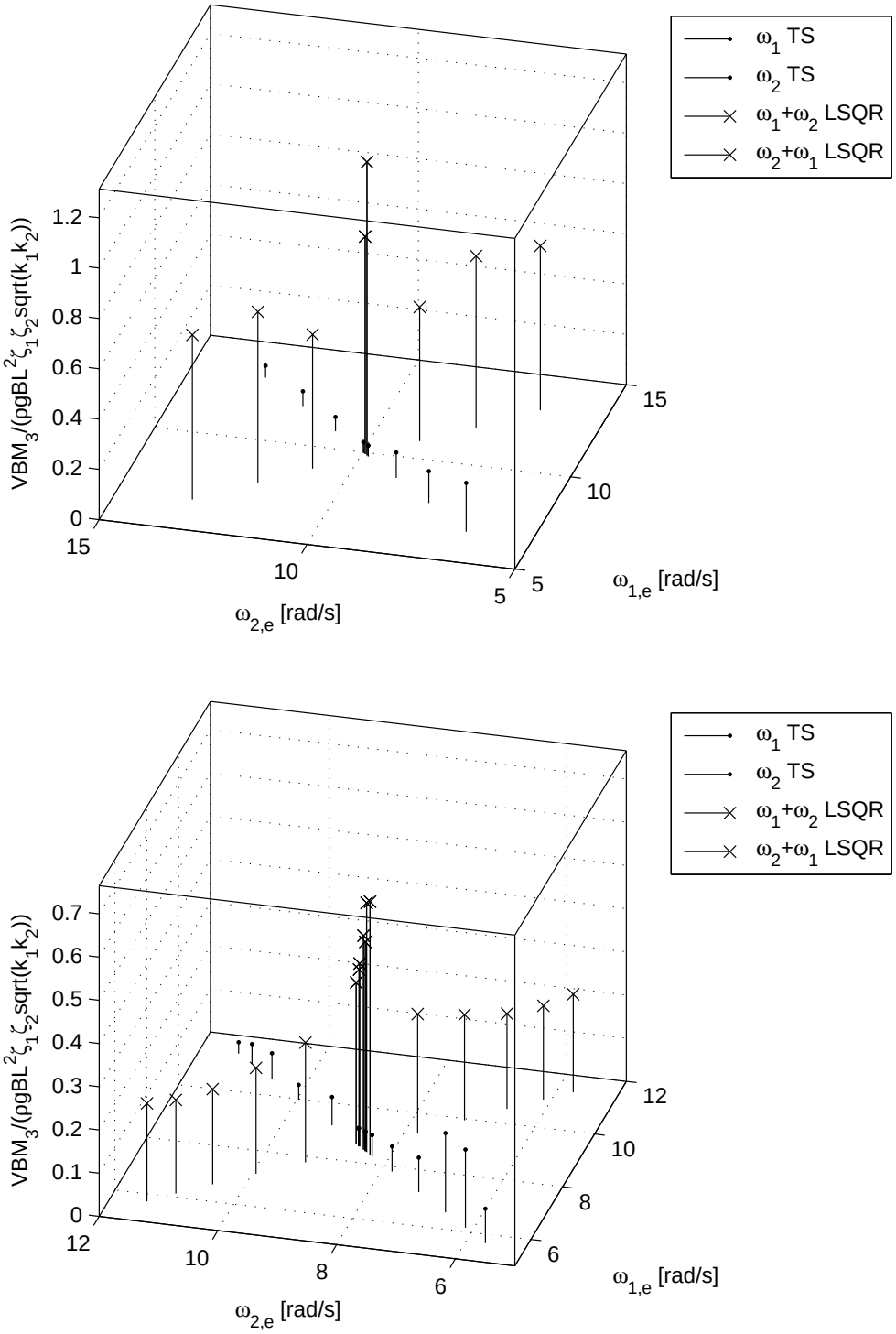

Figure C.5: *Nondim. second order transfer function for ballast 1 condition (upper) and cargo 1 condition (lower) in 15 and 13.2kn.*

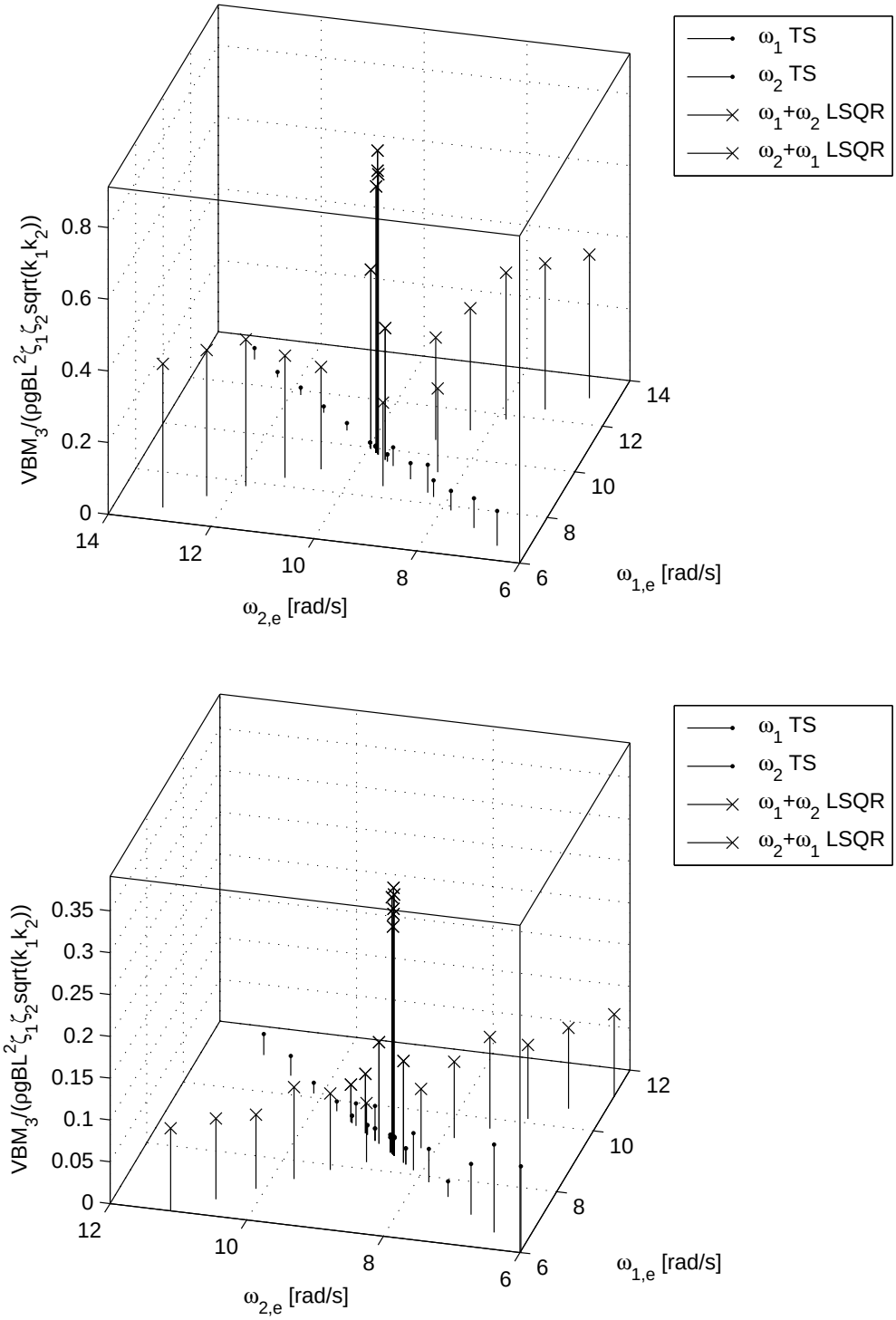

Figure C.6: *Nondim. second order transfer function for ballast 3 condition (upper) and cargo 3 condition (lower) in 15 and 13.2kn.*

C.3 Wave conditions

The model was large and may affect the irregular sea states in subsequent runs, and the wave conditions were evaluated. Table C.1 presents the sea state characteristics from wave probe 3 (WP3) for other loading conditions and bow shapes, while results for ballast 2 condition were presented in Section 5.4.4. For low speeds the exceedance of the requested wave height was observed to be somewhat higher than for high speeds, possibly due to reflection from the bow. The wave height increased slightly for bow 3, possibly caused by slightly smaller waiting time between runs, larger model and different bow shape reflection. Based on the mean and mean confindence interval it can be concluded that the waves were slightly higher than requested for bow 3. It should be noted that this is mainly due to 3D disturbance, hence it may not cause a similar increase in the vibratory response. Actually, it was observed that it caused a slight decrease for subsequent runs.

The same wave probes were used during the different tests. It was noticed that the amplifier setting differed slightly, maybe because the same wave probes were not used at the same positions. This uncertainty was regarded as small, but the bias was not estimated.

Table C.1: *JONSWAP parameters with 95% mean confidence interval from tested sea states. Values were obtained from nonlinear fit to raw and smoothed (sm.) wave spectra and from moments. Results are presented as the ratio of the measured to requested input for WP3.*

Parameter	Mean (raw)	95% mean (raw)	Mean (sm.)	95% mean (sm.)
Ballast 1				
H_S fit	1.014	0.028	1.019	0.025
H_S moment	1.032	0.023		
T_P fit	0.991	0.008	0.993	0.008
γ fit	0.986	0.191		
n fit			1.022	0.013
m fit			0.970	0.018
Cargo 1				
H_S fit	1.028	0.039	1.032	0.039
H_S moment	1.034	0.038		
T_P fit	0.999	0.011	1.001	0.012
γ fit	0.947	0.099		
n fit			1.023	0.009
m fit			0.975	0.008
Cargo 2				
H_S fit	0.975	0.045	0.960	0.032
H_S moment	0.960	0.032		
T_P fit	0.993	0.012	0.999	0.012
γ fit	0.921	0.098		
n fit			1.027	0.012
m fit			0.970	0.011
Ballast 3				
H_S fit	1.057	0.024	1.072	0.028
H_S moment	1.071	0.027		
T_P fit	0.989	0.008	0.993	0.007
γ fit	1.060	0.097		
n fit			1.030	0.009
m fit			0.973	0.007
Cargo 3				
H_S fit	1.044	0.029	1.051	0.032
H_S moment	1.055	0.032		
T_P fit	0.998	0.011	1.002	0.010
γ fit	0.958	0.112		
n fit			1.019	0.008
m fit			0.981	0.007

C.4 Relative contribution of fatigue damage from sea states

The location of the fatigue dominating sea states in North Atlantic head sea trade in realistic speeds is shown in Figure C.7 for ballast 2 condition and Figure C.8 for cargo 2 condition. The response surface method described in Section 2.8.1 were used.

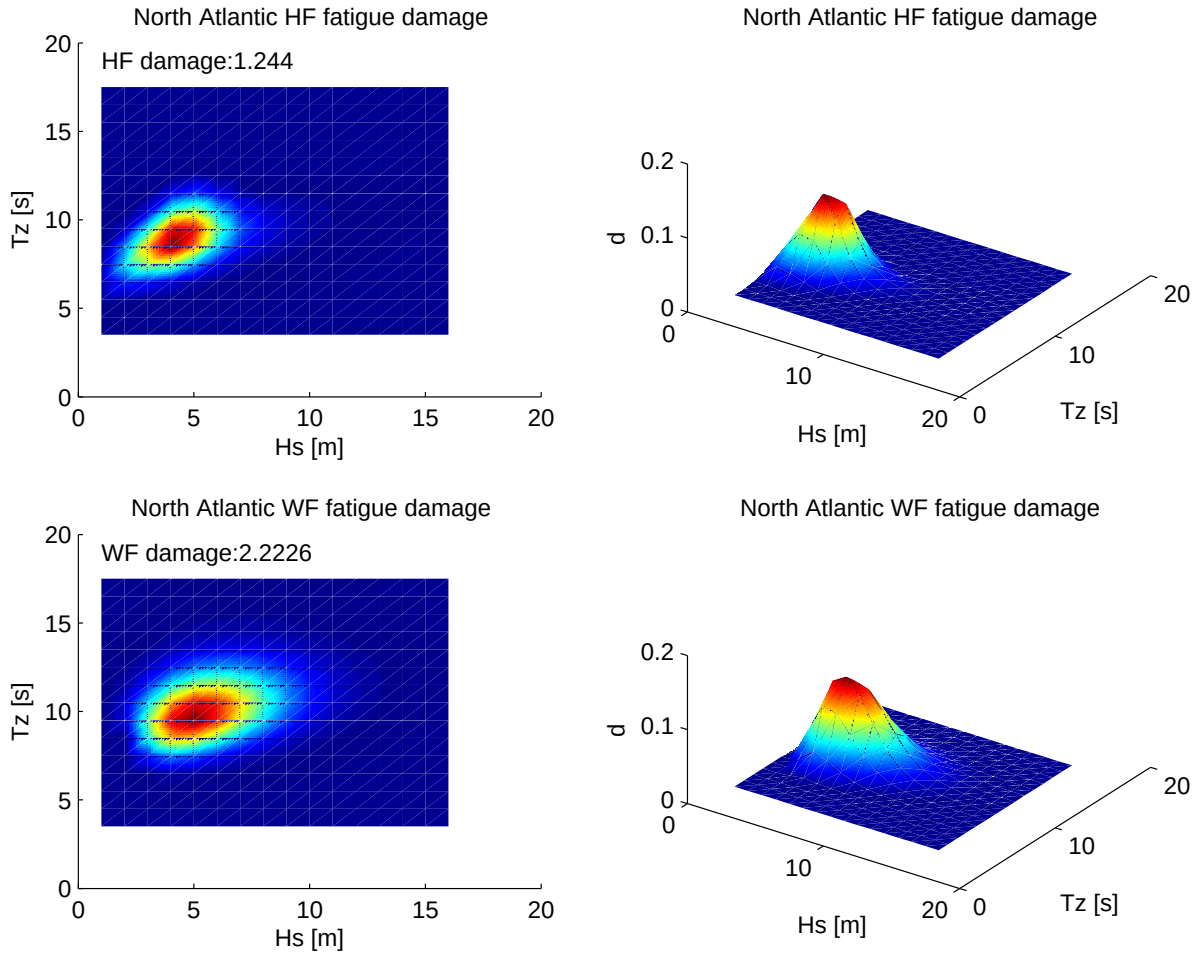

Figure C.7: *Midship HF (upper) and WF (lower) fatigue damage for ballast 2 condition in North Atlantic head sea wave environment at realistic speeds. 19 sea states were considered.*

Ballast 1 condition was only tested at full speed, Figure C.9, while cargo 1 condition was tested at realistic speed, Figure C.10.

Results for cargo 3 condition are displayed in Figure C.11, while results for ballast 3 condition are displayed in Section 5.4.5.

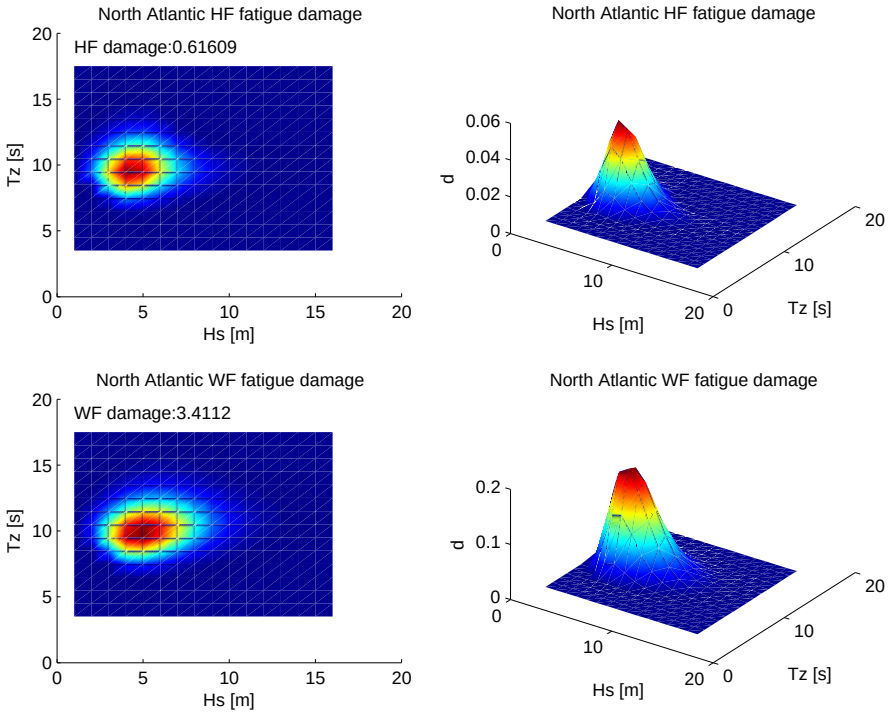

Figure C.8: *Midship HF (upper) and WF (lower) fatigue damage for cargo 2 condition in North Atlantic head sea wave environment at realistic speeds. 14 sea states were considered.*

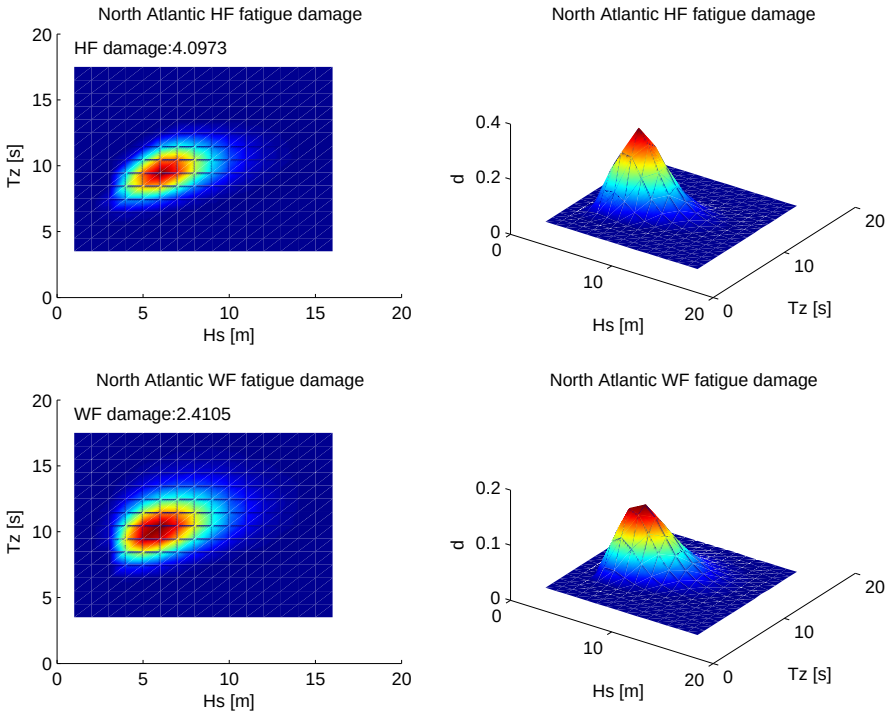

Figure C.9: *Midship HF (upper) and WF (lower) fatigue damage for ballast 1 condition in North Atlantic head sea wave environment at full speeds. 12 sea states were considered.*

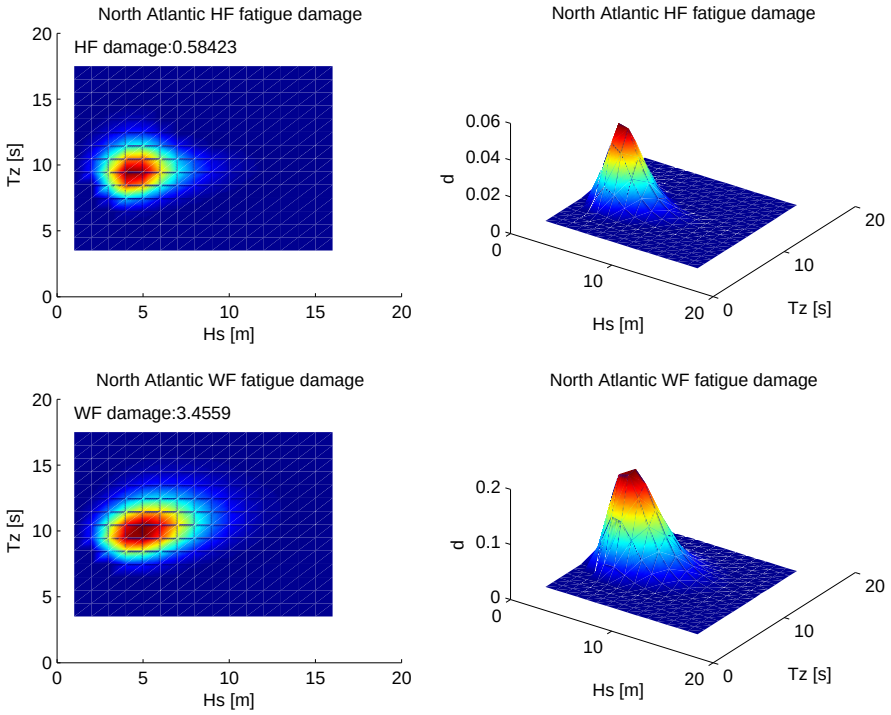

Figure C.10: *Midship HF (upper) and WF (lower) fatigue damage for cargo 1 condition in North Atlantic head sea wave environment at realistic speeds. 14 sea states were considered.*

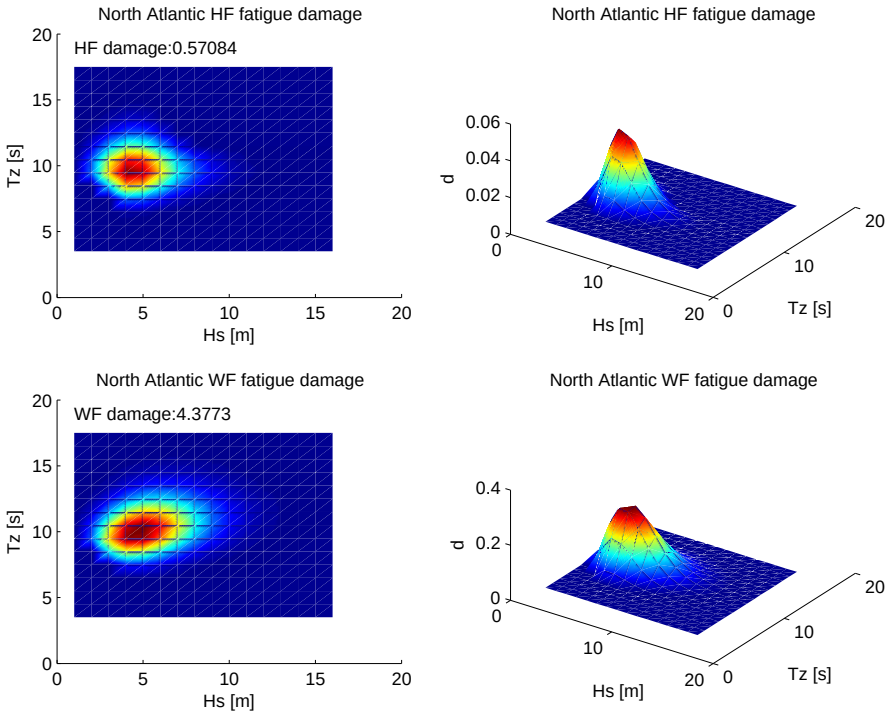

Figure C.11: *Midship HF (upper) and WF (lower) fatigue damage for cargo 3 condition in North Atlantic head sea wave environment at realistic speeds. 14 sea states were considered.*

C.5 Whipping illustrated by measured time traces

Time traces from bow 2 in ballast and cargo condition were presented in Section 5.7 displaying possible excitation sources of the vibratory response. A description of how to read the different responses was included. This section considers the pointed bow 3 in ballast and cargo condition. The bow had vertical sides and a vertical sharp stem with half apex angle of about 36^0. Some bottom flare was necessary to provide a natural transition from the original cross sectional geometry at cut 5. The bottom flare started at BL at FP and increased almost linearly to $37cm$ above the BL and $70cm$ aft of FP. The bottom flare close to FP was less than on bow 2, and $70cm$ aft of FP it was significant first below $17cm$ above BL with reference to Figure 4.4.

Figure C.12 presents vibration events at full speed of ballast 3 condition in low waves with significant wave height of $3m$. The left plot refers to a sea state with peak period of $8.2s$, while the right plot correspond to $13.6s$. The 'stem' pressure, $P3$, was measured $16cm$ to the side, $21cm$ aft of FP and $29cm$ above BL. The relative motion probe was located $9cm$ aft of FP. The draft in ballast was $32.4cm$, while the draft in cargo condition was $51.4cm$.

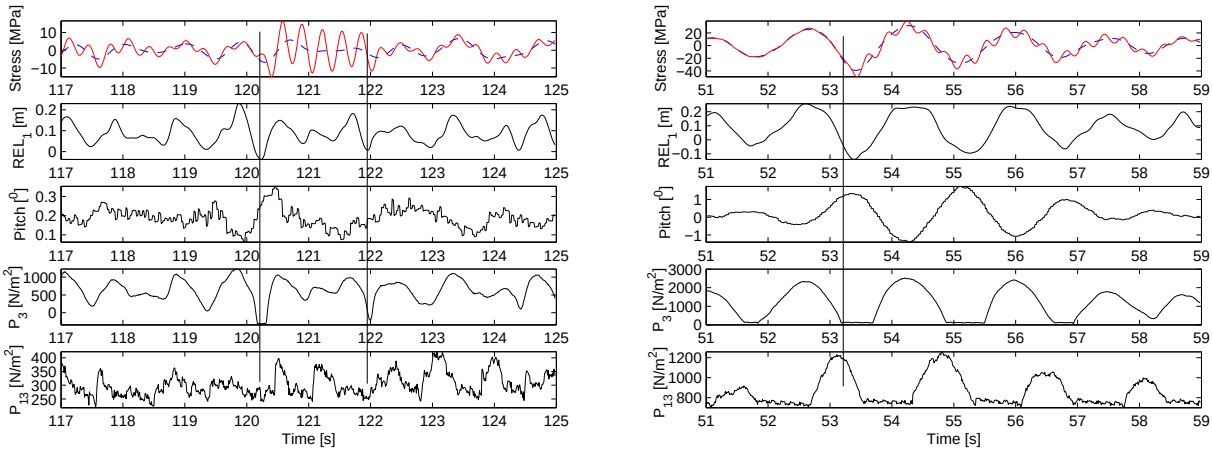

Figure C.12: *Whipping events in ballast 3 condition at $H_S = 3m$ and $U = 15kn$. Left: $T_P = 8.2s$ (run 2350), right: $T_P = 13.6s$ (run 2364). Row 1= Total (continuous) and wave pass filtered (dashed) midship stress, row 2= Relative motion in bow, row 3= Pitch, row 4= 'Stem' pressure, row 5= Stern pressure.*

The left plot presents a vibration event from forces acting on the bow. The pitch motion is small, but it is influenced by a large wave striking the bow. The stem-side pressure shows a rapid variation at the initiation of the vibration and at $122s$, when the vibration dies out due to a similar event. The difference in time corresponds to approximately 5.5 vibration cycles. The time between the peaks of the relative motion is about twice the natural period, and it indicates sum frequency exitation. The zero level of the relative

motion is 8.6cm above the still water line, which agrees with the steady wave elevation in the stationary point. The minimum measured relative motion is -3.7cm, hence the trough is 12.3cm below the steady surface. At the bow quartering, the steady surface is expected to be about -8.6/3 below the still water line. It may be expected that at the bow quartering the trough reaches down to 17cm above the BL. The upper part of the bottom flare at a height of 20cm was located 49cm behind FP. If the relative motion is 'frozen' and moved 40cm due to forward speed and traveling trough, the trough will attack the bottom flare 0.2s later. Actually, 0.2s later the hogging cycle of the vibration appear possibly due to a downward force followed by an upright force. The source therefore appears to come from bottom flare and from sum frequency effects.

The right plot of Figure C.12 shows a similar event in longer waves with significant pitch motion. Again, the bottom flare forces appear to be the source of the whipping. The vibration response is much smaller, and it is apparently in phase with the hogging moment. The phasing may be more well defined in sea states with long periods.

Figure C.13 shows whipping events from ballast 3 condition in realistic speed in 7 and 12m significant wave height. On the left plot bottom flare forces appear to be the source of the vibration, and the bottom pressure, $P4$, located 27cm aft of FP, is negative at the time of the impact. Slamming does occur in the aft ship, possibly contributed by wall interaction, but it does not influence the vibration level. On the right plot bottom impacts are observed even at zero speed, and give whipping from the exit and entry phase, but slamming pressures appear to be small. The whipping response is about 20MPa, but the maximum does not occur simultaneously as the maximum from the WF response, still the maximum hogging is significantly increased.

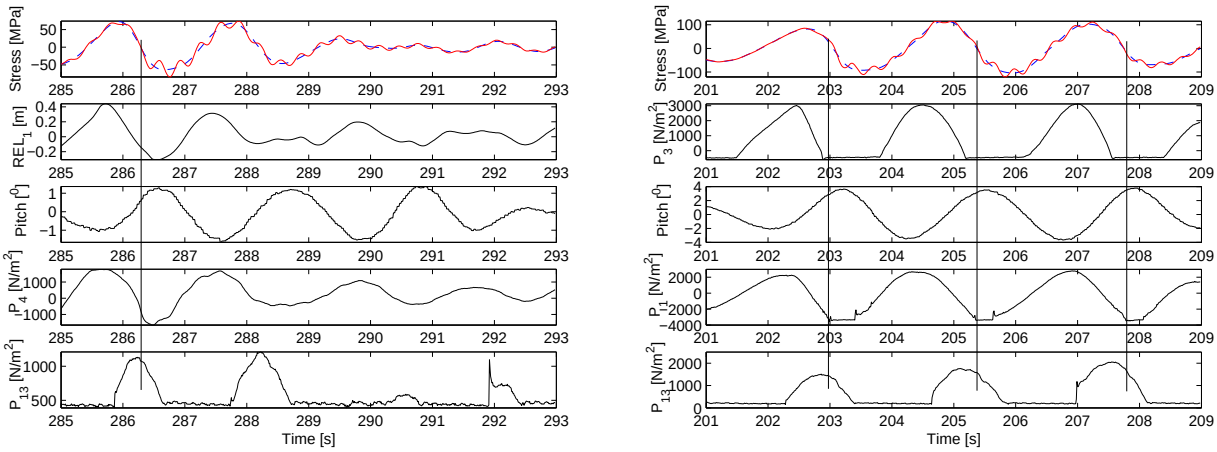

Figure C.13: *Whipping events in ballast 3 condition. Left: $H_S = 7m$, $U = 5kn$, $T_P = 12.2s$ (run 2392), right: $H_S = 12m$, $U = 0kn$, $T_P = 14.3s$ (run 2472). Row 1= Total (continuous) and wave pass filtered (dashed) midship stress, row 2= Relative motion in bow/'stem' pressure, row 3= Pitch, row 4= Bottom bow pressure, row 5= Stern pressure.*

Figure C.14 shows vibration events from cargo 3 condition in realistic speeds with a significant wave height of $3m$. The left plot has a peak period of $8.2s$, while the right plot has a peak period of $13.6s$. In the left plot there is no sign of impact, but the encounter period of the waves are roughly twice the natural period, hence this may be springing from sum frequency effects. The right plot displays a whipping event in longer waves. The steady water elevation is $7cm$ above still water line, and the measured relative motion is $21cm$ below the still water line. Based on a draft of $51cm$, the water surface is expected to move down to $20cm$ above the BL. It gives the same level of vibration with an amplitude of $10MPa$ as in ballast 3 condition in the same sea state. Again, the vibration cycle starts in hogging and increases in sagging before decaying.

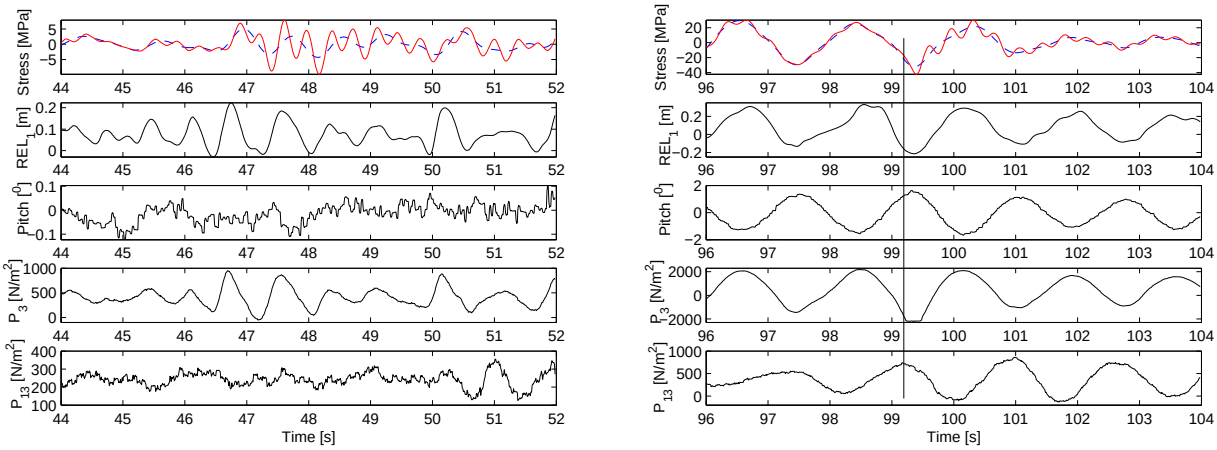

Figure C.14: *Vibration events in cargo 3 condition with $H_S = 3m$ and $U = 13.2kn$. Left: $T_P = 8.2s$ (run 2147), right: $T_P = 13.6s$ (run 2161). Row 1= Total (continuous) and wave pass filtered (dashed) midship stress, row 2= Relative motion in bow, row 3= Pitch, row 4= 'Stem' pressure, row 5= Stern pressure.*

Figure C.15 presents two whipping events from cargo 3 condition in full and zero speed in $9m$ significant wave height. Both whipping events are excited due to bottom flare impacts in the bow, and the magnitude of the whipping response is sensitive to speed. The radiation pressure due to the vibration is pronounced in the stern pressure.

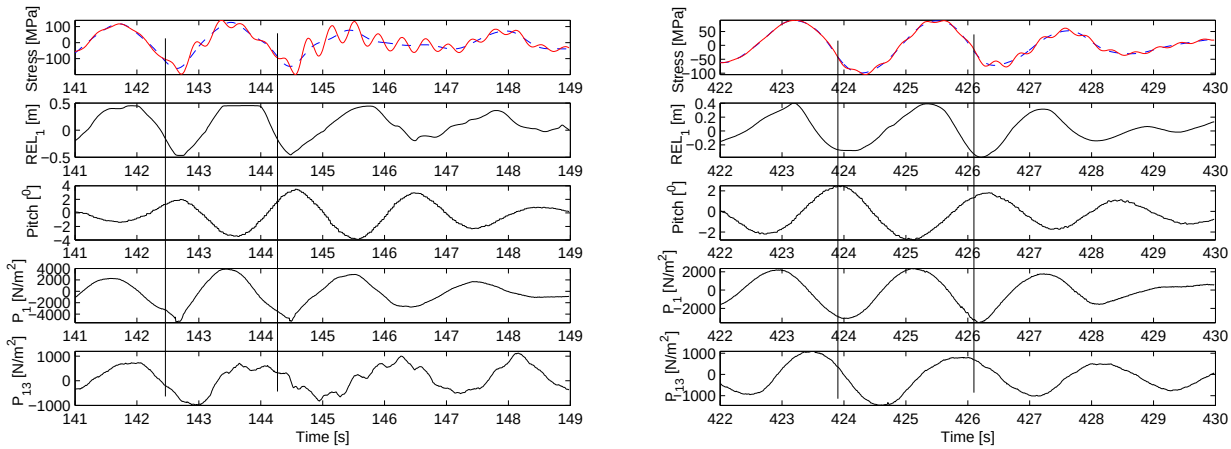

Figure C.15: *Whipping events in cargo 3 condition with $H_S = 9m$, $T_P = 15s$. Left: $U = 13.2kn$ (run 2188), right: $U = 0kn$ (run 2189). Row 1= Total (continuous) and wave pass filtered (dashed) midship stress, row 2= Relative motion in bow, row 3= Pitch, row 4= Bottom bow pressure, row 5= Stern pressure.*

C.5.1 Higher mode vibrations for bow 2 and 3 in ballast cond.

The 2-node and higher mode vibration are presented in Figure C.16 and C.17. The vibration from higher modes may display evidence of whipping. The left plot refers to ballast 2 condition, while the right plot refers to ballast 3 condition. The same sea states are considered at full speed. The axial force at midship section is used to represent the 2-node bending moment, while the forward quarter length is considered for the higher modes. $500N$ corresponds to 12.2 MPa in deck in full scale, while 100 N corresponds to 2.4 MPa (range of y-axes).

Ballast 2 condition experienced more vibration than ballast 3 condition. Three obvious reasons were

- The high damping in ballast 3 condition at low vibration levels may work as a filter reducing small springing and whipping decay responses.
- The sharp pointed bow may have reduced the sum frequency effect from reflection of incident waves
- The bottom flare causing whipping excitation was modified and somewhat reduced for bow 3.

Spikes, visible in the higher modes at 133 and 266s, came from discontinuities in the merged time series.

The whipping process is apparently more evident in the ballast 3 condition, but from the higher modes both bow geometries experience whipping now and then. The standard deviation of the midship nominal deck stress of the sea states for the two conditions are presented in Table C.2. The HF and WF values are shown with their respective zero up-crossing periods in parenthesis. The stress is significantly higher for the HF part in ballast 2 condition, while the WF part is similar.

Table C.2: *Nominal standard deviation stress in deck at midship section for ballast 2 and ballast 3 condition. HF and WF zero up-crossing periods are displayed in the parenthesis.*

Sea state	Ballast 2 WF std. [MPa]	Ballast 2 HF std. [MPa]	Ballast 3 WF std. [MPa]	Ballast 3 HF std. [MPa]
$H_S = 3m\ T_Z = 6s$	3.09 (6.10)	6.37 (1.84)	2.73 (5.88)	2.69 (1.89)
$H_S = 3m\ T_Z = 7s$	4.73 (6.95)	4.95 (1.85)	4.27 (7.22)	2.42 (1.90)
$H_S = 3m\ T_Z = 8s$	7.75 (7.93)	4.35 (1.84)	6.55 (7.97)	2.07 (1.89)
$H_S = 3m\ T_Z = 9s$	8.75 (8.60)	3.45 (1.84)	8.30 (8.65)	1.58 (1.90)
$H_S = 3m\ T_Z = 10s$	10.34 (9.20)	2.73 (1.86)	10.67 (9.28)	2.16 (1.90)
$H_S = 4m\ T_Z = 7s$	6.33 (7.63)	8.96 (1.85)	5.64 (7.05)	4.87 (1.90)
$H_S = 5m\ T_Z = 8s$	12.19 (7.79)	11.37 (1.86)	10.84 (7.79)	6.13 (1.90)

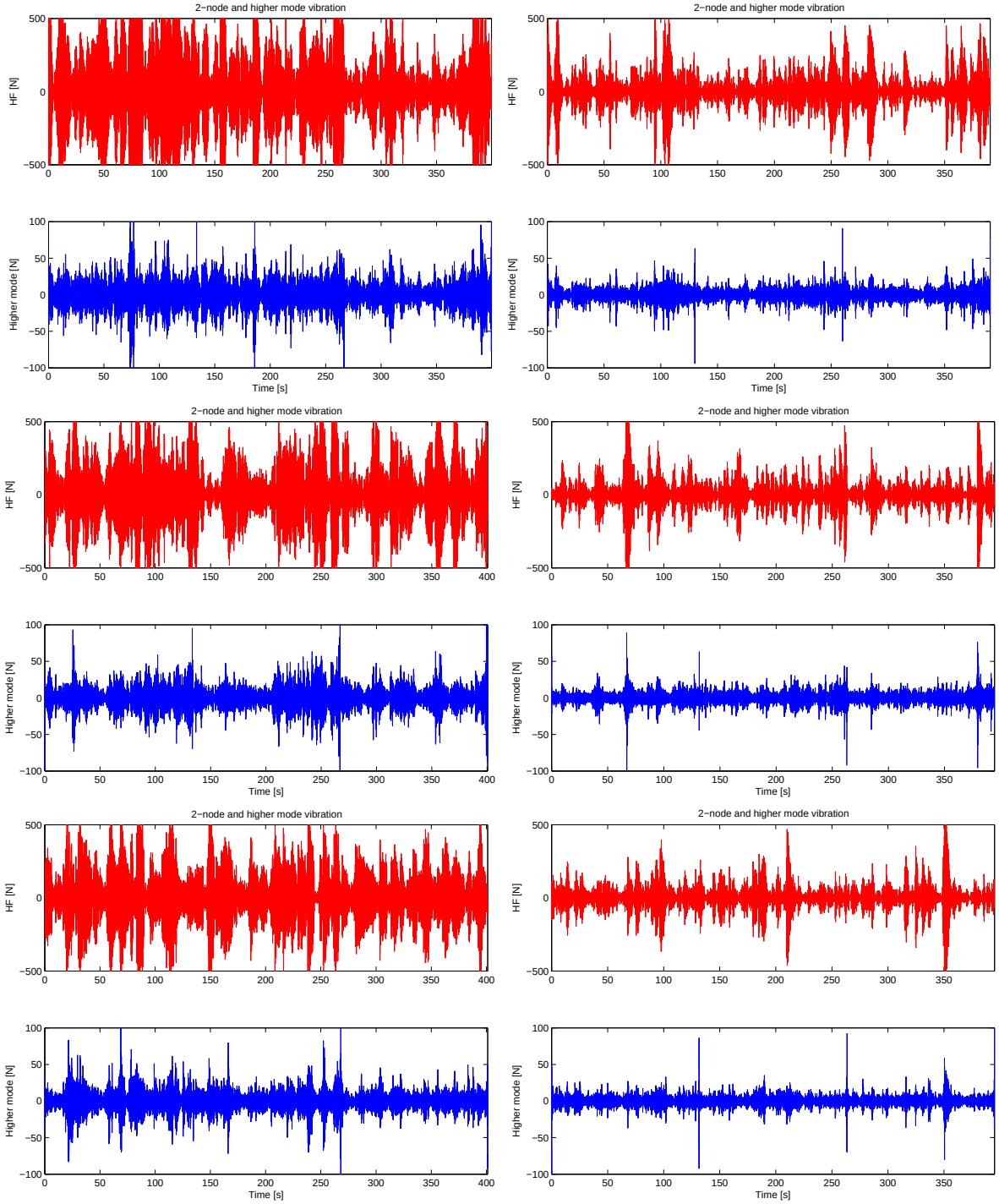

Figure C.16: *2-node vibration at midship (range $\pm 500N$) and higher mode vibration at forward quarter length (range $\pm 100N$) for ballast 2 condition (left) and ballast 3 condition (right) for $H_S = 3m$ and $U = 15kn$. Row 1 and 2: $T_P = 8.2$, row 3 and 4: $T_P = 9.5$, row 5 and 6: $T_P = 10.9s$.*

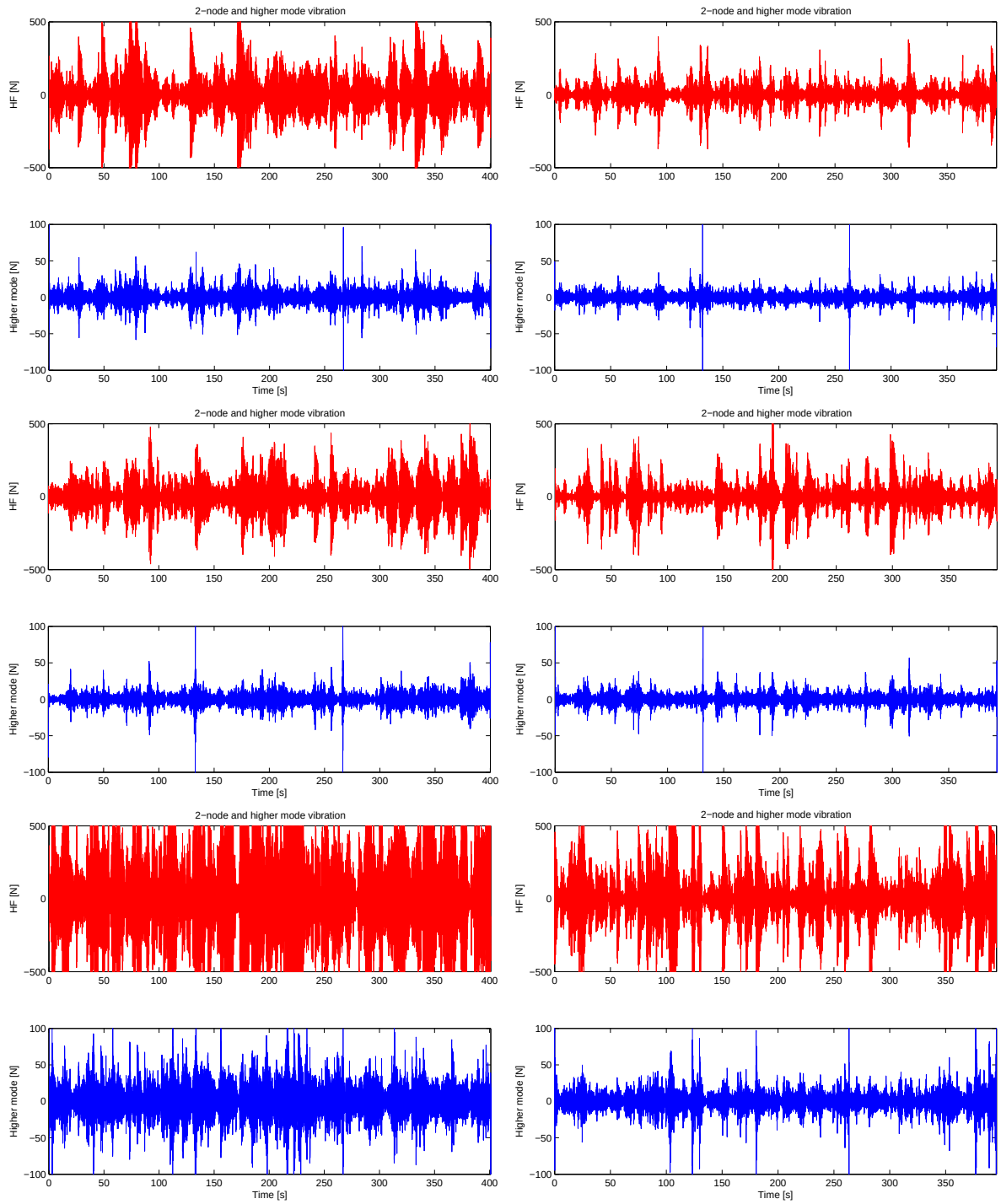

Figure C.17: *2-node vibration at midship (range $\pm 500N$) and higher mode vibration at forward quarter length (range $\pm 100N$) for ballast 2 condition (left) and ballast 3 condition (right) for $U = 15kn$. Row 1 and 2: $H_S = 3m$, $T_P = 12.2$, row 3 and 4: $H_S = 3m$, $T_P = 13.6$, row 5 and 6: $H_S = 4m$, $T_P = 9.5s$.*

R A P P 0 R T E R
UTGITT VED
INSTITUTT FOR MARIN TEKNIKK
(tidligere: FAKULTET FOR MARIN TEKNIKK)
NORGES TEKNISK-NATURVITENSKAPELIGE UNIVERSITET
PhD dissertations (not all) from the Department of Marine Technology, NTNU

UR-79-01	Brigt Hatlestad, MK:	The finite element method used in a fatigue evaluation of fixed offshore platforms. (Dr.Ing.Thesis)
UR-79-02	Erik Pettersen, MK:	Analysis and design of celluar structures. (Dr.Ing.Thesis)
UR-79-03	Sverre Valsgård, MK:	Finite difference and finite element methods applied to nonlinear analysis of plated structures. (Dr.Ing.Thesis)
UR-79-04	Nils T. Nordsve, MK:	Finite element collapse analysis of structural members considering imperfections and stresses due to fabrication. (Dr.Ing.Thesis)
UR-79-05	Ivar J.Fylling, MK:	Analysis of towline forces in ocean towing systems. (Dr.Ing.Thesis)
UR-80-06	Nils Sandsmark, MM:	Analysis of Stationary and Transient Heat Conduction by the Use of the Finite Element Method. (Dr.Ing.Thesis)
UR-80-09	Sverre Haver, MK:	Analysis of uncertainties related to the stochastic modeling of Three-Dimensional Flow Past Lifting Surfaces and Blunt Bodies. (Dr.Ing.Thesis)
UR-85-46	Alf G. Engseth, MK:	Finite element collapse analysis of turbular steel offshore structures. (Dr.Ing.Thesis)
UR-86-47	Dengody Sheshappa, MP:	A Computer Design Model for Optimizing Fishing Vessel Designs Based on Techno-Economic Analysis. (Dr.Ing.Thesis)
UR-86-48	Vidar Aanesland, MH:	A Theoretical and Numerical Study of Ship Wave Resistance. (Dr.Ing.Thesis)
UR-86-49	Heinz-Joachim Wessel, MK:	Fracture Mechanics Analysis of Crack Growth in Plate Girders. (Dr.Ing.Thesis)
UR-86-50	Jon Taby, MK:	Ultimate and Post-ultimate Strength of Dented Tubular Members. (Dr.Ing.Thesis)
UR-86-51	Walter Lian, MH:	A Numerical Study of Two-Dimensional Separated Flow Past Bluff Bodies at Moderate KC-Numbers. (Dr.Ing.Thesis)
UR-86-52	Bjørn Sortland, MH:	Force Measurements in Oscillating Flow on Ship Sections and Circular Cylinders in a U-Tube Water Tank. (Dr.Ing.Thesis)
UR-86-53	Kurt Strand, MM:	A System Dynamic Approach to One-dimensional Fluid Flow. (Dr.Ing.Thesis)
UR-86-54	Arne Edvin Løken, MH:	Three Dimensional Second Order Hydrodynamic Effects on Ocean Structures in Waves. (Dr.Ing.Thesis)
UR-86-55	Sigurd Falch, MH:	A Numerical Study of Slamming of Two-Dimensional Bodies. (Dr.Ing.Thesis)
UR-87-56	Arne Braathen, MH:	Application of a Vortex Tracking Method to the Prediction of Roll

	Damping of a Two-Dimension Floating Body. (Dr.Ing.Thesis)
UR-87-57 Bernt Leira, MR:	Caussian Vector Processes for Reliability Analysis involving Wave-Induced Load Effects. (Dr.Ing.Thesis)
UR-87-58 Magnus Småvik, MM:	Thermal Load and Process Characteristics in a Two-Stroke Diesel Engine with Thermal Barriers (in Norwegian) (Dr.Ing.Thesis)
MTA-88-59 Bernt Arild Bremdal, MP:	An Investigation of Marine Installation Processes - A Knowledge-Based Planning Approach. (Dr.Ing.Thesis)
MTA-88-60 Xu Jun, MK:	Non-linear Dynamic Analysis of Space-framed Offshore Structures. (Dr.Ing.Thesis)
MTA-89-61 Gang Miao, MH:	Hydrodynamic Forces and Dynamic Responses of Circular Cylinders in Wave Zones. (Dr.Ing.Thesis)
MTA-89-62 Martin Greenhow, MH:	Linear and Non-Linear Studies of Waves and Floating Bodies. Part I and Part 11. (Dr.Techn.Thesis)
MTA-89-63 Chang Li, MH:	Force Coefficients of Spheres and Cubes in Oscillatory Flow with and without Current.(Dr.Ing.Thesis)
MTA-89-64 Hu Ying, MP:	A Study of Marketing and Design in Development of Marine Transport Systems. (Dr.Ing.Thesis)
MTA-89-65 Arild Jæger, MH:	Seakeeping, Dynamic Stability and Performance of a Wedge Shaped Planing Hull. (Dr.Ing.Thesis)
MTA-89-66 Chan Siu Hung, MM:	The dynamic characteristics of tilting-pad bearings.
MTA-89-67 Kim Wikstrøm, MP:	Analysis av projekteringen for ett offshore projekt. (Licenciat-avhandl.)
MTA-89-68 Jiao Guoyang, MR:	Reliability Analysis of Crack Growth under Random Loading, considering Model Updating. (Dr.Ing.Thesis)
MTA-89-69 Arnt Olufsen, MK:	Uncertainty and Reliability Analysis of Fixed Offshore Structures. (Dr.Ing.Thesis)
MTA-89-70 Wu Yu-Lin, MR:	System Reliability Analyses of Offshore Structures using improved Truss and Beam Models. (Dr.Ing.Thesis)
MTA-90-71 Jan Roger Hoff, MH:	Three-dimensional Green function of a vessel with forward speed in waves. (Dr.Ing.Thesis)
MTA-90-72 Rong Zhao, MH:	Slow-Drift Motions of a Moored Two-Dimensional Body in Irregular Waves. (Dr.Ing.Thesis)
MTA-90-73 Atle Minsaas, MP:	Economical Risk Analysis. (Dr.Ing. Thesis)
MTA-90-74 Knut-Aril Farnes, MK:	Long-term Statistics of Response in Non-linear Marine Structures. (Dr.Ing. Thesis)
MTA-90-75 Torbjørn Sotberg, MK:	Application of Reliability Methods for Safety Assessment of Submarine Pipelines. (Dr.Ing. Thesis)
MTA-90-76 Zeuthen, Steffen, MP:	SEAMAID. A computional model of the design process in a constraint-based logic programming environment. An example from

the offshore domain. (Dr.Ing. Thesis)

MTA-91-77 Haagensen, Sven, MM: Fuel Dependant Cyclic Variability in a Spark Ignition Engine - An Optical Approach. (Dr.Ing. Thesis)

MTA-91-78 Løland, Geir, MH: Current forces on and flow through fish farms. (Dr.Ing. Thesis)

MTA-91-79 Hoen, Christopher, MK: System Identification of Structures Excited by Stochastic Load Processes. (Dr.Ing. Thesis)

MTA-91-80 Haugen, Stein, MK: Probabilistic Evaluation of Frequency of Collision between Ships and Offshore Platforms. (Dr.Ing. Thesis)

MTA-91-81 Sødahl, Nils, MK: Methods for Design and Analysis of Flexible Risers. (Dr.Ing. Thesis)

MTA-91-82 Ormberg, Harald, MK: Non-linear Response Analysis of Floating Fish Farm Systems. (Dr.Ing. Thesis)

MTA-91-83 Marley, Mark J., MK: Time Variant Reliability Under Fatigue

MTA-91-79 Hoen, Christopher, MK: System Identification of Structures Excited by Stochastic Load Processes. (Dr.Ing. Thesis)

MTA-91-80 Haugen, Stein, MR: Probabilistic Evaluation of Frequency of Collision between Ships and Offshore Platforms. (Dr.Ing. Thesis)

MTA-91-81 Sødahl, Nils, MK: Methods for Design and Analysis of Flexible Risers. (Dr.Ing. Thesis)

MTA-91-82 Ormberg, Harald, MK: Non-linear Response Analysis of Floating Fish Farm Systems. (Dr.Ing. Thesis)

MTA-91-83 Marley, Mark J., MK: Time Variant Reliability Under Fatigue Degradation. (Dr.Ing. Thesis)

MTA-91-84 Krokstad, Jørgen R., MH: Second-order Loads in Multidirectional Seas. (Dr.Ing. Thesis)

MTA-91-85 Molteberg, Gunnar A., MM: The application of system identification techniques to Performance Monitoring of four stroke turbocharged Diesel Engines. (Dr.Ing. Thesis)

MTA-92-86 Mørch, Hans Jørgen Bjelke, MH: Aspects of Hydrofoil Design; with Emphasis on Hydrofoil Interaction in Calm Water. (Dr.Ing. Thesis)

MTA-92-87 Chan Siu Hung, MM: Nonlinear Analysis of Rotordynamic Instabilities in High-speed Turbomachinery. (Dr.Ing. Thesis)

MTA-92-88 Bessason, Bjarni, MK: Assessment of Earthquake Loading and Response of Seismically Isolated Bridges. (Dr.Ing. Thesis)

MTA-92-89 Langli, Geir, MP: Improving Operational Safety through exploitation of Design Knowledge - an investigation of offshore platform safety. (Dr.Ing. Thesis)

MTA-92-90 Sævik, Svein, MK: On Stresses and Fatigue in Flexible Pipes. (Dr.Ing. Thesis)

MTA-92-91 Ask, Tor Ø., MM: Ignition and Flame Growth in Lean Gas-Air Mixtures. An Experimental Study with a Schlieren System. (Dr.Ing. Thesis)

MTA-86-92 Hessen, Gunnar, MK: Fracture Mechanics Analysis of Stiffened Tubular Members. (Dr.Ing. Thesis)

MTA-93-93 Steinebach, Christian, MM: Knowledge Based Systems for Diagnosis of Rotating Machinery. (Dr.Ing. Thesis)

MTA-93-94 Dalane, Jan Inge, MK: System Reliability in Design and Maintenance of Fixed Offshore Structures. (Dr.Ing. Thesis)

MTA-93-95 Steen, Sverre, MH: Cobblestone Effect on SES. (Dr.Ing. Thesis)

MTA-93-96 Karunakaran, Daniel, MK: Nonlinear Dynamic Response and Reliability Analysis of Drag-dominated Offshore Platforms. (Dr.Ing. Thesis)

MTA-93-97 Hagen, Arnulf, MP: The Framework of a Design Process Language. (Dr.Ing. Thesis)

MTA-93-98 Nordrik, Rune, MM: Investigation of Spark Ignition and Autoignition in Methane and Air Using Computational Fluid Dynamics and Chemical Reaction Kinetics. A Numerical Study of Ignition Processes in Internal Combustion Engines. (Dr.Ing.Thesis)

MTA-94-99 Passano, Elizabeth, MK: Efficient Analysis of Nonlinear Slender Marine Structures. (Dr.Ing.Thesis)

MTA-94-100 Kvålsvold, Jan, MH: Hydroelastic Modelling of Wetdeck Slamming on Multihull Vessels. (Dr.Ing.Thesis)

MTA-94-101 (Dr.Ing.Thesis) *Ikke godkjent.*

MTA-94-102 Bech, Sidsel M., MK: Experimental and Numerical Determination of Stiffness and Strength of GRP/PVC Sandwich Structures. (Dr.Ing.Thesis)

MTA-95-103 Paulsen, Hallvard, MM: A Study of Transient Jet and Spray using a Schlieren Method and Digital Image Processing. (Dr.Ing.Thesis)

MTA-95-104 Hovde, Geir Olav, MK: Fatigue and Overload Reliability of Offshore Structural Systems, Considering the Effect of Inspection and Repair. (Dr.Ing.Thesis)

MTA-95-105 Wang, Xiaozhi, MK: Reliability Analysis of Production Ships with Emphasis on Load Combination and Ultimate Strength. (Dr.Ing.Thesis)

MTA-95-106 Ulstein, Tore, MH: Nonlinear Effects of a Flexible Stern Seal Bag on Cobblestone Oscillations of an SES. (Dr.Ing.Thesis)

MTA-95-107 Solaas, Frøydis, MH: Analytical and Numerical Studies of Sloshing in Tanks. (Dr.Ing.Thesis)

MTA-95-108 Hellan, øyvind, MK: Nonlinear Pushover and Cyclic Analyses in Ultimate Limit State Design and Reassessment of Tubular Steel Offshore Structures. (Dr.Ing.Thesis)

MTA-95-109 Hermundstad, Ole A., MK: Theoretical and Experimental Hydroelastic Analysis of High Speed Vessels. (Dr.Ing.Thesis)

MTA-96-110 Bratland, Anne K., MH: Wave-Current Interaction Effects on Large-Volume Bodies in Water of Finite Depth. (Dr.Ing.Thesis)

MTA-96-111 Herfjord, Kjell, MH: A Study of Two-dimensional Separated Flow by a Combination of the Finite Element Method and Navier-Stokes Equations. (Dr.Ing.Thesis)

MTA-96-112 Æsøy, Vilmar, MM: Hot Surface Assisted Compression Ignition in a Direct Injection

Natural Gas Engine. (Dr.Ing.Thesis)

MTA-96-113 Eknes, Monika L., MK: Escalation Scenarios Initiated by Gas Explosions on Offshore Installations. (Dr.Ing.Thesis)

MTA-96-114 Erikstad, Stein O.,MP: A Decision Support Model for Preliminary Ship Design. (Dr.Ing.Thesis)

MTA-96-115 Pedersen, Egil, MH: A Nautical Study of Towed Marine Seismic Streamer Cable Configurations. (Dr.Ing.Thesis)

MTA-97-116 Moksnes, Paul O., MM: Modeling Two-Phase Thermo-Fluid Systems Using Bond Graphs. (Dr.Ing. Thesis)

MTA-97-117 Halse, Karl H., MK: On Vortex Shedding and Prediction of Vortex-Induced Vibrations of Circular Cylinders. (Dr.Ing. Thesis)

MTA-97-118 Igland, Ragnar T., MK: A Thesis Submitted in Partial Fulfilment of the Requirements for the Degree of "Doktor Ingeniør". (Dr.Ing. Thesis)

MTA-97-119 Pedersen, Hans-P., MP: Levendefiskteknologi for fiskefartøy. (Dr.Ing. Thesis)

MTA-98-120 Vikestad, Kyrre, MK: Multi-Frequency Response of a Cylinder Subjected to Vortex Shedding and Support Motions. (Dr.Ing. Thesis)

MTA-98-121 Azadi, Mohammad R.E., MK: Analysis of Static and Dynamic Pile-Soil-Jacket Behaviour. (Dr.Ing. Thesis)

MTA-98-122 Ulltang, Terje, MP: A Communication Model for Product Information. (Dr.Ing. Thesis)

MTA-98-123 Torbergsen, Erik, MM: Impeller/Diffuser Interaction Forces in Centrifugal Pumps. (Dr.Ing. Thesis)

MTA-98-124 Hansen, Edmond, MH: A Descrete Element Model to Study Marginal Ice Zone Dynamics and the Behaviour of Vessels Moored in Broken Ice. (Dr.Ing. Thesis)

MTA-98-125 Videiro, Paulo M., MK: Reliability Based Design of Marine Structures. (Dr.Ing. Thesis)

MTA-99-126 Mainçon, Philippe, MK: Fatigue Reliability of Long Welds Application to Titanium Risers. (Dr.Ing. Thesis)

MTA-99-127 Haugen, Elin M., MH: Hydroelastic Analysis of Slamming on Stiffened Plates with Application to Catamaran Wetdecks. (Dr.Ing. Thesis)

MTA-99-128 Langhelle, Nina K., MK: Experimental Validation and Calibration of Nonlinear Finite Element Models for Use in Design of Aluminium Structures Exposed to Fire. (Dr.Ing. Thesis)

MTA-99-129 Berstad, Are J., MK: Calculation of Fatigue Damage in Ship Structures. (Dr.Ing. Thesis)

MTA-99-130 Andersen, Trond M., MM: Short Term Maintenance Planning. (Dr.Ing.Thesis)

MTA-99-131 Tveiten, Bård Wathne, MK: Fatigue Assessment of Welded Aluminum Ship Details. (Dr.Ing.Thesis)

MTA-99-132 Søreide, Fredrik, MP: Applications of underwater technology in deep water archaeology. Principles and practice. (Dr.Ing.Thesis)

MTA-99-133 Tønnessen, Rune, MH: A Finite Element Method Applied to Unsteady Viscous Flow Around

2D Blunt Bodies With Sharp Corners. (Dr.Ing.Thesis)

MTA-99-134 Elvekrok, Dag R., MP: Engineering Integration in Field Development Projects in the Norwegian Oil and Gas Industry. The Supplier Management of Norne. (Dr.Ing.Thesis)

MTA-99-135 Fagerholt, Kjetil, MP: Optimeringsbaserte Metoder for Ruteplanlegging innen skipsfart. (Dr.Ing.Thesis)

MTA-99-136 Bysveen, Marie, MM: Visualization in Two Directions on a Dynamic Combustion Rig for Studies of Fuel Quality. (Dr.Ing.Thesis)

MTA-2000-137 Storteig, Eskild, MM: Dynamic characteristics and leakage performance of liquid annular seals in centrifugal pumps. (Dr.Ing.Thesis)

MTA-2000-138 Sagli, Gro, MK: Model uncertainty and simplified estimates of long term extremes of hull girder loads in ships. (Dr.Ing.Thesis)

MTA-2000-139 Tronstad, Harald, MK: Nonlinear analysis and design of cable net structures like fishing gear based on the finite element method. (Dr.Ing.Thesis)

MTA-2000-140 Kroneberg, André, MP: Innovation in shipping by using scenarios. (Dr.Ing.Thesis)

MTA-2000-141 Haslum, Herbjørn Alf, MH: Simplified methods applied to nonlinear motion of spar platforms. (Dr.Ing.Thesis)

MTA-2001-142 Samdal, Ole Johan, MM: Modelling of Degradation Mechanisms and Stressor Interaction on Static Mechanical Equipment Residual Lifetime. (Dr.Ing.Thesis)

MTA-2001-143 Baarholm, Rolf Jarle, MH: Theoretical and experimental studies of wave impact underneath decks of offshore platforms.
(Dr.Ing. Thesis)

MTA-2001-144 Wang, Lihua, MK: Probabilistic Analysis of Nonlinear Wave-induced Loads on Ships. (Dr.Ing. Thesis)

MTA-2001-145 Kristensen, Odd H. Holt, MK: Ultimate Capacity of Aluminium Plates under Multiple Loads, Considering HAZ Properties. (Dr.Ing. Thesis)

MTA-2001-146 Greco, Marilena, MH: A Two-Dimensional Study of Green-Water Loading. (Dr.Ing. Thesis)

MTA-2001-147 Heggelund, Svein E., MK: Calculation of Global Design Loads and Load Effects in Large High Speed Catamarans. (Dr.Ing. Thesis)

MTA-2001-148 Babalola, Olusegun T., MK: Fatigue Strength of Titanium Risers - Defect Sensitivity. (Dr.Ing. Thesis)

MTA-2001-149 Mohammed, Abuu K., MK: Nonlinear Shell Finite Elements for Ultimate Strength and Collapse Analysis of Ship Structures. (Dr.Ing. Thesis)

MTA-2002-150 Holmedal, Lars E., MH: Wave-current interactions in the vicinity of the sea bed. (Dr.Ing. Thesis)

MTA20-02-151 Rognebakke, Olav F., MH: Sloshing in rectangular tanks and interaction with ship motions (Dr.ing.thesis)

MTA-2002-152 Lader, Pål Furset, MH: Geometry and Kinematics of Breaking Waves. (Dr.Ing. Thesis)

MTA-2002-153 Yang, Qinzheng, MH: Wash and wave resistance of ships in finite water depth. (Dr.Ing.

	Thesis)
MTA-2002-154 Melhus, Øyvin, MM:	Utilization of VOC in Diesel Engines. Ignition and combustion of VOC released by crude oil tankers. (Dr.Ing. Thesis)
MTA-2002-155 Ronæss, Marit, MH:	Wave Induced Motions of Two Ships Advancing on Parallel Course. (Dr.Ing. Thesis)
MTA-2002-156 Økland, Ole D., MK:	Numerical and experimental investigation of whipping in twin hull vessels exposed to severe wet deck slamming. (Dr.Ing. Thesis)
MTA-2002-157 Ge, Chunhua, MK:	Global Hydroelastic Response of Catamarans due to Wet Deck Slamming. (Dr.Ing. Thesis)
MTA-2002-158 Byklum, Eirik, MK:	Nonlinear Shell Finite Elements for Ultimate Strength and Collapse Analysis of Ship Structures. (Dr.Ing. Thesis).
IMT-2003-1 Chen, Haibo, MK:	Probabilistic Evaluation of FPSO-Tanker Collision in Tandem Offloading Operation. (Dr.Ing.Thesis)
IMT-2003-2 Skaugset, Kjetil Bjørn, MK	On the Suppression of Vortex Induced Vibrations of Circular Cylinders by Radial Water Jets. (Dr.ing.Thesis)
IMT-2003-3 Chezhian, Muthu	Three-Dimensional Analysis of Slamming (Dr.ing. Thesis)
IMT-2003-4 Buhaug, Øyvind	Deposit Formation on cylinder Liner Surfaces in Medium Speed Engines (Dr.ing.thesis)
IMT-2003-5 Tregde, Vidar	Aspects of Ship Design; Optimization of Aft Hull with Inverse Geometry Design (Dr.ing.thesis)
IMT-2003-6 Wist, Hanne Therese	Statistical Properties of Successive Ocean Wave Parameters (Dr.ing.thesis)
IMT-2004-7, Ransau, Samuel	Numerical Methods for Flows with Evolving Interfaces (Dr.ing.thesis)
IMT-2004-8, Soma, Torkel	Blue-Chip or Sub-Standard. A data interrogation approach of identity safety characteristics of shipping organization (Dr.ing.thesis)
IMT-2004-9 Ersdal, Svein	An experimental study of hydrodynamic forces on cylinders and cables in near axial flow (Dr.ing.thesis)
IMT-2005-10 Brodtkorb, Per Andreas	The Probability of Occurrence of Dangerous Wave Situations at Sea (Dr.ing.thesis)
IMT-2005-11 Yttervik, Rune	Ocean current variability in relation to offshore engineering (Dr.ing.thesis)
IMT-2005-12 Fredheim, Arne	Current Forces on Net-Structures (Dr.ing.thesis)
IMT-2005-13 Heggernes, Kjetil	Flow around marine structures (Dr.ing. thesis)
IMT-2005-14 Fouques, Sebastien	Lagrangian Modelling of Ocean Surface Waves and Synthetic Aperture Radar Wave Measurements (Dr.ing. thesis)
IMT-2006-15 Holm, Håvard	Numerical calculation of viscous free surface flow around Marine structures

IMT-2006-16 Bjørheim, Lars G.	Failure Assessment of Long Through Thickness Fatigue Cracks in Ship Hulls (Dr.ing.thesis)
IMT-2006-17 Hansson, Lisbeth	Safety Management for Prevention of Occupational Accidents (Dr.ing.thesis)
IMT-2006-18 Zhu, Xinying	Application of the CIP Method to Strongly Nonlinear Wave-Body Interaction Problems (Dr.ing.thesis)
IMT-2006-19 Reite, Karl Johan	Modeling and Control of Trawl Systems
IMT-2007-20 Storhaug, Gaute	Experimental Investigation of Wave Induced Vibrations and Their Effect on the Fatigue Loading of Ships (Dr. ing. thesis).
IMT-2007-21 Sun, Hui	A Boundary Element Method Applied to Strongly Nonlinear Wave-Body Interaction Problems. (CeSOS).